UNIL | Université de Lausanne

Unicentre
CH-1015 Lausanne
http://serval.unil.ch

Year : 2021

Mathematical modelling of collision orogens

Candioti Lorenzo Giuseppe

Candioti Lorenzo Giuseppe, 2021, Mathematical modelling of collision orogens

Originally published at : Thesis, University of Lausanne

Posted at the University of Lausanne Open Archive http://serval.unil.ch
Document URN : urn:nbn:ch:serval-BIB_1F92FB8092966

Droits d'auteur
L'Université de Lausanne attire expressément l'attention des utilisateurs sur le fait que tous les documents publiés dans l'Archive SERVAL sont protégés par le droit d'auteur, conformément à la loi fédérale sur le droit d'auteur et les droits voisins (LDA). A ce titre, il est indispensable d'obtenir le consentement préalable de l'auteur et/ou de l'éditeur avant toute utilisation d'une oeuvre ou d'une partie d'une oeuvre ne relevant pas d'une utilisation à des fins personnelles au sens de la LDA (art. 19, al. 1 lettre a). A défaut, tout contrevenant s'expose aux sanctions prévues par cette loi. Nous déclinons toute responsabilité en la matière.

Copyright
The University of Lausanne expressly draws the attention of users to the fact that all documents published in the SERVAL Archive are protected by copyright in accordance with federal law on copyright and similar rights (LDA). Accordingly it is indispensable to obtain prior consent from the author and/or publisher before any use of a work or part of a work for purposes other than personal use within the meaning of LDA (art. 19, para. 1 letter a). Failure to do so will expose offenders to the sanctions laid down by this law. We accept no liability in this respect.

UNIL | Université de Lausanne
Institut des sciences
de la Terre

UNIL | Université de Lausanne
Swiss Geocomputing
Centre

Faculté des géosciences et de l'environnement

Institut des sciences de la Terre

Mathematical modelling of collision orogens

Thèse de doctorat

présentée à la Faculté des géosciences et de l'environnement de l'Université de Lausanne par

Lorenzo Giuseppe Candioti

Maîtrise ès Sciences en géosciences de la Johannes Gutenberg–Universität Mainz

Jury

Prof. Dr. Stefan M. Schmalholz	Université de Lausanne	Directeur de thèse
Prof. Dr. Yury Y. Podladchikov	Université de Lausanne	Expert interne
Prof. Dr. Taras V. Gerya	ETH Zürich	Expert externe
Prof. Dr. Christian Kull	Université de Lausanne	Président du jury

Lausanne, 2021

UNIL | Université de Lausanne
Faculté des géosciences et de l'environnement
bâtiment Géopolis bureau 4631

IMPRIMATUR

Vu le rapport présenté par le jury d'examen, composé de

Président de la séance publique :	M. le Professeur Christian Kull
Président du colloque :	M. le Professeur Christian Kull
Directeur de thèse :	M. le Professeur Stefan Schmalholz
Expert interne :	M. le Professeur Yury Podladchikov
Expert externe :	M. le Professeur Taras Gerya

Le Doyen de la Faculté des géosciences et de l'environnement autorise l'impression de la thèse de

Monsieur Lorenzo Giuseppe CANDIOTI

Titulaire d'un Master en sciences de la Terre
de l'Université Johannes Gutenberg

intitulée

Mathematical modelling of collision orogens

Lausanne, le 25 mars 2021

Pour le Doyen de la Faculté des géosciences et de l'environnement

Professeur Christian Kull

I dedicate this work to my beloved grandparents Ida Rossano & Gennaro Candioti
and Johanna & Karl Richter.

Der Mensch kann auf die Natur nicht einwirken, sich keine ihrer Kräfte aneignen,
wenn er nicht die Naturgesetze nach Mass- und Zahlenverhältnissen kennt.
— Alexander von Humboldt

Contents

Abstract

The formation of orogenic belts, like the Western Alps and the Himalayas, is an impressive manifestation of Plate Tectonics. Many physical processes, such as subduction initiation, leading to the formation of collisional orogens are embedded in long-term (>160 Myr) geodynamic cycles often involving subsequent phases of extension, cooling without plate deformation and convergence. Observations from orogenic belts indicate deep burial and exhumation of continental and oceanic crustal rocks during mountain building. In fact, high-pressure (>1.3 GPa) and ultrahigh-pressure (>2.7 GPa), (U)HP, mineral assemblages were first discovered in continental rocks from the Western Alps in 1984 and have since been observed in mountain ranges worldwide. Quantifying the physical mechanisms driving the formation and exhumation of (U)HP units provides crucial insights into plate tectonic processes forming orogenic belts. Many geodynamic aspects related to mountain building remain elusive, including: (i) structural and thermal inheritance impacting on subduction-related processes, (ii) the magnitude and relative importance of forces driving the formation of orogenic belts and (iii) the mechanisms explaining the formation and exhumation of (U)HP units.

This thesis addresses these aspects and aims at shedding new light on the formation of orogenic belts embedded in long-term geodynamic cycles of coupled lithosphere–upper mantle deformation. To this end, two-dimensional high-resolution petrological-thermo-mechanical numerical models are presented and the following deformation phases are modelled: (i) formation of hyperextended magma-poor margins and opening of a marine basin floored by exhumed mantle, (ii) cooling without plate deformation establishing upper mantle convection, (iii) model-internally consistent subduction initiation and closure of the marine basin and (iv) the formation and exhumation of coherent (U)HP units during mountain building. Deformation velocities are constrained by plate motion reconstructions from the European and Adriatic plate. The impact of upper mantle convection on the subduction phase, the dominating forces driving the dynamics within growing collisional orogens, and mechanisms for (U)HP rock exhumation are investigated.

It is demonstrated that: (i) hyperextension, cooling without plate deformation, subduction initiation and the evolution of a subduction zone coupled to upper mantle convection can be predicted by a single model based on the fundamental laws of physics. The location of subduction initiation and the polarity of the evolving subduction forms spontaneously, i.e. without a priori prescription. The vigour of upper mantle convection controls whether single-slab or divergent double-slab subduction evolves. (ii) Shear force-dominated orogen dynamics form thrust wedges and major crustal volumes of the subducting plate escape subduction early. In contrast, buoyancy force-dominated orogen dynamics involve deep burial and either exhumation of minor crustal volumes close to the surface, or relamination of major crustal volumes below the upper plate. (iii) Buckling-induced local upper plate extension triggering buoyant uplift of coherent (U)HP units is a feasible synconvergent exhumation mechanism. Predicted peak metamorphic conditions, exhumation velocities and the deformation history of the exhumed coherent (U)HP units are consistent with petrological estimates, structural observations and geophysical data from natural (U)HP terranes such as the Western Alps and the Himalayas. The petrological–thermomechanical models presented here predict several first-order processes related to the burial and exhumation cycle of the crust within mountain building. Therefore, the models are transferable, robust and provide new insights into the long-term plate tectonic processes forming orogenic belts.

Résumé

La formation d'orogènes, comme les Alpes occidentales et l'Himalaya, est une manifestation impressionnante de la tectonique des plaques. Les processus tectoniques, tels que l'initiation de la subduction, conduisant à la formation de chaînes de collision, s'inscrivent dans des cycles géodynamiques à long terme (>160 Myr) impliquant souvent des phases d'extension, de refroidissement sans déformation des plaques et de convergence. Les observations des ceintures orogéniques indiquent l'enfouissement et l'exhumation de roches crustales continentales et océaniques. En fait, des roches de (ultra)haute pression (UHP) ont été découvertes pour la première fois dans les Alpes occidentales en 1984 et ont, depuis, été observées aux limites des plaques convergentes dans le monde entier. La quantification des mécanismes physiques conduisant à la formation et à l'exhumation des unités (U)HP fournit des informations cruciales sur les processus tectoniques formant des chaînes de montagnes. De nombreux aspects géodynamiques liés aux orogenèses restent méconnus, notamment : (i) les héritages structurels et thermiques ayant un impact sur les processus liés à la subduction, (ii) l'ampleur et l'importance relative de la flottabilité et des forces de cisaillement entraînant la formation de ceintures orogéniques et (iii) les mécanismes, compatibles avec les données naturelles, expliquant la formation et l'exhumation des roches (U)HP.

Cette thèse vise à jeter un nouvel éclairage sur la formation des ceintures orogéniques intégrées dans les cycles géodynamiques à long terme de déformation de la lithosphère. À cette fin, des modèles numériques en deux dimensions et à haute résolution en pétrologie-thermo-mécanique sont présentés. Les phases de déformation suivantes sont modélisées : (i) formation de marges hyper étendues pauvres en magma et ouverture d'un bassin marin dont le sol est constitué de manteau exhumé, (ii) refroidissement sans déformation des plaques tectoniques établissant une convection du manteau supérieur, (iii) initiation et fermeture du bassin marin par subduction cohérente avec le modèle et (iv) formation et exhumation d'unités (U)HP dans une chaîne de montagne en croissance. Les vitesses de déformation appliquées sont limitées par les reconstructions du mouvement des plaques européennes et adriatiques. L'impact de la convection du manteau supérieur sur les différentes étapes, les forces dominantes qui régissent la dynamique au sein des orogènes en croissance et les mécanismes d'exhumation des unités (U)HP sont étudiés.

Il est démontré que (i) l'hyper-extension, le refroidissement sans déformation des plaques, l'initiation de la subduction et l'évolution d'une zone de subduction, couplée à la convection du manteau supérieur, peuvent être prédits par un modèle unique. L'emplacement de l'initiation de la subduction et la polarité de la subduction se mettent en place spontanément. L'intensité de la convection du manteau supérieur contrôle l'évolution d'une seule ou de deux zones de subduction divergentes. (ii) La dynamique des orogenèses, dominées par la force de cisaillement, forme des prismes de poussée et des grands volumes crustaux de la plaque en subduction s'échappent rapidement de la subduction. En revanche, la dynamique des orogenèses dominées par la force de flottabilité implique un enfouissement profond et soit l'exhumation d'importants volumes crustaux, soit la relamination de zones crustales sous la plaque supérieure. (iii) L'exhumation des roches (U)HP s'explique par deux mécanismes successifs : premièrement, le forçage tectonique induit un plissement dans la croûte supérieure de la plaque en subduction. La nappe de plis ainsi exhumée déclenche une extension de la plaque supérieure. Secondement, sous l'effet des forces de flottabilité, des unités crustales profondément subductées s'exhument de manière cohérente sous forme de diapirs individuels le long du canal de subduction. Les chemins pressions-température prédits et l'historique des déformations des unités cohérentes de roches (U)HP exhumées sont conformes aux données naturelles et aux observations structurelles des zones contenant des roches (U)HP des Alpes occidentales et de l'Himalaya. Les modèles à haute résolution présentés ici fournissent de nouvelles informations sur les processus de la tectonique des plaques à long terme qui conduisent à la formation de chaînes de montagnes.

CHAPTER 1

General Introduction

1.1 Geodynamic context

Planet Earth's outermost shell, the lithosphere, is shattered into a number of pieces that move relative to each other; a theory known as Plate Tectonics. Over hundreds of millions of years, plates may diverge or converge above the underlying mantle flowing, or convecting, like a fluid. Eventually, the convergence of tectonic plates leads to the formation of impressive mountain ranges like the Alps and Himalayas. These mountain ranges play an important role in modern societies. Especially for countries like Switzerland where more than 50% of the surface lies 1000 m above the sea-level (Weingartner and Pearson, 2001). For these societies, understanding the fundamental physical processes leading to the formation of mountain ranges is key to build infrastructure and assess environmental risks.

Worldwide observations of high-pressure (>1.3 GPa for eclogite facies) and (ultra)high-pressure (>2.7 GPa), (U)HP, terranes (Guillot et al., 2009) indicate deep burial (>50 km) of upper crustal rocks within subduction zones and exhumation of (U)HP rocks during mountain building. Since the first observations of coesite, the ultrahigh-pressure polymorph of quartz, in continental upper crustal rocks from the Western Alps (Chopin, 1984) the essential question of how such crustal (U)HP rocks have been formed and exhumed in growing orogenic belts is still unanswered.

1.1.1 Formation and exhumation of (ultra)high-pressure rocks

Due to the long-term and large-scale nature of the subduction and exhumation processes, involving the coupling of heat transfer, metamorphic reactions and lithosphere deformation, the main method to study (U)HP terrane formation is using numerical simulations based on deterministic mathematical models. In principle, these models employ fundamental laws of physics and constraints from laboratory experiments and geological observations. Until now, a plethora of deterministic models has been suggested to explain the formation and exhumation of (U)HP rocks. Certain models propose an important contribution of tectonic pressure (Mancktelow, 1995; Reuber et al., 2016) to (U)HP rock formation. Instead of requiring significantly increased lithostatic pressure by deep burial of crustal rocks, (U)HP units mainly form due to rock deformation. An often-employed model explaining the formation of (U)HP rocks at crustal levels is the orogenic wedge model (e.g. Platt, 1986). The first mechanical models of so-called critical wedges considered a frictional-plastic deformation (stresses are controlled by a specific yield criterion) and were originally applied to accretionary wedges. The formation of such wedges has been extensively studied with both analogue and numerical models (e.g. Gutscher et al., 1998; Simpson, 2009; Malavieille, 2010; Graveleau et al., 2012; Ruh et al., 2012; Borderie et al., 2018; Dal Zilio et al., 2020). Wedge models typically consider crustal deformation and predict well structural observations from orogenic belts like the Pyrenees and European Alps (e.g. Escher and Beaumont, 1997). However, these models often do not consider the subduction stage prior to collision which is likely important for the formation of many orogenic belts that preserve (U)HP terranes. Furthermore, many orogens involve the lithosphere in wedging (Nicolas et al., 1990) and result from the closure of an oceanic domain. For example, the Alpine orogen resulted from subduction of the Piemonte–Liguria oceanic domain and collision of the European and Adriatic passive continental margins (e.g. Handy et al., 2010). Ophiolitic units found in the Alps mainly consist of serpentinized mantle material, indicating a Piemonte–Liguria domain floored by exhumed and serpentinized mantle lithosphere (e.g. Manatschal and Müntener, 2009; McCarthy et al., 2020). Recent tomographic images from the Western Alps indicate that these serpentinites may have been partially reorganised along the plate interface during subduction (Zhao et al., 2020). In fact, serpentinites play a crucial role in subduction zones (Hess, 1955; Raleigh and Paterson, 1965; Hacker et al., 2003) and likely control the plate interface strength (Hirth and Guillot, 2013; Guillot et al., 2015).

Other deterministic models explain (U)HP terrane formation exclusively by burial and associated increase of lithostatic pressure (e.g. Gerya et al., 2002; Raimbourg et al., 2007). These models commonly involve an oceanic domain and assume a serpentinized plate interface. From a mechanical point of view the two end-member models presented above are fundamentally different. While the orogenic wedge model is mainly driven by tectonic forces, deep burial and exhumation cycling is driven by buoyancy forces arising from density contrasts between subducted crustal material and the surrounding mantle under gravity. This has fundamental implications for the dynamics within growing orogens (e.g. Forsyth and Uyeda, 1975; Ramberg, 1981; Weijermars and Schmeling, 1986; Turcotte and Schubert, 2014; Gerya, 2019). In fact, the relative importance of tectonic and buoyancy forces in driving orogen formation remains elusive.

Proposed exhumation models for (U)HP rocks within growing orogens are even more variable (England and Holland, 1979; Beaumont et al., 2009; Warren et al., 2008; Warren, 2013; Burov et al., 2014; Butler et al., 2014) and involve either far-field plate convergence or divergence. During plate convergence, subducted material returns to the surface either flowing (i) along the subduction interface (Gerya et al., 2002; Li and Gerya, 2009) or (ii) vertically into the upper plate (Gerya and Stöckhert, 2006). Another mechanism for (U)HP rock exhumation is eduction associated with slab detachment (Andersen et al., 1991; Duretz et al., 2012) or upwelling due to significant upper-plate divergent motion (Liao et al., 2018). A startling question is why there are currently several, significantly contrasting mechanisms proposed that all can apparently explain the formation and exhumation of the same (U)HP units? A possible explanation is that many models focus only on one aspect of the burial-exhumation cycle, e.g. only the exhumation. Earlier processes relevant for the exhumation, for example the subduction initiation controlling the location, orientation, thermal structure and effective strength of the emerging subduction interface are not modelled. Ideally, a model for (U)HP rock formation and exhumation should predict as many as possible processes relevant to the entire burial-exhumation cycle.

1.1.2 Long-term tectonic cycling of the lithosphere

In fact, many studies show that plate tectonic processes, such as subduction initiation or the formation and exhumation of (U)HP units are embedded in longer-term tectonic cycles (Wilson, 1966; Wilson et al., 2019). Over large time scales, tectonic inheritance of earlier extension and cooling events (Chenin et al., 2019) together with mantle convection (Solomatov, 2004) had presumably a major impact on subduction-related processes, such as for example burial and exhumation cycling of crustal rocks. Plenty of numerical studies modelling subduction-related processes do not directly model convection below the lithosphere (e.g. Jaquet and Schmalholz, 2018; Gülcher et al., 2019; Beaussier et al., 2019; Li et al., 2019). Convection in the Earth's mantle regulates the long-term thermal structure of the lithosphere (Richter, 1973; Parsons and McKenzie, 1978) and has, therefore, a fundamental control on the lithospheric strength. Furthermore, mantle flow can exert suction forces on the lithosphere (e.g. Conrad and Lithgow-Bertelloni, 2002). Numerical studies show that these suction forces can assist in the initiation of subduction (Baes et al., 2018). These studies show that the geodynamic history likely impacts on processes governing individual stages of the tectonic cycle of lithosphere–upper mantle deformation.

1.2 Objectives

The aim of this thesis is to provide new insights into the formation of orogenic belts embedded in the long-term geodynamic cycle of coupled lithosphere–upper mantle deformation. To this end, the following pressing scientific challenges are addressed:

- How does the interaction of plate motion and the underlying convecting mantle impact on subduction-related processes? This is important, because subduction is likely crucial in forming orogenic belts that involve the formation of (U)HP terranes, like the Western Alps and the Himalayas.

- Which forces control the dynamics within orogenic belts and what are the magnitudes of these forces? Quantifying the forces dominating the orogen dynamics gives important insights into the conditions under which (U)HP rocks can be exhumed within growing orogens.

- Which model for the formation and exhumation of (U)HP terranes is transferable, robust and predicts essential first-order processes involved in the burial and exhumation cycle of the crust? Answering to this question has huge implications for our understanding of plate tectonic processes at convergent plate boundaries in general.

To this end, state-of-the-art two-dimensional (2D) high-resolution petrological-thermo-mechanical numerical models are presented. Section 1.3 outlines the structure of this thesis.

1.3 Synopsis

This thesis incorporates 3 main chapters which are written in form of scientific articles and are either already published, or submitted to, or in preparation for submission to international peer-reviewed journals. In the following, the main chapters are introduced and their role in the general context of this thesis is explained.

- *Chapter 3*: *Impact of upper mantle convection on lithosphere hyper-extension and subsequent horizontally forced subduction initiation.* This chapter has been published in the EGU journal *Solid Earth.* Co-authors are Stefan M. Schmalholz, who conceptualized the study, helped interpreting the results and writing the manuscript, and Thibault Duretz, who developed the applied algorithm, helped interpreting the results and writing the manuscript. I designed the initial model configuration, conducted the numerical simulations, interpreted the results, created the figures and wrote the manuscript. This chapter is an important milestone as it reports the calibration for modelling long-term tectonic cycles of coupled lithosphere–upper mantle deformation. This thorough calibration lays the modelling ground for the following chapters.

  Here we investigate and quantify the impact of (1) the viscosity structure of the upper mantle and (2) an effective conductivity parameterization on upper mantle convection and lithospheric deformation. Applying this parameterization diminishes the vigour of convection, but maintains a characteristic thermal field for high Rayleigh number convection (explained in more detail in chapter 2). (3) We also test creep law parameters for wet and dry olivine rheology. Finally, we investigate whether forces induced by upper mantle convection have an impact on horizontally forced subduction initiation. We show that the initial model temperature, density and viscosity structure are and remain consistent with natural data for the entire numerical simulation. Further, we report convection benchmark results of the applied numerical algorithm.

- *Chapter 4*: *Buoyancy versus shear forces in building orogenic wedges.* This chapter is submitted for publication to the EGU journal *Solid Earth*. Co-authors are Thibault Duretz, who developed the applied algorithm, Evangelos Moulas, who conducted phase equilibria calculations, and Stefan M. Schmalholz, who conceptualized the study and helped writing the manuscript. I designed the initial model configuration, conducted the numerical simulations, interpreted the results, created the figures and wrote the manuscript.

  Here, we quantify the relative dominance and magnitude of buoyancy and shear forces during the formation of Alpine-type collision orogens. To quantify the relative importance of buoyancy and shear forces at convergent plate boundaries, we compare (1) simple, or linearized equation of state (LEOS) density models to complex density (CD) models that include metamorphic reactions. (2) We vary the strength of the upper crust and of the serpentinites at the top of the mantle exhumed in the basin. When entering the subduction zone, the shear resistance of serpentinites lubricating the subduction interface (Hirth and Guillot, 2013; Guillot et al., 2015, & references therein) facilitates subduction. Also, coupling of the continental crust to the subducting mantle lithosphere impacts on the subduction and, therefore, orogen dynamics (Duretz and Gerya, 2013). We show that the relative dominance of shear and buoyancy forces generates different modes of orogenic wedges, some dominated by buoyancy driven return flow and some by stacking of thrust sheets. We further analyse the importance of the shear resistance of serpentinites and the upper continental crust as well as rock density to make another step towards understanding the dynamics of Alpine-type orogen formation.

- *Chapter 5*: *Deterministic models unveil new subduction–exhumation cycle of (ultra)high-pressure rocks.* This chapter is an article in preparation for submission to *Nature Geoscience*. Co-authors are Joshua D. Vaughan-Hammon, who reviewed the literature for peak metamorphic conditions of (U)HP terranes worldwide and helped preparing the manuscript and figures, Thibault Duretz, who developed the applied algorithm, and Stefan M. Schmalholz, who conceptualized the study, helped interpreting the results and preparing the manuscript. I designed the initial model configuration, conducted the numerical simulations, interpreted the results, created the figures and wrote the manuscript.

We here present a two-dimensional petrological–thermomechanical deterministic model for the lithosphere–upper mantle system that predicts the continuous burial-exhumation cycle starting from spontaneous, i.e. without a priori prescription, subduction initiation to synconvergent exhumation in a single numerical simulation. A new mechanism, which is local upper-plate extension, enables synconvergent exhumation. The local extension is triggered by buckling of subducted crustal units and causes synconvergent episodic buoyancy-induced flow along the subduction interface. Predicted peak metamorphic conditions, exhumation velocities of (U)HP units and the orogen structure agree to first order with natural observations from the European Alps and the Himalayas.

In addition to these articles, I co-authored the studies of McCarthy et al. (2020) and Kiss et al. (2020) for which I designed the mathematical models, conducted the numerical simulations, interpreted the results, helped creating figures and writing the manuscript. Further details on these studies are not reported here.

Bibliography

Andersen, T. B., Jamtveit, B., Dewey, J. F., Swensson, E., 1991. Subduction and eduction of continental crust: Major mechanisms during continent-continent collision and orogenic extensional collapse, a model based on the south norwegian caledonides. Terra Nova 3 (3), 303–310.

Baes, M., Sobolev, S. V., Quinteros, J., 2018. Subduction initiation in mid-ocean induced by mantle suction flow. Geophysical Journal International 215 (3), 1515–1522.

Beaumont, C., Jamieson, R. A., Butler, J., Warren, C., 2009. Crustal structure: A key constraint on the mechanism of ultra-high-pressure rock exhumation. Earth and Planetary Science Letters 287 (1-2), 116–129.

Beaussier, S. J., Gerya, T. V., Burg, J.-P., 2019. 3d numerical modelling of the wilson cycle: structural inheritance of alternating subduction polarity. Geological Society, London, Special Publications 470 (1), 439–461.

Borderie, S., Graveleau, F., Witt, C., Vendeville, B. C., 2018. Impact of an interbedded viscous décollement on the structural and kinematic coupling in fold-and-thrust belts: Insights from analogue modeling. Tectonophysics 722, 118–137.

Burov, E., Francois, T., Yamato, P., Wolf, S., 2014. Mechanisms of continental subduction and exhumation of hp and uhp rocks. Gondwana Research 25 (2), 464–493.

Butler, J. P., Beaumont, C., Jamieson, R. A., 2014. The alps 2: Controls on crustal subduction and (ultra) high-pressure rock exhumation in alpine-type orogens. Journal of Geophysical Research: Solid Earth 119 (7), 5987–6022.

Chenin, P., Picazo, S., Jammes, S., Manatschal, G., Müntener, O., Karner, G., 2019. Potential role of lithospheric mantle composition in the wilson cycle: a north atlantic perspective. Geological Society, London, Special Publications 470 (1), 157–172.

Chopin, C., 1984. Coesite and pure pyrope in high-grade blueschists of the western alps: a first record and some consequences. Contributions to Mineralogy and Petrology 86 (2), 107–118.

Conrad, C. P., Lithgow-Bertelloni, C., 2002. How mantle slabs drive plate tectonics. Science 298 (5591), 207–209.

Dal Zilio, L., Ruh, J., Avouac, J.-P., 2020. Structural evolution of orogenic wedges: interplay between erosion and weak décollements. Tectonics, e2020TC006210.

Duretz, T., Gerya, T., 2013. Slab detachment during continental collision: Influence of crustal rheology and interaction with lithospheric delamination. Tectonophysics 602, 124–140.

Duretz, T., Gerya, T., Kaus, B., Andersen, T., 2012. Thermomechanical modeling of slab eduction. Journal of Geophysical Research: Solid Earth 117 (B8).

England, P., Holland, T., 1979. Archimedes and the tauern eclogites: the role of buoyancy in the preservation of exotic eclogite blocks. Earth and Planetary Science Letters 44 (2), 287–294.

Escher, A., Beaumont, C., 1997. Formation, burial and exhumation of basement nappes at crustal scale: a geometric model based on the western swiss-italian alps. Journal of structural Geology 19 (7), 955–974.

Forsyth, D., Uyeda, S., 1975. On the relative importance of the driving forces of plate motion. Geophysical Journal International 43 (1), 163–200.

Gerya, T., 2019. Introduction to numerical geodynamic modelling. Cambridge University Press.

Gerya, T., Stöckhert, B., 2006. Two-dimensional numerical modeling of tectonic and metamorphic histories at active continental margins. International Journal of Earth Sciences 95 (2), 250–274.

Gerya, T. V., Stöckhert, B., Perchuk, A. L., 2002. Exhumation of high-pressure metamorphic rocks in a subduction channel: A numerical simulation. Tectonics 21 (6), 6–1.

Graveleau, F., Malavieille, J., Dominguez, S., 2012. Experimental modelling of orogenic wedges: A review. Tectonophysics 538, 1–66.

Guillot, S., Hattori, K., Agard, P., Schwartz, S., Vidal, O., 2009. Exhumation processes in oceanic and continental subduction contexts: a review. In: Subduction zone geodynamics. Springer, pp. 175–205.

Guillot, S., Schwartz, S., Reynard, B., Agard, P., Prigent, C., 2015. Tectonic significance of serpentinites. Tectonophysics 646, 1–19.

Gülcher, A. J., Beaussier, S. J., Gerya, T. V., 2019. On the formation of oceanic detachment faults and their influence on intra-oceanic subduction initiation: 3d thermomechanical modeling. Earth and Planetary Science Letters 506, 195–208.

Gutscher, M.-A., Kukowski, N., Malavieille, J., Lallemand, S., 1998. Episodic imbricate thrusting and underthrusting: Analog experiments and mechanical analysis applied to the alaskan accretionary wedge. Journal of Geophysical Research: Solid Earth 103 (B5), 10161–10176.

Hacker, B. R., Peacock, S. M., Abers, G. A., Holloway, S. D., 2003. Subduction factory 2. are intermediate-depth earthquakes in subducting slabs linked to metamorphic dehydration reactions? Journal of Geophysical Research: Solid Earth 108 (B1).

Handy, M. R., Schmid, S. M., Bousquet, R., Kissling, E., Bernoulli, D., 2010. Reconciling plate-tectonic reconstructions of alpine tethys with the geological–geophysical record of spreading and subduction in the alps. Earth-Science Reviews 102 (3-4), 121–158.

Hess, H. H., 1955. Serpentines, orogeny, and epeirogeny. Geol. Soc. Am. Spec. Paper 62, 391–407.

Hirth, G., Guillot, S., 2013. Rheology and tectonic significance of serpentinite. Elements 9 (2), 107–113.

Jaquet, Y., Schmalholz, S. M., 2018. Spontaneous ductile crustal shear zone formation by thermal softening and related stress, temperature and strain rate evolution. Tectonophysics 746, 384–397.

Kiss, D., Candioti, L. G., Duretz, T., Schmalholz, S. M., 2020. Thermal softening induced subduction initiation at a passive margin. Geophysical Journal International 220 (3), 2068–2073.

Li, Z., Gerya, T. V., 2009. Polyphase formation and exhumation of high-to ultrahigh-pressure rocks in continental subduction zone: Numerical modeling and application to the sulu ultrahigh-pressure terrane in eastern china. Journal of Geophysical Research: Solid Earth 114 (B9).

Li, Z.-H., Gerya, T., Connolly, J. A., 2019. Variability of subducting slab morphologies in the mantle transition zone: Insight from petrological-thermomechanical modeling. Earth-Science Reviews.

Liao, J., Malusà, M. G., Zhao, L., Baldwin, S. L., Fitzgerald, P. G., Gerya, T., 2018. Divergent plate motion drives rapid exhumation of (ultra) high pressure rocks. Earth and Planetary Science Letters 491, 67–80.

Malavieille, J., 2010. Impact of erosion, sedimentation, and structural heritage on the structure and kinematics of orogenic wedges: Analog models and case studies. Gsa Today 20 (1), 4–10.

Manatschal, G., Müntener, O., 2009. A type sequence across an ancient magma-poor ocean–continent transition: the example of the western alpine tethys ophiolites. Tectonophysics 473 (1-2), 4–19.

Mancktelow, N. S., 1995. Nonlithostatic pressure during sediment subduction and the development and exhumation of high pressure metamorphic rocks. Journal of Geophysical Research: Solid Earth 100 (B1), 571–583.

McCarthy, A., Tugend, J., Mohn, G., Candioti, L., Chelle-Michou, C., Arculus, R., Schmalholz, S. M., Müntener, O., 2020. A case of ampferer-type subduction and consequences for the alps and the pyrenees. American Journal of Science 320 (4), 313–372.

Nicolas, A., Hirn, A., Nicolich, R., Polino, R., 1990. Lithospheric wedging in the western alps inferred from the ecors-crop traverse. Geology 18 (7), 587–590.

Parsons, B., McKenzie, D., 1978. Mantle convection and the thermal structure of the plates. Journal of Geophysical Research: Solid Earth 83 (B9), 4485–4496.

Platt, J., 1986. Dynamics of orogenic wedges and the uplift of high-pressure metamorphic rocks. Geological society of America bulletin 97 (9), 1037–1053.

Raimbourg, H., Jolivet, L., Leroy, Y., 2007. Consequences of progressive eclogitization on crustal exhumation, a mechanical study. Geophysical Journal International 168 (1), 379–401.

Raleigh, C. B., Paterson, M., 1965. Experimental deformation of serpentinite and its tectonic implications. Journal of Geophysical Research 70 (16), 3965–3985.

Ramberg, H., 1981. Gravity, deformation and the earth's crust: in theory, experiments and geological application. Academic press.

Reuber, G., Kaus, B. J., Schmalholz, S. M., White, R. W., 2016. Nonlithostatic pressure during subduction and collision and the formation of (ultra) high-pressure rocks. Geology 44 (5), 343–346.

Richter, F. M., 1973. Convection and the large-scale circulation of the mantle. Journal of Geophysical Research 78 (35), 8735–8745.

Ruh, J. B., Kaus, B. J., Burg, J.-P., 2012. Numerical investigation of deformation mechanics in fold-and-thrust belts: Influence of rheology of single and multiple décollements. Tectonics 31 (3).

Simpson, G. D., 2009. Mechanical modelling of folding versus faulting in brittle–ductile wedges. Journal of Structural Geology 31 (4), 369–381.

Solomatov, V., 2004. Initiation of subduction by small-scale convection. Journal of Geophysical Research: Solid Earth 109 (B1).

Turcotte, D., Schubert, G., 2014. Geodynamics. Cambridge University Press.

Warren, C., 2013. Exhumation of (ultra)-high-pressure terranes: concepts and mechanisms. Solid Earth 4, 75–92.

Warren, C. J., Beaumont, C., Jamieson, R. A., 2008. Formation and exhumation of ultra-high-pressure rocks during continental collision: Role of detachment in the subduction channel. Geochemistry, Geophysics, Geosystems 9 (4).

Weijermars, R., Schmeling, H., 1986. Scaling of newtonian and non-newtonian fluid dynamics without inertia for quantitative modelling of rock flow due to gravity (including the concept of rheological similarity). Physics of the Earth and Planetary Interiors 43 (4), 316–330.

Weingartner, R., Pearson, C., 2001. A comparison of the hydrology of the swiss alps and the southern alps of new zealand. Mountain Research and Development 21 (4), 370–381.

Wilson, J. T., 1966. Did the atlantic close and then re-open? Nature 211 (5050), 676–681.

Wilson, R., Houseman, G., Buiter, S., McCaffrey, K., Doré, A., 2019. Fifty years of the wilson cycle concept in plate tectonics: an overview.

Zhao, L., Malusà, M. G., Yuan, H., Paul, A., Guillot, S., Lu, Y., Stehly, L., Solarino, S., Eva, E., Lu, G., et al., 2020. Evidence for a serpentinized plate interface favouring continental subduction. Nature Communications 11 (1), 1–8.

CHAPTER 2

Mathematical model

As common in continuum mechanics, the applied numerical algorithm solves the equations for conservation of mass and momentum coupled to conservation of energy. These equations are discretised on a staggered finite difference Eulerian grid. A Marker-in-cell method is employed to transport the physical properties interpolated from the grid onto Lagrangian markers (Gerya and Yuen, 2003). Here, we consider incompressible visco–elasto–plastic materials that slowly (no inertia) flow under gravity and the influence of boundary tractions. Plastic deformation is controlled by a Drucker–Prager yield function. In none of the presented models frictional strain softening is applied. Instead, shear heating together with temperature-dependent rheological flow laws is the main mechanism localizing deformation (Thielmann and Kaus, 2012; Kiss et al., 2020). The algorithm has already been used to model deformation processes at different scales, such as deformation of eclogites on the centimetre-scale (Yamato et al., 2019), crystal-melt segregation of magma during its ascent in a meter-scale conduit (Yamato et al., 2015), rifting of continental lithosphere (Duretz et al., 2016; Petri et al., 2019) and stress calculations within and around a subducting oceanic plate (Bessat et al., 2020). In the next section, a detailed description of the governing equations solved by the numerical algorithm, the approach of modelling coupled lithosphere–upper mantle deformation and how phase transitions are included into the model is presented.

2.1 The applied numerical algorithm

Conservation of mass and momentum for an incompressible slowly flowing (no inertial forces) fluid under gravity are given by

$$\frac{\partial v_i}{\partial x_i} = 0 \tag{2.1}$$

$$\frac{\partial \sigma_{ij}}{\partial x_j} = -\rho \; a_i \; , \tag{2.2}$$

where v_i denotes velocity vector components and x_i spatial coordinate components, where (i,j=1) indicates the horizontal direction and (i,j=2) the vertical direction, σ_{ij} are components of the total stress tensor, ρ is density and $a_i = [0; g]$ is a vector with g being the gravitational acceleration. Density is a function of pressure P (negative mean stress) and temperature T and computed in two possible ways: (1) a linearized equation of state (LEOS) like

$$\rho(P,T) = \rho_0 \, (1 - \alpha \Delta T) \, (1 + \beta \Delta P) \ , \tag{2.3}$$

where ρ_0 is the material density at the reference temperature T_0 and pressure P_0, α is the thermal expansion coefficient, β is the isothermal compressibility coefficient, $\Delta T = T - T_0$ and $\Delta P = P - P_0$. Alternatively, (2) the effective density can be pre-computed using the software package Perple_X (Connolly, 2005) for given bulk rock compositions. During the simulation time, the density is read in from these phase diagram tables according to local pressure and temperature values for each material present in the finite difference grid cell. The total density at the grid cell center is calculated as a weighted density average over all present materials.

The viscoelastic stress tensor components are defined using a backward-Euler scheme (e.g., Schmalholz et al., 2001) as

$$\sigma_{ij} = -P\delta_{ij} + 2\ \eta^{\mathrm{eff}}\ \dot{\varepsilon}_{ij}^{\mathrm{eff}} \ , \tag{2.4}$$

where $\delta_{ij} = 0$ if $i \neq j$, or $\delta_{ij} = 1$ if $i = j$, η^{eff} is the effective viscosity, $\dot{\varepsilon}_{ij}^{\mathrm{eff}}$ are the components of the effective deviatoric strain rate tensor,

$$\dot{\varepsilon}_{ij}^{\mathrm{eff}} = \left(\dot{\varepsilon}_{ij} + \frac{\tau_{ij}^{o}}{2G\Delta t} \right) \ , \tag{2.5}$$

where G is shear modulus, Δt is the time step, τ_{ij}^{o} are the deviatoric stress tensor components of the preceding time step. A visco–elasto–plastic Maxwell model is used to describe the rheology, implying that the components of the total deviatoric strain rate tensor $\dot{\varepsilon}_{\mathrm{ij}}$ are additively decomposed into contributions from the viscous (dislocation, diffusion and Peierls creep), plastic and elastic deformation as

$$\dot{\varepsilon}_{ij} = \dot{\varepsilon}_{ij}^{\mathrm{ela}} + \dot{\varepsilon}_{ij}^{\mathrm{pla}} + \dot{\varepsilon}_{ij}^{\mathrm{dis}} + \dot{\varepsilon}_{ij}^{\mathrm{dif}} + \dot{\varepsilon}_{ij}^{\mathrm{pei}} \ . \tag{2.6}$$

In the case that deformation is effectively viscoelastic, a local iteration cycle is performed on each cell/node until Eq. 2.6 is satisfied (e.g., Popov and Sobolev, 2008).

The effective viscosity for the dislocation and Peierls creep flow law is a function of the second invariant of the respective strain rate components $\dot{\varepsilon}_{\mathrm{II}}^{\mathrm{dis,pei}} = \tau_{\mathrm{II}}/(2\eta^{\mathrm{dis,pei}})$

$$\eta^{\mathrm{dis}} = \frac{2^{\frac{1-n}{n}}}{3^{\frac{1+n}{2n}}} \ \zeta \ A^{-\frac{1}{n}} \ \left(\dot{\varepsilon}_{\mathrm{II}}^{\mathrm{dis}}\right)^{\frac{1}{n}-1} \ \exp\left(\frac{Q+PV}{nRT}\right) \ \left(f_{\mathrm{H_2O}}\right)^{-\frac{r}{n}} \ , \tag{2.7}$$

where the ratio in front of the pre-factor ζ results from conversion of the experimentally derived 1D flow law, obtained from laboratory experiments, to a flow law for tensor components (e.g., Schmalholz and Fletcher, 2011). A, n, Q, V, $f_{\mathrm{H_2O}}$ and r are material parameters. For the mantle material diffusion creep is taken into account and its viscosity takes the following form

$$\eta^{\mathrm{dif}} = \frac{1}{3} \ A^{-1} \ d^{m} \ \exp\left(\frac{Q+PV}{RT}\right) \ \left(f_{\mathrm{H_2O}}\right)^{-r}, \tag{2.8}$$

where d is grain size and m is a grain size exponent. Effective Peierls viscosity is calculated using the regularised form of Kameyama et al. (1999) for the experimentally derived flow law by Goetze and Evans (1979) as

$$\eta^{\mathrm{pei}} = \frac{2^{\frac{1-s}{s}}}{3^{\frac{1+s}{2s}}} \ \hat{A} \ \left(\dot{\varepsilon}_{\mathrm{II}}^{\mathrm{pei}}\right)^{\frac{1}{s}-1} \ , \tag{2.9}$$

where s is an effective, temperature dependent stress exponent:

$$s = 2 \ \gamma \ \frac{Q}{RT}(1-\gamma) \ . \tag{2.10}$$

$\hat{A}$ in Eq. (2.9) is

$$\hat{A} = \left[A_{\mathrm{P}}\ \exp\left(-\frac{Q\left(1-\gamma\right)^{2}}{RT} \right) \right]^{-\frac{1}{s}} \gamma \sigma_{\mathrm{P}}\ , \tag{2.11}$$

where A_{P} is a pre-factor, γ is a fitting parameter and σ_{P} is a characteristic stress value. In the frictional domain, stresses are limited by the Drucker-Prager yield function

$$F = \tau_{\mathrm{II}} - P\ \sin\phi - C\ \cos\phi\ , \tag{2.12}$$

where ϕ is the internal angle of friction and C is the cohesion. If the yield condition is met ($F \geq 0$), the equivalent plastic viscosity is computed as

$$\eta^{\mathrm{pla}} = \frac{P\ \sin\phi + C\ \cos\phi}{2\dot{\varepsilon}_{\mathrm{II}}^{\mathrm{eff}}} \tag{2.13}$$

and the effective deviatoric strain rate is equal to the plastic contribution of the deviatoric strain rate (Eq. 2.5). At the end of the iteration cycle, the effective viscosity in Eq. 2.4 is either computed as the quasi-harmonic average of the viscoelastic contributions

$$\eta^{\mathrm{eff}} = \begin{cases} \left(\frac{1}{G\Delta t} + \frac{1}{\eta^{\mathrm{dis}}} + \frac{1}{\eta^{\mathrm{dif}}} + \frac{1}{\eta^{\mathrm{pei}}} \right)^{-1} & ,\ F < 0 \\ \eta^{\mathrm{pla}} & ,\ F \geq 0 \end{cases} \tag{2.14}$$

or is equal to the viscosity η^{pla} calculated at the yield stress according to Eq. 2.13. Stress rotation is computed analytically at the end of each time step as

$$\tau_{ij} = \mathbf{R}^{\intercal}\ \tau_{ij}\ \mathbf{R}\ , \tag{2.15}$$

$$\mathbf{R} = \begin{bmatrix} \cos\theta & -\sin\theta \\ \sin\theta & \cos\theta \end{bmatrix}\ , \tag{2.16}$$

$$\theta = \Delta t\ \omega_{ij}\ , \tag{2.17}$$

$$\omega_{ij} = \frac{1}{2}\left(\frac{\partial v_j}{\partial x_i} - \frac{\partial v_i}{\partial x_j}\right)\ , \tag{2.18}$$

$$\tag{2.19}$$

where $\mathbf{R}$ is the rotation matrix, $^{\intercal}$ is the transpose operator, θ is the rotation angle and ω_{ij} are components of the vorticity tensor. Thermal evolution of the model is calculated with the energy balance equation expressed with respect to temperature, T, as

$$\rho\ c_{\mathrm{P}}\ \frac{\mathrm{D}T}{\mathrm{D}t} = \frac{\partial}{\partial x_i}\left(k\ \frac{\partial T}{\partial x_i}\right) + H_{\mathrm{A}} + H_{\mathrm{D}} + H_{\mathrm{R}}\ , \tag{2.20}$$

where c_P is the specific heat capacity at constant pressure, $\mathrm{D}/\mathrm{D}t$ is the material time derivative, k is thermal conductivity, $H_{\mathrm{A}} = T\alpha v_z g\rho$ is a heat source or sink resulting from adiabatic processes assuming lithostatic pressure conditions, $H_{\mathrm{D}} = \tau_{ij}^2/\left(2\eta^{\mathrm{eff}}\right)$ results from the conversion of dissipative work into heat (so-called shear heating) and H_{R} is radiogenic heat production per unit volume.

2.2 Nusselt number scaling laws

Modelling thermal convection beneath an actively deforming lithosphere can be numerically expensive, because the convection velocities can be as high as or even higher than the motion of the lithospheric plates, depending on the vigour of the convecting system. This significantly reduces the maximum time step necessary to ensure numerical stability. In consequence, it takes more time steps to run a simulation to the same physical time when convection is modelled together with deformation in the lithosphere. Hence, the computational time can be twice as long compared to models, where only the deforming lithosphere is modelled. However, it is possible to include the effect of convection in the mantle on the thermal field and keep a constant vertical heat flux through the lithosphere–asthenosphere boundary (LAB) into a numerical model without explicitly modelling convection by using an effective thermal conductivity for the mantle material below the lithosphere. Two dimensionless quantities have to be defined, namely the Rayleigh and Nusselt numbers. The Rayleigh number is the ratio of the thermal diffusion and advection time scale

$$Ra = \frac{t_{\mathrm{Dif}}}{t_{\mathrm{Adv}}} = \frac{\rho g \alpha \Delta T D^3}{\kappa \eta_{\mathrm{eff}}} , \tag{2.21}$$

where ρ is density, g is gravitational acceleration, α is a coefficient of thermal expansion, ΔT is the temperature difference between the top and the bottom and D is the thickness of the convecting layer, $\kappa = k/\rho/c_P$ is the thermal diffusivity and η_{eff} is the effective viscosity. The Nusselt number can be expressed in terms of the Rayleigh number as

$$Nu = \left(\frac{Ra}{Ra_{\mathrm{crit}}} \right)^{\beta} , \tag{2.22}$$

where Ra_{crit} is the critical Rayleigh number at which convection starts, typically in the order of 10^3, and β is a power-law exponent (Schubert et al., 2001). The Nusselt number is the ratio of advective heat flux, q_{Adv}, which is the vertical heat flux through the base of the lithosphere, imposed by the convecting upper mantle to the diffusive heat flux, q_{Dif}, imposed by the lithosphere on top of the convecting upper mantle as

$$Nu = \frac{q_{\mathrm{Adv}}}{q_{\mathrm{Dif}}} . \tag{2.23}$$

Using this relationship, it is possible to scale the thermal conductivity to the Nusselt number of the Earth's mantle and to maintain a constant heat flow through the base of the lithosphere via conduction when convection is absent. Assuming $Ra = 2 \times 10^6$ and $\beta = 1/3$ for the Earth's upper mantle convection, Eq. 2.22 predicts $Nu = 13$. This implies that the heat flow provided by advection is 13× higher than the heat flow provided by conduction. Using an effective conductivity approach, the heat flow provided by advection is mimicked using an enhanced conductive heat flow in the upper mantle. The effective conductivity can be determined by scaling the standard value of thermal conductivity of the upper mantle material to the Nusselt number of the convecting system like

$$k_{\mathrm{eff}} = Nu\ k. \tag{2.24}$$

For this study, the standard value for $k = 2.75$ of the upper mantle material and $Nu = 13$. The effective conductivity according to Eq. 2.24 is $k_{\mathrm{eff}} \approx 36$.

2.3 The initial thermal structure of the upper mantle

As mentioned above, the vigour of convection is defined by the Rayleigh number (Eq. 2.21). For $Ra >> Ra_{\mathrm{crit}}$, the time scale for thermal diffusion is much larger than the time scale for advection of material. This means that the entropy of the system remains relatively constant in time. By definition, such a system is adiabatic (Kondepudi and Prigogine, 2014). In the presented models, the density and entropy for the mantle phases is pre-computed using Perple_X for a given bulk rock composition. Assuming that the temperature gradient in the upper mantle is adiabatic and stress conditions are close to lithostatic (i.e., deviatoric stresses are negligible), the temperature at any depth can be determined by following an isentrop from the Perple_X database. Starting coordinates in pressure-temperature space are the (lithostatic) conditions at the base of the lithosphere. From these pressure and temperature values one can follow the closest isentrop (black line Fig. 3.11) until the (lithostatic) pressure value at target depth (in this thesis 660 km, red diamond Fig. 3.11) is reached and extract the corresponding temperature value. Trubitsyn and Trubitsyna (2015) derived an analytical solution to calculate temperatures assuming an adiabatic gradient for given depths. The temperature magnitude at the model bottom determined by both approaches differs by only 0.01 °C.

2.4 Including metamorphic phase transitions in the upper mantle – benefits and limitations

Involving phase transitions necessitates mainly two major assumptions: (1) is compressibility of material due to large density variations important and (2) does latent heat released or consumed at a phase transition significantly change the convective pattern? Bercovici et al. (1992) concluded that compressibility effects on the spatial structure of mantle convection are minor when the superadiabatic temperature drop is close to the adiabatic temperature of the mantle, which is the case for the Earth. Although the net density may vary largely in P-T space (Fig. 3.11), the maximum value for the density time derivative is still much lower compared to the velocity divergence in the models presented here. It can therefore be assumed that density changes due to volumetric deformation are still negligible and density changes are accounted for in the buoyancy force only. This means the classical Boussinesq approximation is still valid. However, not considering adiabatic heating in the energy conservation equation leads to a significant deviation of the thermal structure from the initially imposed temperature gradient over large time scales (>100 Myr). The resulting temperature profile is constant throughout the upper mantle and the newly equilibrated constant temperature is equal to the imposed temperature at the bottom boundary. In consequence, the density structure read in from the phase diagram table according to pressure and temperature values is significantly wrong. To avoid these problems, we use the extended Boussinesq approximation, i.e., the adiabatic heating term is included in the energy conservation equation. As a result, the initially imposed adiabatic (or isentropic) temperature gradient can be maintained over large time scales. The resulting density structure agrees well with the PREM model (Dziewonski and Anderson, 1981) as shown in *chapter* 3. A detailed comparison between different approximations of the system of equations is clearly beyond the scope of this thesis.

Latent heat that is released or consumed by a phase transition can perturb the thermal field by up to 100 K and induce a buoyancy force aiding or inhibiting the motion of cold, especially low-angle, subducting slabs (van Hunen et al., 2001) or hot rising plumes. However, when the lateral differences in temperature are small, the deflection of the phase transition by an ascending plume or a subducting slab has a much bigger impact on the buoyancy stresses than the latent heat released or consumed by the phase transition (Christensen, 1995). Because a detailed parametric investigation of the impact of latent heat on buoyancy stresses is beyond the scope of this work, for simplicity, latent heat is neglected in all models presented here.

Bibliography

Bercovici, D., Schubert, G., Glatzmaier, G. A., 1992. Three-dimensional convection of an infinite-prandtl-number compressible fluid in a basally heated spherical shell. Journal of Fluid Mechanics 239, 683–719.

Bessat, A., Duretz, T., Hetényi, G., Pilet, S., Schmalholz, S. M., 2020. Stress and deformation mechanisms at a subduction zone: insights from 2d thermo-mechanical numerical modelling. Geophysical Journal International.

Christensen, U., 1995. Effects of phase transitions on mantle convection. Annual Review of Earth and Planetary Sciences 23 (1), 65–87.

Connolly, J. A., 2005. Computation of phase equilibria by linear programming: a tool for geodynamic modeling and its application to subduction zone decarbonation. Earth and Planetary Science Letters 236 (1-2), 524–541.

Duretz, T., Petri, B., Mohn, G., Schmalholz, S., Schenker, F., Müntener, O., 2016. The importance of structural softening for the evolution and architecture of passive margins. Scientific reports 6, 38704.

Dziewonski, A. M., Anderson, D. L., 1981. Preliminary reference earth model. Physics of the earth and planetary interiors 25 (4), 297–356.

Gerya, T. V., Yuen, D. A., 2003. Characteristics-based marker-in-cell method with conservative finite-differences schemes for modeling geological flows with strongly variable transport properties. Physics of the Earth and Planetary Interiors 140 (4), 293–318.

Goetze, C., Evans, B., 1979. Stress and temperature in the bending lithosphere as constrained by experimental rock mechanics. Geophysical Journal International 59 (3), 463–478.

Kameyama, M., Yuen, D. A., Karato, S.-I., 1999. Thermal-mechanical effects of low-temperature plasticity (the peierls mechanism) on the deformation of a viscoelastic shear zone. Earth and Planetary Science Letters 168 (1-2), 159–172.

Kiss, D., Candioti, L. G., Duretz, T., Schmalholz, S. M., 2020. Thermal softening induced subduction initiation at a passive margin. Geophysical Journal International 220 (3), 2068–2073.

Kondepudi, D., Prigogine, I., 2014. Modern thermodynamics: from heat engines to dissipative structures. John Wiley & Sons.

Petri, B., Duretz, T., Mohn, G., Schmalholz, S. M., Karner, G. D., Müntener, O., 2019. Thinning mechanisms of heterogeneous continental lithosphere. Earth and Planetary Science Letters 512, 147–162.

Popov, A., Sobolev, S., 2008. Slim3d: A tool for three-dimensional thermomechanical modeling of lithospheric deformation with elasto-visco-plastic rheology. Physics of the Earth and Planetary Interiors 171 (1-4), 55–75.

Schmalholz, S., Podladchikov, Y., Schmid, D., 2001. A spectral/finite difference method for simulating large deformations of heterogeneous, viscoelastic materials. Geophysical Journal International 145 (1), 199–208.

Schmalholz, S. M., Fletcher, R. C., 2011. The exponential flow law applied to necking and folding of a ductile layer. Geophysical Journal International 184 (1), 83–89.

Schubert, G., Turcotte, D. L., Olson, P., 2001. Mantle convection in the Earth and planets. Cambridge University Press.

Thielmann, M., Kaus, B. J., 2012. Shear heating induced lithospheric-scale localization: Does it result in subduction? Earth and Planetary Science Letters 359, 1–13.

Trubitsyn, V., Trubitsyna, A., 2015. Effects of compressibility in the mantle convection equations. Izvestiya, Physics of the Solid Earth 51 (6), 801–813.

van Hunen, J., van den Berg, A. P., Vlaar, N. J., 2001. Latent heat effects of the major mantle phase transitions on low-angle subduction. Earth and Planetary Science Letters 190 (3-4), 125–135.

Yamato, P., Duretz, T., Angiboust, S., 2019. Brittle/ductile deformation of eclogites: insights from numerical models. Geochemistry, Geophysics, Geosystems.

Yamato, P., Duretz, T., May, D. A., Tartese, R., 2015. Quantifying magma segregation in dykes. Tectonophysics 660, 132–147.

CHAPTER 3

Impact of upper mantle convection on lithosphere hyper-extension and subsequent horizontally forced subduction initiation

Lorenzo G. Candioti[1], **Stefan M. Schmalholz**[1], **Thibault Duretz**[2]

[1]Institut des Sciences de la Terre, University of Lausanne, Lausanne, Switzerland.

[2]Univ Rennes, CNRS, Géosciences Rennes UMR 6118, Rennes, France.

Abstract

Many plate tectonic processes, such as subduction initiation, are embedded in long-term (>100 Myr) geodynamic cycles often involving subsequent phases of extension, cooling without plate deformation and convergence. However, the impact of upper mantle convection on lithosphere dynamics during such long-term cycles is still poorly understood. We have designed two-dimensional upper mantle-scale (down to a depth of 660 km) thermomechanical numerical models of coupled lithosphere–mantle deformation. We consider visco–elasto–plastic deformation including a combination of diffusion, dislocation and Peierls creep law mechanisms. Mantle densities are calculated from petrological phase diagrams (Perple_X) for a Hawaiian pyrolite. Our models exhibit realistic Rayleigh numbers between 10^6 and 10^7 and model temperature, density and viscosity structures agree with geological and geophysical data and observations. We tested the impact of the viscosity structure in the asthenosphere on upper mantle convection and lithosphere dynamics. We also compare models in which mantle convection is explicitly modelled with models in which convection is parameterized by Nusselt number scaling of the mantle thermal conductivity. Further, we quantified the plate driving forces necessary for subduction initiation in 2D thermomechanical models of coupled lithosphere–mantle deformation. Our model generates a 120 Myr long geodynamic cycle of subsequent extension (30 Myr), cooling (70 Myr) and convergence (20 Myr) coupled to upper mantle convection in a single and continuous simulation. Fundamental features such as the formation of hyper-extended margins, upper mantle convective flow and subduction initiation are captured by the simulations presented here. Compared to a strong asthenosphere, a weak asthenosphere leads to the following differences: smaller value of plate driving forces necessary for subduction initiation (15 $\mathrm{TN\,m^{-1}}$ instead of 22 $\mathrm{TN\,m^{-1}}$) and locally larger suction forces. The latter assists in establishing single-slab subduction rather than double-slab subduction. Subduction initiation is horizontally forced, occurs at the transition from the exhumed mantle to the hyper-extended passive margin and is caused by thermal softening. Spontaneous subduction initiation due to negative buoyancy of the 400 km wide, cooled exhumed mantle is not observed after 100 Myr in model history. Our models indicate that long-term lithosphere

dynamics can be strongly impacted by sub-lithosphere dynamics. The first-order processes in the simulated geodynamic cycle are applicable to orogenies that resulted from the opening and closure of embryonic oceans bounded by magma-poor hyper-extended rifted margins, which might have been the case for the Alpine orogeny.

3.1 Introduction

3.1.1 Convection in the Earth's mantle

In general, the term convection can be used to describe any motion of a fluid driven by external or internal forces (Ricard et al., 1989). Prout (1834) derived this term from the Latin word "convectio" (to carry, or to convey) to distinguish between advection dominated heat transfer and conduction, radiation dominated heat transfer.

On Earth, heat transfer through the lithosphere is dominated by thermal conduction while heat transfer through the underlying mantle is dominated by advection of material (e.g. Turcotte and Schubert, 2014). Convection may involve either the whole mantle, down to the core–mantle boundary, or only specific mantle layers. At temperature and pressure conditions corresponding to a depth of about 660 km, the mineralogy of peridotite changes from γ-spinel to perovskite + magnesiowüstite. This phase transition is endothermic, which means it has a negative pressure–temperature, so-called Clapeyron slope. Therefore, the penetration of cold slabs subducting into the lower mantle and hot plumes rising into the upper mantle may be delayed (Schubert et al., 2001). The 660-km phase transition can therefore represent a natural boundary, that separates two convecting layers. Laboratory experiments, tomographic images and calculations on the Earth's heat budget deliver evidence that a mixed mode of both types best explains convection in the present-day Earth's mantle (Li et al., 2008; Chen, 2016).

Any convecting system can be described by a dimensionless number, the so-called Rayleigh number. It is defined as the ratio of the diffusive and the advective time scale of heat transfer (see also, Eq. 3.2). The critical value of the Rayleigh number necessary for the onset of convection in the Earth's mantle is typically in the order of 1000 (Schubert et al., 2001). Convection in the Earth's mantle can occur at Rayleigh numbers in the range of 10^6–10^9 depending on the heating mode of the system and whether convection is layered or it includes the whole mantle (Schubert et al., 2001). The higher the Rayleigh number, the more vigorous is the convection, i.e. advection of material occurs at a higher speed. Vigour of both whole and layered mantle convection is inter alia controlled by the mantle density, the temperature gradient across and the effective viscosity of the mantle. However, unlike the density and thermal structures, the viscosity structure of the mantle is subject to large uncertainty. Viscosity is not a direct observable and can only be inferred by inverting observable geophysical data such as data for glacial isostatic adjustment (e.g. Mitrovica and Forte, 2004) or seismic anisotropy data (e.g. Behn et al., 2004). Especially at depths of ca. 100–300 km, in the so-called asthenosphere, the inferred value for viscosity varies greatly (see Fig. 2 in Forte et al. (2010)). Values for effective viscosity in this region can be up to two orders of magnitude lower than estimates for the average upper mantle viscosity of $\approx 10^{21}$ Pa s (Hirth and Kohlstedf, 2003; Becker, 2017).

3.1.2 Long-term geodynamic cycle and coupled lithosphere–mantle deformation

Many coupled lithosphere–mantle deformation processes, such as the formation of hyper-extended passive margins and the mechanisms leading to the initiation of subduction (e.g. Peron-Pinvidic et al., 2019; Stern and Gerya, 2018), are still elusive. Crameri et al. (2020) compiled a database from recent subduction zones to investigate whether subduction initiation was vertically (spontaneous) or horizontally forced (induced, see also Stern (2004) for terminology). They concluded that, during the last ca. 100 Myr, the majority of subduction initiation events were likely horizontally forced. Recent numerical studies have investigated thermal softening as a feasible mechanism for horizontally forced subduction initiation (Thielmann and Kaus, 2012; Jaquet and Schmalholz, 2018; Kiss et al., 2020). In these models, horizontally forced subduction was initiated without prescribing a major weak zone cross-cutting through the lithosphere. These models do not require further assumptions on other softening mechanisms, such as micro-scale grain growth or fluid- and reaction-induced softening. Therefore, these models are likely the simplest to study horizontally forced subduction initiation.

Geodynamic processes, such as lithosphere extension or convergence, are frequently studied separately. In fact, many studies show that these processes are embedded in longer term cycles, such as the Wilson cycle (Wilson, 1966; Wilson et al., 2019). Over large time scales ($\gtrapprox$80 Myr), tectonic inheritance of earlier extension and cooling events (Chenin et al., 2019) together with mantle convection (Solomatov, 2004) had presumably a major impact on subsequent convergence and subduction. Certainly, subduction initiation at passive margins during convergence can be studied without a previous extension and cooling stage (e.g., Kiss et al. (2020)). An initial passive margin geometry and thermal field must be then constructed ad-hoc for the model configuration. However, it is then uncertain whether the applied model would have generated a stable margin geometry and its characteristic thermal structure during an extension simulation. In other words, it is unclear whether the initial margin configuration is consistent with the applied model.

Plenty of numerical studies modelling the deformation of the lithosphere and the underlying mantle do not directly model convective flow below the lithosphere (e.g. Jaquet and Schmalholz, 2018; Gülcher et al., 2019; Beaussier et al., 2019; Erdos et al., 2019; Li et al., 2019). Ignoring convection below the lithosphere in numerical simulations is unlikely problematic, if the duration of the simulated deformation is not exceeding a few tens of millions of years. In such short time intervals, the diffusive cooling of the lithosphere is likely negligible. However, convection in the Earth's mantle regulates the long-term thermal structure of the lithosphere (Richter, 1973; Parsons and McKenzie, 1978) and has, therefore, a fundamental control on the lithospheric strength. Furthermore, mantle flow can exert suction forces on the lithosphere (e.g. Conrad and Lithgow-Bertelloni, 2002). Numerical studies show that these suction forces can assist in the initiation of subduction (Baes et al., 2018). Therefore, coupling mantle convection to lithospheric scale deformation can potentially improve our understanding of processes acting on long-term geodynamic cycles of the lithosphere.

Here, we present two-dimensional (2D) thermomechanical numerical simulations modelling the long-term cycle of coupled lithosphere–mantle deformation. The modelled geodynamic cycle comprises a 120 Myr history of extension–cooling–convergence leading to horizontally forced subduction. We include the mantle down to a depth of 660 km assuming that convection is layered. Timings and deformation velocities for the distinct periods have been chosen to allow for comparison of the model results to the Alpine orogeny. With these models, we investigate and quantify the impact of (1) the viscosity structure of the upper mantle and (2) an effective conductivity parameterization on upper mantle convection and lithospheric deformation. Applying this parameterization diminishes the vigour of convection, but maintains a characteristic thermal field for high Rayleigh number convection (explained in more detail in the next section and in appendix 3.6.1). (3) We also test creep law parameters for wet and dry olivine rheology. Finally, we investigate whether forces induced by upper mantle convection have an impact on horizontally forced subduction initiation.

3.2 The applied numerical model

3.2.1 Modelling assumptions and applicability

For simplicity, we consider lithosphere extension that generates magma-poor hyper-extended margins and crustal separation leading to mantle exhumation. This means that we do not need to model melting, lithosphere break-up, mid-ocean ridge formation and generation of new oceanic crust and lithosphere. Such Wilson-type cycles, involving only embryonic oceans, presumably formed orogens such as the Pyrenees, the Western and Central Alps and most of the Variscides of Western Europe (e.g. Chenin et al., 2019). Values for deformation periods and rates in the models presented here are chosen to allow for comparison of the model evolution to the Alpine orogeny.

Further, tomographic images from the Mediterranean show large p-wave anomalies in the transition zone (Piromallo and Morelli, 2003) indicating that the 660-km phase transition inhibits the sinking material to penetrate further into the lower mantle. Therefore, we do not include the lower mantle into the model domain and assume that mantle convection is layered.

3.2.2 Model configuration

The model domain is 1600 km wide and 680 km high and the applied model resolution is 801×681 grid points (Fig. 3.1). Minimum z-coordinate is set to -660 km and the top +20 km are left free (no sticky air) to allow for build-up of topography. The top surface (initially at z = 0 km) is stress free. Thus, its position evolves dynamically as topography develops. Mechanical boundary conditions on the remaining boundaries are set to free slip at the bottom and constant material inflow/outflow velocities at the left and right boundary. The boundary velocity is calculated such that the total volume of material flowing through the lateral boundary is conserved. The transition between inflow and outflow occurs at z = -330 km and not at the initially imposed lithosphere–asthenosphere boundary (LAB). Values for deviatoric stresses at this depth are significantly lower compared to those at the base of the lithosphere. This choice avoids boundary effects close to the mechanical lithosphere and the LAB can develop freely away from the lateral model boundaries. We use material flow velocity boundary condition rather than bulk extension rates to deform the model units. Applying bulk extension rates and deforming the model domain would change the height of the model domain which has strong control on the Rayleigh number of the system (Eq. 3.2). Also, evolution of passive margin geometries becomes dependent on the model width when using bulk extension rates as mechanical boundary condition (Chenin et al., 2018). It is therefore more practical to use constant velocity boundary conditions with material flow in the type of models presented here.

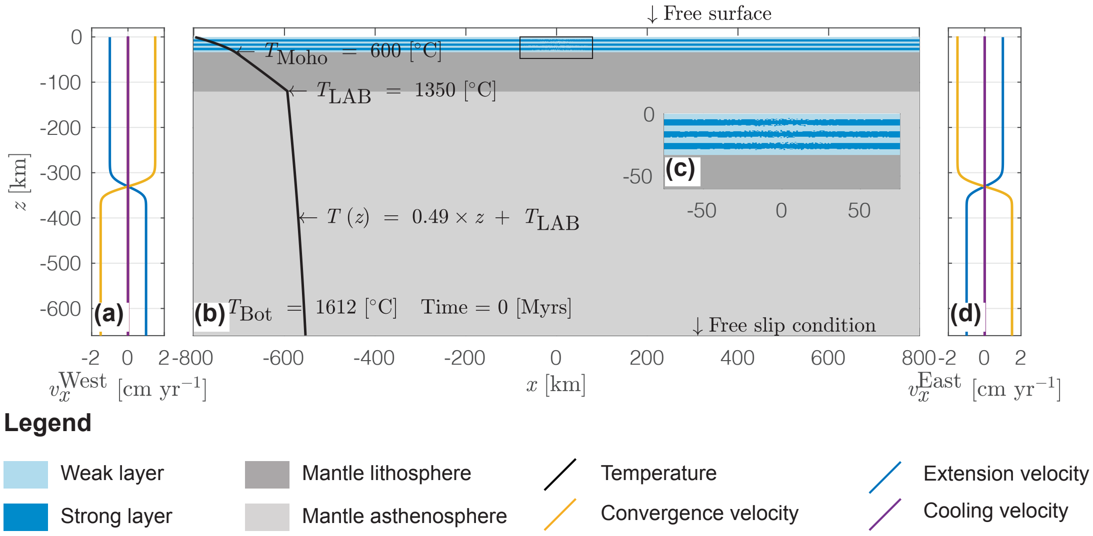

Figure 3.1: Initial model configuration and boundary conditions. Dark blue colours represent strong and light blue colours represent weak crustal units, dark grey colours represent the mantle lithosphere and light grey colours the upper mantle. (a) Profile of horizontal velocity for material inflow and outflow along the western model boundary. Blue line indicates the profile for the extension, purple line indicates the profile for the cooling and the yellow line indicates the profile for the convergence stage. (b) Entire model domain including the material phases (colour-code as explained above) and initial vertical temperature profile (black line), (c) enlargement of the centre of the model domain showing the initial random perturbation on the marker field (see appendix 3.2) used to localise deformation in the centre of the domain and (d) is the same profile as shown in (a), but along the eastern model boundary.

Initial temperature at the surface is set to 15 °C and temperatures at the crust–mantle (Moho) and at the LAB are 600 °C and 1350 °C, respectively. Assuming an adiabatic gradient of 0.49 °C km^{-1} (see appendix 3.6.1), the temperature at the model bottom is 1612 °C. Thermal boundary conditions are set to isothermal at the bottom and at the top of the domain and the left and right boundaries are assumed to be insulating (i.e. no heat flows through lateral boundaries). Model units include a 33 km thick, mechanically layered crust which overlies an 87 km thick mantle lithosphere on top of the upper mantle. The resulting initial thickness of the lithosphere is thus 120 km. The crust includes three mechanically strong and four mechanically weak layers. The thickness of the weak layers is set to 5 km each, the thickness of the uppermost and lowermost strong layer is set to 4 km, whereas the strong layer in the middle is 5 km thick. This thickness variation allows to match the total 33 km thickness of the crust without introducing an additional vertical asymmetry. Mechanical layering of the crust was chosen, because it is a simple way of considering mechanical heterogeneities in the crust. The layering leads to the formation of numerous structural features observed in natural hyper-extended passive margins (Duretz et al., 2016) without relying on pre-defined strain softening.

We consider viscous, elastic and brittle–plastic deformation of material in all models presented here. Viscous flow of material is described as a combination of several flow laws. We use dislocation creep for the crustal units and dislocation, diffusion and Peierls creep for mantle units (see also appendix 3.2). The initial viscosity profile through the upper mantle is calibrated to match viscosity data obtained by Ricard et al. (1989). The applied flow law parameters lie within the error range of the corresponding laboratory flow law estimates (see Table 3.1). All physical parameters are summarised in Table 3.1.

The difference between mantle lithosphere and upper mantle is temperature only, i.e. all material parameters are the same. Density of the crustal phases is computed with an equation of state (Eq. 2.3), whereas density of the mantle phase is pre-computed using Perple_X (Connolly, 2005) for the bulk rock composition of a pyrolite (Workman and Hart (2005), Fig. 3.11). A detailed description of the phase transitions and how the initial thermal field is calibrated is given in appendix 3.6.1. Surface processes (e.g., erosion and sedimentation) are taken into account by a kinematic approach: if the topography falls below a level of 5 km depth or rises above 2 km height, it undergoes either sedimentation or erosion with a constant velocity of 0.5 mm yr^{-1}. In case of sedimentation, the generated cavity between the old and corrected topographic level is filled with sediments, alternating between calcites and pelites every 2 Myr. This simple parameterization of surface processes moderates the amplitude of topography and may affect geodynamic processes such as subduction.

To initiate the deformation, we perturbed the initial marker field with a random amplitude vertical displacement like

$$z_{\mathrm{M}} = z_{\mathrm{M}} + A \ \exp\left(- \frac{x_{\mathrm{M}}}{\lambda} \right) , \tag{3.1}$$

where z_{M} is the vertical marker coordinate in km, A is a random amplitude varying between -1.25 km and 1.25 km, x_{M} is the horizontal marker coordinate in km and $\lambda = 25$ km is the half-width of the curve. The perturbation is applied to the horizontal centre of the domain between -75 km and 75 km.

3.2.3 Investigated parameters

Among the physical parameters controlling the long-term geodynamic evolution (f.e., mantle density, plate velocities), the viscosity structure of the mantle is one of the least constrained. Therefore, we test (1) models with different upper mantle viscosity structures. In model M1, the reference model, the asthenosphere is assumed to be weak with values for viscosity in the order of $\approx 10^{19}$ Pa s resulting from the applied flow laws. In models M2 and M3 the asthenosphere is assumed to be stronger. Values for viscosities in the asthenosphere are limited by a numerical cut-off value of 1×10^{20} Pa s in M2 and 5×10^{20} Pa s in M3. Coupling of lithosphere–mantle deformation is achieved by resolving numerically both lithospheric deformation and upper mantle convection in M1-3. (2) We further test the impact of parameterizing convection on the cycle by scaling the thermal conductivity to the Nusselt number of upper mantle convection (see app. 3.6.1). In these models, we also assume both a weak asthenosphere (as in M1) in model M4 and a strong asthenosphere (as in M2) in model M5. The effective conductivity approach has been used, for example, in mantle convection studies for planetary bodies when convection in the mantle is too vigorous to be modelled explicitly (e.g. Zahnle et al.,

Table 3.1: Physical parameters used in the numerical simulations M1-6.

Parameter	Unit	Strong Crust[1]	Weak Crust[2]	Calcite[3]	Mica[4]	Dry Mantle[5]	Wet Mantle[6]
ρ_0	$\mathrm{kg\,m^{-3}}$	2800	2800	2800	2800	-	-
G	Pa	2×10^{10}	2×10^{10}	2×10^{10}	2×10^{10}	2×10^{10}	2×10^{10}
c_P	$\mathrm{J\,kg^{-1}\,K^{-1}}$	1050	1050	1050	1050	1050	1050
k	$\mathrm{W\,m^{-1}\,K^{-1}}$	2.25	2.25	2.37	2.55	2.75	2.75
H_R	$\mathrm{W\,m^{-3}}$	0.9×10^{-6}	0.9×10^{-6}	0.56×10^{-6}	2.9×10^{-6}	2.1139×10^{-8}	2.1139×10^{-8}
C	Pa	10^7	10^6	10^7	10^6	10^7	10^7
φ	°	30	5	30	5	30	30
α	$\mathrm{K^{-1}}$	3×10^{-5}	3×10^{-5}	3×10^{-5}	3×10^{-5}	3×10^{-5}	3×10^{-5}
β	$\mathrm{Pa^{-1}}$	1×10^{-11}	1×10^{-11}	1×10^{-11}	1×10^{-11}	1×10^{-11}	1×10^{-11}
Dislocation							
A	$\mathrm{Pa}^{-n-r}\,\mathrm{s^{-1}}$	5.0477×10^{-28}	5.0717×10^{-18}	1.5849×10^{-25}	10^{-138}	1.1×10^{-16}	5.6786×10^{-27}
n	-	4.7	2.3	4.7	18	3.5	3.5
Q	$\mathrm{J\,mol^{-1}}$	485×10^3	154×10^3	297×10^3	51×10^3	530×10^3	460×10^3
V	$\mathrm{m^3\,mol^{-1}}$	0	0	0	0	14×10^{-6}	11×10^{-6}
r	-	0	0	0	0	0	1.2
$f_{\mathrm{H_2O}}$	Pa	0	0	0	0	0	10^9
Diffusion							
A^*	$\mathrm{Pa}^{-n-r}\,\mathrm{m}^m\,\mathrm{s^{-1}}$	-	-	-	-	1.5×10^{-15}	2.5×10^{-23}
n	-	-	-	-	-	1	1
Q	$\mathrm{J\,mol^{-1}}$	-	-	-	-	370×10^3	375×10^3
V	$\mathrm{m^3\,mol^{-1}}$	-	-	-	-	7.5×10^{-6}	20×10^{-6}
m	-	-	-	-	-	3	3
r	-	-	-	-	-	0	1
$f_{\mathrm{H_2O}}$	Pa	-	-	-	-	0	10^9
d	m	-	-	-	-	10^{-3}	10^{-3}
Peierls							
A	$\mathrm{s^{-1}}$	-	-	-	-	5.7×10^{11}	5.7×10^{11}
Q	$\mathrm{J\,mol^{-1}}$	-	-	-	-	540×10^3	540×10^3
σ_P	Pa	-	-	-	-	8.5×10^9	8.5×10^9
γ	-	-	-	-	-	0.1	0.1

Flow law parameters: [1]Maryland Diabase (Mackwell et al., 1998), [2]Wet Quartzite (Ranalli, 1995), [3]Calcite (Schmid et al., 1977), [4]Mica (Kronenberg et al., 1990), [5]Dry Olivine (Hirth and Kohlstedf, 2003) and [6]Wet Olivine (Hirth and Kohlstedf, 2003). Peierls creep: (Goetze and Evans, 1979) regularised by Kameyama et al. (1999). *Converted to SI units from original units: $A = 2.5\times10^7\ ([\mathrm{MPa}])^{-n-r}\ ([\mathrm{\mu m}])^m\ ([\mathrm{s}])^{-1} = 2.5\times10^7 \times (10^{-6n-6r}\ [\mathrm{Pa}]^{-6n-6r}) \times (10^{-6m}\ [\mathrm{m}]^m)\ \times ([s]^{-1}) = 2.5\times10^{-23}\ [\mathrm{Pa^{-2} m^3\,s^{-1}}]$.

1988; Tackley et al., 2001; Golabek et al., 2011). Also, it has been used in models of back-arc lithospheric thinning through mantle flow that is induced by subduction of an oceanic plate (e.g. Currie et al., 2008) and in models of lithosphere extension and subsequent compression (e.g. Jammes and Huismans, 2012). (3) We finally investigate the role of the olivine rheology. To this end, we perform an additional model M6 in which the material parameters of the dislocation and diffusion creep mechanism of a dry olivine rheology is replaced by the parameters of a wet olivine rheology (Table 3.1). In M6, values for all the other parameters, both physical and numerical, are initially equal to those set in M1. Within the error range of values for activation volume and energy of the wet olivine rheology, the viscosity is calibrated to the data obtained by Ricard et al. (1989). However, using the highest possible values for the wet olivine flow law parameters, the maximum viscosity in the upper mantle is initially one order of magnitude lower compared to models M1-5. A summary of all simulations is given in Table 3.2 and all material parameters are summarised in Table 3.1.

Table 3.2: Parameters varied in models M1-6.

Parameter	Unit	M1	M2	M3	M4	M5	M6
k	$\mathrm{W\,m^{-1}\,K^{-1}}$	2.75	2.75	2.75	**36**	**36**	2.75
η_{cutoff}	Pa s	1×10^{18}	$\mathbf{1\times10^{20}}$	$\mathbf{5\times10^{20}}$	1×10^{18}	$\mathbf{1\times10^{20}}$	1×10^{18}
Ra_{avg}	-	9.95×10^{6}	3.92×10^{6}	1.18×10^{6}	1.97×10^{6}	5.48×10^{5}	9.26×10^{7}
Rheology mantle	-	Dry Olivine	Dry Olivine	Dry Olivine	Dry Olivine	Dry Olivine	**Wet Olivine**

k is thermal conductivity and η_{cutoff} is the lower viscosity limiter. Ra_{avg} is the arithmetic average of Rayleigh numbers >1000. Rayleigh numbers are computed locally at each cell center according to Eq. 3.2 after 99 Myr in model history for models M1-5 and after 26 Myr for model M6. Bold font highlights the parameters varied compared to the reference model M1.

3.3 Results

We first describe the evolution of the reference model M1 and of M6. Model M6 is stopped after the extensional stage, because its later evolution is not applicable to present-day Earth. Thereafter, we compare the results of M2-5 to the results of M1 for the individual deformation stages. Finally, we compare the evolution of the plate driving forces in models M1-5 during the entire cycle. The arithmetic average Rayleigh number in all models is significantly larger compared to the critical Rayleigh number $Ra_{\mathrm{crit}} = 1000$. The rifting and cooling period laterally perturb the thermal field sufficiently to initiate and drive the convection over large time scales in all models presented here.

3.3.1 Dry Olivine rheology: Model M1 - Reference run

Crustal break-up during the rifting phase in M1 occurs after ca. 8 Myr (Fig. 3.3a & e). The left continental margin has a length of ca. 200 km and the right margin has a length of ca. 150 km (Fig. 3.3e). Velocity arrows indicate upward motion of hot material in the centre of the domain (Fig. 3.3e). Two convection cells begin to establish at this stage below each margin. The viscosity of the upper mantle decreases to minimal values in the order of 10^{19} Pa s and increases again up to values in the order of 10^{21} Pa s at the bottom of the model domain (Fig. 3.3a and Fig. 3.2c). Towards the end of the cooling period (at 97 Myr), M1 has developed circular shaped convection cells in the upper region of the upper mantle (above $z \approx$ -400 km, Fig 3.3b). The average Rayleigh-number (see footnote of Table 3.2) of the system computed at this late stage of the cooling period is ca. 9.95×10^{6} and the size of the cells varies between ca. 50 km and ca. 300 km in diameter below the left and right margin respectively (Fig.3.3b). Below the right margin at $z \approx$ -150 km and $x \approx$ +300 km the downward directed mantle flow of two neighbouring convection cells unifies (Fig. 3.3f). The top ca. 100 km of the modelled domain remain undeformed; no material is flowing in this region (area without velocity arrows in Fig. 3.3f). Convergence starts at 100 Myr and at ca. 102 Myr, a major shear zone forms breaking the lithosphere below the right margin (inclined zone of reduced effective viscosity in Fig. 3.3c & g). Velocity arrows in the

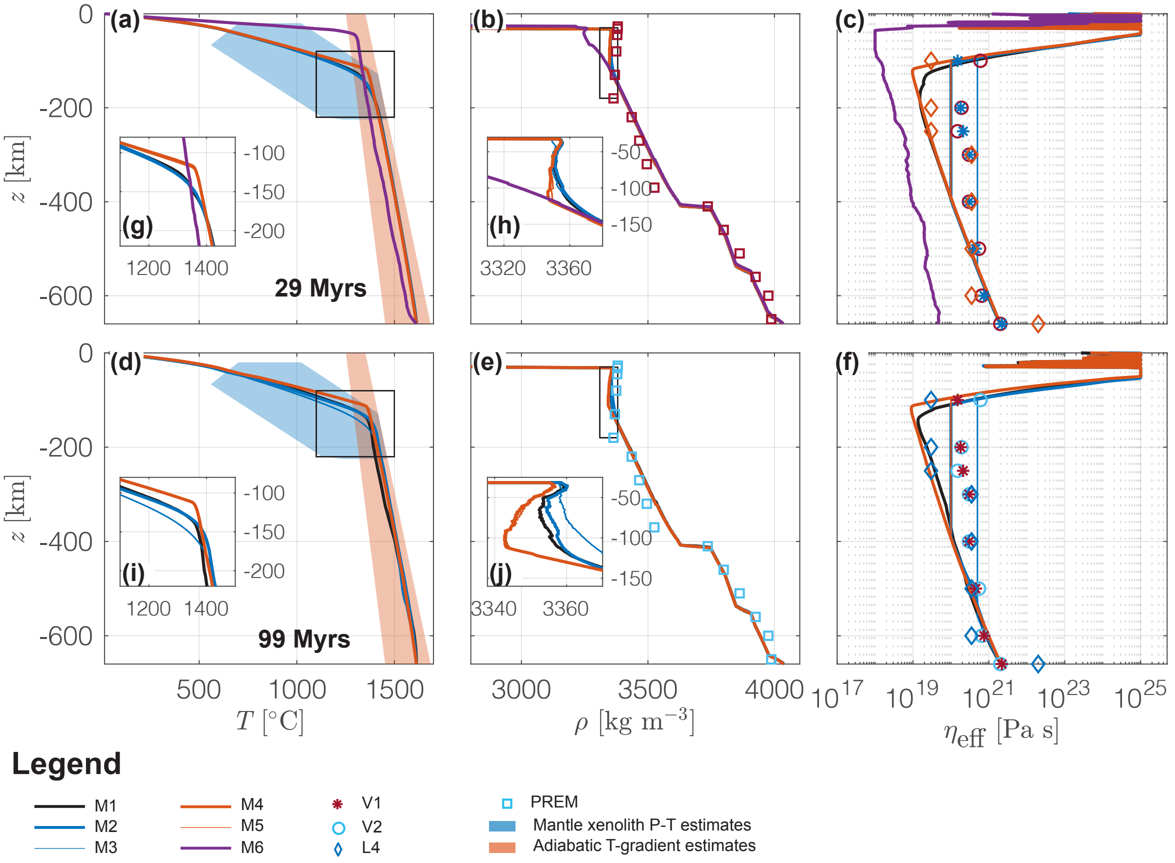

Figure 3.2: Horizontally averaged vertical profiles of temperature, T, density, ρ, and effective viscosity, η_{eff}. Top row: after 29 Myr, bottom row: after 99 Myr in model history. (a) and (d) show horizontally averaged temperature, (b) and (e) show horizontally averaged density and (c) and (f) show horizontally averaged viscosity. (g)-(j) show an enlargement of the parental subfigure. Coloured lines show the results of models M1-6 as indicated in the legend. In (a) and (d): blue area indicates P-T condition estimates from mantle xenolith data and orange area indicates estimates for a range of adiabatic gradients both taken from Hasterok and Chapman (2011) (Fig. 5). Estimates for adiabatic temperature gradients are extrapolated to 660 km depth. In (b) and (e): squares indicate density estimates from the preliminary reference Earth model (PREM) (Dziewonski and Anderson, 1981). In (c) and (f): circles and stars indicate viscosity profiles inferred from Occam-style inversion of glacial isostatic adjustment and convection related data originally by Mitrovica and Forte (2004), diamonds show a four-layer model fit of mantle flow to seismic anisotropy originally by Behn et al. (2004). All profiles taken from Forte et al. (2010) (Fig. 2). The median is used as statistical quantity for averaging, because it is less sensitive to extreme values compared to the arithmetic mean.

lithosphere indicate the far-field convergence, whereas velocity arrows in the upper mantle show that convection cells are still active. The exhumed mantle is subducted in one stable subduction zone below the right continental margin. Several convection cells are active in the upper mantle during subduction (see velocity arrows Fig. 3.3d & h). A trench forms in which sediments are deposited (Fig.3.3d & h). Folding of the crustal layers in the overriding plate indicates significant deformation of the crust. The crustal layers of the subducting plate remain relatively undeformed. The viscosity in the asthenosphere remains stable at values of 10^{19} Pa s during the entire model history.

3.3.2 Wet Olivine rheology: Model M6

Crustal necking in M6 starts at ca. 2 Myr in model history (Fig. 3.4a & e). Two convecting cells develop in the horizontal centre of the domain transporting material from z≈-200 km to z≈-100 km (Fig. 3.4b & f). At ca. 13 Myr convection cells are active in the upper 500 km of the domain (Fig. 3.4c). Crustal thickness varies laterally between ca. 20 km and ¡5 km (Fig. 3.4g). The mantle lithosphere is thermally eroded, indicated by a rising level of the 10^{21} Pa s contour in Fig. 3.4f-h after 26 Myr in model history. In contrast to M1, M6 does not reach the stage of crustal break-up (Fig. 3.4d & h) within 30 Myr. Two large convection cells are active: in the left half of the domain convection occurs at relatively enhanced flow speeds, whereas in the right half of the domain flow speeds are relatively lower (compare relative length of velocity arrows in Fig. 3.4d). The average Rayleigh number of the system at this stage is 9.26×10^{7}. Values for temperature at the Moho reach ca. 1000 °C locally (Fig. 3.4h and Fig. 3.2a). The horizontally-averaged density profile (Fig. 3.2b) shows that values for density in the lithosphere are on average 100 $\mathrm{kg\,m^{-3}}$ lower in M6 compared to M1. Values for effective viscosity in the asthenosphere decrease to minimal values in the order of 10^{18} Pa s and increase up to values of 10^{19} Pa s at a depth of 660 km at the end of the extension period (Fig. 3.2c).

3.3.3 Comparison of reference run with models M2-5: Extension phase

In contrast to M1, M2 produces two conjugate passive margins that are both approximately 150 km long (Fig. 3.5b) after 13 Myr. Crustal separation has not occurred up to this stage in M3: the two passive margins are still connected by a crustal bridge of ca. 10 km thickness. Mantle material rises below the centre of the domain and then diverges below the plates in M2

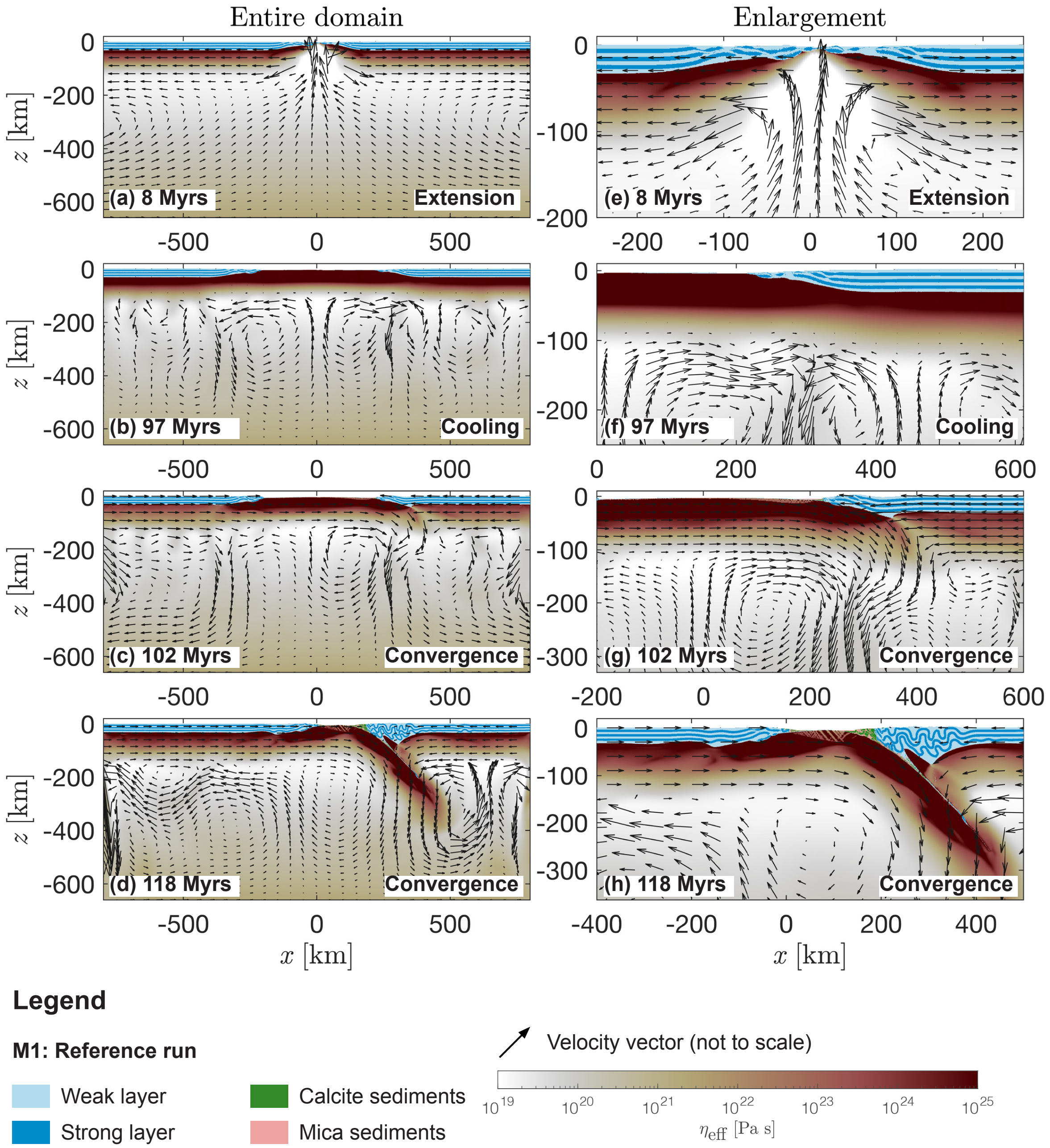

Figure 3.3: Model evolution of M1 (reference run). Left column: Entire domain. Right column: Enlargement. Dark and light blue colours, salmon and green colours indicate the material phase of weak and strong layers and mica and calcite sediments, respectively. White to red colours indicate the effective viscosity field calculated by the algorithm. Arrows represent velocity vectors and the length of the arrows is not to scale. Scientific colour maps used in all figures are provided by Crameri (2018).

and M3, but no convection cells have formed yet (Fig. 3.5b & c), which is different compared to M1. The minimal value for effective viscosity in the upper mantle is at the applied cut-off

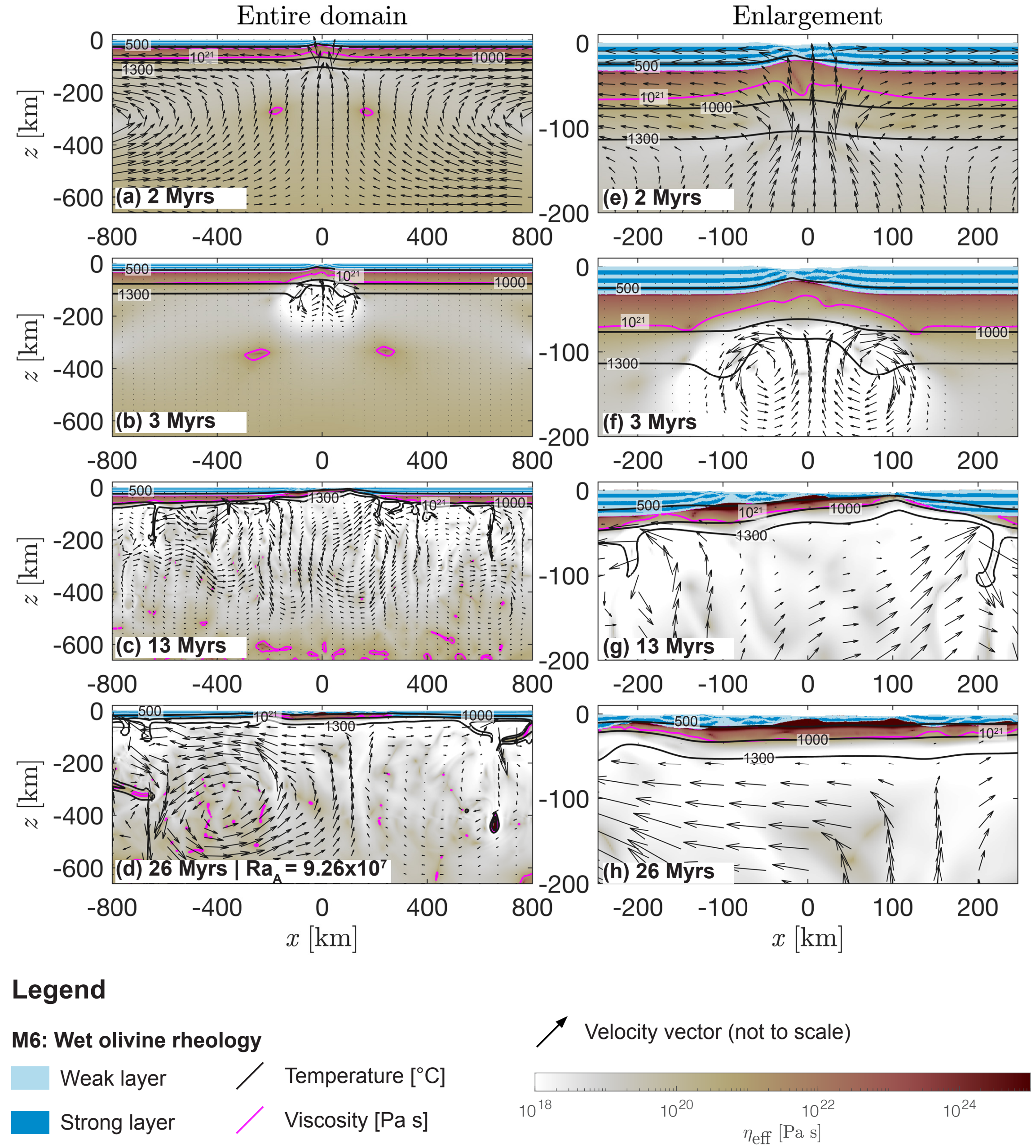

Figure 3.4: Evolution of model M6 at (a) & (e) 2 Myr, (b) & (f) 3 Myr, (c) & (g) 13 Myr and (d) & (h) 26 Myr. Blue colours indicate mechanically weak (light) and strong (dark) crustal units. White to red colours show the effective viscosity field calculated by the numerical algorithm. Black lines show the level of 500 °C, 1000 °C and 1300 °C isotherm and the magenta coloured line shows the level of the 10^{21} Pa s viscosity isopleth. This contour line represents the mechanical boundary between the mantle lithosphere and the convecting upper mantle. Arrows represent velocity vectors and the length of the arrows is not to scale.

value of 1×10^{20} Pa s in M2 and 5×10^{20} Pa s in M3 and increases up to ca. 1×10^{21} Pa s at a depth of 660 km (Fig. 3.2c) in both models. Similar to the reference model (M1), in M4, the left continental margin has a length of ca. 200 km and the right margin has a length of ca. 150 km (Fig. 3.5d). Like in M1, two convection cells have formed below the two passive margins in this model (see arrows in Fig. 3.5d) and the minimal value for effective viscosity below the lithosphere is in the order of 1×10^{19} Pa s and increases to approximately 1×10^{21} Pa s at a depth of 660 km (Fig. 3.2c). Both margins in M5 are approximately equally long (ca. 150 km, Fig. 3.5e) and values for viscosity are at the lower cut-off value of 1×10^{20} Pa s in the upper mantle and increase up to ca. 1×10^{21} Pa s at a depth of 660 km (Fig. 3.2c). The overall evolution of the extension period in M5 is more similar to M2 than to M1. In M1-5, the 1350 °C isotherm does not come closer than ca. 30 km to the surface. Horizontally-averaged vertical temperature profiles are similar in M1-5 (Fig. 3.2a & g). The level of the 1350 °C isotherm remains at its initial depth in M4 and M5, whereas it subsides by ca. 20 km in M1-3. Horizontally-averaged density profiles (Fig. 3.2b) show density differences of ¡10 $\mathrm{kg\,m^{-3}}$ between ca. 35 km and ca. 120 km depth.

3.3.4 Comparison of reference run with models M2-5: Cooling phase without plate deformation

Models M1-5 maintain a stable lithospheric thickness of ca. 90–100 km over 100 Myr (top magenta viscosity contour in Fig. 3.6) and no thermal erosion of the lithosphere occurs. Below, the upper mantle is convecting at decreasing Rayleigh numbers from M1-5. In M1, the vertical mantle flow speed within the convecting cell at $x\approx+350$ km is elevated (indicated by darker blue coloured region in Fig. 3.6a) compared to the average flow speed of $\approx$1–2 $\mathrm{cm\,yr^{-1}}$ in neighbouring cells). The size of the convection cells in M2 is larger compared to M1 and in the order of ca. 100–300 km in diameter. Characteristic is the more elliptical shape of the cells compared to the circular cells in M1. The magnitude of material flow velocity is similar but distributed more horizontally symmetric below both margins compared to M1 (compare arrows and colour field of Fig.3.6a & b). A zone of strong downward directed movement develops below both margins (dark blue cells at $x\approx$ -300 km and $x\approx$ +300 km in Fig.3.6b). Magnitude of material flow speed is in the order of 1.5 $\mathrm{cm\,yr^{-1}}$. The average Rayleigh-number of the convecting system in M2 is approximately 3.92×10^{6} and is about a factor 2.5 lower

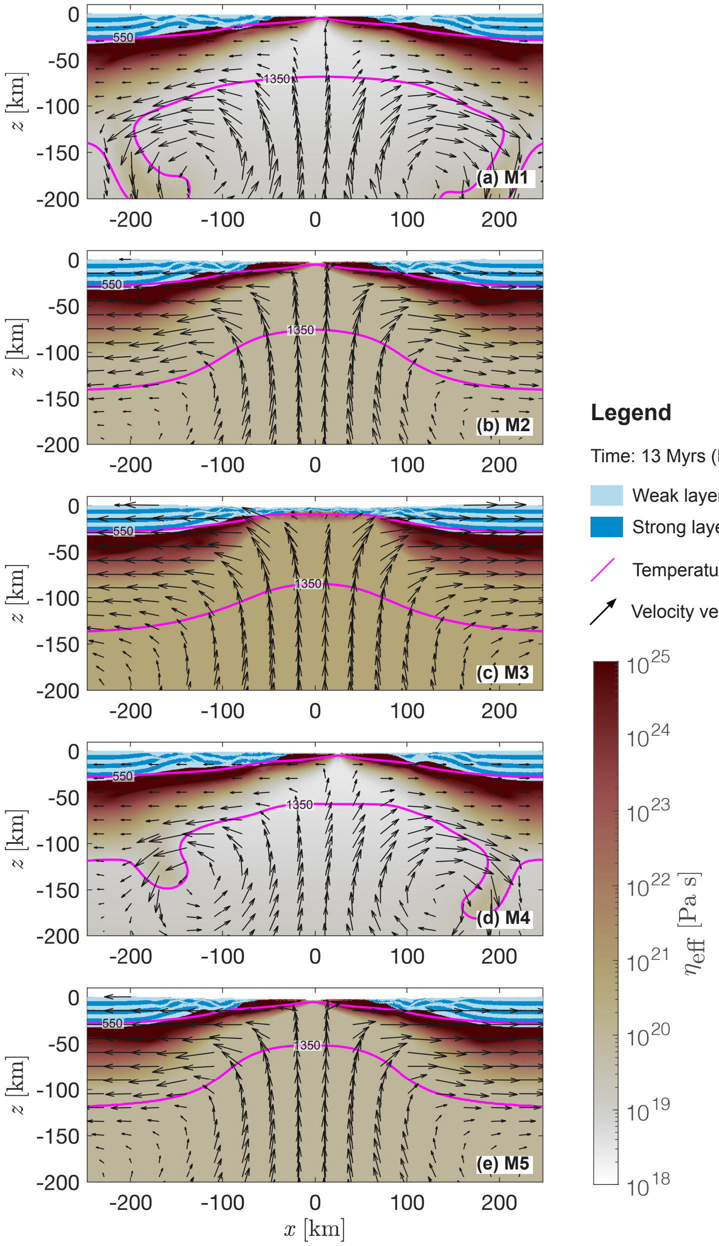

Figure 3.5: Comparison of M1-5 during the extension stage. (a)-(e) Enlargements of results of models M1-5 at 13 Myr of modelled time. Blue colours indicate mechanically weak (light) and strong (dark) crustal units. White to red colours show the effective viscosity field calculated by the numerical algorithm. Magenta lines show the level of 550 °C and 1350 °C isotherm. Arrows represent velocity vectors and the length of the arrows is not to scale.

compared to M1. M3 develops four large convection cells, two below each margin, that are active up to depths of approximately 600 km (see arrows Fig. 3.6c). Downward directed movement of material occurs with ca. 2 $\mathrm{cm\,yr^{-1}}$ (darker blue regions at $x \approx$ -500 km and x

$\approx$ 500 km in Fig.3.6c). The average Rayleigh number of the system is ca. 1.18×10^6, which is about a factor 8.4 smaller compared to M1. In M4 and M5, material transport occurs at absolute values for vertical velocity ¡0.5 $\mathrm{cm\,yr^{-1}}$ (see coloured velocity field in Fig. 3.6d & e) which is one order of magnitude lower compared to M1-3. Two horizontally symmetric convection cells develop in these models that are active between $z \approx$ -150 km and $z \approx$ -400 km (arrows in Fig. 3.6d & e). The average Rayleigh number is ca. 1.97×10^6 and 5.48×10^5 in M4 and M5, respectively. Figure 3.6f-j shows the difference between the entire density field and the horizontally averaged vertical density profile at 99 Myr (see Fig. 3.2e) and Fig. 3.10b shows a horizontal profile of this field averaged vertically over $-200 \leq z \leq -100$ km. The distribution of density differences becomes more horizontally symmetric with decreasing Rayleigh number (M1-5, see Fig. 3.10b). In M1, the 2 $\mathrm{cm\,yr^{-1}}$ density contour line encloses a high-density anomaly below the right passive margin (see black contour line at $x\approx$300 km, $z\approx$-200 km in Fig. 3.6f). Calculating the suction, or buoyancy, force for this body according to Eq. 3.16 yields a value of 0.25 $\mathrm{TN\,m^{-1}}$. Since the distribution of density differences is laterally symmetric in M2-5 (Fig. 3.10b) and defining an integration area is not trivial, a calculation of suction forces is not attempted for M2-5. Figure 3.10a shows the topography at ca. 99 Myr in model history, that is 1 Myr before the start of convergence. Topography does not exceed 1.5 km and the average depth of the basin is ca. 3.75 km.

Figure 3.7a-e shows the conductive heat flow of the entire domain in absolute values. M1-5 reproduce a heat flux of 20–30 $\mathrm{mW\,m^{-2}}$ through the base of the lithosphere (indicated by the 10^{21} Pa s isopleth at a depth between 100–110 km). The conductive heat flow below the lithosphere is close to 0 $\mathrm{mW\,m^{-2}}$ in M1-3. In M4 and M5, values for conductive heat flow remain at ca. 20 $\mathrm{mW\,m^{-2}}$ through the entire upper mantle. Density differences in the upper part of the mantle lithosphere reach ca. 20 $\mathrm{kg\,m^{-3}}$ between ca. 35–120 km in depth (Fig. 3.2e & j). Values for effective viscosity range in the order of 10^{19} Pa s for M1 and M5 and in the order 10^{20} Pa s in M2-4 directly below the lithosphere and 10^{21} Pa s at the bottom of the upper mantle (Fig. 3.2f).

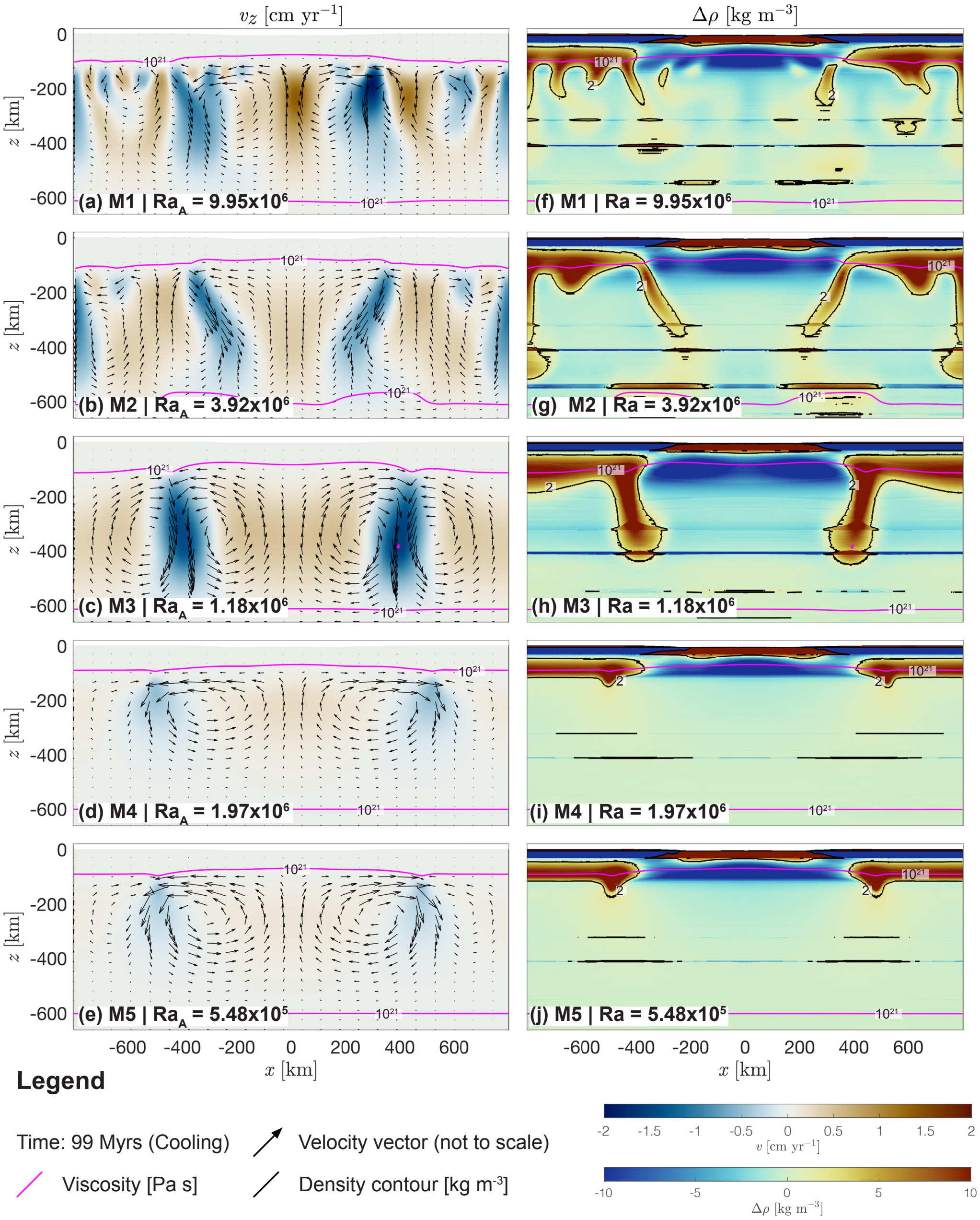

Figure 3.6: Results of models M1-5 at 99 Myr (end of cooling period). (a)-(e) Blue to red colours indicate the vertical velocity magnitude calculated by the numerical algorithm. Black arrows show not to scale velocity vectors to visualise the material flow field. (f)-(j) Blue to red colours indicate the difference between the entire density field and the horizontal average density profile as shown in Fig. 3.2(e). Black lines are the 2 kg m^{-3} density contour. The magenta coloured line shows the level of the 10^{21} Pa s viscosity isopleth in all sub-figures. This contour line represents the mechanical boundary between the rigid mantle lithosphere (no velocity glyphs) and the convecting upper mantle.

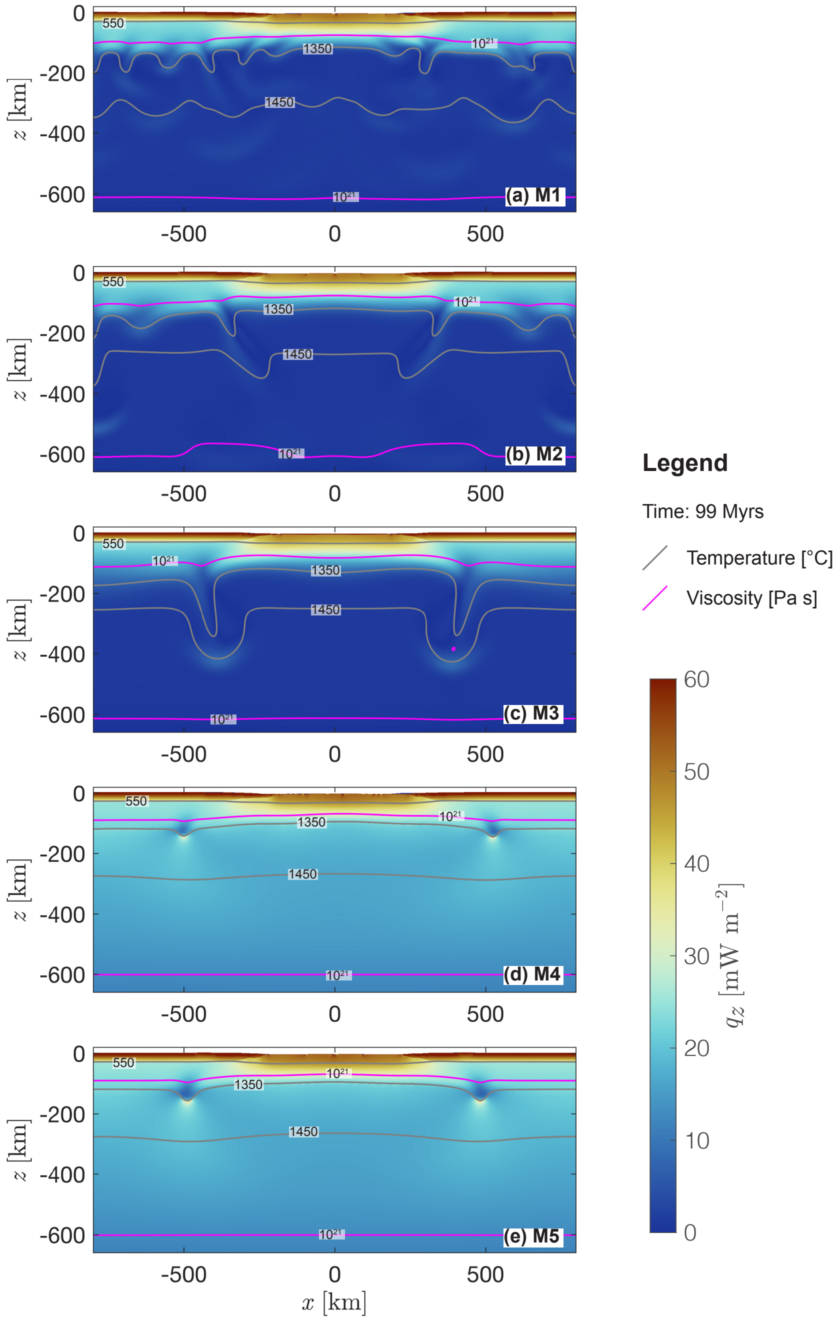

Figure 3.7: Vertical conductive heat flow represented by blue to red colours for models M1-5 ((a)-(e)) after 99 Myr. The grey lines indicate the depth of the 550 °C, 1350 °C and 1450 °C isotherm. The magenta line indicates the depth of the 10^{21} Pa s isopleth which represents approximately the mechanical transition between the mantle lithosphere and the convecting upper mantle.

3.3.5 Comparison of reference run with models M2-5: Convergence and subduction phase

In contrast to M1, two major symmetric shear zones develop in the lithosphere in M2, M3 and M5, one shear zone at each of the continental margins (Fig.3.8b, c & e). Like in M1, one shear zone forms below the right margin in M4 (Fig. 3.8d). At this early stage of subduction initiation, the strain rate in the shear zone is in the order 10^{-14}-10^{-13} s^{-1}. In the region of the shear zones, the temperature is increased, which is indicated by the deflection of the isotherms (red contour lines in Fig.3.8a-e). Horizontal profiles of gravitational potential energy (*GPE*, see appendix 3.6.3) are in general similar (Fig. 3.10c) for M1-5.

In contrast to the single-slab subduction evolving in M1, double-slab subduction is observed below both margins in M2-5 and sediments are deposited in two trenches as the subduction evolves (Fig.3.9b-e). Folding of the crustal layers indicates deformation in both margins of M2-5. Values for viscosity in the upper mantle remain stable at values of 10^{19} Pa s in M4, whereas the viscosity values are at the applied lower cut-off value in M2, M3 and M5 throughout the entire simulation history. Convection cells remain active during subduction. Similar to M1, a stable convection cell is active below one subducting slab in M4. The distribution of convection cells is more symmetric in front of the slabs in M2, M3 and M5 compared to M1. Defined by the applied boundary condition, material flows into the model domain up to z = -330 km at the lateral boundaries in all models (see section 3.2). Though, far away from the boundary in the centre of the domain in M1 and M2 the horizontal material inflow from the lateral boundaries is limited up to a depth of ca. 100–150 km (see horizontally directed arrows in Fig. 3.9a & b). In M3-5 the lateral inflow of material reaches a depth of about 200 km in the centre of the domain (Fig. 3.9c-e).

3.3.6 Estimates for plate driving forces

The vertically-integrated second invariant of the deviatoric stress tensor, $\bar{\tau}_{\mathrm{II}}$, is a measure for the strength of the lithosphere and twice its value is representative for the horizontal driving force (per unit length, F_{D} hereafter) during lithosphere extension and compression (appendix

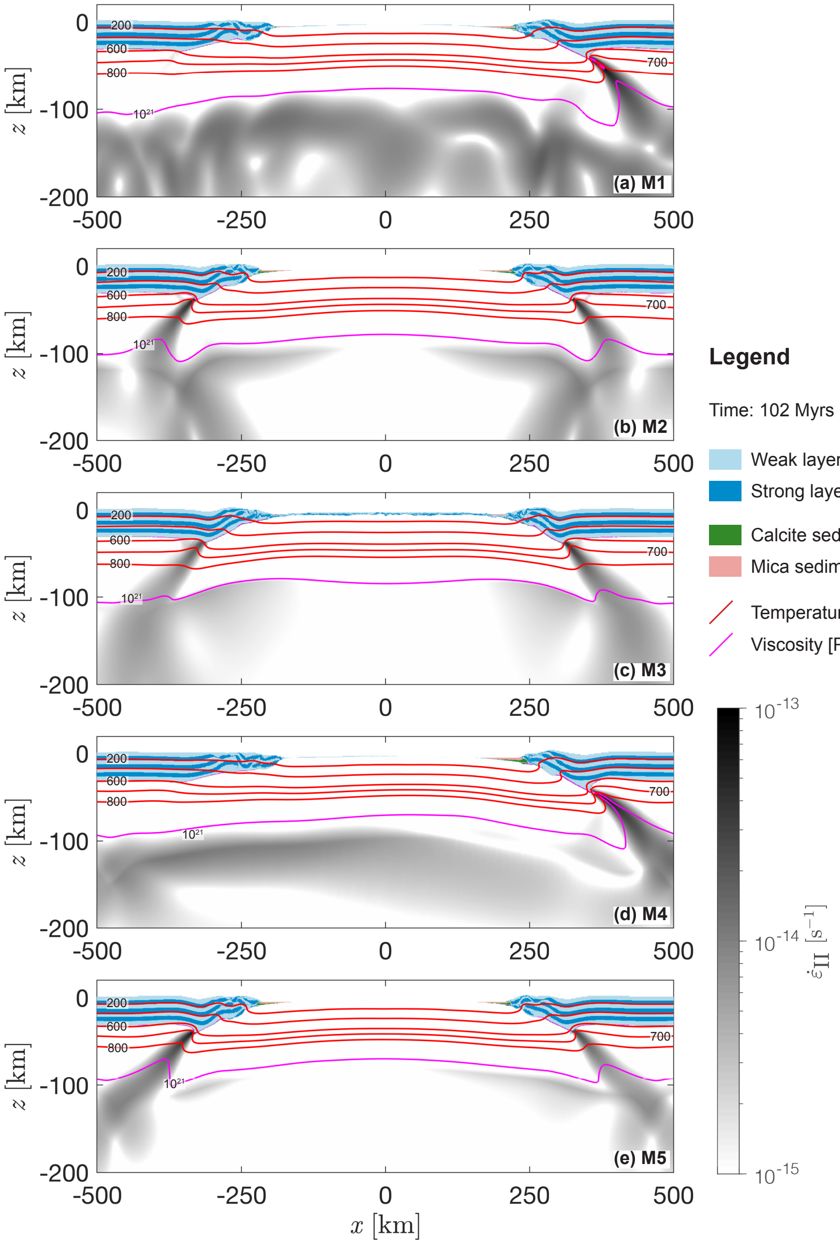

Figure 3.8: Stage of subduction initiation. (a)-(e) Results of models M1-5 after 102 Myr of simulated deformation. Blue colours indicate mechanically weak (light) and strong (dark) crustal units, green and salmon colours indicate the sedimentary units (only minor volumes in trench regions). White to black colours indicate the second invariant of the strain rate tensor field calculated by the numerical algorithm. Red lines show levels of several isotherms and the magenta coloured line shows the level of the 10^{21} Pa s viscosity isopleth. This contour line represents approximately the mechanical transition between the mantle lithosphere and the convecting upper mantle.

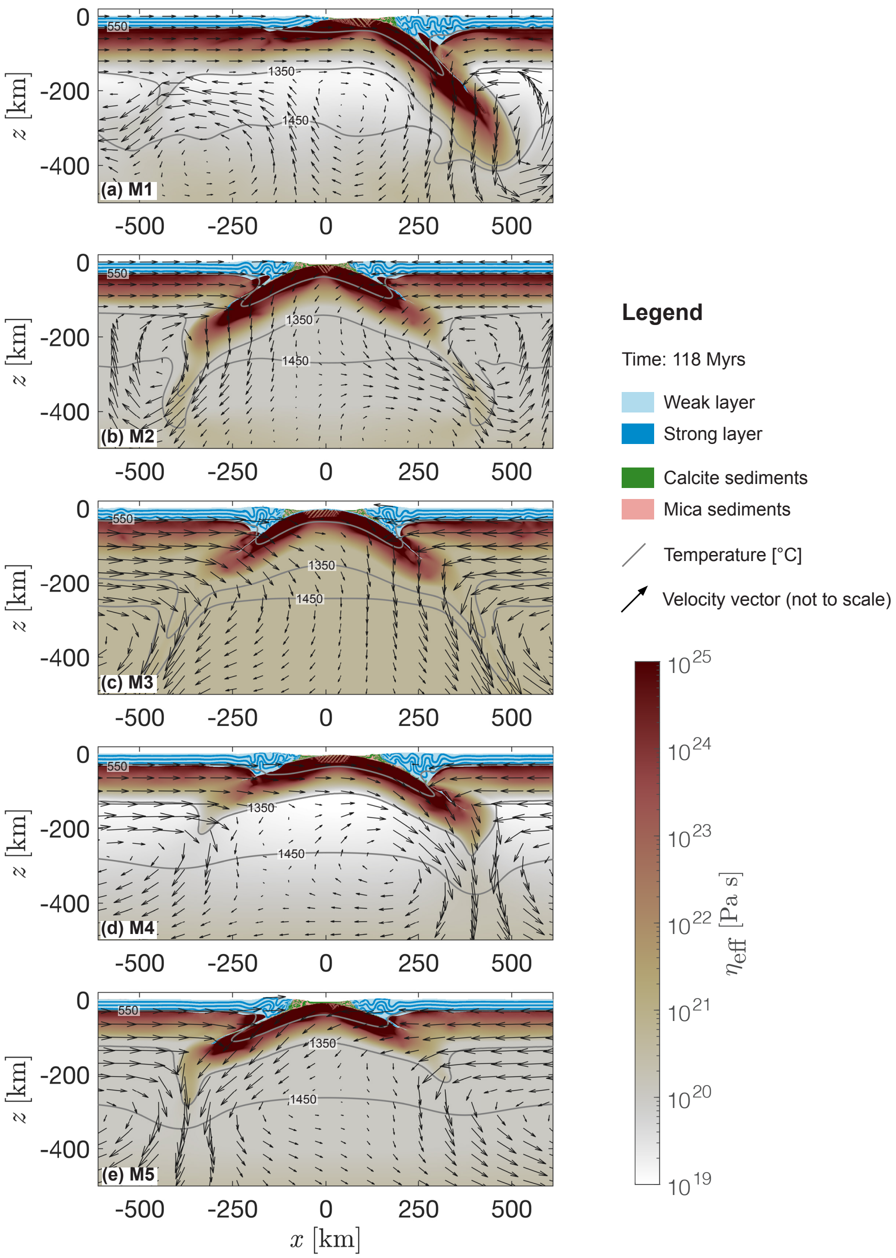

Figure 3.9: Evolution of subduction zones. (a)-(e) Results of models M1-5 after 118 Myr of simulated deformation. Blue colours indicate mechanically weak (light) and strong (dark) crustal units, green and salmon colours indicate the sedimentary units. White to red colours show the effective viscosity field calculated by the numerical algorithm for the mantle lithosphere and the upper mantle. Arrows represent velocity vectors and the length of the arrows is not to scale. Grey lines indicate the 550 °C, 1350 °C and 1450 °C isotherm.

3.6.3). Figure 3.10d shows the evolution of F_{D} during the entire cycle. During the pure shear thinning phase in the first ca. 2 Myr of extension, values for F_{D} reach 14 $\mathrm{TN\,m^{-1}}$. At ca.

2–3 Myr (1 in Fig. 3.10d), this value drops below ca. 5 $\mathrm{TN\,m^{-1}}$ at ca. 8 Myr. At the end of the extension period F_{D} is stabilised at values between ca. 2–3 $\mathrm{TN\,m^{-1}}$ for all models (2 in Fig. 3.10d). This value remains relatively constant for all models during the entire cooling period. The maximum value for F_{D} necessary to initiate subduction in all models is observed in M3 and is ca. 23 $\mathrm{TN\,m^{-1}}$ (thin blue curve in Fig. 3.10d). The minimum value necessary for subduction initiation of ca. 13 $\mathrm{TN\,m^{-1}}$ is observed in M4. The reference run M1 initiates subduction with a value of $F_{\mathrm{D}} \approx 17$ $\mathrm{TN\,m^{-1}}$. Strain localization at ca. 102 Myr is associated with a rapid decrease of F_{D} by ca. 2–5 $\mathrm{TN\,m^{-1}}$ in all models (3 in Fig. 3.10d). At ca. 105 Myr, values for F_{D} increase again until the end of the simulation.

3.4 Discussion

3.4.1 Impact of mantle viscosity structure and effective conductivity on passive margin formation

Higher values for the lower viscosity cut-off (M2 & M3 compared to M1) do not only change the viscosity structure of the mantle, but also increase the strength of the weak layers. In consequence, the multi-layered crust necks effectively as a single layer. The resulting passive margins are slightly shorter and more symmetric (Duretz et al., 2016, see also M3). The highest cut-off value of $5{\times}10^{20}$ Pa s (M3) leads to a two-stage necking as investigated by Huismans and Beaumont (2011). First, the lithosphere is necking while the crust deforms by more or less homogeneous thinning, leading to the development of a large continuous zone of hyper-extended crust, below which the mantle lithosphere has been removed. Second, the hyper-extended crust is breaking up later than the continental mantle lithosphere. During the rifting stage, the thermal field in all simulations is very similar (see Fig. 3.2a), presumably because effects of heat loss due to diffusion are not significant over the relatively short time scale.

3.4.2 Onset of upper mantle convection and thermo-mechanical evolution of the lithospheric plates

Rifting in M1-5 causes up-welling of hot asthenospheric material in the horizontal centre of the domain. The resulting lateral thermal gradients are high enough to induce small-scale convection (Buck, 1986). Huang et al. (2003) derived scaling laws to predict the onset time for small-scale convection in 2D and 3D numerical simulations. They investigated the impact of plate motion, layered viscosity, temperature perturbations and surface fracture zones on the onset time. The observed onset time in layered viscosity systems becomes larger when the thickness of the weak asthenosphere decreases. Also, plate motion can delay the onset of small-scale convection. In contrast, fracture zones at the surface may lead to earlier onset of convection depending on the thermal structure of the fracture zones. Using their scaling law and the parameters used in our reference model M1, onset time of convection is predicted for ca. 43 Myr. However, onset of convection in M1 is observed as early as ca. 8 Myr (see Fig. 3.3) which is consistent with onset times observed in numerical simulations conducted by Van Wijk et al. (2008). There may be several reasons for the discrepancy between the prediction and observation. First, the models presented here are likely a combination of the configurations tested by Huang et al. (2003). Second, the choice of boundary conditions and initial configuration is different which is probably important when testing the impact of plate motion on the onset time. They located the rift centre at the left lateral boundary, whereas the rift centre in our models is located far away from the lateral boundaries in the horizontal centre of the domain. This likely impacts the flow direction of hot material ascending beneath the rift centre and, consequently, alters lateral thermal gradients which are important for the onset of convection. The onset time for convection is delayed and at ca. 20 Myr in M2 and at ca. 30 Myr in M3. This delay is likely due to the increased viscosity in the asthenosphere in M2 & M3 compared to M1 which decreases the Rayleigh number of the system. This observation is in agreement with the general inverse proportionality of the onset time of convection to the Rayleigh number as predicted by Huang et al. (2003).

Once convection has started, it stabilises the temperature field (Richter, 1973; Parsons and McKenzie, 1978) over large time scales and controls the thickness of the lithosphere. Although we allow for material inflow up to z = -330 km, the arrows in Fig. 3.9a & b indicate that lateral inflow of material far away from the boundary is limited up to z $\gtrapprox$ -150 km. Below this coordinate, the convection cells transport material even towards the lateral boundary, in the opposite direction of material inflow. This observation suggests, that the thermal thickness of the lithosphere adjusts self-consistently and far away from the boundary during the geodynamic cycle. The thermal thickness of the lithosphere seems to vary with decreasing Rayleigh number: in M5 the value for the thermal thickness of the lithosphere is $\approx$ 200 km (see arrows in Fig. 3.9e). This observation suggests that the thermal thickness of the moving lithosphere is presumable regulated by the vigour of convection.

For realistic values for thermal conductivity in the upper mantle (M1-3), heat flow through the base of the mechanical lithosphere is between 20–30 $\mathrm{mW\,m^{-2}}$ (Fig. 3.7a-c). These values are in the range of heat flow estimates for heating at the base of the lithosphere confirmed by other numerical studies (Petersen et al., 2010; Turcotte and Schubert, 2014). Below the lithosphere, the conductive heat flux is essentially zero, because heat transport is mainly due to advection of material in the convecting cells. The effective conductivity approach maintains a reasonable heat flux directly at the base of the lithosphere (figs. 3.7d & e) and convection cells develop. However, all processes in the upper mantle are conduction dominated (see elevated values for q_z in Fig. 3.7d & e). This implies that the characteristic physics of mantle convection are not captured correctly in these models. This becomes evident when comparing Fig. 3.6a to Fig. 3.6d: although the physical parameters - except the thermal conductivity in the upper mantle - are the same in both simulations and temperature profiles are similar (see Fig. 3.2d & i), the Rayleigh-numbers of the systems differ by one order of magnitude (see Table 3.2) and the convective patterns are entirely different.

3.4.3 Mantle convection, thermal erosion and tectonics in the Archean

Model M6 underlines the importance of better constraining the rheology of the mantle. Due to significantly reduced viscosities (see Fig. 3.2c), convection in the upper mantle occurs at an average Rayleigh number of ca. 9×10^7 in M6. Compared to estimates for present-day Earth's upper mantle convection (Torrance and Turcotte, 1971; Schubert et al., 2001) this Rayleigh-number is an order of magnitude higher. The lithosphere is recycled rapidly and the resulting values for density directly below the lithosphere are ca. 100 $\mathrm{kg\,m^{-3}}$ lower in M6 compared to M1-5. The resulting density structure in the upper region of the mantle deviates significantly from the PREM model (Dziewonski and Anderson (1981), see Fig. 3.2b). Convection at such high Rayleigh numbers leads to an enhanced temperature field. Resulting values for temperature at the Moho locally reach ca. 1000 °C. Our models suggest that such weak mantle rheology is actually not feasible for present-day plate tectonics, but this non-feasibility can only be observed when performing coupled mantle–lithosphere models as we have presented. In lithosphere-only models, a weak mantle would not generate the thermal erosion of the lithosphere bottom as observed in model M6, because the lithosphere bottom would be "stabilized" by the bottom boundary condition. In the Archean eon, the mantle potential temperature was probably 200–300 °C higher (Herzberg et al., 2010) and therefore convection was more vigorous (Schubert et al., 2001). Agrusta et al. (2018) have investigated the impact of variations in mantle potential temperature compared to present-day's value on slab-dynamics. Assuming a 200 °C higher value for the mantle potential temperature compared to present-day estimates leads to viscosity structures similar to the average viscosity structure we report for M6 (compare Fig. 6c in Agrusta et al. (2018) to Fig. 3.2c of this study). Hence, we argue that such vigorously convecting systems as presented in M6 may be applicable to the mantle earlier in Earth's history.

3.4.4 Spontaneous vs. induced subduction initiation and estimates for plate driving forces

Currently, the processes and tectonic settings leading to subduction initiation remain unclear (Stern, 2004; Stern and Gerya, 2018; Crameri et al., 2019). Stern (2004) proposed two fundamental mechanisms for subduction initiation:

(1) Spontaneous (or vertically forced, Crameri et al. (2020)) subduction initiation occurs, for example, due to densification of the oceanic lithosphere during secular cooling. Cloos (1993) proposed that the density increase of cooling, 80 Myr old oceanic lithosphere compared to the underlying asthenosphere is in the order of 40 $\mathrm{kg\,m^{-3}}$. According to Cloos (1993), this difference is sufficient to initiate subduction spontaneously by negative buoyancy of the oceanic lithosphere (see Stern (2004); Stern and Gerya (2018, & references therein) for detailed explanation). However, McKenzie (1977) and Mueller and Phillips (1991) showed that the forces acting on the lithosphere due to buoyancy contrasts are not high enough to overcome the strength of the cold oceanic lithosphere. Observations of old plate ages (>100 Myr) around passive margins in the South Atlantic (Müller et al., 2008) indicate their long-term stability.

In the models presented here, the applied thermodynamic density of the Hawaiian pyrolite leads to density differences between the exhumed mantle in the basin and the underlying asthenosphere of ca. 10–20 $\mathrm{kg\,m^{-3}}$ after 99 Myr in model history. These buoyancy contrasts are ca. 2× smaller than the contrast proposed by Cloos (1993). Boonma et al. (2019) calculated a density difference ($\rho_{\mathrm{ast}} - \rho_{\mathrm{lit}}$) of +19 $\mathrm{kg\,m^{-3}}$ for an 80 km thick continental lithosphere and -17 $\mathrm{kg\,m^{-3}}$ for an oceanic lithosphere of 120 Myr of age. These values are in agreement with the values we report in our study. In the 2D models presented here, these buoyancy contrasts are insufficient to overcome the internal strength of the cooled exhumed mantle and initiate subduction at the passive margin spontaneously.

However, modelling spontaneous subduction initiation for an ad-hoc constructed passive margin geometry is possible, if the employed mechanical resistance is small, the density difference between lithospheric and oceanic mantle is large, and/or if an additional weak zone is imposed. Such passive margin configurations are indeed unstable and lead to spontaneous subduction initiation within a few million years (Stern and Gerya, 2018, & references therein). However, the passive margins we consider in our study have been stable for at least 60 Myr before subduction initiation. Therefore, spontaneous subduction initiation for unstable passive margins is in contrast with the observation of long-term stability of the ancient Alpine Tethys margins (McCarthy et al., 2018) and the recent passive margins in the South Atlantic (Müller et al., 2008). Our results are, hence, in agreement with the stability of these passive margins. Modelling long-term geodynamic cycles, applicable to the evolution of the Alpine Tethys and the South Atlantic, requires appropriate density and rheological models which generate passive margins that are stable for more than 60 Myr (Alpine Tethys) or more than 180 Myr (South Atlantic). To evaluate whether models of spontaneous SI at passive margins are feasible, these models need to explain why the passive margins have been stable for more than 60 Myr and only afterwards ”collapsed” spontaneously, although they are cooled and mechanically strong.

(2) Induced (or horizontally forced, Crameri et al. (2020)) subduction initiation occurs, for example, due to far-field plate motion. In fact, many numerical studies that investigate subduction processes do not model the process of subduction initiation. In these studies, a major weak zone across the lithosphere is usually prescribed ad-hoc in the initial model configuration to enable subduction (Ruh et al., 2015; Zhou et al., 2020). Another possibility to model subduction is to include a prescribed slab in the initial configuration. This means

that subduction has already initiated at the onset of the simulation (Kaus et al., 2009; Garel et al., 2014; Holt et al., 2017; Dal Zilio et al., 2018). In our models, subduction is initiated self-consistently, which means here: (i) we do not prescribe any major weak zone or an already existing slab, and (ii) the model geometry and temperature field at the onset of convergence (100 Myr) were simulated during a previous extension and cooling phase with the same numerical model and parameters. Subduction is initiated during the initial stages of convergence and subduction initiation is, hence, induced by horizontal shortening. Notably, Crameri et al. (2020) analysed more than a dozen documented subduction zone initiation events from the last hundred million years and found that horizontally forced subduction zone initiation is dominant over the last 100 Myr. During convergence in our models, shear heating together with the temperature and strain rate dependent viscosity formulation (dislocation creep flow law, Eq. **??**) causes the spontaneous generation of a lithosphere-scale shear zone that evolves into a subduction zone (Thielmann and Kaus, 2012; Kiss et al., 2020). However, shear heating is a transient process which means the increase in temperature is immediately counterbalanced by thermal diffusion. Efficiency of shear heating is restricted to the first ca. 2–3 Myr after shear zone formation in the presented models. After this time span, heat generated by mechanical work is diffused away. Therefore, thermal softening is unlikely the mechanism responsible for stabilisation of long-term subduction zones, but likely important for initiating and triggering subduction zones.

The value of F_{D} (see appendix 3.6.3) represents the plate driving force. In M1, the maximal value of F_{D} just before stress drop caused by subduction initiation at ≈103 Myrs is ≈17 $\mathrm{TN\,m^{-1}}$ (Fig. 3.10(d)). However, $F_{\mathrm{D}} \approx 2$ $\mathrm{TN\,m^{-1}}$ at the end of the cooling stage, resulting from stresses due to mantle convection and lateral variation of GPE between continent and basin. Therefore, this value can be subtracted from the ≈17 $\mathrm{TN\,m^{-1}}$. The required plate tectonic driving force for convergence-induced subduction initiation is then ≈15 $\mathrm{TN\,m^{-1}}$ for M1. Kiss et al. (2020) modelled thermal softening induced subduction initiation during convergence of a passive margin, whose geometry and thermal structure was generated ad-hoc as initial model configuration. Their initial passive margin structure was significantly less heterogeneous than ours. To initiate subduction, they needed a driving force of ≈37 $\mathrm{TN\,m^{-1}}$

which is significantly larger than the ≈15 $\mathrm{TN\,m^{-1}}$ required in our model M1. Obviously, the ≈15 $\mathrm{TN\,m^{-1}}$ cannot be exceeded by the mantle convection (≈ 2 $\mathrm{TN\,m^{-1}}$) modelled here. Even assuming an additional ridge push force of 3.9 $\mathrm{TN\,m^{-1}}$ (Turcotte and Schubert, 2014) would not be sufficient to initiate subduction spontaneously in the models presented here. The boundary convergence providing the remaining ca. 9 $\mathrm{TN\,m^{-1}}$ to initiate subduction in our models are assumed to be caused by far-field plate driving forces. These are generated by global processes that are not modelled inside our domain, such as slab pull, whole mantle convection, ridge push etc. For example, the closure of the Piemonte–Liguria basin is assumed to be caused by the much larger scale convergence of the African and European plates (McCarthy et al., 2018).

We suggest that mechanical and geometrical heterogeneity inherited by previous deformation periods and thermal heterogeneity due to mantle convection reduces the required driving force necessary for subduction initiation by thermal softening. Additionally, we suppose that the plate driving force necessary for horizontally forced subduction initiation in our models could be further reduced by considering more heterogeneities, or a smaller yield stress in the mantle lithosphere. However, the minimum value for F_{D} which can still generate horizontally forced subduction initiation via thermal softening has to be quantified in future studies. This is relevant, because the main argument against thermal softening as an important localization mechanism during lithosphere strain localization and subduction initiation is commonly that the required stresses, and hence driving forces, are too high. In nature, more softening mechanisms act in concert with thermal softening, such as grain damage (e.g. Bercovici and Ricard, 2012; Thielmann and Schmalholz, 2020), fabric and anisotropy evolution (e.g. Montési, 2013) or reaction-induced softening (e.g. White and Knipe, 1978), likely further reducing forces required for subduction initiation. Furthermore, Mallard et al. (2016) showed with 3D spherical full-mantle convection models that a constant yield stress between 150 and 200 MPa in their outer boundary layer, representing the lithosphere, provides the most realistic distribution of plate sizes in their models. The yield stress in their models corresponds to a deviatoric, von Mises, stress which is comparable to the value of τ_{II} calculated for our models. If we assume a 100 km thick lithosphere, then $F_{\mathrm{D}} = 15$ $\mathrm{TN\,m^{-1}}$ yields a vertically-averaged deviatoric stress, τ_{II}, of 75 MPa for our model lithosphere. Therefore, vertically-averaged deviatoric stresses for our model lithosphere are even smaller than deviatoric, or shear, stresses employed in global mantle convection models. Based on the above-mentioned arguments, we propose that ≈15 $\mathrm{TN\,m^{-1}}$ is a feasible value for the horizontal driving force per unit length.

3.4.5 Mantle convection stabilising single-slab subduction

Figure 3.10c shows the difference in *GPE* at 103 Myr. The horizontal profiles do not reveal significant differences between the models. The *GPE* is sensitive to topography and density distribution throughout the model domain. Values for density differences are ca. 10–20$\mathrm{kg\,m^{-3}}$ across the mantle lithosphere. When integrated over the entire depth, such variations do not significantly impact the *GPE* profiles. Instead, the signal reflects the topography, which is similar in all the models due to the similar margin geometry (see Fig. 3.10a and Fig. 3.5a-e). In consequence, stress concentrations lead to localised deformation and shear zone formation at both margins in all models during the onset of convergence. Therefore, the evolution and stabilisation of a single-sided subduction requires an additional asymmetry of the system.

The average Rayleigh number (see appendix Eq. 3.2) in M1 is ca. 9.95×10^{6} (see Table 3.2) which is close to estimated values for upper mantle convection (Torrance and Turcotte, 1971; Schubert et al., 2001). Potential lateral asymmetry caused by the convecting cells in the upper mantle is inherited from the cooling period. The vertical velocity field at the end of the cooling period of M1 (Fig. 3.6a) reveals one convection cell at $x \approx +350$ km with flow speeds in the order of the convergence velocity applied later. This convection cell is induced by a high-density anomaly directly below the passive margin at which subduction will be initiated later in the model (see black contour line below right margin in Fig. 3.6f). This sinking, high-density body probably induces an asymmetry in form of an additional suction force exerted on the lithospheric plate. Conrad and Lithgow-Bertelloni (2002) quantified the importance of slab-pull vs. slab-suction force and showed that the slab pull force and the suction force of a detached slab sinking into the mantle induces similar mantle flow fields. They argued that a detached fraction of a slab sinking into the mantle can exert shear traction forces at the base of the plate and drive the plate. Baes et al. (2018) showed with numerical simulations that sinking of a detached slab below a passive margin can contribute significantly to the initiation of subduction. We suggest that the high-density anomaly observed in M1 and the associated mantle flow also generates a force similar to a slab-suction force. To quantify the suction force induced by the sinking, high-density body in M1, we calculated the difference of the density in this region with respect to the horizontally averaged density field presented in Fig. 3.2e and integrated this buoyancy difference spatially over the area enclosed by the 2 $\mathrm{kg\,m^{-3}}$ density contour below the right passive margin (see Fig. 3.6f). The resulting buoyancy force per unit length is ca. 0.25 $\mathrm{TN\,m^{-1}}$. This value is relatively low compared to the plate driving forces acting in the model, but likely induces a sufficiently high asymmetry to stabilise the single-slab subduction in simulation M1.

Values for the Rayleigh number in M2 and M3 are lower (3.92×10^6 and 1.18×10^6 respectively) compared to M1 (see Table 3.2), because of the relatively higher viscosity (see Eq. 3.2). With decreasing Rayleigh-number the asymmetry of convection also decreases (Schubert et al., 2001). In consequence, the size of the convecting cells becomes larger and more elliptic (M2 compared to M1) and the number of active cells decreases (M3 compared to M1). Enhancing the thermal conductivity (included in the denominator in Eq. 3.2) by ca. one order of magnitude in models M4 and M5 also decreases the Rayleigh number by one order of magnitude compared to M1 (see Table 3.2). Decreasing the Rayleigh-number (M2-5) leads to more laterally symmetric convective flow patterns and decreases the speed and distribution of material flow (see Fig. 3.6b-e). In turn, this probably leads to more equally distributed density differences (Fig. 3.10b) and, therefore, suction forces exerted on the plates. Hence, we argue that decreasing the Rayleigh-number, assuming a relatively strong asthenosphere or applying an enhanced thermal conductivity likely favours the initiation of divergent double-slab subduction. The resulting slab geometries resemble a symmetric push-down (M2-5), rather than a stable asymmetric subduction (M1). This impacts the deformation in the lithosphere, especially in the crust: the crustal layers of both plates are strongly folded (see Fig. 3.9b-e). In M1, the deformation of the crustal layers only occurs in the overriding plate.

3.4.6 Comparison with estimates of Earth's mantle viscosity and thermal structure

To apply our models to geodynamic processes on Earth, we compare several model quantities with measurements and indirect estimates of these quantities. Even after 118 Myr of model evolution, the mantle density structure of our model remains in good agreement with the preliminary reference Earth model (PREM Dziewonski and Anderson (1981), see Fig. 3.2b & e). The geotherm of the conduction dominated regime remains well in the range of pressure–temperature (P-T) estimates from mantle xenolith data. Also, the geotherm of the convection dominated regime remains within the range for adiabatic gradients and potential temperatures applicable to the Earth's mantle (Hasterok and Chapman (2011), see Fig. 3.2a & d) during the entire long-term cycle. Viscosity profiles lie within the range of estimates inferred by inversion of observable geophysical data and from experimentally determined flow law parameters of olivine rheology (Mitrovica and Forte (2004); Behn et al. (2004); Hirth and Kohlstedf (2003), see Fig. 3.2c & f). Lithosphere and mantle velocities are in a range of several $\mathrm{cm\,yr^{-1}}$ which is in agreement with predictions from boundary layer theory of layered mantle convection (Schubert et al., 2001) and plate velocity estimates from GPS measurements (Reilinger et al., 2006).

3.4.7 Formation and reactivation of magma-poor rifted margins: potential applications

Our model can be applied to some first-order geodynamic processes that were likely important for the orogeny of the Alps. Rifting in the Early to Middle Jurassic (Favre and Stampfli, 1992; Froitzheim and Manatschal, 1996; Handy et al., 2010) lead to the formation of the Piemont–Liguria ocean which was bounded by the hyper-extended magma-poor rifted margins of the Adriatic plate and the Briançonnais domain on the side of the European plate. We follow here the interpretation that the Piemont–Liguria ocean was an embryonic ocean which formed during ultra-slow spreading and was dominated by exhumed subcontinental mantle (e.g. Picazo et al., 2016; McCarthy et al., 2018; Chenin et al., 2019; McCarthy et al., 2020).

If true, there was no stable mid-ocean ridge producing a several 100 km wide ocean with a typically 8 km thick oceanic crust and our model would be applicable to the formation of an embryonic ocean with exhumed mantle bounded by magma-poor hyper-extended rifted margins. Our models show the formation of a basin with exhumed mantle bounded by hyper-extended margins above a convecting mantle. Hence, our model may describe the first-order thermomechanical processes during formation of an embryonic ocean. During closure of the Piemont–Liguria ocean, remnants of those magma-poor ocean–continent transitions escaped subduction and are preserved in the Eastern Alps (Manatschal and Müntener, 2009). We follow the interpretation that the initiation and at least the early stages of ocean closure were caused by far-field convergence between the African and European plates (e.g. Handy et al., 2010). We further assume that subduction was induced, or horizontally forced, by this convergence and was not initiated spontaneously due to buoyancy of a cold oceanic lithosphere (De Graciansky et al., 2010). This interpretation agrees with recent results of Crameri et al. (2020) who suggest that most subduction zones that formed during the last 100 Myr were likely induced by horizontal shortening. Our models show that a cooling exhumed mantle does not subduct spontaneously because buoyancy forces are not significant enough to overcome the strength of the lithosphere. However, the models show that convergence of the basin generates a horizontally forced subduction initiation at the hyper-extended passive margin causing subduction of the exhumed mantle below the passive margin. Such subduction initiation at the passive margin agrees with geological reconstructions which suggest that the Alpine subduction initiated at the hyper-extended margin of Adria (e.g. Manzotti et al., 2014) and not, for example, within the ocean. Overall, the here modelled, more than 100 Myr long, geodynamic cycle is thus in agreement with several geological reconstructions of the Alpine orogeny. During convergence, several of our models show the formation of a divergent double-slab subduction. Such divergent double-slab subduction likely applies to the eastward and westward dipping subduction of the Adriatic plate (Faccenna and Becker, 2010; Hua et al., 2017). Subduction started significantly earlier below the Dinarides compared to the westward directed subduction (Handy et al., 2010). Since about 30 Ma, the Adriatic plate undergoes a divergent double slab subduction, for which the two subduction zones have started at different times. In model M4, subduction initiation does not occur simultaneously below both margins. The subduction initiation below the left margin occurs ca. 10 Myr after subduction initiation below the right margin. During the evolution of the model, the subduction switches from the right margin to the left margin and then back again (see also video supplement). Therefore, divergent double-slab subduction does not require that subduction initiation at the passive margins occurs at the same time. However, the Alpine orogeny exhibits a distinct three-dimensional evolution including major stages of strike-slip deformation and a considerably radial shortening direction so that any 2D model can always only address the fundamental aspects of the involved geodynamic processes.

Another example of divergent double-slab subduction is presumably the Paleo-Asian Ocean, which has been subducted beneath both the southern Siberian Craton in the north and the northern margin of the North China Craton in the south during the Paleozoic (Yang et al., 2017). Furthermore, a divergent double-slab subduction was also suggested between the North Qiangtang and South Qiangtang terrane (Li et al., 2020; Zhao et al., 2015). Our models show that a divergent double-slab subduction is a thermomechanically feasible process during convergence of tectonic plates.

Tomographic images from the Mediterranean show large p-wave anomalies in the transition zone (Piromallo and Morelli, 2003) indicating that the 660-km phase transition inhibits the sinking material to penetrate further into the lower mantle. This observation suggests that convection in the Alpine–Mediterranean region could be two-layered and largely confined to the upper region of the upper mantle. The convective patterns resulting from the presence of a weak asthenosphere simulated in our study are in agreement with these observations. We speculate that upper mantle convection might have played a role in the formation of the Alpine orogeny in the form of inducing an additional suction force below the Adriatic margin and assisting in the onset of subduction.

3.5 Conclusion

Our 2D thermomechanical numerical models of coupled lithosphere–mantle deformation are able to generate a 120 Myr long geodynamic cycle of subsequent extension (30 Myr), cooling (70 Myr) and convergence (20 Myr) in a continuous simulation. The simulations capture the fundamental features of such cycles, such as formation of hyper-extended margins, upper mantle convective flow or subduction initiation, with model outputs that are applicable to Earth. We propose that the ability of a model to generate such long-term cycles in a continuous simulation with constant parameters provides further confidence that the model has captured correctly the first-order physics.

Our models show that the viscosity structure of the asthenosphere and the associated vigour of upper mantle convection has a significant impact on lithosphere dynamics during a long-term geodynamic cycle. In comparison to a strong asthenosphere with minimum viscosities of 5×10^{20} Pa s, a weak asthenosphere with minimum viscosities of ca. 10^{19} Pa s generates the following differences: (1) locally larger suction forces due to convective flow, which are able to assist in establishing a single-slab subduction instead of a divergent double-slab subduction, and (2) smaller horizontal driving forces to initiate horizontally forced subduction, namely ca. 15 $\mathrm{TN\,m^{-1}}$ instead of ca. 22 $\mathrm{TN\,m^{-1}}$. Therefore, quantifying the viscosity structure of the asthenosphere is important for understanding the actual geodynamic processes acting in specific regions.

In our models, subduction at a hyper-extended passive margin is initiated during horizontal shortening and by shear localization due to mainly thermal softening. In contrast, after 70 Myr of cooling without far-field deformation, subduction of a 400 km wide exhumed and cold mantle is not spontaneously initiated. The buoyancy force due to the density difference between lithosphere and asthenosphere is too small to overcome the mechanical strength of the lithosphere.

The first-order geodynamic processes simulated in the geodynamic cycle of subsequent extension, cooling and convergence are applicable to orogenies that resulted from the opening and closure of embryonic oceans, which might have been the case for the Alpine orogeny.

3.6 Appendix

3.6.1 Nusselt number scaling laws and phase transitions

Modelling thermal convection beneath an actively deforming lithosphere can be numerically expensive, because the convection velocities can be as high as or even higher than the motion of the lithospheric plates, depending on the vigour of the convecting system. This significantly reduces the maximum time step necessary to ensure numerical stability. In consequence, it takes more time steps to run a simulation to the same physical time when convection is modelled together with deformation in the lithosphere. Hence, the computational time can be twice as long compared to models, where only the deforming lithosphere is modelled. However, it is possible to include the effect of convection in the mantle on the thermal field and keep a constant vertical heat flux through the lithosphere–asthenosphere boundary (LAB) into a numerical model without explicitly modelling convection by using an effective thermal conductivity for the mantle material below the lithosphere. Two dimensionless quantities have to be defined, namely the Rayleigh and Nusselt numbers. The Rayleigh number is the ratio of the thermal diffusion and advection time scale

$$Ra = \frac{t_{\mathrm{Dif}}}{t_{\mathrm{Adv}}} = \frac{\rho g \alpha \Delta T D^3}{\kappa \eta_{\mathrm{eff}}} \ , \tag{3.2}$$

where ρ is density, g is gravitational acceleration, α is a coefficient of thermal expansion, ΔT is the temperature difference between the top and the bottom and D is the thickness of the convecting layer, $\kappa = k/\rho/c_P$ is the thermal diffusivity and η_{eff} is the effective viscosity. The Nusselt number can be expressed in terms of the Rayleigh number as

$$Nu = \left(\frac{Ra}{Ra_{\mathrm{crit}}}\right)^{\beta} \ , \tag{3.3}$$

where Ra_{crit} is the critical Rayleigh number at which convection starts, typically in the order of 10^3, and β is a power-law exponent (Schubert et al., 2001). The Nusselt number is the ratio of advective heat flux, q_{Adv}, which is the vertical heat flux through the base of the lithosphere, imposed by the convecting upper mantle to the diffusive heat flux, q_{Dif}, imposed by the lithosphere on top of the convecting upper mantle as

$$Nu = \frac{q_{\mathrm{Adv}}}{q_{\mathrm{Dif}}} \, . \tag{3.4}$$

Using this relationship, it is possible to scale the thermal conductivity to the Nusselt number of the Earth's mantle and to maintain a constant heat flow through the base of the lithosphere via conduction when convection is absent. Assuming $Ra = 2 \times 10^6$ and $\beta = 1/3$ for the Earth's upper mantle convection, Eq. 3.3 predicts $Nu = 13$. This implies that the heat flow provided by advection is 13× higher than the heat flow provided by conduction. Using an effective conductivity approach, the heat flow provided by advection is mimicked using an enhanced conductive heat flow in the upper mantle. The effective conductivity can be determined by scaling the standard value of thermal conductivity of the upper mantle material to the Nusselt number of the convecting system like

$$k_{\mathrm{eff}} = Nu \; k. \tag{3.5}$$

For this study, the standard value for $k = 2.75$ of the upper mantle material and $Nu = 13$. The effective conductivity according to Eq. 3.5 is $k_{\mathrm{eff}} = 36$. To avoid a strong contrast of conductivities directly at the base of the lithosphere, we linearly increase the conductivity from 2.75-36 $\mathrm{W\,m^{-1}\,K^{-1}}$ over a temperature range of 1350-1376 °C. Applying this effective conductivity approach reduces the number of time steps necessary for computation up to the same physical time by ca. a factor 2 in M4 compared to M1.

As mentioned above, the vigour of convection is defined by the Rayleigh number (Eq. 3.2). For $Ra >> Ra_{\mathrm{crit}}$, the time scale for thermal diffusion is much larger than the time scale for advection of material. This means that the entropy of the system remains relatively constant in time. By definition, such a system is adiabatic (Kondepudi and Prigogine, 2014). In the presented models, the density and entropy for the mantle phases is pre-computed using Perple_X for a given bulk rock composition. Assuming that the temperature gradient in the upper mantle is adiabatic and stress conditions are close to lithostatic (i.e., deviatoric stresses are negligible), the temperature at any depth can be determined by following an isentrop from the Perple_X database. Starting coordinates in pressure-temperature space are the (lithostatic) conditions at the base of the lithosphere. From these pressure and temperature values one can follow the closest isentrop (black line Fig. 3.11) until the (lithostatic) pressure value at target depth (in this study 660 km, red diamond Fig. 3.11) is reached and extract the corresponding temperature value. Trubitsyn and Trubitsyna (2015) derived an analytical solution to calculate temperatures assuming an adiabatic gradient for given depths. We determined the temperature at the bottom of the model domain using both approaches and the obtained values that differ by only 0.01 °C.

Involving phase transitions necessitates mainly two major assumptions: (1) is compressibility of material due to large density variations important and (2) does latent heat released or consumed at a phase transition significantly change the convective pattern? Bercovici et al. (1992) concluded that compressibility effects on the spatial structure of mantle convection are minor when the superadiabatic temperature drop is close to the adiabatic temperature of the mantle, which is the case for the Earth. Although the net density varies largely in P-T space of the phase diagram used in this study (Fig. 3.11), the maximum value for the density time derivative computed from M1 is two orders of magnitude lower than the velocity divergence. We assume that density changes due to volumetric deformation are, hence, still negligible and density changes are accounted for in the buoyancy force only. This means the classical Boussinesq approximation is still valid. However, not considering adiabatic heating in the energy conservation equation leads to a significant deviation of the thermal structure from the initially imposed temperature gradient over large time scales (>100 Myr). The resulting temperature profile is constant throughout the upper mantle and the newly equilibrated constant temperature is equal to the imposed temperature at the bottom boundary. In consequence, the density structure read in from the phase diagram table according to pressure and temperature values is significantly wrong. To avoid these problems, we use the extended Boussinesq approximation, i.e., the adiabatic heating term is included in the energy conservation equation. As a result, the initially imposed adiabatic (or isentropic) temperature gradient can be maintained over large time scales. The resulting density structure agrees well with the PREM model (Dziewonski and Anderson, 1981) as shown in this study. A detailed comparison between different approximations of the system of equations is clearly beyond the scope of this study.

Latent heat that is released or consumed by a phase transition can perturb the thermal field by up to 100 K and induce a buoyancy force aiding or inhibiting the motion of cold, especially low-angle, subducting slabs (van Hunen et al., 2001) or hot rising plumes. However, when the lateral differences in temperature are small, the deflection of the phase transition by an ascending plume or a subducting slab has a much bigger impact on the buoyancy stresses than the latent heat released or consumed by the phase transition (Christensen, 1995). Because a detailed parametric investigation of the impact of latent heat on buoyancy stresses is beyond the scope of study, we neglect latent heat for simplicity.

3.6.2 Convection benchmark

In this section, we present the results of a convection benchmark performed by the algorithm used in this study. Equations for continuity and force balance are solved as in Eq. 2.1 and 2.2, density is a function of temperature only and calculated as

$$\rho(T) = \rho_0(1 - \alpha T) \tag{3.6}$$

and the total stress tensor is decomposed into a pressure and a deviatoric part as

$$\sigma_{ij} = -P\delta_{ij} + \tau_{ij} \; . \tag{3.7}$$

Transfer of heat is calculated as in Eq. 2.20 with $H_\mathrm{A} = 0$, $H_\mathrm{D} = 0$ and $H_\mathrm{R} = 0$. Stresses and strain rates ($\dot{\varepsilon}_{ij}$) are related to each other via the viscosity η as

$$\tau_{ij} = 2\eta\dot{\varepsilon}_{ij} \; . \tag{3.8}$$

Viscosity is computed via a linearized Arrhenius law, also called Frank–Kamenetskii approximation (Kamenetskii, 1969):

$$\eta(T, z) = \exp(-\gamma_T + \gamma_z) \ , \tag{3.9}$$

with $\gamma_T = \log(\eta_T)$ and $\gamma_z = \log(\eta_z)$. By choosing $\eta_z = 1$, $\gamma_z = 0$ in Eq. 3.9 and, therefore, the viscosity is only temperature dependent.

The dimensionless equations are discretized over a domain that extends from 0 to 1 in both horizontal and vertical directions and a small amplitude perturbation ($A = 0.01$) is applied to the initial temperature profile as

$$T(x, z) = (1 - z) + A\cos(\pi x)\sin(\pi z) \ . \tag{3.10}$$

As mentioned above, the vigour of the convecting system is described by its Rayleigh number (Eq. 3.2). A local $Ra = 10^2$ is applied to the top boundary by setting $\alpha = 10^{-2}$, $g = 10^4$ and all other parameters of Eq. 3.2 are set to 1. The applied viscosity decrease by choosing $\eta_T = 10^5$ in Eq. 3.9 results in a global $Ra = 10^7$. All mechanical boundaries are set to free slip, the thermal boundary conditions are constant temperature at the top ($T = 0$) and bottom ($T = 1$) and insulating (i.e., zero flux) at the two vertical boundaries. Tosi et al. (2015) tested several algorithms, including finite element, finite differences, finite volume and spectral discretization, on their capability of modelling distinct rheologies of the mantle, from temperature dependent viscosity only up to viscoplastic rheologies. We have chosen the simplest test, case one in Tosi et al. (2015), and report the results of two distinct diagnostic quantities: the average temperature over the entire modelling domain

$$\langle T \rangle = \int_0^1 \int_0^1 T \,\mathrm{d}x\mathrm{d}z \tag{3.11}$$

and the root mean square velocity at the surface

$$u_{\mathrm{RMS}}^{\mathrm{surf}} = \left(\int_0^1 v_x^2 \Big|_{z=1} \mathrm{d}x \right)^{\frac{1}{2}} . \tag{3.12}$$

The model develops one convection cell below a stagnant lid (Fig. 3.12a). We tested numerical resolutions of 50^2, 100^2, 150^2 and 300^2. Only for resolutions $>100^2$ the desired convective pattern developed. The numerical algorithms tested by Tosi et al. (2015) passed the benchmark already for lower resolutions. This is due to the fact that the algorithm presented here uses a uniform grid size across the domain. The algorithms tested by Tosi et al. (2015) used refined meshes. Sufficient resolution of the thermal boundary layers at the top and at the bottom is crucial to develop the desired pattern. Using a refined mesh in these regions, allows for lower total resolution, whereas using a regular mesh necessitates a much higher resolution in total. Nevertheless, values for the diagnostic quantities reproduced by the presented algorithm lie well within the minimum and maximum values calculated by the algorithms tested in Tosi et al. (2015) (grey areas in Fig. 3.12b & d). This shows that the convection in the upper mantle, where the viscosity is essentially temperature dependent, in the models presented in this study in which convection is not parameterized, is accurately modelled.

3.6.3 Gravitational potential energy and plate driving forces

We use the gravitational potential energy per unit surface (GPE) to quantify the impact of convection induced density variations in the upper mantle during the distinct stages of the simulations. The GPE varies along the horizontal x-direction and is computed as

$$GPE(x) = \int_{Sb}^{St(x)} P_{\mathrm{L}}(x,z)\ \mathrm{d}z, \tag{3.13}$$

where P_{L} is the lithostatic pressure calculated as

$$P_{\mathrm{L}}(x,z) = \int_{z}^{St(x)} \rho(x,z')\ g\ \mathrm{d}z' \tag{3.14}$$

and $St(x)$ is the stress-free surface and Sb is the model bottom. Horizontal variations in GPE, ΔGPE, are calculated by subtracting the leftmost value as a reference value from all other values. The GPE gives an estimate on the plate driving forces per unit length (Molnar and Lyon-Caen, 1988; Schmalholz et al., 2019; Bessat et al., 2020) acting in the system during the different stages of the hyper-extension and convergence cycle. We also calculate the vertical integral of the second invariant of the deviatoric stress tensor

$$\bar{\tau}_{\mathrm{II}}(x) = \int_{Sb}^{St(x)} \tau_{\mathrm{II}}(x, z)\ \mathrm{d}z\ . \tag{3.15}$$

The value of $F_{\mathrm{D}} = 2 \times \bar{\tau}_{\mathrm{II}}^{\mathrm{avg}}(x)$, where $\bar{\tau}_{\mathrm{II}}^{\mathrm{avg}}(x)$ is calculated averaging the average of $\bar{\tau}_{\mathrm{II}}(x)$ both over the left and rightmost 100 km of the domain, is also identical to the vertical integral of the difference between the horizontal total stress and the lithostatic pressure, if shear stresses are negligible (Molnar and Lyon-Caen, 1988; Schmalholz et al., 2019). This condition is strictly satisfied by the choice of boundary conditions at the top and the bottom of the model domain. We therefore chose to show the profiles which have been integrated over the entire domain height (z=-660 km). Since the deviatoric stresses below the lithosphere are indeed negligibly small, values for F_{D} integrated from depths of $z = -660$ km, $z = -330$ km and $z = -120$ km do not reveal significant differences. Therefore, the value of F_{D} is essentially independent on the integration depth (if deeper than the lithosphere thickness). F_{D} can therefore be used to estimate the plate driving force (see Fig.3.10d). For calculation of the suction force per unit length (F_{S}) induced by the mantle flow (Fig. 3.6a & f) we used the following formula

$$F_{\mathrm{S}} = \int_{b}^{a} \int_{d}^{c} \Delta\rho g\ \mathrm{d}z\ \mathrm{d}x\ , \tag{3.16}$$

where a, b, c and d are the integration bounds and $\Delta\rho$ is the difference in density between the entire density field at the end of the cooling period and a reference density value (profiles in Fig. 3.2(e)).

Bibliography

Agrusta, R., van Hunen, J., Goes, S., 2018. Strong plates enhance mantle mixing in early earth. Nature communications 9 (1), 1–10.

Baes, M., Sobolev, S. V., Quinteros, J., 2018. Subduction initiation in mid-ocean induced by mantle suction flow. Geophysical Journal International 215 (3), 1515–1522.

Beaussier, S. J., Gerya, T. V., Burg, J.-P., 2019. 3d numerical modelling of the wilson cycle: structural inheritance of alternating subduction polarity. Geological Society, London, Special Publications 470 (1), 439–461.

Becker, T. W., 2017. Superweak asthenosphere in light of upper mantle seismic anisotropy. Geochemistry, Geophysics, Geosystems 18 (5), 1986–2003.

Behn, M. D., Conrad, C. P., Silver, P. G., 2004. Detection of upper mantle flow associated with the african superplume. Earth and Planetary Science Letters 224 (3-4), 259–274.

Bercovici, D., Ricard, Y., 2012. Mechanisms for the generation of plate tectonics by two-phase grain-damage and pinning. Physics of the Earth and Planetary Interiors 202, 27–55.

Bercovici, D., Schubert, G., Glatzmaier, G. A., 1992. Three-dimensional convection of an infinite-prandtl-number compressible fluid in a basally heated spherical shell. Journal of Fluid Mechanics 239, 683–719.

Bessat, A., Duretz, T., Hetényi, G., Pilet, S., Schmalholz, S. M., 2020. Stress and deformation mechanisms at a subduction zone: insights from 2d thermo-mechanical numerical modelling. Geophysical Journal International.

Boonma, K., Kumar, A., García-Castellanos, D., Jiménez-Munt, I., Fernández, M., 2019. Lithospheric mantle buoyancy: the role of tectonic convergence and mantle composition. Scientific Reports 9 (1), 1–8.

Buck, W. R., 1986. Small-scale convection induced by passive rifting: the cause for uplift of rift shoulders. Earth and Planetary Science Letters 77 (3-4), 362–372.

Chen, J., 2016. Lower-mantle materials under pressure. Science 351 (6269), 122–123.

Chenin, P., Picazo, S., Jammes, S., Manatschal, G., Müntener, O., Karner, G., 2019. Potential role of lithospheric mantle composition in the wilson cycle: a north atlantic perspective. Geological Society, London, Special Publications 470 (1), 157–172.

Chenin, P., Schmalholz, S. M., Manatschal, G., Karner, G. D., 2018. Necking of the lithosphere: A reappraisal of basic concepts with thermo-mechanical numerical modeling. Journal of Geophysical Research: Solid Earth 123 (6), 5279–5299.

Christensen, U., 1995. Effects of phase transitions on mantle convection. Annual Review of Earth and Planetary Sciences 23 (1), 65–87.

Cloos, M., 1993. Lithospheric buoyancy and collisional orogenesis: Subduction of oceanic plateaus, continental margins, island arcs, spreading ridges, and seamounts. Geological Society of America Bulletin 105 (6), 715–737.

Connolly, J. A., 2005. Computation of phase equilibria by linear programming: a tool for geodynamic modeling and its application to subduction zone decarbonation. Earth and Planetary Science Letters 236 (1-2), 524–541.

Conrad, C. P., Lithgow-Bertelloni, C., 2002. How mantle slabs drive plate tectonics. Science 298 (5591), 207–209.

Crameri, F., 2018. Geodynamic diagnostics, scientific visualisation and staglab 3.0. Geoscientific Model Development 11 (6), 2541–2562.

Crameri, F., Conrad, C. P., Montési, L., Lithgow-Bertelloni, C. R., 2019. The dynamic life of an oceanic plate. Tectonophysics 760, 107–135.

Crameri, F., Magni, V., Domeier, M., Shephard, G. E., Chotalia, K., Cooper, G., Eakin, C. M., Grima, A. G., Gürer, D., Király, Á., et al., 2020. A transdisciplinary and community-driven database to unravel subduction zone initiation. Nature Communications 11 (1), 1–14.

Currie, C. A., Huismans, R. S., Beaumont, C., 2008. Thinning of continental backarc lithosphere by flow-induced gravitational instability. Earth and Planetary Science Letters 269 (3-4), 436–447.

Dal Zilio, L., Faccenda, M., Capitanio, F., 2018. The role of deep subduction in supercontinent breakup. Tectonophysics 746, 312–324.

De Graciansky, P.-C., Roberts, D. G., Tricart, P., 2010. The Western Alps, from rift to passive margin to orogenic belt: an integrated geoscience overview. Elsevier.

Duretz, T., Petri, B., Mohn, G., Schmalholz, S., Schenker, F., Müntener, O., 2016. The importance of structural softening for the evolution and architecture of passive margins. Scientific reports 6, 38704.

Dziewonski, A. M., Anderson, D. L., 1981. Preliminary reference earth model. Physics of the earth and planetary interiors 25 (4), 297–356.

Erdos, Z., Huismans, R. S., van der Beek, P., 2019. Control of increased sedimentation on orogenic fold-and-thrust belt structure–insights into the evolution of the western alps. Solid Earth 10 (2), 391–404.

Faccenna, C., Becker, T. W., 2010. Shaping mobile belts by small-scale convection. Nature 465 (7298), 602–605.

Favre, P., Stampfli, G., 1992. From rifting to passive margin: the examples of the red sea, central atlantic and alpine tethys. Tectonophysics 215 (1-2), 69–97.

Forte, A. M., Quéré, S., Moucha, R., Simmons, N. A., Grand, S. P., Mitrovica, J. X., Rowley, D. B., 2010. Joint seismic–geodynamic-mineral physical modelling of african geodynamics: A reconciliation of deep-mantle convection with surface geophysical constraints. Earth and Planetary Science Letters 295 (3-4), 329–341.

Froitzheim, N., Manatschal, G., 1996. Kinematics of jurassic rifting, mantle exhumation, and passive-margin formation in the austroalpine and penninic nappes (eastern switzerland). Geological society of America bulletin 108 (9), 1120–1133.

Garel, F., Goes, S., Davies, D., Davies, J. H., Kramer, S. C., Wilson, C. R., 2014. Interaction of subducted slabs with the mantle transition-zone: A regime diagram from 2-d thermo-mechanical models with a mobile trench and an overriding plate. Geochemistry, Geophysics, Geosystems 15 (5), 1739–1765.

Goetze, C., Evans, B., 1979. Stress and temperature in the bending lithosphere as constrained by experimental rock mechanics. Geophysical Journal International 59 (3), 463–478.

Golabek, G. J., Keller, T., Gerya, T. V., Zhu, G., Tackley, P. J., Connolly, J. A., 2011. Origin of the martian dichotomy and tharsis from a giant impact causing massive magmatism. Icarus 215 (1), 346–357.

Gülcher, A. J., Beaussier, S. J., Gerya, T. V., 2019. On the formation of oceanic detachment faults and their influence on intra-oceanic subduction initiation: 3d thermomechanical modeling. Earth and Planetary Science Letters 506, 195–208.

Handy, M. R., Schmid, S. M., Bousquet, R., Kissling, E., Bernoulli, D., 2010. Reconciling plate-tectonic reconstructions of alpine tethys with the geological–geophysical record of spreading and subduction in the alps. Earth-Science Reviews 102 (3-4), 121–158.

Hasterok, D., Chapman, D., 2011. Heat production and geotherms for the continental lithosphere. Earth and Planetary Science Letters 307 (1-2), 59–70.

Herzberg, C., Condie, K., Korenaga, J., 2010. Thermal history of the earth and its petrological expression. Earth and Planetary Science Letters 292 (1-2), 79–88.

Hirth, G., Kohlstedf, D., 2003. Rheology of the upper mantle and the mantle wedge: A view from the experimentalists. Geophysical Monograph-American Geophysical Union 138, 83–106.

Holt, A., Royden, L., Becker, T., 2017. The dynamics of double slab subduction. Geophysical Journal International 209 (1), 250–265.

Hua, Y., Zhao, D., Xu, Y., 2017. P wave anisotropic tomography of the alps. Journal of Geophysical Research: Solid Earth 122 (6), 4509–4528.

Huang, J., Zhong, S., van Hunen, J., 2003. Controls on sublithospheric small-scale convection. Journal of Geophysical Research: Solid Earth 108 (B8).

Huismans, R., Beaumont, C., 2011. Depth-dependent extension, two-stage breakup and cratonic underplating at rifted margins. Nature 473 (7345), 74–78.

Jammes, S., Huismans, R. S., 2012. Structural styles of mountain building: Controls of lithospheric rheologic stratification and extensional inheritance. Journal of Geophysical Research: Solid Earth 117 (B10).

Jaquet, Y., Schmalholz, S. M., 2018. Spontaneous ductile crustal shear zone formation by thermal softening and related stress, temperature and strain rate evolution. Tectonophysics 746, 384–397.

Kamenetskii, D. F., 1969. Diffusion and heat transfer in chemical kinetics. Plenum Press, New York.

Kameyama, M., Yuen, D. A., Karato, S.-I., 1999. Thermal-mechanical effects of low-temperature plasticity (the peierls mechanism) on the deformation of a viscoelastic shear zone. Earth and Planetary Science Letters 168 (1-2), 159–172.

Kaus, B. J., Liu, Y., Becker, T., Yuen, D. A., Shi, Y., 2009. Lithospheric stress-states predicted from long-term tectonic models: Influence of rheology and possible application to taiwan. Journal of Asian Earth Sciences 36 (1), 119–134.

Kiss, D., Candioti, L. G., Duretz, T., Schmalholz, S. M., 2020. Thermal softening induced subduction initiation at a passive margin. Geophysical Journal International 220 (3), 2068–2073.

Kondepudi, D., Prigogine, I., 2014. Modern thermodynamics: from heat engines to dissipative structures. John Wiley & Sons.

Kronenberg, A. K., Kirby, S. H., Pinkston, J., 1990. Basal slip and mechanical anisotropy of biotite. Journal of Geophysical Research: Solid Earth 95 (B12), 19257–19278.

Li, C., van der Hilst, R. D., Engdahl, E. R., Burdick, S., 2008. A new global model for p wave speed variations in earth's mantle. Geochemistry, Geophysics, Geosystems 9 (5).

Li, D., Wang, G., Bons, P., Zhao, Z., Du, J., Wang, S., Yuan, G., Liang, X., Zhang, L., Li, C., et al., 2020. Subduction reversal in a divergent double subduction zone drives the exhumation of southern qiangtang blueschist-bearing mélange, central tibet. Tectonics.

Li, Z.-H., Gerya, T., Connolly, J. A., 2019. Variability of subducting slab morphologies in the mantle transition zone: Insight from petrological-thermomechanical modeling. Earth-Science Reviews.

Mackwell, S., Zimmerman, M., Kohlstedt, D., 1998. High-temperature deformation of dry diabase with application to tectonics on venus. Journal of Geophysical Research: Solid Earth 103 (B1), 975–984.

Mallard, C., Coltice, N., Seton, M., Müller, R. D., Tackley, P. J., 2016. Subduction controls the distribution and fragmentation of earth's tectonic plates. Nature 535 (7610), 140–143.

Manatschal, G., Müntener, O., 2009. A type sequence across an ancient magma-poor ocean–continent transition: the example of the western alpine tethys ophiolites. Tectonophysics 473 (1-2), 4–19.

Manzotti, P., Ballevre, M., Zucali, M., Robyr, M., Engi, M., 2014. The tectonometamorphic evolution of the sesia–dent blanche nappes (internal western alps): review and synthesis. Swiss Journal of Geosciences 107 (2-3), 309–336.

McCarthy, A., Chelle-Michou, C., Müntener, O., Arculus, R., Blundy, J., 2018. Subduction initiation without magmatism: The case of the missing alpine magmatic arc. Geology 46 (12), 1059–1062.

McCarthy, A., Tugend, J., Mohn, G., Candioti, L., Chelle-Michou, C., Arculus, R., Schmalholz, S. M., Müntener, O., 2020. A case of ampferer-type subduction and consequences for the alps and the pyrenees. American Journal of Science 320 (4), 313–372.

McKenzie, D., 1977. The initiation of trenches: a finite amplitude instability. Island arcs, deep sea trenches and back-arc basins 1, 57–61.

Mitrovica, J., Forte, A., 2004. A new inference of mantle viscosity based upon joint inversion of convection and glacial isostatic adjustment data. Earth and Planetary Science Letters 225 (1-2), 177–189.

Molnar, P., Lyon-Caen, H., 1988. Some simple physical aspects of the support, structure, and evolution of mountain belts. Processes in continental lithospheric deformation 218, 179–207.

Montési, L. G., 2013. Fabric development as the key for forming ductile shear zones and enabling plate tectonics. Journal of Structural Geology 50, 254–266.

Mueller, S., Phillips, R. J., 1991. On the initiation of subduction. Journal of Geophysical Research: Solid Earth 96 (B1), 651–665.

Müller, R. D., Sdrolias, M., Gaina, C., Roest, W. R., 2008. Age, spreading rates, and spreading asymmetry of the world's ocean crust. Geochemistry, Geophysics, Geosystems 9 (4).

Parsons, B., McKenzie, D., 1978. Mantle convection and the thermal structure of the plates. Journal of Geophysical Research: Solid Earth 83 (B9), 4485–4496.

Peron-Pinvidic, G., Manatschal, G., et al., 2019. Rifted margins: state of the art and future challenges. Frontiers in Earth Science 7, 218.

Petersen, K. D., Nielsen, S., Clausen, O., Stephenson, R., Gerya, T., 2010. Small-scale mantle convection produces stratigraphic sequences in sedimentary basins. Science 329 (5993), 827–830.

Picazo, S., Müntener, O., Manatschal, G., Bauville, A., Karner, G., Johnson, C., 2016. Mapping the nature of mantle domains in western and central europe based on clinopyroxene and spinel chemistry: Evidence for mantle modification during an extensional cycle. Lithos 266, 233–263.

Piromallo, C., Morelli, A., 2003. P wave tomography of the mantle under the alpine-mediterranean area. Journal of Geophysical Research: Solid Earth 108 (B2).

Prout, W., 1834. Chemistry, meteorology and the function of digestion [bridgewater treatise no. 8]. London: W. Pickering.

Ranalli, G., 1995. Rheology of the Earth. Springer Science & Business Media.

Reilinger, R., McClusky, S., Vernant, P., Lawrence, S., Ergintav, S., Cakmak, R., Ozener, H., Kadirov, F., Guliev, I., Stepanyan, R., et al., 2006. Gps constraints on continental deformation in the africa-arabia-eurasia continental collision zone and implications for the dynamics of plate interactions. Journal of Geophysical Research: Solid Earth 111 (B5).

Ricard, Y., Vigny, C., Froidevaux, C., 1989. Mantle heterogeneities, geoid, and plate motion: A monte carlo inversion. Journal of Geophysical Research: Solid Earth 94 (B10), 13739–13754.

Richter, F. M., 1973. Convection and the large-scale circulation of the mantle. Journal of Geophysical Research 78 (35), 8735–8745.

Ruh, J. B., Le Pourhiet, L., Agard, P., Burov, E., Gerya, T., 2015. Tectonic slicing of subducting oceanic crust along plate interfaces: Numerical modeling. Geochemistry, Geophysics, Geosystems 16 (10), 3505–3531.

Schmalholz, S. M., Duretz, T., Hetényi, G., Medvedev, S., 2019. Distribution and magnitude of stress due to lateral variation of gravitational potential energy between indian lowland and tibetan plateau. Geophysical Journal International 216 (2), 1313–1333.

Schmid, S., Boland, J., Paterson, M., 1977. Superplastic flow in finegrained limestone. Tectonophysics 43 (3-4), 257–291.

Schubert, G., Turcotte, D. L., Olson, P., 2001. Mantle convection in the Earth and planets. Cambridge University Press.

Solomatov, V., 2004. Initiation of subduction by small-scale convection. Journal of Geophysical Research: Solid Earth 109 (B1).

Stern, R. J., 2004. Subduction initiation: spontaneous and induced. Earth and Planetary Science Letters 226 (3-4), 275–292.

Stern, R. J., Gerya, T., 2018. Subduction initiation in nature and models: A review. Tectonophysics 746, 173–198.

Tackley, P. J., Schubert, G., Glatzmaier, G. A., Schenk, P., Ratcliff, J. T., Matas, J.-P., 2001. Three-dimensional simulations of mantle convection in io. Icarus 149 (1), 79–93.

Thielmann, M., Kaus, B. J., 2012. Shear heating induced lithospheric-scale localization: Does it result in subduction? Earth and Planetary Science Letters 359, 1–13.

Thielmann, M., Schmalholz, S. M., 2020. Contributions of grain damage, thermal weakening, and necking to slab detachment. Frontiers in Earth Science 8, 254.

Torrance, K., Turcotte, D., 1971. Structure of convection cells in the mantle. Journal of Geophysical Research 76 (5), 1154–1161.

Tosi, N., Stein, C., Noack, L., Hüttig, C., Maierova, P., Samuel, H., Davies, D. R., Wilson, C. R., Kramer, S. C., Thieulot, C., et al., 2015. A community benchmark for viscoplastic thermal convection in a 2-d square box. Geochemistry, Geophysics, Geosystems 16 (7), 2175–2196.

Trubitsyn, V., Trubitsyna, A., 2015. Effects of compressibility in the mantle convection equations. Izvestiya, Physics of the Solid Earth 51 (6), 801–813.

Turcotte, D., Schubert, G., 2014. Geodynamics. Cambridge University Press.

van Hunen, J., van den Berg, A. P., Vlaar, N. J., 2001. Latent heat effects of the major mantle phase transitions on low-angle subduction. Earth and Planetary Science Letters 190 (3-4), 125–135.

Van Wijk, J., Van Hunen, J., Goes, S., 2008. Small-scale convection during continental rifting: Evidence from the rio grande rift. Geology 36 (7), 575–578.

White, S. t., Knipe, R., 1978. Transformation-and reaction-enhanced ductility in rocks. Journal of the Geological Society 135 (5), 513–516.

Wilson, J. T., 1966. Did the atlantic close and then re-open? Nature 211 (5050), 676–681.

Wilson, R., Houseman, G., Buiter, S., McCaffrey, K., Doré, A., 2019. Fifty years of the wilson cycle concept in plate tectonics: an overview.

Workman, R. K., Hart, S. R., 2005. Major and trace element composition of the depleted morb mantle (dmm). Earth and Planetary Science Letters 231 (1-2), 53–72.

Yang, F., Santosh, M., Tsunogae, T., Tang, L., Teng, X., 2017. Multiple magmatism in an evolving suprasubduction zone mantle wedge: the case of the composite mafic–ultramafic complex of gaositai, north china craton. Lithos 284, 525–544.

Zahnle, K. J., Kasting, J. F., Pollack, J. B., 1988. Evolution of a steam atmosphere during earth's accretion. Icarus 74 (1), 62–97.

Zhao, Z., Bons, P., Wang, G., Soesoo, A., Liu, Y., 2015. Tectonic evolution and high-pressure rock exhumation in the qiangtang terrane, central tibet. Solid Earth 6 (2), 457.

Zhou, X., Li, Z.-H., Gerya, T. V., Stern, R. J., 2020. Lateral propagation–induced subduction initiation at passive continental margins controlled by preexisting lithospheric weakness. Science Advances 6 (10), eaaz1048.

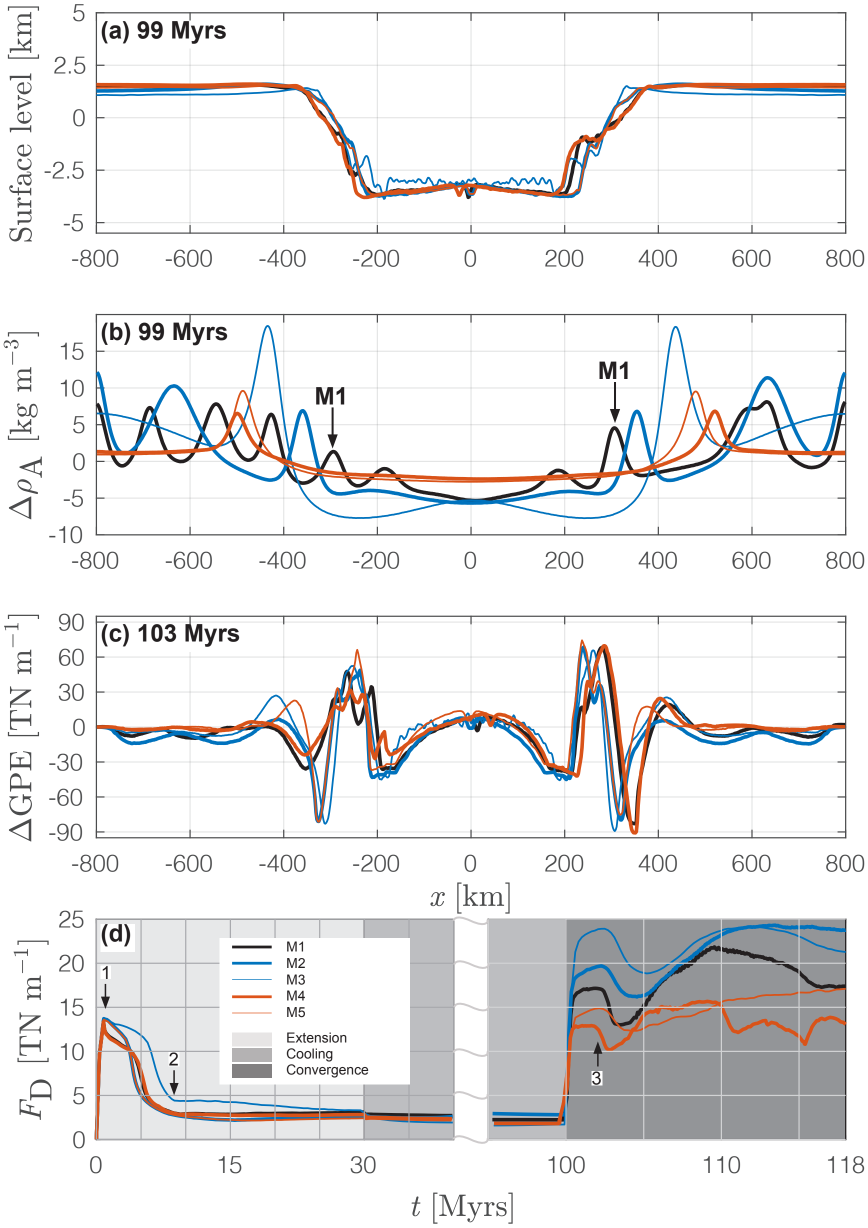

Figure 3.10: (a) Model topography at the end of the cooling period. (b) Vertically averaged ($-200\text{km} \leq z \leq -100\text{km}$) difference between entire density field and horizontal average density (see also Fig. 3.6((f)-(j)). (c) Difference in *GPE* of models M1-5 after 103 Myr. (d) Estimated plate driving forces (F_D, see appendix 3.6.3) through the entire model time. Grey regions indicate the stages of extension (light grey), cooling without plate deformation (grey) and convergence (dark grey). The cooling period is not entirely displayed, because values for F_D remain constant when no deformation is applied to the system. Numbers indicate important events in the evolution of the models: 1 = Initiation of crustal necking, 2 = crustal break-up, opening of the marine basin in which the mantle is exhumed to the sea floor, 3 = subduction initiation via thermal softening. The legend shown in (d) is valid for all panels above as well.

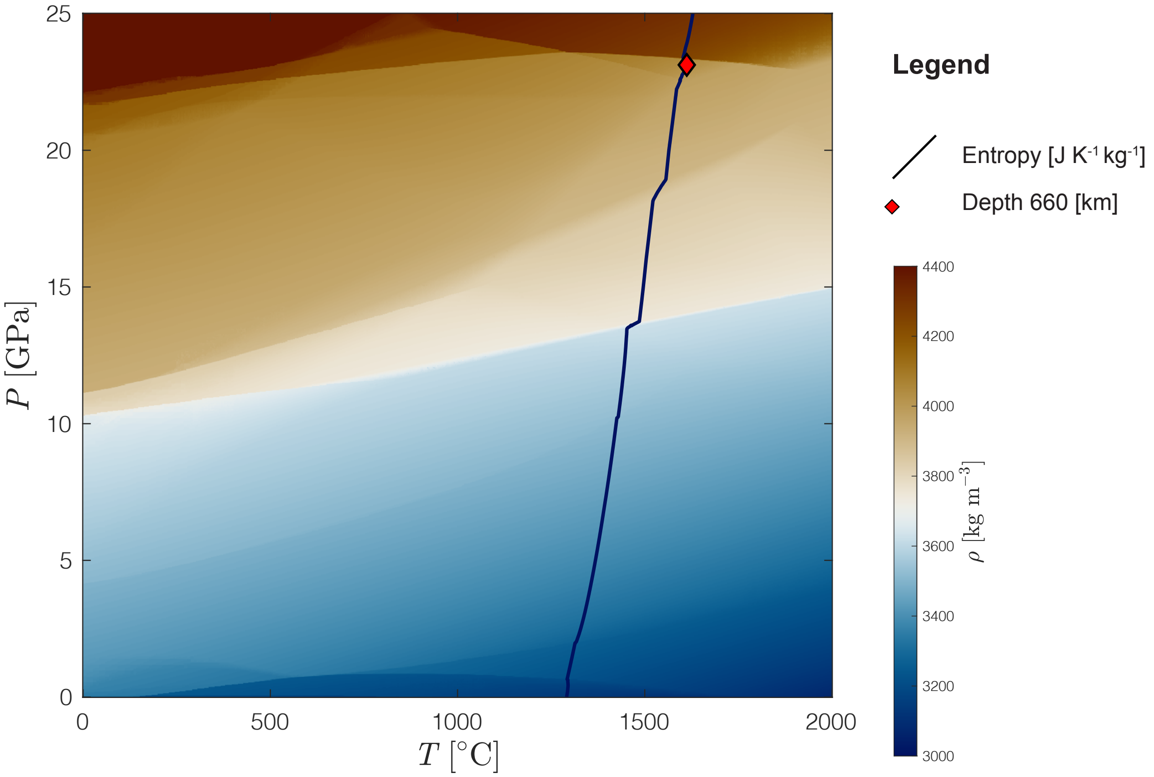

Figure 3.11: Hawaiian pyrolite phase diagram calculated with Perple_X (Connolly, 2005). Bulk rock composition in weight amount: 44.71 (SiO_2), 3.98 (Al_2O_3), 8.18 (FeO), 38.73 (MgO), 3.17 (CaO) and 0.13 (Na_2O). Bulk rock composition taken from Workman and Hart (2005). Blue to red colours indicate density calculated for the given pressure and temperature range, black line indicates the isentrop for a temperature of 1350 °C at the base of a 120 km thick lithosphere and the red diamond shows the pressure and temperature conditions at 660 km depth following this isentrop.

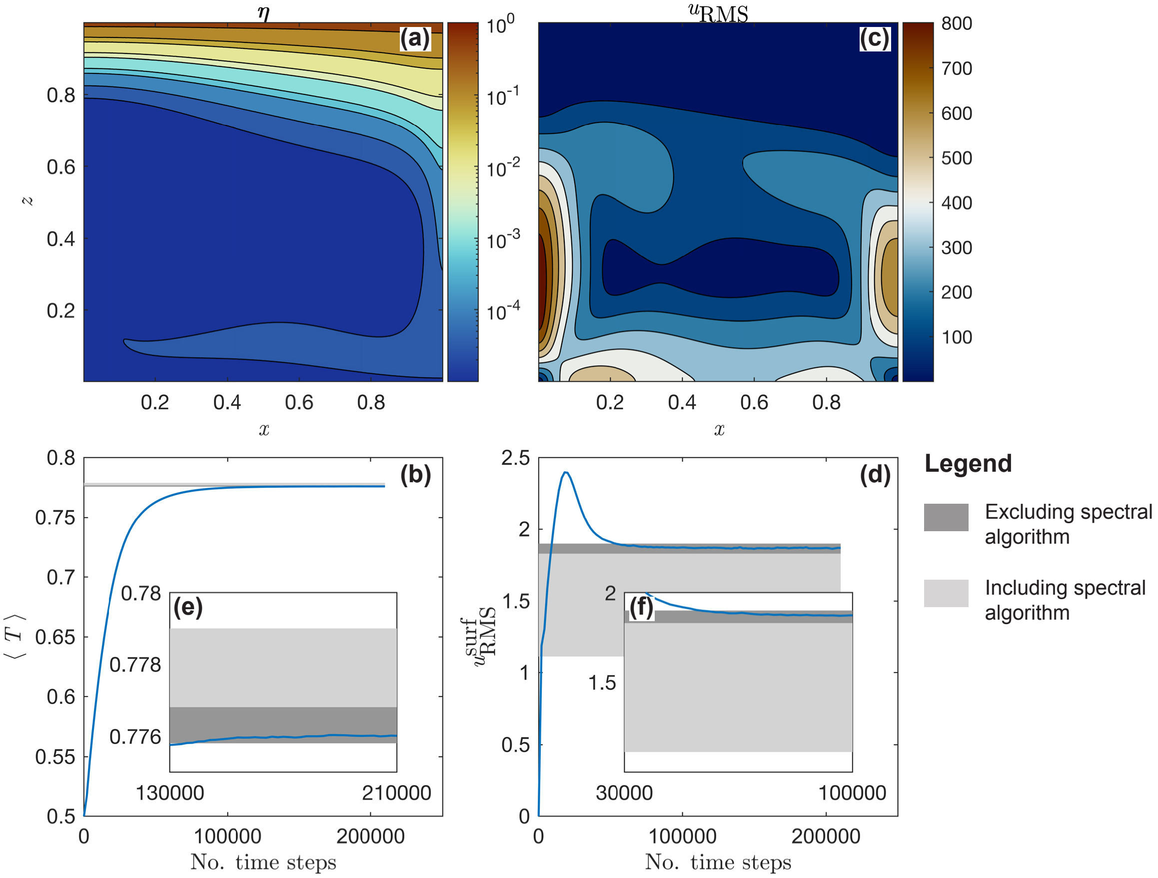

Figure 3.12: Results of 2D convection benchmark. (a) effective viscosity after convection reached a steady state, (b) normal average temperature calculated as in Eq. 3.11 for the entire model history, (c) root mean square velocity field for the entire domain after convection reached a steady state, (d) root mean square velocity at the surface of the modelled domain of the entire model history calculated as in Eq. 3.12, (e) normal average temperature calculated as in Eq. 3.11 for the time period at which the convection reaches a steady state and (f) root mean square velocity at the surface of the modelled domain calculated as in Eq. 3.12 for the time period at which the convection reaches a steady state. In Fig. 3.12(b) and Fig. 3.12(d)-(f), the dark grey area only shows the range of minimum maximum values for the given diagnostic quantity obtained by the algorithms tested by Tosi et al. (2015) excluding the spectral algorithm. Dark combined with light grey areas indicate the range obtained by all algorithms tested by Tosi et al. (2015) including the spectral algorithm.

CHAPTER 4

Buoyancy versus shear forces in building orogenic wedges

Lorenzo G. Candioti[1], Thibault Duretz[2], Evangelos Moulas[3], Stefan M. Schmalholz[1],

[1]Institut des Sciences de la Terre, University of Lausanne, Lausanne, Switzerland.

[2]Univ Rennes, CNRS, Géosciences Rennes UMR 6118, Rennes, France.

[3]Johannes-Gutenberg Universtät Mainz

Abstract

Orogenic belts formed by collision are impressive manifestations of plate tectonics. Observations from orogenic belts, like the Western Alps, indicate an important involvement of the mantle lithosphere, significant burial and exhumation of continental and oceanic crustal rocks and the importance of the plate interface strength that can be modified, for example, by the presence of serpentinites. A popular model for the formation of such belts is the so-called orogenic wedge model. However, most wedge models consider crustal deformation only and do, hence, not consider subduction, the impact of related buoyancy forces arising from density differences between subducted crust and surrounding mantle and the effects of different plate interface strength. Here, we quantify the relative importance of buoyancy and shear forces in building collisional orogenic wedges. We leverage two-dimensional (2D) petrological-thermo-mechanical numerical simulations of a long-term (ca. 170 Myr) lithosphere deformation cycle involving subsequent hyperextension, cooling, convergence, subduction and collision. We compare simulations employing density fields calculated with linearized equations of state with simulations employing density fields calculated by phase equilibria models including metamorphic reactions. Further, we consider serpentinisation of the mantle material, exhumed in the hyperextended basin. Our models show that differences in density structure and in shear strength of serpentinites or upper crust have a strong impact on the evolution of orogenic wedges. Higher serpentinite strength causes a dominance of shear over buoyancy forces, resulting in either thrust-sheet dominated orogenic wedges, involving some diapiric exhumation at their base, or relamination of crustal material below the overriding plate. Lower serpentinite strength (equal importance of shear and buoyancy forces) generates orogenic wedges that are dominated by diapiric or channel-flow exhumation. Deep subduction (>80 km) and subsequent surface exhumation of continental crust along the subduction interface occurs in these models. Employing phase equilibria density models decreases the average buoyancy contrasts, allows for deeper subduction of continental crust and reduces the average topography of the wedge by several kilometers. A decrease of upper crustal shear strength causes smaller maximal crustal burial depths. Progressive subduction of continental crust increases

upward-directed buoyancy forces of the growing wedge and in turn increases horizontal driving forces. These driving forces eventually reach magnitudes ($\approx$18 $\mathrm{TN\,m^{-1}}$) which were required to initiate subduction during convergence. We suggest that the evolving relation between shear and buoyancy forces and the increase of horizontal driving force related to the growing Alpine orogenic wedge has significantly slowed down (or "choked") subduction of the European plate below the Adriatic one between 35 and 25 Ma. This buoyancy-related "choking" could have caused the reorganization of plate motion and the initiation of subduction of the Adriatic plate. We discuss potential applications and implications of our model results to the Pyrenean and Alpine orogenies.

4.1 Introduction

The formation of collisional orogenic belts is an impressive manifestation of plate tectonics, and many studies have investigated the mechanisms causing mountain building in collisional settings (e.g. Malinverno and Ryan, 1986; Platt, 1986; Beaumont et al., 1996; Malavieille, 2010; Jaquet et al., 2018; Dal Zilio et al., 2020b). A popular geodynamic model explaining the formation of collisional orogens, such as the Western Alps, the Pyrenees or the Himalayas, is the wedge model (e.g. Chapple, 1978; Dahlen et al., 1984; Platt, 1986; Willett et al., 1993; Vanderhaeghe et al., 2003; Malavieille, 2010; Dal Zilio et al., 2020b). The first mechanical models of so-called critical wedges considered a frictional-plastic deformation (stresses are controlled by a specific yield criterion) and were originally applied to accretionary wedges. The formation of such wedges has been extensively studied with both analogue and numerical models (e.g. Gutscher et al., 1998; Simpson, 2009; Malavieille, 2010; Graveleau et al., 2012; Ruh et al., 2012; Borderie et al., 2018; Dal Zilio et al., 2020b). Wedge models typically consider crustal deformation only and are driven by a kinematic boundary condition at the base of the crust, involving a rigid indenter, or backstop, which creates a kinematic singularity point at the base of the wedge. Such crustal wedge models have also been used to study the impact of surface processes on wedge formation (e.g. Willett, 1999).

These crustal wedge models have also been applied to entire collisional orogens and are frequently referred to as orogenic wedge models (e.g. Platt, 1986; Willett et al., 1993; Dal Zilio et al., 2020b). However, the geodynamic evolution of collisional orogens, such as the Alps or the Himalayas, typically involves the closure of oceanic domains and the subduction of oceanic and continental rocks before actual collision. Also, large regions of some of these orogens are characterised by exhumed high-pressure (>1 GPa), and sometimes ultrahigh-pressure (>2.7 GPa), rocks with peak temperatures ranging typically from 500 to 700 °C (e.g. Lardeaux, 2014). Furthermore, tomographic images from the Western Alps and the Pyrenees (Zhao et al., 2015; Schmid et al., 2017; Teixell et al., 2018) indicate that the lithospheric mantle is involved in the formation of orogenic wedges (see Fig. 4.1), implying that orogenic wedges are rather lithospheric wedges (Nicolas et al., 1990) and not just crustal wedges.

The above mentioned pre-collisional subduction, the associated formation and exhumation of (ultra)high-pressure rocks and the density contrast between the subducted crustal material and the surrounding mantle likely significantly impact the orogen dynamics (e.g. Beaumont et al., 1996; Burov et al., 2014; Butler et al., 2014; Sizova et al., 2014). Particularly, the subduction related burial of crustal material to depths deeper than the isostatically balanced depth will cause upward-directed buoyancy forces, which act against the forces driving subduction and may assist rock exhumation.

From a mechanical point of view, the tectonic deformation (no inertia) of the lithosphere is controlled by the balance of gravitational forces (acting everywhere inside a representative rock volume) and shear forces (or surface forces, acting on the surface of a representative rock volume) (e.g. Forsyth and Uyeda, 1975; Ramberg, 1981; Weijermars and Schmeling, 1986; Turcotte and Schubert, 2014; Gerya, 2019). In absence of volumetric deformation, shear forces include forces acting normal or tangential to surfaces of the representative volume and induce shear deformation, such as pure or simple shear. Crustal wedge models typically consider shear forces and gravitational forces. The gravitational forces impact frictional deformation via a depth-increasing confining pressure and the gravitational adjustment of topographic gradients. However, the crustal wedge models do not consider upward-directed buoyancy forces resulting from density differences between subducted crust and surrounding mantle lithosphere. Furthermore, these crustal wedge models do not consider shear forces at the subduction interface. Here, we study the formation of orogenic wedges in a large-scale lithosphere–upper mantle framework, including subduction, to investigate the impact of shear and buoyancy forces on orogenic wedge formation.

We further aim to investigate orogenic wedge formation relevant to the Alpine orogeny. The formation of many collisional orogens, such as the Alps, is embedded in larger geodynamic cycles (Wilson, 1965; Wilson et al., 2019) including pre-orogenic rifting events. The Alpine orogen resulted from subduction of the Piemonte–Liguria oceanic domain and collision of the European and Adriatic passive continental margins (e.g. Handy et al., 2010). Ophiolitic units found in the Alps mainly consist of serpentinized mantle material, indicating a Piemonte–Liguria domain with exhumed and serpentinized mantle lithosphere (e.g. Manatschal and

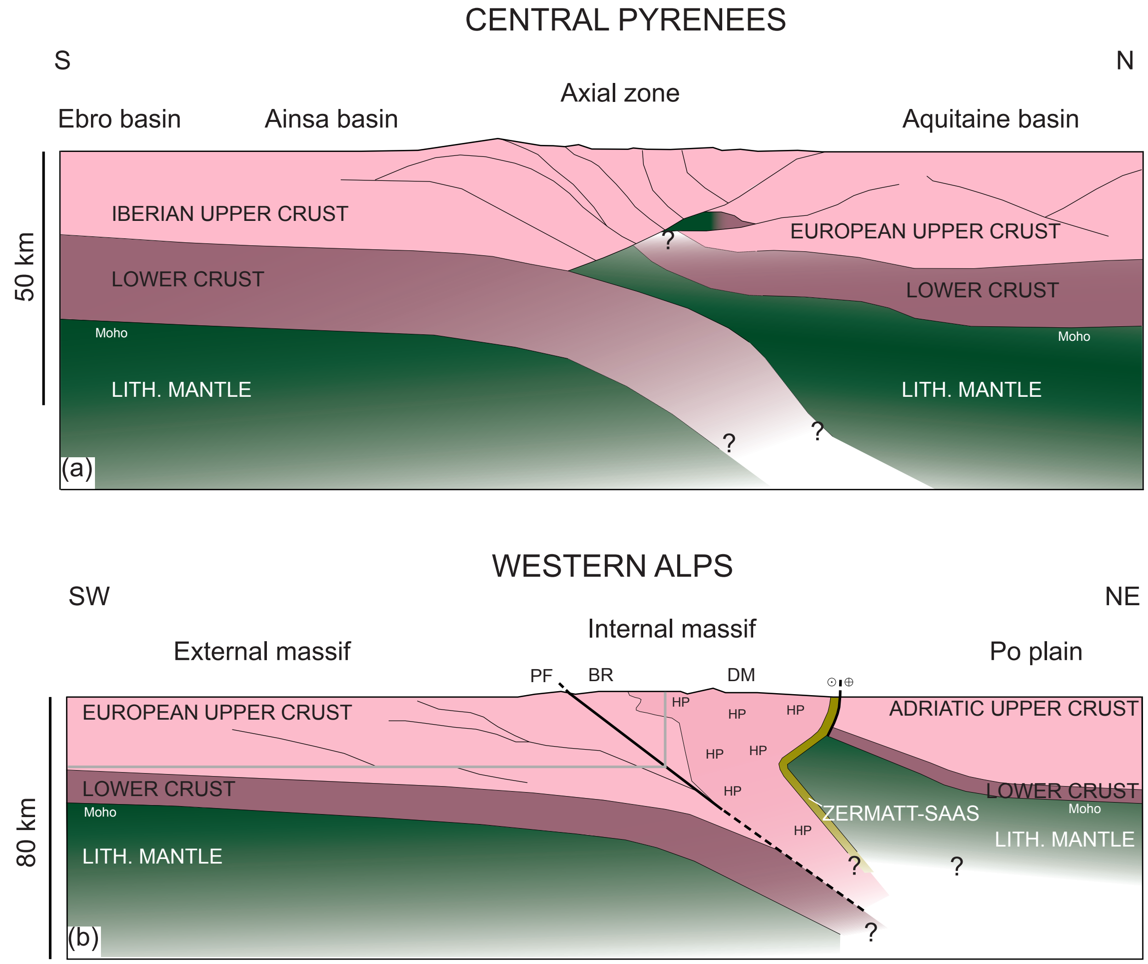

Figure 4.1: Tectonic sections: (a) Across the Central Pyrenees, modified after Teixell et al. (2018) and (b) across the Western Alps, modified after Zhao et al. (2015) and Schmid et al. (2017). Light violet represents the upper crust, dark violet represents the lower crust and green represents the mantle lithosphere. The region of mixed violet and green in (a) represents an unit of lower crust or mantle thrust slices. Black lines are unit boundaries and the grey framed region in (b) indicates the domain captured by most wedge models (compare to f.e. Malavieille, 2010; Dal Zilio et al., 2020b). Abbreviations: Penninic Front, PF, Briançonnais, BR, Dora–Maira, DM and high-pressure units, HP.

Müntener, 2009; McCarthy et al., 2020). For such Alpine–type orogens, structures inherited from continental margin formation presumably had a strong control on the dynamics of orogen formation (Chenin et al., 2017, 2019). Furthermore, subducted serpentinites and sediments may weaken the plate interface (Shreve and Cloos, 1986; Lamb and Davis, 2003; Behr and Becker, 2018) and impact on the balance between shear and buoyancy forces. Therefore, we consider models which involve a pre-collisional rifting phase and subduction involving serpentinites and sediments.

Here, we quantify the relative dominance and magnitude of buoyancy and shear forces during the formation of Alpine–type collisional orogens. We leverage two-dimensional (2D) petrological-thermo-mechanical numerical models of a long-term (ca. 170 Myr) extension–cooling–convergence cycle including subduction and continent-continent collision coupled to petrological phase equilibria modelling (Gerya et al., 2004; Kaus et al., 2005; Yamato et al., 2007; Hetényi et al., 2007; Rummel et al., 2020). To quantify the relative importance of buoyancy and shear forces at convergent plate boundaries, we compare (1) simple, or linearized equation of state (LEOS) density models to complex density (CD) models that include metamorphic reactions. The density structure of subducted continental crust and the surrounding mantle controls the magnitude of buoyancy forces. Increased buoyancy forces eventually lead to slab detachment, vanishing of slab-pull forces (Duretz et al., 2012) and a rearrangement of forces throughout orogeny (Dal Zilio et al., 2020a). (2) We vary the strength of the upper crust and of serpentinites at the top of the mantle exhumed in the basin. When entering the subduction zone, the shear resistance of serpentinite lubricating the subduction interface (Hirth and Guillot, 2013; Guillot et al., 2015, & references therein) facilitates subduction. Also, coupling of the continental crust to the subducting mantle lithosphere impact on the subduction and, therefore, orogen dynamics (Duretz and Gerya, 2013). We show that the relative dominance of shear and buoyancy forces generates different modes of orogenic wedges, some dominated by buoyancy driven return flow and some by stacking of thrust sheets. We further analyse the importance of the shear resistance of serpentinites and the upper continental crust as well as rock density to make another step towards understanding the dynamics of Alpine-type orogen formation.

4.2 Numerical model

4.2.1 Model configuration

The modelled domain extends over 1600 km in the horizontal x-direction and 680 km in the vertical z-direction (see Fig. 4.2). Model resolution is set to 1601×681 grid points in x and z (1x1 km), respectively. The bottom z-coordinate is set to -660 km and the stress-free surface (Duretz et al., 2016a) is set initially at z = 0 km. To allow for dynamic build-up of topography, the topmost +20 km of the model domain are left free of material. Mechanical boundary conditions on the remaining boundaries are set to free slip at the bottom and constant material inflow/outflow velocities at the left and right boundary. The transition between inflow and outflow occurs at z = -330 km and not at the initially imposed lithosphere-asthenosphere boundary (LAB). Initial surface temperature is set to 15 °C and temperatures at the Moho (i.e. the crust mantle boundary) and at the LAB are set to 550 °C and 1350 °C, respectively. An adiabatic gradient of 0.49 $°\mathrm{C\,km}^{-1}$ is assumed resulting in a value for temperature at the model bottom of 1612 °C. Thermal boundary conditions are isothermal at the bottom and at the top of the domain and no heat flows through lateral model boundaries. To model viscous deformation, we use dislocation creep for crustal units and a combination of dislocation, diffusion and Peierls creep for mantle units (see also *chapter* 2). Density of the materials is a function of pressure (P) and temperature (T) and is either calculated via a linearized equation of state (LEOS, see Eq. 2.3), or a pre-computed value which is based on equilibrium phase-diagram sections for specific bulk-rock composition. Phase diagram section calculations are performed using the software package Perple_X that utilizes the minimization of Gibbs free energy for a given chemical composition (Connolly, 2005). Values for density are stored in look-up tables (see Fig. 4.3) and are read-in according to local P and T conditions during run-time by the numerical algorithm. The choice of boundary conditions and model approximations is motivated by the modelling approach of Candioti et al. (2020). For more detailed justifications of model assumptions and explanations for the implementation of surface processes and boundary conditions, the reader is referred to their study. Model units include an initially 25 km thick upper crust with two vertical levels of 11 elliptical inclusions each, whose rheology is different from the upper crustal matrix. These elliptical inclusions represent structural and petrological units inherited from previous orogenic cycles. Weak and strong inclusions may represent metasedimentary units and mafic intrusions, respectively. Below the upper crust an 8 km thick lower crust is employed. The initial Moho is set to $z = -33$ km and the mantle lithosphere extends down to $z = -120$ km. In total, 12 weak elliptical inclusions over two vertical levels are included into the mantle lithosphere. These inclusions represent weaknesses caused by, for example, more hydrated peridotites (see also Barnhoorn et al. (2010); Petri et al. (2019) for more details). The elliptical inclusions help generating more realistic and asymmetric margin geometries (Duretz et al., 2016b; Petri et al., 2019). We include the upper mantle and transition zone down to $z = -660$ km. The distribution and emplacement of the inclusions is described in detail in appendix 4.6.1. The difference between mantle lithosphere and upper mantle and transition zone is due to temperature only, i.e. all material parameters are the same.

4.2.2 Simulations

Four types of simulations are performed: (1) The reference model (REF), generates a long-term (>160 Myr) geodynamic cycle of subsequent extension–cooling–convergence in a single and continuous simulation. During a 50 Myr rifting period, an ≈ 360 km wide basin is formed. This basin is floored by exhumed continental mantle and bounded by two hyper-extended magma-poor rifted margins. We apply an absolute extension velocity of 1 $\mathrm{cm\,yr^{-1}}$ and, we assume an ultra-slow to slow spreading rift system with minor melt production and therefore neglect decompressional melting of the peridotites. No far-field plate velocity is applied to the system for the following 60 Myr. This choice of applied deformation velocity and duration of the periods leads to margin geometries comparable to reconstructions from the ancient Alpine Tethys margin system and Piemonte–Liguria ocean (Le Breton et al., 2020). In all models presented here, the subsequent convergence is driven by a kinematic boundary velocity of 1.5 $\mathrm{cm\,yr^{-1}}$ (absolute value). The convergence phase involves subduction initiation, closure of the basin floored by exhumed mantle, continental collision and orogenic wedge formation. Model REF simulates a scenario without serpentinisation of the exhumed mantle peridotite.

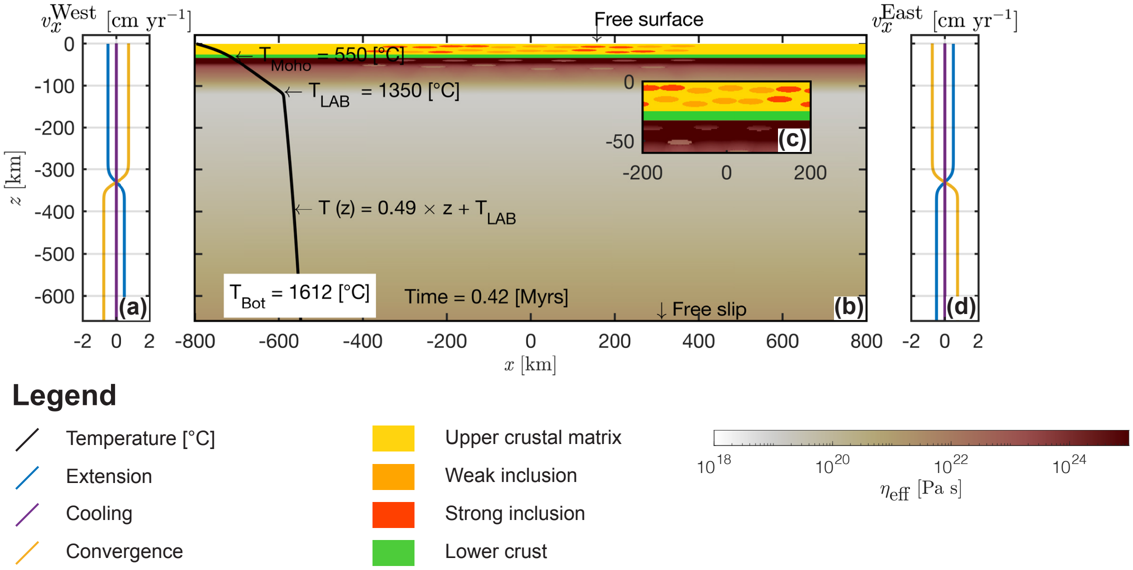

Figure 4.2: Model configuration and boundary conditions. (a) Profile of horizontal velocity for material inflow and outflow along the western model boundary. Blue line indicates the profile for the extension, purple line indicates the profile for the cooling and the yellow line indicates the profile for the convergence. (b) Entire model domain. Crustal phases: yellow represents the crustal matrix, dark orange represents strong elliptical inclusions and light orange represents weak elliptical inclusions. White to red shows the effective viscosity field as calculated by the numerical algorithm. All colour maps used to visualise physical fields in this study are provided by Crameri (2018). Black line shows the vertical temperature profile. (c) Enlargement of the central region of the domain. (d) Same profile as shown in (a), but along the eastern model boundary.

Except for the mantle lithology that utilizes a complex density (CD) model, the density of all other model lithologies is calculated using a linearized EOS (LEOS) (Eq. 2.3).

The geodynamic evolution of REF at the end of the cooling stage (109 Myr) serves as a self-consistently generated initial configuration for 3 additional types of simulations. (2) We parameterise a serpentinisation front propagating through the topmost layer of exhumed peridotites, to test the impact of serpentinite strength on the convergent deformation. In this parametrization, we replace the dry olivine flow law parameters of the exhumed peridotites in the basin above $z = -9$ km with parameters for antigorite rheology (Hilairet et al., 2007). This approach results in an effective average thickness of the serpentinite layer of ca. 5.5 km. In order to investigate the effects of variable serpentinite strength, we multiply the viscosity computed from the dislocation creep flow law for antigorite (Hilairet et al., 2007) by prefactors of 1 and 18 (ζ in Eq. 2.7). The background upper and lower crust is feldspar-dominated (see

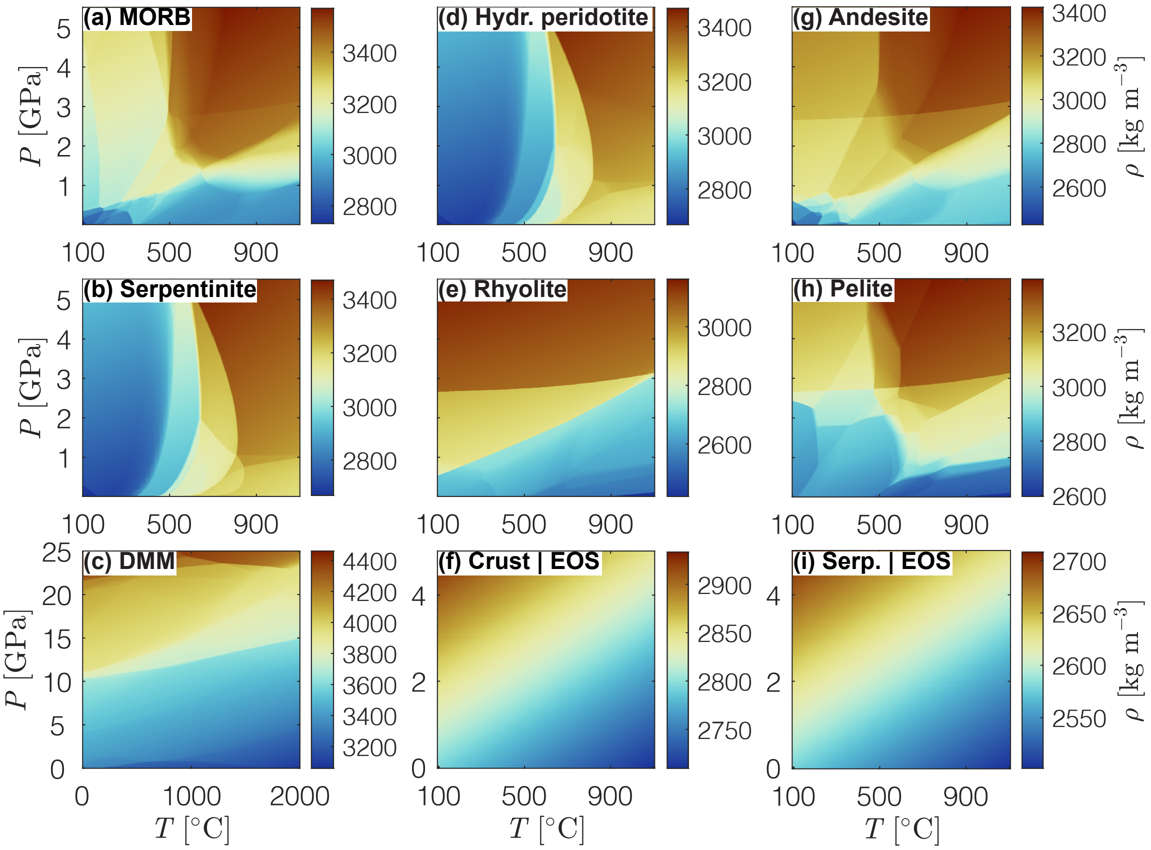

Figure 4.3: Density structures employed in the models presented here. (a)-(e) And (g)-(h): Phase diagram density fields calculated with Perple_X for the bulk rock compositions given in Table 4.2. (f) And (i): Density fields calculated using a linearized equation of state (Eq. 2.3) for an upper crustal reference density of 2800 $\mathrm{kg\,m^{-3}}$ and a serpentinite reference density of 2585 $\mathrm{kg\,m^{-3}}$, respectively.

Table 4.3 for details). As in REF, density is computed with a LEOS except for the mantle where a CD-model is employed. (3) We consider serpentinisation and investigate the impact of buoyancy forces on the collisional stage employing a CD-model for all lithologies. Type (4) is identical to type (3), except that a quartz-dominated upper crust is employed. A summary of all simulations is given in Table 4.1. The applied material parameters are given in Table 4.3 and the bulk rock compositions as well as the solution models used for phase diagram calculations are given in Table 4.2.

Table 4.1: Summary of all simulations presented in this study.

Parameter	Unit	REF	AS1	AS18	AC1	AC18	GC1	GC18
Crustal Matrix*	-	feldspar[1]	feldspar[1]	feldspar[1]	feldspar[1]	feldspar[1]	**quartz**[2]	**quartz**[2]
Complex density (CD) model	-	NO	NO	NO	**YES**	**YES**	**YES**	**YES**
Serpentinisation front	-	NO	**YES**	**YES**	**YES**	**YES**	**YES**	**YES**
Serpentinite pre-factor (ζ)	-	-	**1**	**18**	**1**	**18**	**1**	**18**
Starting time	Myr	0	**109**	**109**	**109**	**109**	**109**	**109**

Bold entries highlight the differences compared to the reference model REF. * Numbers indicate the flow law used for the crustal matrix, see also Table 4.3 for parameters.

4.3 Results

We first describe the results of the reference model, REF, for the entire geodynamic extension–cooling–convergence cycle. We then describe the impact of serpentinite shear resistance on the evolution of the models during convergence. Finally, we report results of linearized and complex density models as well as the impact of upper crustal shear resistance. We focus on the continent–continent collision stage of the individual models. Stages of basin closure, serpentinite channel formation, as well as the subduction dynamics are documented in the video supplement of models REF (Candioti, 2020b) and GC1 (Candioti, 2020a), but are not described in further detail here.

4.3.1 Reference model - REF

Figure 4.4 shows the geodynamic evolution of the reference model (REF). Crustal break-up occurs at ≈ 19 Myr in model history (Fig. 4.4a). At this stage, hot mantle material rises in the horizontal centre and diverges laterally below the plates (see arrows in Fig. 4.4a). The 1300 °C isotherm remains at a depth of ≈ 20-30 km. Two asymmetric continental margins have formed. The necking zone of the left margin is ≈ 20 km wide. In total, the width of this margin is ca. 80-90 km. The right margin is in total ca. 140-160 km wide including an ≈ 60-80 km wide necking zone. At the end of the cooling period (109 Myr, Fig. 4.4b), an ≈ 360 km wide basin has opened, which is floored by exhumed mantle material. Convection in the upper mantle stabilises the thermal and mechanical thickness of the lithosphere to ca. 90-100 km (no velocity glyphs in Fig. 4.4b, see also discussion in Candioti et al. (2020) for more detail). At 112 Myr subduction is initiated at the transition from the proximal to the distal

Table 4.2: Bulk rock composition for phase equilibrium calculations.

Oxides [wt%]	Pelite (avg.)[1,4]	Rhyolite[1,4]	Andesite[1,4]	MORB[1,4]	Hydr. Peridotite[1,4]	Serpentinite[2,4]	Bulk DMM[3,5]
SiO_2	61.500	72.800	57.900	49.200	44.710	44.210	44.710
Al_2O_3	18.600	13.300	17.000	16.100	4.160	3.130	3.980
FeO	10.000	2.440	6.980	10.220	8.070	8.898	8.180
MgO	3.810	0.390	3.330	6.440	39.200	39.240	38.730
CaO	-	-	6.790	10.500	2.420	3.060	3.170
Na_2O	1.460	3.550	3.480	3.010	0.220	-	0.130
K_2O	3.020	4.300	1.620	1.100	-	-	-
H_2O	sat	sat	sat	sat	sat	sat	-
Solution models							
Opx(HP)	+	+	+	+	+	+	-
Gt(GCT)	+	+	+	+	+	+	-
feldspar	+	+	+	+	+	+	-
Chl(HP)	+	+	+	+	+	+	-
Sp(HP)	+	+	+	+	+	+	-
O(HP)	+	+	+	+	+	+	-
Stlp(M)	+	+	+	+	-	-	-
Carp	+	+	+	+	-	-	-
Sud	+	+	+	+	-	-	-
Bio(TCC)	+	+	+	+	-	-	-
St(HP)	+	+	+	+	-	-	-
Ctd(HP)	+	+	+	+	-	-	-
Pheng(HP)	+	+	+	+	-	-	-
hCrd	+	+	+	+	+	+	-
Omph	-	-	+	+	+	+	-
GlTrTsPg	-	-	+	+	+	+	-
Pu(M)	-	-	+	+	+	-	-
Act(M)	-	-	+	+	+	+	-
T	-	-	+	-	+	+	-
A-phase	-	-	-	-	+	+	-
Chum	-	-	-	-	+	+	-
B	-	-	-	-	+	+	-
Wus	-	-	-	-	+	+	-
Fperh	-	-	-	-	+	+	-
Atg(PN)	-	-	-	-	+	+	-
C2/c	-	-	-	-	-	-	+
Wus	-	-	-	-	-	-	+
Pv	-	-	-	-	-	-	+
Pl	-	-	-	-	-	-	+
Sp	-	-	-	-	-	-	+
O	-	-	-	-	-	-	+
Wad	-	-	-	-	-	-	+
Ring	-	-	-	-	-	-	+
Opx	-	-	-	-	-	-	+
Cpx	-	-	-	-	-	-	+
Aki	-	-	-	-	-	-	+
Gt_maj	-	-	-	-	-	-	+
Ppv	-	-	-	-	-	-	+
CF	-	-	-	-	-	-	+

Modified bulk rock after [1]Winter (2013), [2]Pelletier et al. (2008) [3]Workman and Hart (2005). We assume water saturation in all calculations.

Crosses denote solution models used for given lithologies.

Thermodynamic databases used: [4]Holland and Powell (1998) updated in 2002 and [5]Stixrude and Lithgow-Bertelloni (2011) for depleted MORB mantle (DMM).

Details on the solution models can be found in the solution_model.dat data file in Perple_X.

continental margin in the right model side (see Sutra et al. (2013) for nomenclature). Partly, the necking zone of this margin has been subducted to ca. 40 km depth (Fig. 4.4c & f). At

Table 4.3: Physical parameters used in the numerical simulations.

Model unit	Rheology (Reference)		k [$\mathrm{W\,m^{-1}\,K^{-1}}$]	H_R [$\mathrm{W\,m^{-3}}$]	C [Pa]	φ [°]
Crustal matrix 1^{*,a}	Wet Anorthite (Rybacki and Dresen, 2004)		2.25	1.0200×10^{-6}	1×10^{7}	30
Crustal matrix 2^{*,a}	Westerly Granite (Hansen et al., 1983)		2.25	1.0200×10^{-6}	1×10^{7}	30
Weak inclusion^{*,a}	Wet Quartzite (Ranalli, 1995)		2.25	1.0200×10^{-6}	1×10^{6}	5
Strong inclusion^{*,a}	Maryland Diabase (Mackwell et al., 1998)		2.25	1.0200×10^{-6}	1×10^{7}	30
Calcite^{*,a}	Calcite (Schmid et al., 1977)		2.37	0.5600×10^{-6}	1×10^{7}	30
Mica^{*,a}	Mica (Kronenberg et al., 1990)		2.55	2.9000×10^{-6}	1×10^{7}	15
Lower crust^{*,b}	Wet Anorthite (Rybacki and Dresen, 2004)		2.25	0.2600×10^{-6}	1×10^{7}	30
Strong mantle^{*,c}	Dry Olivine (Hirth and Kohlstedf, 2003)		2.75	2.1139×10^{-8}	1×10^{7}	30
Weak mantle^{*,c}	Wet Olivine (Hirth and Kohlstedf, 2003)		2.75	2.1139×10^{-8}	1×10^{7}	30
Serpentinite^{*,d}	Antigorite (Hilairet et al., 2007)		2.75	2.1139×10^{-8}	1×10^{7}	25
Dislocation creep	A [$\mathrm{Pa^{-n-r}\,s^{-1}}$]	ζ [ ]	n [ ]	Q [$\mathrm{J\,mol^{-1}}$]	V [$\mathrm{m^3\,mol^{-1}}$]	r [ ]
Crustal matrix 1	3.9811×10^{-16}	0.3	3.0	356×10^{3}	0.00×10^{-6}	0.0
Crustal matrix 2	3.1623×10^{-26}	1.0	3.3	186.5×10^{3}	0.00×10^{-6}	0.0
Weak inclusion	5.0717×10^{-18}	1.0	2.3	154×10^{3}	0.00×10^{-6}	0.0
Strong inclusion	5.0477×10^{-28}	1.0	4.7	485×10^{3}	0.00×10^{-6}	0.0
Calcite	1.5849×10^{-25}	1.0	4.7	297×10^{3}	0.00×10^{-6}	0.0
Mica	1.0000×10^{-138}	1.0	18.0	51.0×10^{3}	0.00×10^{-6}	0.0
Lower crust	3.9811×10^{-16}	1.0	3.0	356×10^{3}	0.00×10^{-6}	0.0
Strong mantle	1.1000×10^{-16}	1.0	3.5	530×10^{3}	14.0×10^{-6}	0.0
Weak mantle†	5.6786×10^{-27}	1.0	3.5	480×10^{3}	11.0×10^{-6}	1.2
Serpentinite	4.4738×10^{-38}	see Table 4.1	3.8	8.90×10^{3}	3.20×10^{-6}	0.0
Diffusion creep‡	A [$\mathrm{Pa^{-n-r}\,m^{m}\,s^{-1}}$]	m [ ]	n [ ]	Q [$\mathrm{J\,mol^{-1}}$]	V [$\mathrm{m^3\,mol^{-1}}$]	r [ ]
Strong mantle	1.5000×10^{-15}	3.0	1.0	370×10^{3}	7.5×10^{-6}	0.0
Weak mantle†	2.5000×10^{-23}	3.0	1.0	375×10^{3}	9.0×10^{-6}	1.0
Peierls creep	A_P [$\mathrm{s^{-1}}$]	Q [$\mathrm{J\,mol^{-1}}$]	V [$\mathrm{m^3\,mol^{-1}}$]	σ_P [Pa]	γ [ ]	
Mantle$^{\$}$	5.7000×10^{11}	540×10^{3}	0.0×10^{-6}	8.5×10^{9}	0.1	

Constant parameters: *A heat capacity $c_P = 1050$ [$\mathrm{J\,kg^{-1}\,K^{-1}}$] is employed in Eq. 2.20 for all phases.
^{a,b,c}A constant shear modulus $G = 2\times10^{10}$ [Pa] is used in Eq. 2.3. ^{d}A constant shear modulus $G = 1.81\times10^{10}$ [Pa] is used in Eq. 2.4.
$^{a}\rho_0 = 2800$ [$\mathrm{kg\,m^{-3}}$], $^{b}\rho_0 = 2900$ [$\mathrm{kg\,m^{-3}}$] and $^{d}\rho_0 = 2585$ [$\mathrm{kg\,m^{-3}}$], $^{a,b}\alpha = 3.5\times10^{-5}$ [$\mathrm{K^{-1}}$] and $^{d}\alpha = 4.7\times10^{-5}$ [$\mathrm{K^{-1}}$] and $^{a,b,d}\beta = 1\times10^{-11}$ [$\mathrm{Pa^{-1}}$] are used for density calculations using a simplified equation of state according to Eq. 2.4.
†A water fugacity $f_{\mathrm{H_2O}} = 1.0\times10^{9}$ [Pa] is used in equation Eq. 2.7. For all other phases $f_{\mathrm{H_2O}} = 0.0$ [Pa].
‡A constant grain size $d = 1\times10^{-3}$ [m] is used in Eq. 2.8.
$^{\$}$Reference: Goetze and Evans (1979) regularized by Kameyama et al. (1999). These parameters are used for both strong and weak mantle rheology.

144 Myr in model history, the continental crust of the left margin (blue colours in Fig. 4.5a & b) is subducted to ca. 60 km depth. Sediments, originally deposited in the trench have been incorporated in between the subducting and the overriding plate. With ongoing convergence, the upper crust of the subducting plate is buried to a maximum depth of ca. 120 km. At 155 Myr, upper crustal units are sheared off the subducting plate at the transition to the lower crust and begin to form thrust sheets (see deflected isotherms at $x\approx$-80 km and $z\approx$-30 km Fig. 4.5e). Major parts of continental crust are sheared-off the subducting plate before entering the subduction zone. An orogenic wedge with several thrust sheets has formed at 164 Myr (Fig. 4.5f). At this stage, the lower part of the subducting slab detaches and the deeper subducted upper crustal material flows upward. This return flow is limited to depths between ca. 60 and 80 km (see arrows in Fig. 4.5f).

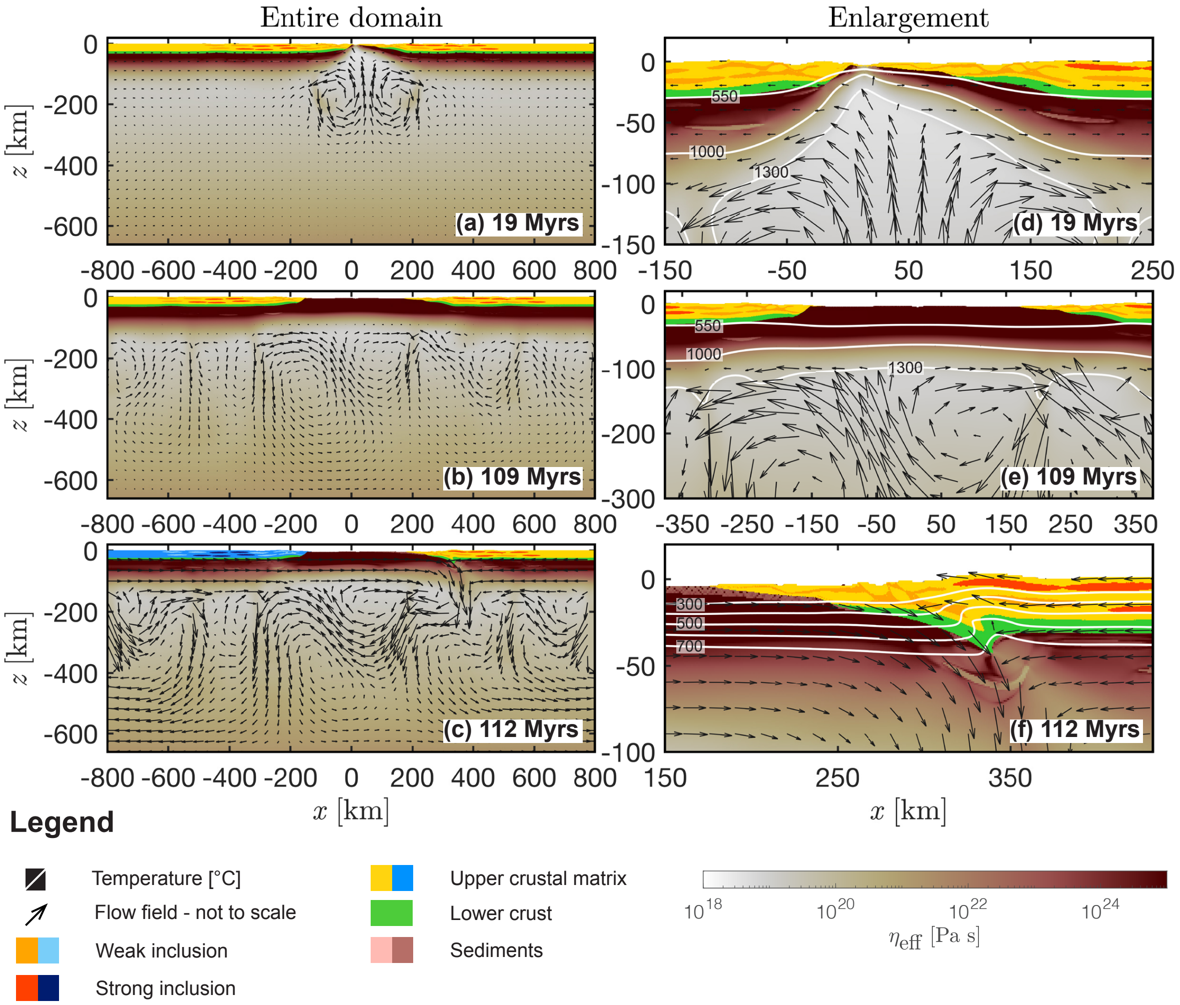

Figure 4.4: Evolution of the reference run REF during rifting, cooling and subduction initiation. White to red indicates the effective viscosity field calculated by the algorithm, yellow to orange indicates the crustal matrix and the weak and strong inclusions of the overriding plate, light to dark blue indicates the corresponding crustal units of the subducting plate. Green indicates the lower crust of both plates and salmon and brown indicates the sedimentary units. White lines show different isotherms and the arrows indicate the velocity field.

4.3.2 Impact of low (AS1) and high (AS18) serpentinite shear resistance

As in REF, subduction is initiated at the transition from the proximal to the distal right continental margin in AS1 and AS18. A large volume of serpentinite material is sheared-off the subducting plate in AS1 and AS18 (Fig. 4.6a & e). In AS1, the serpentinites form a coherent, inclined channel down to ca. 100-120 km depth (Fig. 4.6a). At 148 Myr, the upper continental crust of the left margin (blue colours in Fig. 4.6) has been subducted

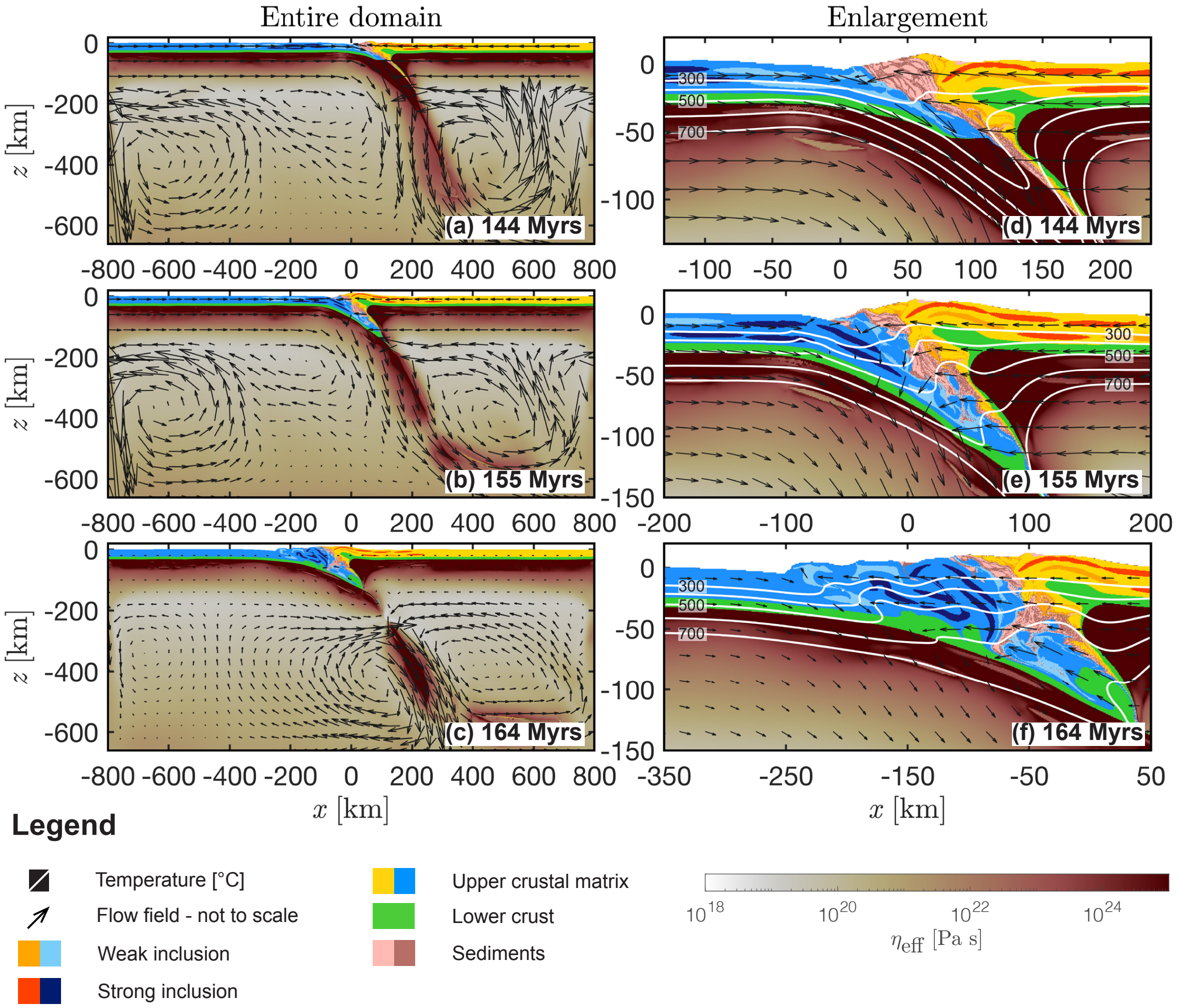

Figure 4.5: Evolution of the reference run REF during closure of the marine basin and continent–continent collision. White to red indicates the effective viscosity field calculated by the algorithm, yellow to orange indicates the crustal matrix and the weak and strong inclusions of the overriding plate, light to dark blue indicates the corresponding crustal units of the subducting plate. Green indicates the lower crust of both plates and salmon and brown indicates the sedimentary units. White lines show different isotherms and the arrows indicate the velocity field.

to ca. 90-100 km depth (Fig. 4.6a). Between 154 and 162 Myr, the subducted upper continental crust returns to the surface through the weak serpentinite channel in AS1. An ≈ 50 km wide block of the overriding plate's upper crust is separated from the right margin by subducted crustal material that is being exhumed to the surface. At 164 Myr, large parts of the subducted continental crust have been exhumed to the surface (Fig. 4.6d). Units containing weak inclusions are internally deformed during the exhumation. Strong units are folded, but exhumed coherently (Fig. 4.6d). The serpentinite material is surrounding the exhumed upper crustal material and the separated continental upper crustal block of the overriding plate. In AS18, the serpentinite channel is intersected by the two colliding plates at z≈-30 km (Fig. 4.6e). In contrast to AS1, the continental upper crust is partly sheared off the subducting plate at z≈-25 km in AS18 (Fig. 4.6e). Maximum burial depth of upper continental crust in this model is ca. 80-90 km. Exhumation of subducted crustal material is limited to z≈-70 km (Fig. 4.6f & g). Instead, the upper continental crust is wedged at shallower depths, similar to REF (see deflected isotherms at x≈-125 km in Fig. 4.6g). Thrust sheets propagate along the upper continental crust of the subducting plate (Fig. 4.6h). The serpentinized mantle material forms a coherent unit emplaced in between the wedged continental upper crust of the subducting plate and the relatively undeformed continental upper crust of the overriding plate. Dimensions of the evolved orogenic wedge in AS18 are similar to the wedge dimensions evolved in REF (compare Fig. 4.5f to Fig. 4.6h).

4.3.3 Impact of complex density models - Models AC1 and AC18

Density models that include predicted metamorphic assemblages (CD-models) lead to more variable density fields and larger density changes compared to LEOS-models (compare Fig. 4.3g to f). Similar to AS1, a serpentinite channel forms after subduction initiation in AC1 (Fig. 4.7a). The continental upper crust of the subducting plate (blue colours) is subducted to ca. 150 km depth, which is deeper compared to AS1 (compare Fig. 4.6b to Fig. 4.7b & c). In contrast to AS1, exhumation of the subducted upper continental crust has not occurred until 163 Myr (compare Fig. 4.6c to Fig. 4.7c) in model history. At 170 Myr, the subducted continental crust in AC1 has been exhumed to the surface through the weak subduction interface (Fig. 4.7d). In contrast to AS1, the continental upper crust of the overriding plate has not been separated by the returning continental crust of the subducting plate in AC1 (compare Fig. 4.6d to Fig. 4.7d). Figure 4.8a & b shows the density field of models AS1 and AC1, respectively, computed by the algorithm at 170 Myr in model history. Compared to AS1, in AC1 the density of the material in the wedge is much more variable. The density of the subducted crustal units in AC1 is up to ca. 100 $\mathrm{kg\,m^{-3}}$ higher than in AS1. The resulting buoyancy contrasts are much smaller leading to significantly less uplift of topography in AC1

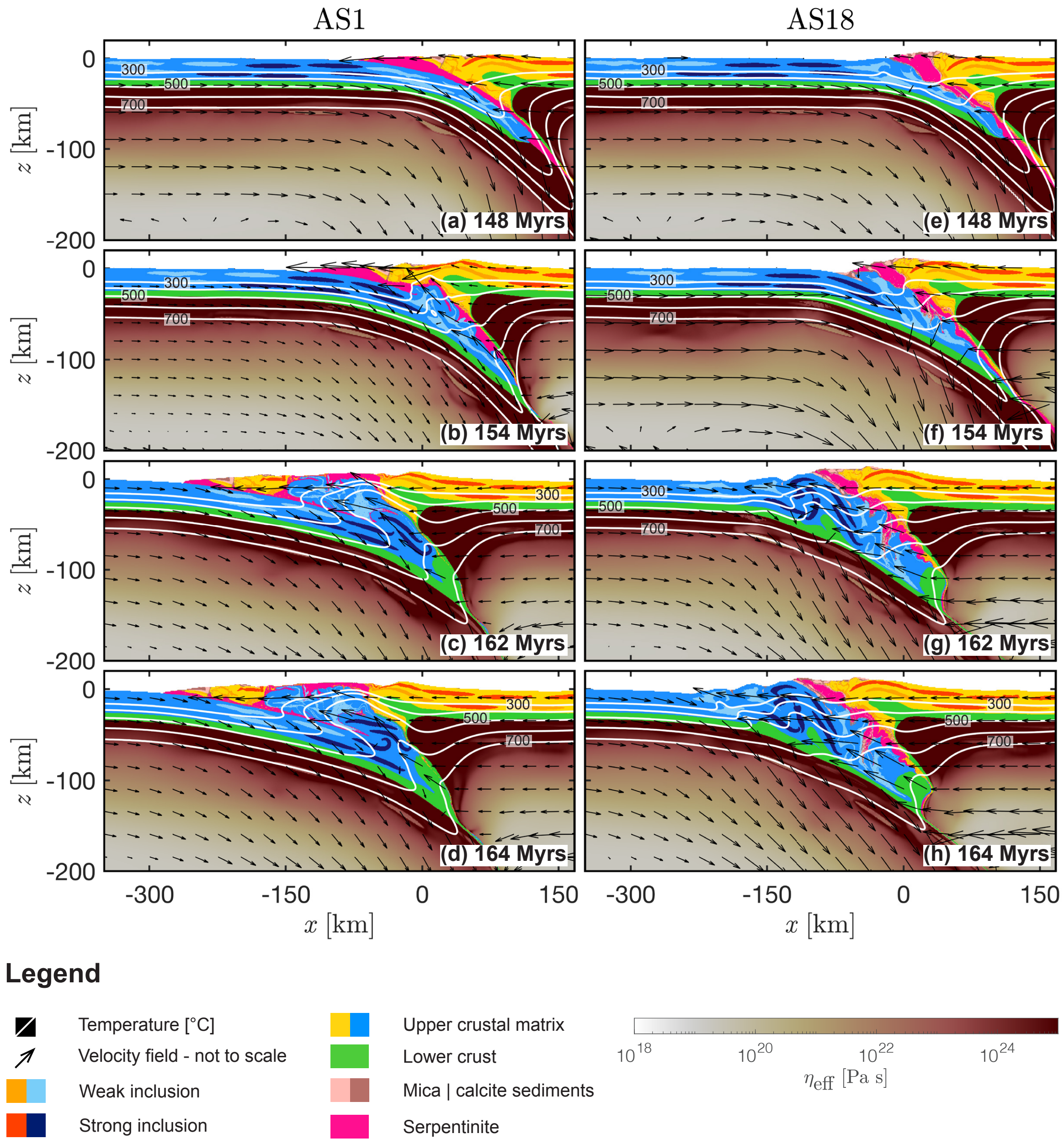

Figure 4.6: Convergence and collisional stage of AS1 and AS18 (low and high shear resistance of serpentinite, LEOS density model, feldspar-dominated upper crust). White to red indicates the effective viscosity field calculated by the algorithm, yellow to orange indicates the crustal matrix and the weak and strong inclusions of the overriding plate, light to dark blue indicates the corresponding crustal units of the subducting plate. Green indicates the lower crust of both plates and salmon and brown indicates the sedimentary units. White lines show different isotherms and the arrows indicate the velocity field.

compared to AS1. In AS1, the maximum elevation of topography exceeds 10 km; in AC1 the maximum elevation is locally ≈ 7 km, but high topographies are in average ≈ 5 km. The width of the wedge is ≈350 km and ≈275 km in AS1 and AC1, respectively. Compared to AS18, only minor volume of serpentinite material has been sheared off the subducting slab in AC18 (compare Fig. 4.6e to Fig. 4.7e). The majority of serpentinite material is coupled to the slab and subducted into the upper mantle (Fig. 4.7f). Subduction of continental upper crust reaches a depth of ca. 180 km after 163 Myr (Fig. 4.7g). In absence of a weak, serpentinized subduction interface, the resistance of the subduction channel is increased in AC18 (compare Fig. 4.7a-c to f & g). The deeply subducted continental upper crust cannot be exhumed along the strong subduction interface and breaks through the less resistant mantle wedge (Fig. 4.7h), relaminating below the overriding plate (similar to the models presented in Currie et al. (2007) & Li and Gerya (2009)).

4.3.4 Impact of crustal strength - Models GC1 and GC18

Similar to AS1 and AC1, in GC1 the serpentinites form a channel along the subduction interface down to ca. 120 km depth (Fig. 4.9a). Continental upper crust of the subducting plate is buried to z≈-120 km (Fig. 4.9a & b). At ca. 153 Myr, the subducting slab detaches at a depth of ca. 400 km (see Candioti (2020a)). Between 156 and 162 Myr, the subducted continental upper crust flows back to the surface along the weak subduction interface breaking through the continental upper crust of the overriding plate (Fig. 4.9c). The serpentinite material is surrounding the exhumed crustal material (Fig. 4.9d) within the orogenic wedge. Exhumation of upper continental crust from z≈-80 km to z≈-30 km occurs between 162 and 164 Myr. At ca. 165 Myr, a second slab detachment occurs at z≈-250 km (see Candioti (2020a)). In contrast to AC18, less crustal volume is subducted in GC18 (Fig. 4.9e). Instead, the continental upper crust is largely sheared-off the subducting lithosphere at z≈-40 km (Fig. 4.9f) and several thrust sheets form (Fig. 4.9f). Compared to GC1, the relatively stronger serpentinite in GC18 is largely subducted and sediments originally deposited in the trench are incorporated into a growing orogenic thrust wedge (Fig. 4.9f-h).

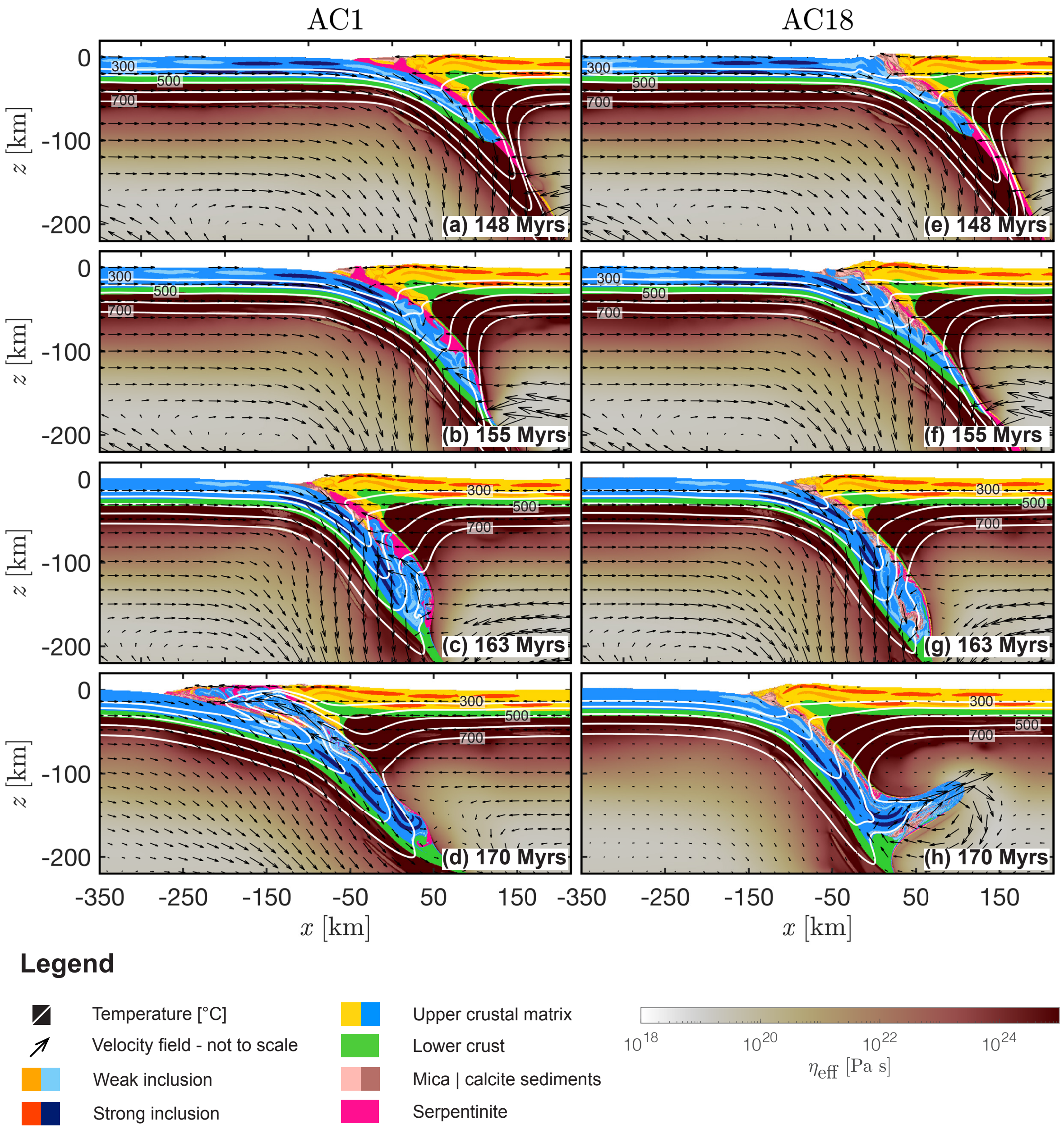

Figure 4.7: Convergence and collisional stage of AC1 and AC18 (low and high shear resistance of serpentinite, complex density model, feldspar-dominated upper crust). White to red indicates the effective viscosity field calculated by the algorithm, yellow to orange indicates the crustal matrix and the weak and strong inclusions of the overriding plate, light to dark blue indicates the corresponding crustal units of the subducting plate. Green indicates the lower crust of both plates and salmon and brown indicates the sedimentary units. White lines show different isotherms and the arrows indicate the velocity field.

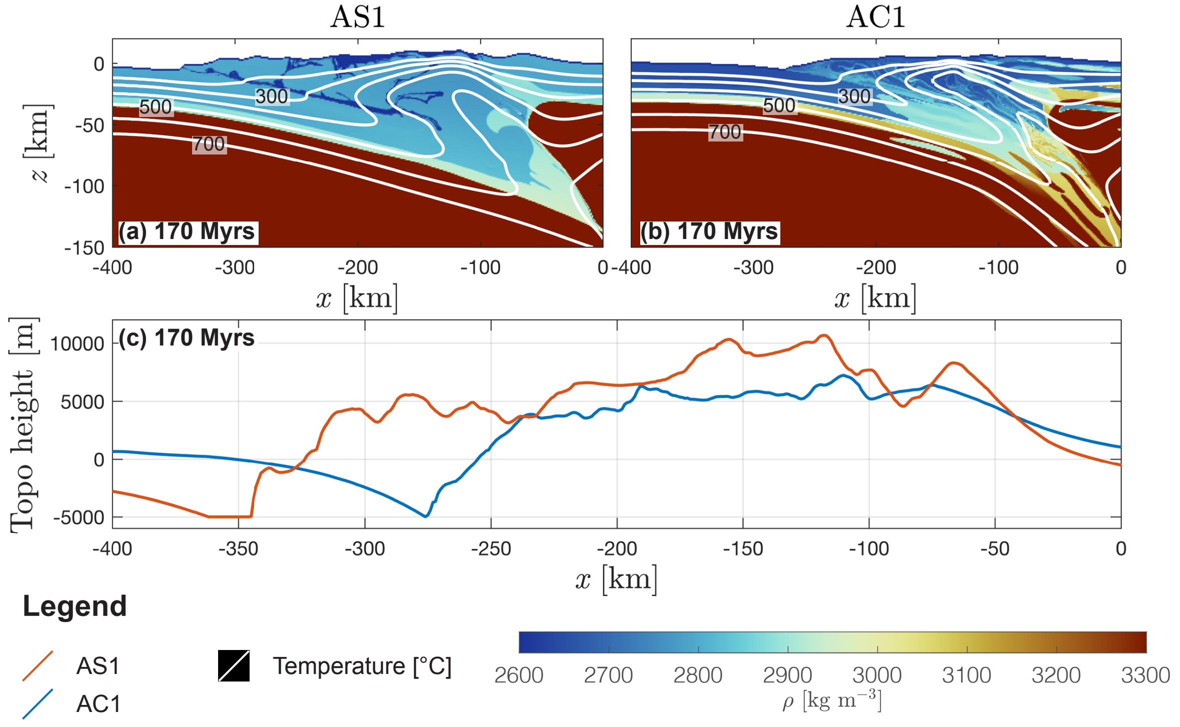

Figure 4.8: Wedge geometry at 170 Myr in model history. Blue to red indicates the density field calculated by the algorithm for (a) AS1 (LEOS) and (b) AC1 (CD-model). White lines are several isotherms. (c) Topographic elevation of AS1 (red line) and AC1 (blue line).

4.3.5 Evolution of buoyancy and shear forces

In order to investigate the relative impact of buoyancy and shear forces on collision, we quantify the temporal evolution of the horizontal driving force per unit length (Fig. 4.10b, F_{D} hereafter; see Appendix C) and of the buoyancy forces of subducted crustal material (Fig. 4.10c, F_{B} hereafter; see Appendix C). Buoyancy forces calculated here represent an upward directed (negative) buoyancy force of the subducted crust acting against further subduction. The ratio $F_{\mathrm{B}}/F_{\mathrm{D}}$ (Fig. 4.10a, Ar_F, hereafter) is a measure for the relative dominance of buoyancy and shear forces driving the deformation and exhumation within the orogenic wedge (see Appendix 4.6.2). Points 1-5 in Fig. 4.10a-e represent important stages of model GC1 (thick dashed turquoise blue line) and are representative for the evolution of all presented models.

Subduction initiation occurs for F_{D} ≈22 TN m^{-1} in models of feldspar dominated continental upper crust (AS1, AS18, AC1 and AC18) and for F_{D} ≈18 TN m^{-1} in models of quartz

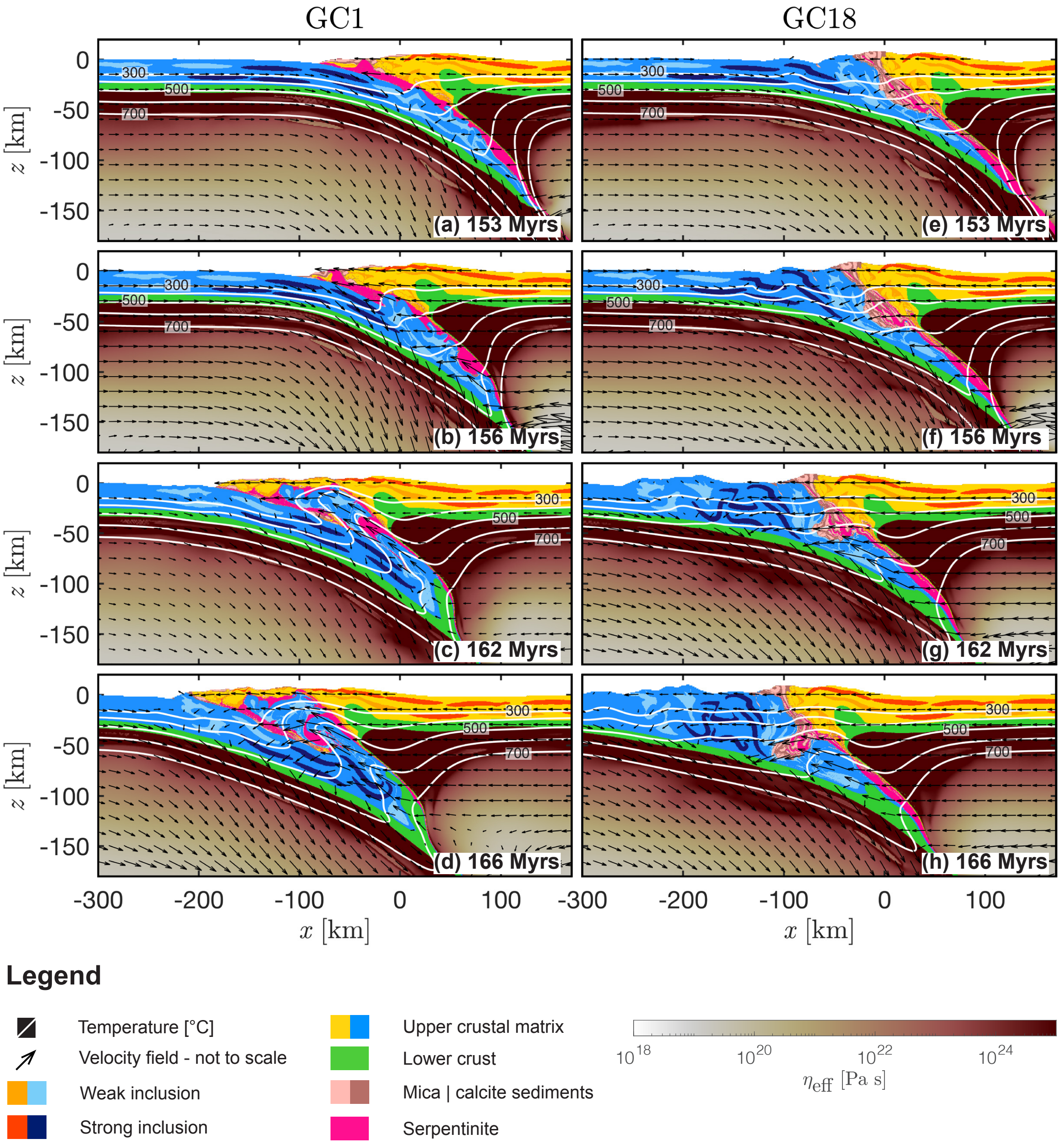

Figure 4.9: Convergence and collisional stage of GC1 and GC18 (low and high shear resistance of serpentinite, CD-model, quartz-dominated upper crust). White to red indicates the effective viscosity field calculated by the algorithm, yellow to orange indicates the crustal matrix and the weak and strong inclusions of the overriding plate, light to dark blue indicates the corresponding crustal units of the subducting plate. Green indicates the lower crust of both plates and salmon and brown indicates the sedimentary units. White lines show different isotherms and the arrows indicate the velocity field.

dominated upper crust (GC1 GC18, 1 and grey area in Fig 4.10b). Magnitudes of F_{D} decrease after subduction initiation to ca. 10-15 $\mathrm{TN\,m^{-1}}$ and remain, on average, relatively constant

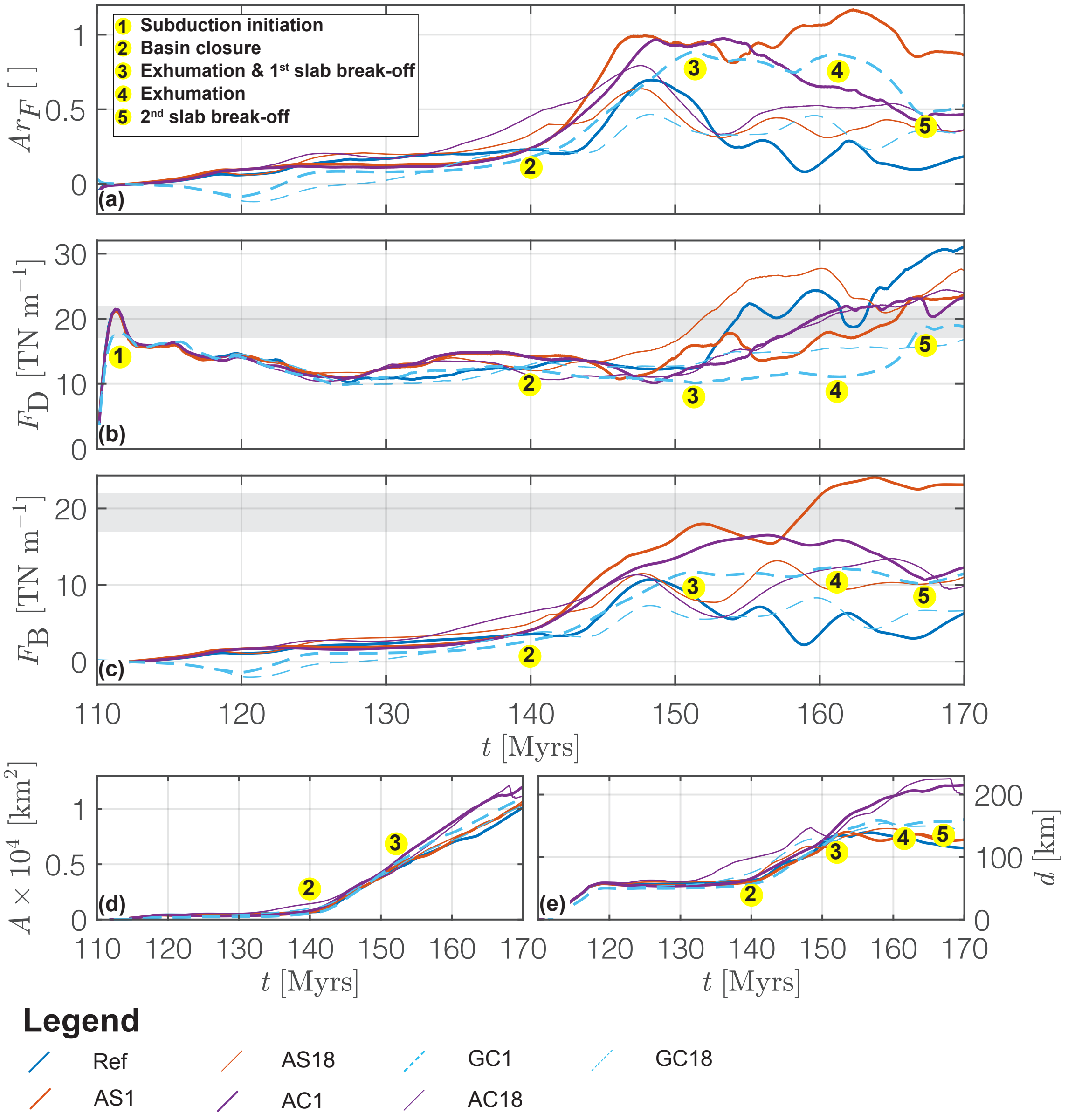

Figure 4.10: Force evolution. (a) Ratio of buoyancy and shear forces, Ar_F, (b) shear forces, (c) buoyancy forces, (d) average area of subducted material and (e) maximum depth of the orogenic wedge. The calculation of quantities presented in this figure is explained in appendix 4.6.2.

during basin closure (between 1 and 2 in Fig. 4.10). Until basin closure, $Ar_F \approx 0.25$ and remains relatively constant in all models. Magnitudes of F_{B} increase with increasing volume of crustal material involved in subduction (see Fig. 4.10c & d) between 140 and 153 Myr.

In response, magnitudes of $Ar_F \approx 1$ are reached in AS1, AC1 and GC1. Between ca. 153 and 156 Myr, shallower buried crustal material is exhumed in GC1 (3 in Fig. 4.10, see also Fig. 4.9a) coinciding with a deep slab detachment (see Candioti (2020a)). At ca. 162 Myr, the deeper subducted units are exhumed (see also Fig. 4.9c). This exhumation event is followed by a shallow slab detachment leading to a rapid increase in magnitude of F_D at ca. 165 Myr. The buoyancy pull of the subducting slab is lost and a larger horizontal driving force is needed to overcome the upward-directed buoyancy push of subducted crust and to continue subduction with the prescribed kinematic boundary velocity. While the buoyancy forces remain relatively constant, the increase of F_D decreases the magnitude of Ar_F (between 4 and 5 in Fig. 4.10a-c). The maximum burial depth of continental crust is reached in AC1 and AC18 (feldspar-dominated upper crust) and is ca. 200 km. In REF, GC1, GC18, AS1 and AS18 the maximum burial depth varies between 120-150 km. During the formation of the collisional orogen, the magnitude of F_D increases and eventually exceeds the magnitude that was necessary for subduction initiation (grey area in Fig. 4.10b). Magnitudes of F_D and F_B are on average higher in models of feldspar-dominated continental upper crust compared to models of quartz-dominated upper crust. The increased shear resistance in these feldspar-dominated models allows for deeper subduction of continental upper crust when the serpentinite is weak. High values for F_D in AS18 and REF are explained by a more resistant subduction interface caused by either an increased shear resistance of the serpentinite material, or absence of serpentinisation.

4.3.6 Different modes of orogenic wedge formation

The geometry, kinematics and dynamics of the evolving collision zone and orogenic wedge varies significantly in the presented models (Fig. 4.11a). We refer here to these variations as different modes of orogenic wedge formation. These varying modes depend mainly on the shear resistance of upper crust and serpentinite, and its buoyancy contrast to the surrounding mantle material. The magnitude of Ar_F is used to classify the different modes of orogenic wedge formation.

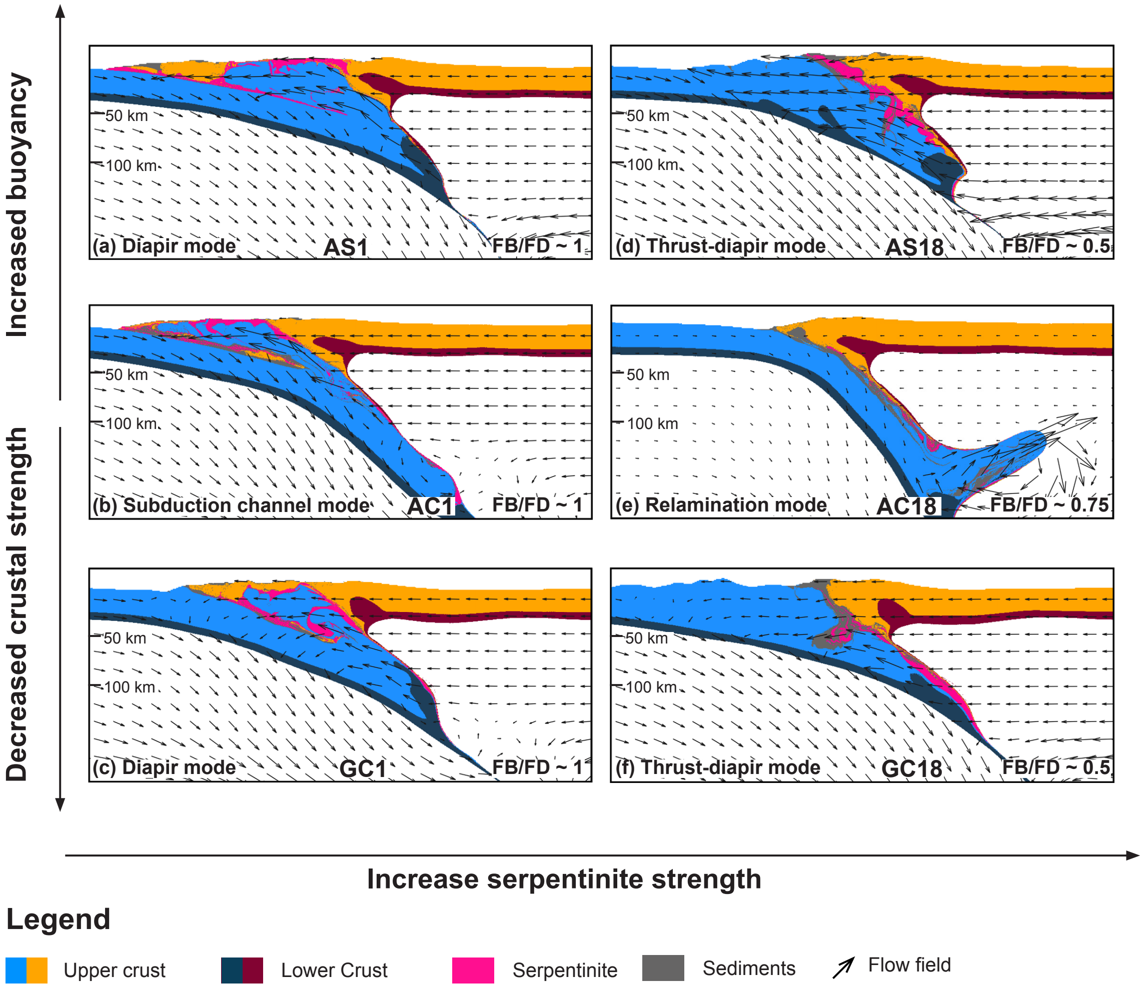

Figure 4.11: Orogen dynamics observed in the models presented here. Light blue and orange indicates the upper crustal phases, dark blue and merlot red indicates the lower crustal phases of the subducting and overriding plate, respectively. Dark grey and magenta represent the sediments and the serpentinite unit, respectively. Arrows indicate the velocity field.

For low shear resistance of serpentinites, $Ar_F \approx 1$ indicating equal importance of buoyancy and shear forces building the orogenic wedge. Two modes are observed: (1) a diapir-like mode of exhumation due to either (i) increased buoyancy contrast (LEOS-models) and high shear resistance of the upper crust (AS1, see Fig. 4.11a) or (ii) a decreased buoyancy contrast (CD-models) and low shear resistance of the upper crust (GC1, see Fig. 4.11c). (2) A channel-flow mode of exhumation occurs for a decreased buoyancy contrast (complex-EOS) and increased shear resistance of the upper crust (AC1, see Fig. 4.11b).

In models of high serpentinite shear resistance, also two different modes are observed: (3) A thrust-diapir mode of deformation for either (i) an increased buoyancy contrast and high shear resistance of the upper crust, or (ii) a decreased buoyancy contrast and low shear resistance of upper crust. In both cases $Ar_F \approx 0.5$, indicating that shear forces dominate the building of the orogenic wedge (Fig. 4.11d & f). (4) A relamination mode due to relamination of deeply subducted continental crust is observed for a decreased buoyancy contrast and high shear resistance of the upper crust ($Ar_F \approx 0.75$, see Fig. 4.11e).

4.4 Discussion

4.4.1 Buoyancy vs. shear forces controlling modes of orogenic wedge formation

The shear resistance of (i) serpentinites and (ii) the upper continental crust directly impacts on the shear forces (compare GC1 to AC1 in Fig. 4.10b). Determining the shear resistance, or effective viscosity, of the lithosphere deforming under geological time scales remains challenging (Burov et al., 2006). Rock deformation experiments are performed at deformation rates that are many orders of magnitude higher than tectonic deformation rates. Best fitting curves have to be extrapolated to natural conditions, which introduces large uncertainties on the actual strength of rocks deforming under natural conditions (Mancktelow and Pennacchioni, 2010; Idrissi et al., 2020). Serpentinite plays a crucial role in subduction zones and, ultimately, in the formation of Alpine-type collisional orogens (Hess, 1955; Raleigh and Paterson, 1965; Hacker et al., 2003; McCarthy et al., 2020). Despite its importance, the rheology of serpentinite at lithospheric-scale pressure and temperature (PT) conditions remains elusive (David et al., 2018; Hirauchi et al., 2020, & reference therein). Several deformation mechanisms for serpentinite material, often based on experiments with antigorite, have been discussed in the literature including: dislocation creep (Hilairet et al., 2007), semi-brittle or plastic deformation behaviour (Chernak and Hirth, 2010; Hirth and Guillot, 2013), grain boundary sliding (Idrissi et al., 2020), and sliding on shear cracks (Hansen et al., 2020). Numerical models are useful to test different end-member rock rheologies and to investigate the impact of rock strength on subduction and formation of collisional orogens. To first order, weak serpentinite material may indeed form a subduction channel and lubricate the subduction interface. The subduction channel in model AC1 has formed self-consistently, because subduction was initiated without a pre-scribed major weak zone in the lithosphere. Deep subduction and exhumation to the surface of crustal material is feasible in these models. Instead, strong serpentinite material leads to detaching and thrusting of crustal material escaping subduction already at shallow depths.

In natural settings, the effective strength of serpentinites may vary along the upper regions of the subduction plate in direction parallel and/or orthogonal (along-trench) to the subduction direction, for example due to varying degrees of serpentinization. Such spatial strength variation may cause temporal and/or along-trench alternations between channel mode and thrust-diapir mode when serpentinites of different strength enter the subduction zone. The shear resistance of the upper crust resulting from the rheological flow laws employed here, wet anorthite Rybacki and Dresen (2004) and westerly granite (Hansen et al., 1983)), is similar and neither extremely low, nor extremely high (see also Fig. 1 in Bürgmann and Dresen (2008)). However, employing these two different flow laws for the upper crust changes the mode of orogenic wedge formation significantly. Similar to the strength of serpentinites, in natural settings also the effective strength of the upper crust may vary and cause temporal and along-trench variations of the orogenic wedge modes during the evolution of continental collision.

Magnitudes of buoyancy forces in our models are enhanced by large density contrasts between the subducted material and the surrounding mantle. We tested end-member models of simple and complex density calculations. The precomputed density tables are based on calculated equilibrium phase diagrams. In our calculations we have assumed H_2O saturation and therefore our system is open with respect to its H_2O content, but closed with respect to other elements. This is a valid approximation for the km-scale that we are considering. However, the preservation of high-grade metamorphic rocks at the near-surface environment indicates that the crustal metamorphic rocks are not always at thermodynamic equilibrium as it is assumed here. The rate of metamorphic re-equilibration is strongly affected by temperature and by the availability of fluids (Rubie, 1986; Austrheim, 1987; Malvoisin et al., 2020). Coupling mineral scale phase equilibria modelling to large scale geodynamic models remains challenging. Although coupling of petrological and thermo-mechanical modelling via CD-models as presented here is simplified, this approach has proven useful to explain observations that cannot be predicted by the commonly used LEOS-models. These observations include (i) varying sediment thickness accumulated during basin subsidence (Kaus et al., 2005), (ii) evolution of subducting slab dynamics (van Hunen et al., 2001; Toussaint et al.,

2004) and (iii) the exhumation of (U)HP rocks (Yamato et al., 2007; Warren et al., 2008). In addition, our results demonstrate that CD-models avoid unrealistically high topographic elevation during orogen formation.

Varying mechanical strength of (i) serpentinites and (ii) the upper crust in combination with varying buoyancy contrasts changes the mode of orogenic wedge formation modelled here (Fig. 4.11). Hence, it is important to (1) better constrain the mechanical strength of crustal rocks and serpentinites under natural deformation conditions and (2) to proceed towards more realistic density structures including metamorphic reactions in numerical models of collisional orogen formation.

4.4.2 Subduction initiation

We follow here the modelling approach by Candioti et al. (2020). The margin geometry and thermal structure, prior to convergence, is generated during a modelled rifting and cooling period. This way, the generated passive margin and marine basin system is modelled internally-consistent with respect to the subsequent convergence. Subduction initiation is horizontally forced (Stern, 2004; Stern and Gerya, 2018; Crameri et al., 2020) and a major lithosphere shear zone forms around the transition from the distal to the proximal margin (see also discussion Candioti et al. (2020)). The ad hoc parameterized layer of serpentinite is not relevant for subduction initiation, as subduction is initiated also in the reference model without serpentinite (see Fig. 4.4f). Instead, geometrical focusing of stresses below the margin together with thermal softening and a temperature-dependent viscosity leads to spontaneous formation of a shear zone transecting the lithosphere (Thielmann and Kaus, 2012; Jaquet and Schmalholz, 2018; Kiss et al., 2020; Candioti et al., 2020; Auzemery et al., 2020). In our models, magnitudes of F_{D} between 18 and 22 $\mathrm{TN\,m^{-1}}$ are necessary to initiate subduction for quartz- and feldspar-dominated upper crust, respectively. These magnitudes are significantly lower compared to F_{D} $\approx$37 $\mathrm{TN\,m^{-1}}$ obtained by Kiss et al. (2020). They studied subduction initiation at an idealised, ad hoc constructed passive margin without mechanical heterogeneities in the form of a multi-layer or elliptical geometry (see also Candioti et al.

(2020) for a detailed comparison). The Peierls flow law parameters describing the rheology of olivine used here have been elaborated by Goetze and Evans (1979). Recent studies suggest that the olivine strength resulting from this parameterisation is likely overestimated (Idrissi et al., 2016). If true, stresses in the mantle lithosphere would be lower than predicted by our models, which could further reduce the magnitude of shear forces necessary for subduction initiation. However, the minimum value of F_{D} required for subduction initiation in our models should be determined in future studies.

4.4.3 Potential applications to natural collisional orogens

Implications for the Pyrenean orogeny

Orogenic wedge formation in the Pyrenees involved mainly the upper 20 km of the upper crust (Teixell et al. (2018, & references therein), see Fig. 4.1a). The absence of subduction related high-pressure metamorphism (Muñoz, 1992) indicates, that only insignificant volumes of upper crust have been involved in subduction. Instead, the majority of the upper crust has been presumably sheared-off the subducting lower crust and formed thrust sheets at mid to upper crustal level (Muñoz, 1992; Teixell et al., 2018, & references therein). Rifting-related inheritances are likely important for the formation of crustal thrust sheets during the Pyrenean orogeny (Jammes et al., 2014; Erdős et al., 2014). In our models, a ca. 360-400 km wide basin with exhumed serpentinized mantle is generated during a rifting period modelled prior to convergence. The model geometry before the onset of convergence is, thus, not directly applicable to the pre-orogen geodynamic setting in the Pyrenees, because the basin resulting from the opening of the Bay of Biscay was most likely considerably narrower (Jammes et al., 2009; McCarthy et al., 2020, & references therein). However, during the collisional stage, our thrust-mode models seem to reproduce some of the first order features observed in the Pyrenees. We therefore suggest, that the buoyancy push of subducted crust was insignificant during the Pyrenean orogeny. Instead, convergence between Iberia and Europe induced shear force driven crustal wedging without deep (¿80 km) subduction of continental upper crust, as for example modelled by Grool et al. (2019).

Model implications for the Alpine orogeny

In the Western Alps, a rifting phase prior to subduction lead to the formation of a ca. 300-400 km wide basin floored by exhumed mantle, and presumably only minor volumes of mature oceanic crust have been produced (Le Breton et al., 2020). Instead, ophiolites preserved in the Western Alps indicate serpentinisation of the mantle exhumed in the basin (McCarthy et al., 2020, & reference therein). The serpentinized material likely formed a relatively weak subduction interface (Zhao et al., 2020) and inhibited subduction of hydrous sediments explaining the sparse arc-magmatism in the European Alps (McCarthy et al., 2018, 2020; Yang et al., 2020). Field evidence of (ultra)high-pressure units (Chopin, 1984) in the Western Alps indicate either deep subduction of upper continental crust (Berger and Bousquet, 2008) at close to lithostatic stress state, or significant deviation from the lithostatic stress state (Schenker et al., 2015) (Fig. 4.1b). Tomographic images (Zhao et al., 2015; Schmid et al., 2017) indicate that major volumes of upper continental crust have been involved in subduction. While the crustal wedge model may be applicable to the deformation during the post-collisional ($\lesssim$ 30 Ma) stage of the Alpine orogeny (e.g. Erdos et al., 2019), it does not predict the exhumation of subduction related (ultra)high-pressure continental and oceanic crustal rocks prior to collision. Instead, a subduction channel model has been proposed to explain deep subduction of continental upper crust and subsequent exhumation of (ultra)high-pressure units along the subduction interface (Gerya et al., 2002; Raimbourg et al., 2007; Butler et al., 2014). The subduction channel model, as proposed by Butler et al. (2014), has been criticised mainly for two reasons: (1) exhumation relies on significant removal, or erosion, of major crustal volumes, which is not in agreement with the sediment volume recorded in the Eocene-Oligocene basins (Malusà et al., 2015). (2) The exhuming units are strongly mixed (tectonic mélange) and significant volumes of lower crust are also exhumed, which is at odds with interpretations from seismic tomography showing no significant exhumation of lower crust (Schmid et al., 2017). In our models, significant synconvergent exhumation of upper crust can occur by either diapirism or channel-flow and is enabled by spatially localized upper plate extension (Fig. 4.11) and not by significant erosion. Exhumation of lower crust does not occur in our model, which is in agreement with interpretations from tomographic images. We focused here on the general evolution of different modes of orogenic wedges. We will present a detailed analysis of (i) the mechanisms causing local upper plate extension, (ii) the exhumation mechanisms of (ultra)high-pressure rocks and (iii) the pressure and temperatures paths and associated exhumation velocities in a subsequent study and we will not further discuss these issues here.

Our models are restricted to two dimensions and driven by far-field kinematic boundary conditions. Therefore, we can only capture first order fundamental features of natural orogens. During model evolution, more and more crustal material is forced into subduction (Fig. 4.10d). In fact, in our models plate driving forces eventually reach again the magnitude necessary for subduction initiation after basin closure (see grey area in Fig. 4.10b). From this point on, the model probably becomes unrealistic, because in nature a new subduction zone would form at a different location and the active subduction zone would cease or slow down significantly. Plate reconstructions from the Western Alps indicate that European subduction below Adria was presumably slowed down significantly (”choked”) between ca. 35-25 Ma (Malusà et al. (2015); Schmid et al. (2017), see Fig. 4.12). Estimating subduction initiation at the Adriatic margin between ca. 90 and 85 Ma (Manzotti et al., 2014), there has been ca. 50-65 Myr of convergence before European subduction was ”choked”. This duration approximately coincides with the time span (ca. 55-60 Myr of convergence) in our models necessary to build up plate driving forces exceeding the magnitude for subduction initiation (at ca. 167 Myr, see 5 in Fig. 4.10b) in model GC1. Hence, we suggest that increase of driving forces during the Alpine orogeny exceeded a critical value leading to: (1) significant slow-down of the European subduction and (2) plate boundary reorganization leading to subduction initiation of the remaining Adriatic oceanic lithosphere below Iberia.

Challenges in applying wedge models to the Alpine orogeny

The ”classical” crustal wedge models (Platt, 1986; Dahlen, 1990; Malavieille, 2010; Dal Zilio et al., 2020b) focus mainly on upper-crustal levels (see grey framed area in Fig. 4.1b). The

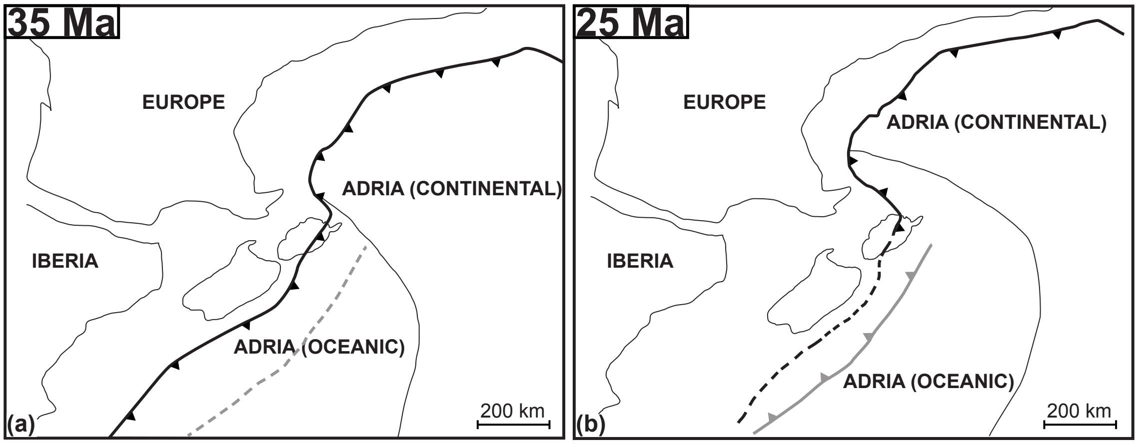

Figure 4.12: Plate motion reconstruction of Europe, Iberia and Adria at (a) 35 Ma and (b) 25 Ma. Europe and Iberia are fixed, Adria is moving northward. Thick black and grey solid lines indicate active subduction zones, dashed lines indicate inactive subduction zones. Sketches modified after Schmid et al. (2017) & Malusà et al. (2015).

evolution of the Alpine orogeny, however, involves the entire lithosphere in wedging (Nicolas et al., 1990). Some studies extended the "classical" wedge model to the lithospheric scale Platt (1986); Vanderhaeghe et al. (2003); Beaumont et al. (2010). Vanderhaeghe et al. (2003) concluded that temperature dependence of material parameters indeed modulates wedge geometries, impacts on the transition between wedge and plateau behaviour and controls the topographic evolution. In crustal wedge models, deformation is usually driven by an internal kinematic boundary condition at the base of the continental crust pulling the material towards a rigid backstop. Of course, subduction and collision in our models are also controlled by the kinematic boundary conditions. However, in our models boundary conditions are imposed far away from the evolving wedge, and not directly at the base of the continental crust, which is likely important when the mantle lithosphere is involved in wedging (Beaumont et al., 2010). The first-order dynamics within the evolving wedge are controlled by the interaction of buoyancy and shear forces according to shear resistance and density structure of material. Our models, therefore, presumably provide a more realistic insight into orogen dynamics compared to orogenic wedge models considering only crustal deformation.

As mentioned in Section 4.4.1, the density structure impacts on the force balance and reduces the mean topographic elevation. This is important, because orogenic wedge models applied to the Western Alps have been criticised for overestimating the mean topographic elevation

(Kissling, 1993; Dal Zilio et al., 2020a). Certainly, the average topography in our models is still higher compared to the average topography of the Alps. However, we suggest that employing more realistic density models is an important step to avoid exaggerated mean topographic elevation in orogenic wedge models. Furthermore, the topography in our models would likely decrease if we would reduce significantly the convergence velocities at the mature stage of orogenic wedge formation, so that delamination of the subducted mantle lithosphere would become important. Such delamination, or so-called rollback orogeny (Kissling and Schlunegger, 2018; Dal Zilio et al., 2020a), applies to the latest Alpine evolution in the post-collisional stage (younger than ca. 30 Ma), but does not apply to the formation of the major (ultra)high-pressure regions (including oceanic, e.g. Zermatt-Saas, and Adriatic, e.g. Sesia and Dent Blanche, domains) of the Alps.

Absolute values for shear and buoyancy forces reported here strongly depend on the amount and strength of crustal material carried into the subduction zone. How much crustal material has been involved in Alpine subduction depends on the pre-orogenic crustal thickness (Mohn et al., 2014) and is still contentious (Butler, 2013; Schmid et al., 2017). The orogenic wedges modelled here are wider and deeper than the natural Alpine orogenic wedge. The size of the mechanical heterogeneities employed here is chosen based on the numerical resolution (1 km) and probably strongly impacts on the size of the modelled wedge. At higher numerical resolution, the size of the mechanical heterogeneities could be reduced and the modelled rifted margins might be thinner, leading to a more realistic pre-orogenic crustal thickness generated during the rifting period. In consequence, less material would be involved in subduction and the absolute magnitude of forces would change. However, the general model evolution, i.e. the relative increase of buoyancy forces with continuous subduction, would be most likely unchanged. Therefore, our models likely provide a representative model for the relative evolution of shear and buoyancy forces building orogenic wedges.

4.5 Conclusion

Our models show that upward-directed buoyancy forces, caused by subduction of continental crust, can be as high as the shear forces induced by far-field plate convergence and should, therefore, be considered in models of continent collision and associated orogenic wedge formation. Parameters controlling the force balance and the mode of deformation and exhumation within the evolving orogenic wedge are: (1) The shear resistance of serpentinites, controlling the shear resistance of the subduction interface, and of the continental upper crust, controlling the maximal depth of crustal subduction. (2) The density structure of the subducted material. The density structure significantly impacts on the mean topographic elevation and leads to more realistic topography evolution.

The strength of serpentinites and of the upper crust, as well as the density structure exert a first-order control on the formation of orogenic wedges. Varying these three parameters only in our models generates a wide spectrum of different orogenic wedge modes, including thrust-sheet dominated wedges, buoyancy flow dominated wedges, and minor wedge formation due to significant relamination of subducted crust below the upper plate. The spatial variation of these three parameters may explain many differences in deformation style observed in natural collisional orogens.

The increase of upward-directed buoyancy forces during orogenic wedge growth causes an increase of the required horizontal driving forces, which may cause a slow down, or ”choking” of the associated subduction. This increase of horizontal driving forces may cause horizontally-forced subduction initiation in other regions. Therefore, quantifying the magnitudes of buoyancy and shear forces during orogenic wedge formation may prove useful to unravel changes in relative plate motion and subduction initiation during the Alpine orogeny.

4.6 Appendix

4.6.1 Emplacement of elliptical heterogeneous inclusions

The semi major axis $a = 30$ km and the semi minor axis $b = 2.5$ km for all elliptical inclusions. The inclusions are emplaced between -400 km $< x <$ 400 km at two different vertical levels. The x-coordinate of the 1st elliptical inclusion's center x_n^{C} at each vertical level is calculated as

$$x_n^{\mathrm{C}} = \big(R_{\mathrm{E}} - R_{\mathrm{S}}\big) \times A + R_{\mathrm{S}} \tag{4.1}$$

$$R_{\mathrm{S}} = \big(d - c\big) \times A - d \tag{4.2}$$

$$R_{\mathrm{E}} = \big(f - h\big) \times A - f \tag{4.3}$$

where R_{S} is a random starting x-coordinate, R_{E} is a random ending x-coordinate, $d = 400$ km, $c = 350$ km, $0 < A < 1$ is a random amplitude, $f = 300$ km and $h = 250$ km. The starting coordinate of the next horizontally emplaced inclusion x_{n+1}^{C} is then calculated as

$$x_{n+1}^{\mathrm{C}} = x_n^{\mathrm{C}} + R_{dx} \tag{4.4}$$

$$R_{dx} = a \times \big(1.75 + A\big) \tag{4.5}$$

where R_{dx} is a random spacing ensuring that the ellipses do not overlap each other. The z-coordinate of the elliptical inclusion's center z_m^{C} at the vertical level m is calculated as

$$z_{\mathit{1}}^{\mathrm{C}} = \big(\frac{1}{3} z_{\mathrm{Moho}} - 3b\big) \times A - \frac{1}{3} z_{\mathrm{Moho}} + b \tag{4.6}$$

$$z_{\mathit{2}}^{\mathrm{C}} = \big(\frac{1}{3} z_{\mathrm{Moho}} - 2b\big) \times A - \frac{2}{3} z_{\mathrm{Moho}} + b \ , \tag{4.7}$$

where $z_{\mathrm{Moho}} = 33$ km is the initial depth of the Moho. Finally, all particles within the circumference of the elliptical inclusion are assigned with a random phase, i.e. either mechanically weak or strong material, according to the condition

$$\frac{\left(x_{\mathrm{M}} - x_n^{\mathrm{C}}\right)^2}{a^2} + \frac{\left(z_{\mathrm{M}} - z_m^{\mathrm{C}}\right)^2}{b^2} < 1 \ , \tag{4.8}$$

where x_{M} and z_{M} are the horizontal and vertical coordinate of the marker, respectively. All random numbers used here are seeded at a value of 197 using the C-function *srand*. Choosing the above mentioned values yields an increased number of weak elliptical inclusions in the center of the domain. This yields localisation of deformation without an additional perturbation of the marker field in the center of the domain.

4.6.2 Buoyancy and driving forces

The vertical integral of the second invariant of the deviatoric stress tensor

$$\bar{\tau}_{\mathrm{II}}(x) = \int_{Sb}^{St(x)} \tau_{\mathrm{II}}(x, z)\ \mathrm{d}z \ . \tag{4.9}$$

is a measure for lithospheric strength. Twice its value is representative for the driving force, $F_{\mathrm{D}} = 2 \times \bar{\tau}_{\mathrm{II}}^{\mathrm{avg}}(x)$, acting on the deformed system. $\bar{\tau}_{\mathrm{II}}^{\mathrm{avg}}(x)$ is calculated averaging the average of $\bar{\tau}_{\mathrm{II}}(x)$ both over the left and rightmost 100 km of the domain. This value is also identical to the vertical integral of the difference between the horizontal total stress and the lithostatic pressure, if shear stresses are negligible (Molnar and Lyon-Caen, 1988; Schmalholz et al., 2019). The reader is referred to Candioti et al. (2020) for further detail.

For calculation of the buoyancy force per unit length

$$F_{\mathrm{B}} = \int_{\Omega} \Delta\rho g\ \mathrm{d}\Omega \ , \tag{4.10}$$

the density difference, $\Delta\rho$, between the subducted material and the surrounding mantle is integrated over the area Ω of material subducted below z=-40 km. To obtain a significant value for the negative (upward-directed) buoyancy force of subducted material, which is not isostatically balanced by high topography, we subtract the force contributing to the build-up of topography. As an approximation for this topographic contribution, the density of material lifted above z=1.5 km is integrated over its area and then subtracte from F_{B}. As a measure for buoyancy or shear forces dominating orogen dynamics, we here define $Ar_F = F_{\mathrm{B}}/F_{\mathrm{D}}$ which is comparable to the Argand number (England and McKenzie, 1982).

Bibliography

Austrheim, H., 1987. Eclogitization of lower crustal granulites by fluid migration through shear zones. Earth and Planetary Science Letters 81 (2-3), 221–232.

Auzemery, A., Willingshofer, E., Yamato, P., Duretz, T., Sokoutis, D., 2020. Strain localization mechanisms for subduction initiation at passive margins. Global and Planetary Change 195, 103323.

Barnhoorn, A., Drury, M. R., van Roermund, H. L., 2010. Evidence for low viscosity garnet-rich layers in the upper mantle. Earth and Planetary Science Letters 289 (1-2), 54–67.

Beaumont, C., Ellis, S., Hamilton, J., Fullsack, P., 1996. Mechanical model for subduction-collision tectonics of alpine-type compressional orogens. Geology 24 (8), 675–678.

Beaumont, C., Jamieson, R., Nguyen, M., 2010. Models of large, hot orogens containing a collage of reworked and accreted terranes. Canadian Journal of Earth Sciences 47 (4), 485–515.

Behr, W. M., Becker, T. W., 2018. Sediment control on subduction plate speeds. Earth and Planetary Science Letters 502, 166–173.

Berger, A., Bousquet, R., 2008. Subduction-related metamorphism in the alps: review of isotopic ages based on petrology and their geodynamic consequences. Geological Society, London, Special Publications 298 (1), 117–144.

Borderie, S., Graveleau, F., Witt, C., Vendeville, B. C., 2018. Impact of an interbedded viscous décollement on the structural and kinematic coupling in fold-and-thrust belts: Insights from analogue modeling. Tectonophysics 722, 118–137.

Bürgmann, R., Dresen, G., 2008. Rheology of the lower crust and upper mantle: Evidence from rock mechanics, geodesy, and field observations. Annual Review of Earth and Planetary Sciences 36.

Burov, E., François, T., Agard, P., Le Pourhiet, L., Meyer, B., Tirel, C., Lebedev, S., Yamato, P., Brun, J.-P., 2014. Rheological and geodynamic controls on the mechanisms of subduction and hp/uhp exhumation of crustal rocks during continental collision: Insights from numerical models. Tectonophysics 631, 212–250.

Burov, E., Watts, A., et al., 2006. The long-term strength of continental lithosphere:" jelly sandwich" or" crème brûlée"? GSA today 16 (1), 4.

Butler, J. P., Beaumont, C., Jamieson, R. A., 2014. The alps 2: Controls on crustal subduction and (ultra) high-pressure rock exhumation in alpine-type orogens. Journal of Geophysical Research: Solid Earth 119 (7), 5987–6022.

Butler, R. W., 2013. Area balancing as a test of models for the deep structure of mountain belts, with specific reference to the alps. Journal of Structural Geology 52, 2–16.

Candioti, L. G., 2020a. Evolution of numerical simulation gc1. Copernicus Publications, https://doi.org/10.5446/50528 $Lastaccessed : 22Dec2020$.

Candioti, L. G., 2020b. Evolution of numerical simulation ref. Copernicus Publications, https://doi.org/10.5446/50527 $Lastaccessed : 22Dec2020$.

Candioti, L. G., Schmalholz, S. M., Duretz, T., 2020. Impact of upper mantle convection on lithosphere hyperextension and subsequent horizontally forced subduction initiation. Solid Earth 11 (6), 2327–2357.

Chapple, W. M., 1978. Mechanics of thin-skinned fold-and-thrust belts. Geological Society of America Bulletin 89 (8), 1189–1198.

Chenin, P., Manatschal, G., Picazo, S., Müntener, O., Karner, G., Johnson, C., Ulrich, M., 2017. Influence of the architecture of magma-poor hyperextended rifted margins on orogens produced by the closure of narrow versus wide oceans. Geosphere 13 (2), 559–576.

Chenin, P., Picazo, S., Jammes, S., Manatschal, G., Müntener, O., Karner, G., 2019. Potential role of lithospheric mantle composition in the wilson cycle: a north atlantic perspective. Geological Society, London, Special Publications 470 (1), 157–172.

Chernak, L. J., Hirth, G., 2010. Deformation of antigorite serpentinite at high temperature and pressure. Earth and Planetary Science Letters 296 (1-2), 23–33.

Chopin, C., 1984. Coesite and pure pyrope in high-grade blueschists of the western alps: a first record and some consequences. Contributions to Mineralogy and Petrology 86 (2), 107–118.

Connolly, J. A., 2005. Computation of phase equilibria by linear programming: a tool for geodynamic modeling and its application to subduction zone decarbonation. Earth and Planetary Science Letters 236 (1-2), 524–541.

Crameri, F., 2018. Geodynamic diagnostics, scientific visualisation and staglab 3.0. Geoscientific Model Development 11 (6), 2541–2562.

Crameri, F., Magni, V., Domeier, M., Shephard, G. E., Chotalia, K., Cooper, G., Eakin, C. M., Grima, A. G., Gürer, D., Király, Á., et al., 2020. A transdisciplinary and community-driven database to unravel subduction zone initiation. Nature Communications 11 (1), 1–14.

Currie, C. A., Beaumont, C., Huismans, R. S., 2007. The fate of subducted sediments: A case for backarc intrusion and underplating. Geology 35 (12), 1111–1114.

Dahlen, F., 1990. Critical taper model of fold-and-thrust belts and accretionary wedges. Annual Review of Earth and Planetary Sciences 18 (1), 55–99.

Dahlen, F., Suppe, J., Davis, D., 1984. Mechanics of fold-and-thrust belts and accretionary wedges: Cohesive coulomb theory. Journal of Geophysical Research: Solid Earth 89 (B12), 10087–10101.

Dal Zilio, L., Kissling, E., Gerya, T., van Dinther, Y., 2020a. Slab rollback orogeny model: A test of concept. Geophysical Research Letters 47 (18), e2020GL089917.

Dal Zilio, L., Ruh, J., Avouac, J.-P., 2020b. Structural evolution of orogenic wedges: interplay between erosion and weak décollements. Tectonics, e2020TC006210.

David, E. C., Brantut, N., Hansen, L. N., Mitchell, T. M., 2018. Absence of stress-induced anisotropy during brittle deformation in antigorite serpentinite. Journal of Geophysical Research: Solid Earth 123 (12), 10–616.

Duretz, T., Gerya, T., 2013. Slab detachment during continental collision: Influence of crustal rheology and interaction with lithospheric delamination. Tectonophysics 602, 124–140.

Duretz, T., May, D. A., Yamato, P., 2016a. A free surface capturing discretization for the staggered grid finite difference scheme. Geophysical Journal International 204 (3), 1518–1530.

Duretz, T., Petri, B., Mohn, G., Schmalholz, S., Schenker, F., Müntener, O., 2016b. The importance of structural softening for the evolution and architecture of passive margins. Scientific reports 6, 38704.

Duretz, T., Schmalholz, S., Gerya, T., 2012. Dynamics of slab detachment. Geochemistry, Geophysics, Geosystems 13 (3).

England, P., McKenzie, D., 1982. A thin viscous sheet model for continental deformation. Geophysical Journal International 70 (2), 295–321.

Erdos, Z., Huismans, R. S., van der Beek, P., 2019. Control of increased sedimentation on orogenic fold-and-thrust belt structure–insights into the evolution of the western alps. Solid Earth 10 (2), 391–404.

Erdős, Z., Huismans, R. S., van der Beek, P., Thieulot, C., 2014. Extensional inheritance and surface processes as controlling factors of mountain belt structure. Journal of Geophysical Research: Solid Earth 119 (12), 9042–9061.

Forsyth, D., Uyeda, S., 1975. On the relative importance of the driving forces of plate motion. Geophysical Journal International 43 (1), 163–200.

Gerya, T., 2019. Introduction to numerical geodynamic modelling. Cambridge University Press.

Gerya, T. V., Perchuk, L. L., Maresch, W. V., Willner, A. P., 2004. Inherent gravitational instability of hot continental crust: Implications for doming and diapirism in granulite facies terrains. SPECIAL PAPERS-GEOLOGICAL SOCIETY OF AMERICA, 97–116.

Gerya, T. V., Stöckhert, B., Perchuk, A. L., 2002. Exhumation of high-pressure metamorphic rocks in a subduction channel: A numerical simulation. Tectonics 21 (6), 6–1.

Goetze, C., Evans, B., 1979. Stress and temperature in the bending lithosphere as constrained by experimental rock mechanics. Geophysical Journal International 59 (3), 463–478.

Graveleau, F., Malavieille, J., Dominguez, S., 2012. Experimental modelling of orogenic wedges: A review. Tectonophysics 538, 1–66.

Grool, A. R., Huismans, R. S., Ford, M., 2019. Salt décollement and rift inheritance controls on crustal deformation in orogens. Terra Nova 31 (6), 562–568.

Guillot, S., Schwartz, S., Reynard, B., Agard, P., Prigent, C., 2015. Tectonic significance of serpentinites. Tectonophysics 646, 1–19.

Gutscher, M.-A., Kukowski, N., Malavieille, J., Lallemand, S., 1998. Episodic imbricate thrusting and underthrusting: Analog experiments and mechanical analysis applied to the alaskan accretionary wedge. Journal of Geophysical Research: Solid Earth 103 (B5), 10161–10176.

Hacker, B. R., Peacock, S. M., Abers, G. A., Holloway, S. D., 2003. Subduction factory 2. are intermediate-depth earthquakes in subducting slabs linked to metamorphic dehydration reactions? Journal of Geophysical Research: Solid Earth 108 (B1).

Handy, M. R., Schmid, S. M., Bousquet, R., Kissling, E., Bernoulli, D., 2010. Reconciling plate-tectonic reconstructions of alpine tethys with the geological–geophysical record of spreading and subduction in the alps. Earth-Science Reviews 102 (3-4), 121–158.

Hansen, F., Carter, N., et al., 1983. Semibrittle creep of dry and wet westerly granite at 1000 mpa. In: The 24th US Symposium on Rock Mechanics (USRMS). American Rock Mechanics Association.

Hansen, L. N., David, E. C., Brantut, N., Wallis, D., 2020. Insight into the microphysics of antigorite deformation from spherical nanoindentation. Philosophical Transactions of the Royal Society A 378 (2165), 20190197.

Hess, H. H., 1955. Serpentines, orogeny, and epeirogeny. Geol. Soc. Am. Spec. Paper 62, 391–407.

Hetényi, G., Cattin, R., Brunet, F., Bollinger, L., Vergne, J., Nábělek, J. L., Diament, M., 2007. Density distribution of the india plate beneath the tibetan plateau: Geophysical and petrological constraints on the kinetics of lower-crustal eclogitization. Earth and Planetary Science Letters 264 (1-2), 226–244.

Hilairet, N., Reynard, B., Wang, Y., Daniel, I., Merkel, S., Nishiyama, N., Petitgirard, S., 2007. High-pressure creep of serpentine, interseismic deformation, and initiation of subduction. Science 318 (5858), 1910–1913.

Hirauchi, K.-i., Katayama, I., Kouketsu, Y., 2020. Semi-brittle deformation of antigorite serpentinite under forearc mantle wedge conditions. Journal of Structural Geology, 104151.

Hirth, G., Guillot, S., 2013. Rheology and tectonic significance of serpentinite. Elements 9 (2), 107–113.

Hirth, G., Kohlstedf, D., 2003. Rheology of the upper mantle and the mantle wedge: A view from the experimentalists. Geophysical Monograph-American Geophysical Union 138, 83–106.

Holland, T., Powell, R., 1998. An internally consistent thermodynamic data set for phases of petrological interest. Journal of metamorphic Geology 16 (3), 309–343.

Idrissi, H., Bollinger, C., Boioli, F., Schryvers, D., Cordier, P., 2016. Low-temperature plasticity of olivine revisited with in situ tem nanomechanical testing. Science advances 2 (3), e1501671.

Idrissi, H., Samaee, V., Lumbeeck, G., van der Werf, T., Pardoen, T., Schryvers, D., Cordier, P., 2020. In situ quantitative tensile testing of antigorite in a transmission electron microscope. Journal of Geophysical Research: Solid Earth 125 (3), e2019JB018383.

Jammes, S., Huismans, R. S., Muñoz, J. A., 2014. Lateral variation in structural style of mountain building: controls of rheological and rift inheritance. Terra Nova 26 (3), 201–207.

Jammes, S., Manatschal, G., Lavier, L., Masini, E., 2009. Tectonosedimentary evolution related to extreme crustal thinning ahead of a propagating ocean: Example of the western pyrenees. Tectonics 28 (4).

Jaquet, Y., Duretz, T., Grujic, D., Masson, H., Schmalholz, S. M., 2018. Formation of orogenic wedges and crustal shear zones by thermal softening, associated topographic evolution and application to natural orogens. Tectonophysics 746, 512–529.

Jaquet, Y., Schmalholz, S. M., 2018. Spontaneous ductile crustal shear zone formation by thermal softening and related stress, temperature and strain rate evolution. Tectonophysics 746, 384–397.

Kameyama, M., Yuen, D. A., Karato, S.-I., 1999. Thermal-mechanical effects of low-temperature plasticity (the peierls mechanism) on the deformation of a viscoelastic shear zone. Earth and Planetary Science Letters 168 (1-2), 159–172.

Kaus, B. J., Connolly, J. A., Podladchikov, Y. Y., Schmalholz, S. M., 2005. Effect of mineral phase transitions on sedimentary basin subsidence and uplift. Earth and Planetary Science Letters 233 (1-2), 213–228.

Kiss, D., Candioti, L. G., Duretz, T., Schmalholz, S. M., 2020. Thermal softening induced subduction initiation at a passive margin. Geophysical Journal International 220 (3), 2068–2073.

Kissling, E., 1993. Deep structure of the alps—what do we really know? Physics of the Earth and Planetary Interiors 79 (1-2), 87–112.

Kissling, E., Schlunegger, F., 2018. Rollback orogeny model for the evolution of the swiss alps. Tectonics 37 (4), 1097–1115.

Kronenberg, A. K., Kirby, S. H., Pinkston, J., 1990. Basal slip and mechanical anisotropy of biotite. Journal of Geophysical Research: Solid Earth 95 (B12), 19257–19278.

Lamb, S., Davis, P., 2003. Cenozoic climate change as a possible cause for the rise of the andes. Nature 425 (6960), 792–797.

Lardeaux, J.-M., 2014. Deciphering orogeny: a metamorphic perspective. examples from european alpine and variscan belts: Part i: Alpine metamorphism in the western alps. a review. Bulletin de la Société Géologique de France 185 (2), 93–114.

Le Breton, E., Brune, s., Ustaszewski, K., Zahirovic, S., Seton, M., Müller, R. D., 2020. Kinematics and extent of the piemont-liguria basin – implications for subduction processes in the alps. Solid Earth Discuss. in review (https://doi.org/10.5194/se-2020-161).

Li, Z., Gerya, T. V., 2009. Polyphase formation and exhumation of high-to ultrahigh-pressure rocks in continental subduction zone: Numerical modeling and application to the sulu ultrahigh-pressure terrane in eastern china. Journal of Geophysical Research: Solid Earth 114 (B9).

Mackwell, S., Zimmerman, M., Kohlstedt, D., 1998. High-temperature deformation of dry diabase with application to tectonics on venus. Journal of Geophysical Research: Solid Earth 103 (B1), 975–984.

Malavieille, J., 2010. Impact of erosion, sedimentation, and structural heritage on the structure and kinematics of orogenic wedges: Analog models and case studies. Gsa Today 20 (1), 4–10.

Malinverno, A., Ryan, W. B., 1986. Extension in the tyrrhenian sea and shortening in the apennines as result of arc migration driven by sinking of the lithosphere. Tectonics 5 (2), 227–245.

Malusà, M. G., Faccenna, C., Baldwin, S. L., Fitzgerald, P. G., Rossetti, F., Balestrieri, M. L., Danišík, M., Ellero, A., Ottria, G., Piromallo, C., 2015. Contrasting styles of (u) hp rock exhumation along the cenozoic adria-europe plate boundary (western alps, calabria, corsica). Geochemistry, Geophysics, Geosystems 16 (6), 1786–1824.

Malvoisin, B., Austrheim, H., Hetényi, G., Reynes, J., Hermann, J., Baumgartner, L. P., Podladchikov, Y. Y., 2020. Sustainable densification of the deep crust. Geology.

Manatschal, G., Müntener, O., 2009. A type sequence across an ancient magma-poor ocean–continent transition: the example of the western alpine tethys ophiolites. Tectonophysics 473 (1-2), 4–19.

Mancktelow, N. S., Pennacchioni, G., 2010. Why calcite can be stronger than quartz. Journal of Geophysical Research: Solid Earth 115 (B1).

Manzotti, P., Ballevre, M., Zucali, M., Robyr, M., Engi, M., 2014. The tectonometamorphic evolution of the sesia–dent blanche nappes (internal western alps): review and synthesis. Swiss Journal of Geosciences 107 (2-3), 309–336.

McCarthy, A., Chelle-Michou, C., Müntener, O., Arculus, R., Blundy, J., 2018. Subduction initiation without magmatism: The case of the missing alpine magmatic arc. Geology 46 (12), 1059–1062.

McCarthy, A., Tugend, J., Mohn, G., Candioti, L., Chelle-Michou, C., Arculus, R., Schmalholz, S. M., Müntener, O., 2020. A case of ampferer-type subduction and consequences for the alps and the pyrenees. American Journal of Science 320 (4), 313–372.

Mohn, G., Manatschal, G., Beltrando, M., Haupert, I., 2014. The role of rift-inherited hyper-extension in alpine-type orogens. Terra Nova 26 (5), 347–353.

Molnar, P., Lyon-Caen, H., 1988. Some simple physical aspects of the support, structure, and evolution of mountain belts. Processes in continental lithospheric deformation 218, 179–207.

Muñoz, J. A., 1992. Evolution of a continental collision belt: Ecors-pyrenees crustal balanced cross-section. In: Thrust tectonics. Springer, pp. 235–246.

Nicolas, A., Hirn, A., Nicolich, R., Polino, R., 1990. Lithospheric wedging in the western alps inferred from the ecors-crop traverse. Geology 18 (7), 587–590.

Pelletier, L., Müntener, O., Kalt, A., Vennemann, T. W., Belgya, T., 2008. Emplacement of ultramafic rocks into the continental crust monitored by light and other trace elements: An example from the geisspfad body (swiss-italian alps). Chemical Geology 255 (1-2), 143–159.

Petri, B., Duretz, T., Mohn, G., Schmalholz, S. M., Karner, G. D., Müntener, O., 2019. Thinning mechanisms of heterogeneous continental lithosphere. Earth and Planetary Science Letters 512, 147–162.

Platt, J., 1986. Dynamics of orogenic wedges and the uplift of high-pressure metamorphic rocks. Geological society of America bulletin 97 (9), 1037–1053.

Raimbourg, H., Jolivet, L., Leroy, Y., 2007. Consequences of progressive eclogitization on crustal exhumation, a mechanical study. Geophysical Journal International 168 (1), 379–401.

Raleigh, C. B., Paterson, M., 1965. Experimental deformation of serpentinite and its tectonic implications. Journal of Geophysical Research 70 (16), 3965–3985.

Ramberg, H., 1981. Gravity, deformation and the earth's crust: in theory, experiments and geological application. Academic press.

Ranalli, G., 1995. Rheology of the Earth. Springer Science & Business Media.

Rubie, D. C., 1986. The catalysis of mineral reactions by water and restrictions on the presence of aqueous fluid during metamorphism. Mineralogical Magazine 50 (357), 399–415.

Ruh, J. B., Kaus, B. J., Burg, J.-P., 2012. Numerical investigation of deformation mechanics in fold-and-thrust belts: Influence of rheology of single and multiple décollements. Tectonics 31 (3).

Rummel, L., Baumann, T. S., Kaus, B. J., 2020. An autonomous petrological database for geodynamic simulations of magmatic systems. Geophysical Journal International 223 (3), 1820–1836.

Rybacki, E., Dresen, G., 2004. Deformation mechanism maps for feldspar rocks. Tectonophysics 382 (3-4), 173–187.

Schenker, F. L., Schmalholz, S. M., Moulas, E., Pleuger, J., Baumgartner, L. P., Podladchikov, Y., Vrijmoed, J., Buchs, N., Müntener, O., 2015. Current challenges for explaining (ultra) high-pressure tectonism in the pennine domain of the central and western alps. Journal of Metamorphic Geology 33 (8), 869–886.

Schmalholz, S. M., Duretz, T., Hetényi, G., Medvedev, S., 2019. Distribution and magnitude of stress due to lateral variation of gravitational potential energy between indian lowland and tibetan plateau. Geophysical Journal International 216 (2), 1313–1333.

Schmid, S., Boland, J., Paterson, M., 1977. Superplastic flow in finegrained limestone. Tectonophysics 43 (3-4), 257–291.

Schmid, S. M., Kissling, E., Diehl, T., van Hinsbergen, D. J., Molli, G., 2017. Ivrea mantle wedge, arc of the western alps, and kinematic evolution of the alps–apennines orogenic system. Swiss Journal of Geosciences 110 (2), 581–612.

Shreve, R. L., Cloos, M., 1986. Dynamics of sediment subduction, melange formation, and prism accretion. Journal of Geophysical Research: Solid Earth 91 (B10), 10229–10245.

Simpson, G. D., 2009. Mechanical modelling of folding versus faulting in brittle–ductile wedges. Journal of Structural Geology 31 (4), 369–381.

Sizova, E., Gerya, T., Brown, M., 2014. Contrasting styles of phanerozoic and precambrian continental collision. Gondwana Research 25 (2), 522–545.

Stern, R. J., 2004. Subduction initiation: spontaneous and induced. Earth and Planetary Science Letters 226 (3-4), 275–292.

Stern, R. J., Gerya, T., 2018. Subduction initiation in nature and models: A review. Tectonophysics 746, 173–198.

Stixrude, L., Lithgow-Bertelloni, C., 2011. Thermodynamics of mantle minerals-ii. phase equilibria. Geophysical Journal International 184 (3), 1180–1213.

Sutra, E., Manatschal, G., Mohn, G., Unternehr, P., 2013. Quantification and restoration of extensional deformation along the western iberia and newfoundland rifted margins. Geochemistry, Geophysics, Geosystems 14 (8), 2575–2597.

Teixell, A., Labaume, P., Ayarza, P., Espurt, N., de Saint Blanquat, M., Lagabrielle, Y., 2018. Crustal structure and evolution of the pyrenean-cantabrian belt: A review and new interpretations from recent concepts and data. Tectonophysics 724, 146–170.

Thielmann, M., Kaus, B. J., 2012. Shear heating induced lithospheric-scale localization: Does it result in subduction? Earth and Planetary Science Letters 359, 1–13.

Toussaint, G., Burov, E., Jolivet, L., 2004. Continental plate collision: Unstable vs. stable slab dynamics. Geology 32 (1), 33–36.

Turcotte, D., Schubert, G., 2014. Geodynamics. Cambridge University Press.

van Hunen, J., van den Berg, A. P., Vlaar, N. J., 2001. Latent heat effects of the major mantle phase transitions on low-angle subduction. Earth and Planetary Science Letters 190 (3-4), 125–135.

Vanderhaeghe, O., Medvedev, S., Fullsack, P., Beaumont, C., Jamieson, R. A., 2003. Evolution of orogenic wedges and continental plateaux: insights from crustal thermal–mechanical models overlying subducting mantle lithosphere. Geophysical Journal International 153 (1), 27–51.

Warren, C. J., Beaumont, C., Jamieson, R. A., 2008. Formation and exhumation of ultra-high-pressure rocks during continental collision: Role of detachment in the subduction channel. Geochemistry, Geophysics, Geosystems 9 (4).

Weijermars, R., Schmeling, H., 1986. Scaling of newtonian and non-newtonian fluid dynamics without inertia for quantitative modelling of rock flow due to gravity (including the concept of rheological similarity). Physics of the Earth and Planetary Interiors 43 (4), 316–330.

Willett, S., Beaumont, C., Fullsack, P., 1993. Mechanical model for the tectonics of doubly vergent compressional orogens. Geology 21 (4), 371–374.

Willett, S. D., 1999. Orogeny and orography: The effects of erosion on the structure of mountain belts. Journal of Geophysical Research: Solid Earth 104 (B12), 28957–28981.

Wilson, J. T., 1965. A new class of faults and their bearing on continental drift. Nature 207 (4995), 343–347.

Wilson, R., Houseman, G., Buiter, S., McCaffrey, K., Doré, A., 2019. Fifty years of the wilson cycle concept in plate tectonics: an overview.

Winter, J. D., 2013. Principles of igneous and metamorphic petrology. Pearson education.

Workman, R. K., Hart, S. R., 2005. Major and trace element composition of the depleted morb mantle (dmm). Earth and Planetary Science Letters 231 (1-2), 53–72.

Yamato, P., Agard, P., Burov, E., Le Pourhiet, L., Jolivet, L., Tiberi, C., 2007. Burial and exhumation in a subduction wedge: Mutual constraints from thermomechanical modeling and natural p-t-t data (schistes lustrés, western alps). Journal of Geophysical Research: Solid Earth 112 (B7).

Yang, J., Lu, G., Liu, T., Li, Y., Wang, K., Wang, X., Sun, B., Faccenda, M., Zhao, L., 2020. Amagmatic subduction produced by mantle serpentinization and oceanic crust delamination. Geophysical Research Letters 47 (9), e2019GL086257.

Zhao, L., Malusà, M. G., Yuan, H., Paul, A., Guillot, S., Lu, Y., Stehly, L., Solarino, S., Eva, E., Lu, G., et al., 2020. Evidence for a serpentinized plate interface favouring continental subduction. Nature Communications 11 (1), 1–8.

Zhao, L., Paul, A., Guillot, S., Solarino, S., Malusà, M. G., Zheng, T., Aubert, C., Salimbeni, S., Dumont, T., Schwartz, S., et al., 2015. First seismic evidence for continental subduction beneath the western alps. Geology 43 (9), 815–818.

CHAPTER 5

Deterministic models unveil new subduction–exhumation cycle of (ultra)high-pressure rocks

Lorenzo G. Candioti[1], **Joshua D. Vaughan-Hammon**[1], **Thibault Duretz**[2], **Stefan M. Schmalholz**[1],

[1]Institut des Sciences de la Terre, University of Lausanne, Lausanne, Switzerland.

[2]Univ Rennes, CNRS, Géosciences Rennes UMR 6118, Rennes, France.

Abstract

Worldwide observations of (ultra)high-pressure, (U)HP, rocks at convergent plate boundaries indicate deep (>50 km) burial–exhumation cycling of crustal rocks during subduction and associated mountain building. However, the mechanisms of (U)HP rock exhumation are still contentious and cycling of crustal (U)HP rocks during mountain building remains elusive.

Here, we present a petrological–thermomechanical model for a mechanically heterogeneous lithosphere–upper mantle system that predicts the entire evolution from spontaneous subduction initiation to (U)HP rock exhumation within a single and continuous numerical simulation. A newly identified mechanism of buckling-induced, local upper-plate extension triggering episodic buoyancy-driven flow along the subduction interface enables the synconvergent and coherent exhumation of upper crustal (U)HP rocks. The model also highlights the importance of serpentinites for weakening the subduction interface and enabling (U)HP rock exhumation. The model results agree with geodynamic reconstructions, estimated exhumation rates, peak metamorphic pressure–temperature conditions and structural coherency of exhumed (U)HP units in the European Western Alps and are applicable to other (U)HP terranes.

5.1 Main

Planet Earth's outermost shell, the lithosphere, is broken into plates that move relative to each other above the convecting mantle; a theory known as Plate Tectonics. Convergent plate boundaries cause subduction of the lithosphere into the mantle and are often associated with the formation of impressive mountain ranges. Worldwide observations of high-pressure (>1.3 GPa for eclogite facies) and (ultra)high-pressure (>2.7 GPa), (U)HP, terranes (Guillot et al., 2009) at both ancient and recent convergent plate boundaries (Fig. 5.1a) indicate deep burial (>50 km) of upper crustal rocks within subduction zones and exhumation of (U)HP rocks during mountain building. Since the first observations of coesite, the ultrahigh-pressure polymorph of quartz, in continental upper crustal rocks from the Western Alps (Chopin, 1984) the essential question of how such crustal UHP rocks have been formed and exhumed is still unanswered.

Due to the long-term and large-scale nature of the subduction and exhumation processes, involving the coupling of heat transfer, metamorphic reactions and lithosphere deformation, the main method to study (U)HP terrane formation is using numerical simulations based on deterministic models, which employ fundamental laws of physics and constraints from laboratory experiments and geological observations. Until now, a plethora of deterministic models has been suggested to explain the formation and exhumation of (U)HP rocks. Most models explain (U)HP terrane formation exclusively by burial and associated increase of lithostatic pressure (Raimbourg et al., 2007). Fewer models propose an important contribution of tectonic pressure due to rock deformation (Mancktelow, 1995; Reuber et al., 2016). Proposed exhumation models for (U)HP rocks are even more variable (England and Holland, 1979; Beaumont et al., 2009; Warren et al., 2008; Warren, 2013; Burov et al., 2014; Butler et al., 2014) and involve either far-field plate convergence or divergence. During plate convergence, subducted material returns to the surface flowing either (i) along the subduction interface (Gerya et al., 2002; Li and Gerya, 2009) or (ii) vertically into the upper plate (Gerya and Stöckhert, 2006). Although synconvergent exhumation is a suitable process during subduction and mountain building, synconvergent exhumation models were criticized because they require (i) unrealistic erosion, (ii) often exhume large volumes of the entire crust and (iii) generate considerable tectonic mixing within exhumed units; all features not in agreement with first-order observations from, for example, the Western Alps (Escher and Beaumont, 1997; Malusà et al., 2015). An alternative mechanism for (U)HP rock exhumation is eduction associated with slab detachment (Andersen et al., 1991; Duretz et al., 2012) or upwelling due to significant upper-plate divergent motion (Liao et al., 2018). However, applied to the Western Alps these models are likely incompatible with the overall convergent motion of the Adriatic and European plates since ca. 80 Ma (Le Breton et al., 2020). A startling question is why there are currently several, significantly contrasting mechanisms proposed that all can apparently explain the formation and exhumation of the same (U)HP units? Reasons are most likely that (i) many models focus only on one aspect of the burial-exhumation cycle, e.g.

only the exhumation. Earlier processes relevant for the exhumation, for example the subduction initiation controlling the location, orientation, thermal structure and effective strength of the emerging subduction interface are not modelled. (ii) Many models are frequently tested only by a limited set of observables, e.g. only the estimated pressure–temperature paths. Prediction of additional observables, e.g. the required amount of erosion or the final crustal structure in which (U)HP rocks are presently observed, are commonly not tested. Ideally, a model for (U)HP formation and exhumation should predict as many as possible processes relevant to the entire burial-exhumation cycle and reproduce as many as possible first order observations.

We here present a two-dimensional petrological–thermomechanical deterministic model for the lithosphere–upper mantle system that meets these challenges. Our model predicts the continuous burial-exhumation cycle starting from spontaneous, i.e. without a priori prescription, subduction initiation to synconvergent exhumation in a single numerical simulation. A new mechanism which is local upper-plate extension taking place simultaneously with regional scale convergence enables synconvergent exhumation without unrealistic erosion. The local extension is triggered by buckling of subducted crustal units and causes synconvergent episodic buoyancy-induced flow along the subduction interface. Predicted peak metamorphic conditions, exhumation velocities of (U)HP units and orogen structure agree to first order with natural observations from the European Alps and the Himalayas (Fig. 5.1b,c,d).

5.1.1 The petrological–thermomechanical deterministic model

We here build upon previous numerical studies on subduction initiation (Kiss et al., 2020; Auzemery et al., 2020) and synconvergent (U)HP rock exhumation (Warren et al., 2008; Butler et al., 2014). Unlike these models, we do not design a specific initial passive margin geometry for the convergence model. Instead, we aim to prescribe as little as possible. Therefore, we start from the simplest possible initial configuration and model the formation of magma-poor continental margins bounding a marine basin (see sec. 5.3 and Fig. A.1,A.2). The generated margin–basin system is thermally equilibrated and serves as initial configuration for the convergence model. We then model subduction initiation and (U)HP rock exhumation within a single and continuous numerical simulation with the same underlying assumptions. The model is calibrated for long-term deformation of the lithosphere–upper mantle system (Candioti et al., 2020) and exhibits: (i) realistic Rayleigh and Nusselt numbers attesting realistic long-term coupling of heat transfer and deformation. (ii) Realistic depth variation of temperature, effective viscosity and density, calculated from thermodynamic pseudosection modelling ensure a realistic balance between buoyancy and shear stresses. Further, we do not employ ad hoc weakening parameterizations (e.g. frictional softening). Although weakening may occur in nature, subducting crustal units are likely also strengthened due to dehydration reactions and formation of high-grade mineral assemblages. In the context of subduction dynamics, these processes are incompletely understood and we, therefore, do not include any additional weakening parameterizations. Instead, the model relies on coupling of visco-elasto-plastic rock deformation, nonlinear rheological flow laws, heat transfer and metamorphic reaction-induced density changes.

Most exhumation models, synconvergent or divergent, employ a weak, often serpentinized plate interface along which the (U)HP units exhume. Recent seismic tomographic images from the Western Alps indicate that serpentinized plate interfaces may indeed form in nature (Zhao et al., 2020). Here, we parameterise a serpentinisation front propagating through the lithospheric mantle exhumed in the basin and perform sensitivity tests on the depth of mantle serpentinisation (see sec. 5.3, Fig. A.2b). Additionally, we test the impact of the applied far-field convergence velocity and the upper crustal flow law parameters on the burial exhumation cycle (see sec. 5.3). While all investigated parameter combinations result in subduction initiation, only certain parameter combinations allow for deep burial of continental crust and (U)HP rock exhumation (Fig. A.6,A.5). For other parameter combinations either underplating of subducted continental crust, or imbricated thrusting is observed. Here we report the convergence stage of a model predicting subduction initiation, deep burial of continental crust and synconvergent exhumation of coherent (U)HP units.

Fig.1: Petrological and geophysical context

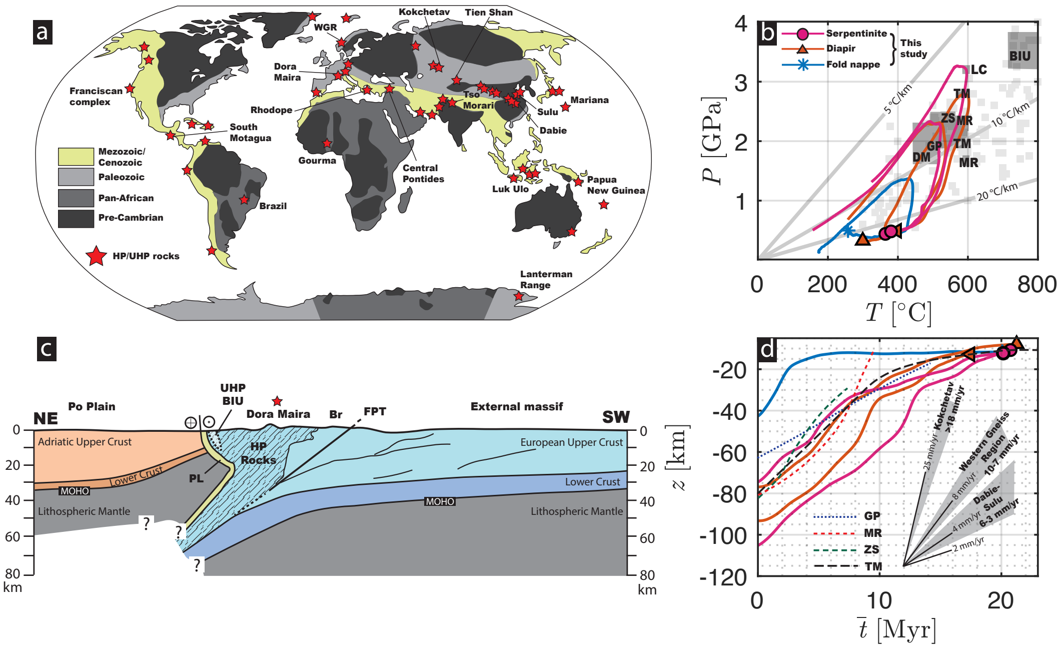

Figure 5.1: **a** Location of selected (U)HP terranes worldwide (Guillot et al., 2009). Colouring indicates an age estimate for the (U)HP terranes. **b** Comparison of peak pressure and temperature estimates from natural data to estimates predicted by this study. Light grey boxes indicate peak metamorphic conditions estimated for the Alps and continental Asia (Penniston-Dorland et al., 2015) and light grey lines are characteristic subduction zone thermal gradients. Abbreviations: ZS = Zermatt–Saas (Angiboust et al., 2009), LC = Lago di Cignana (Groppo et al., 2009), GP = Gran Paradiso (Manzotti et al., 2018), TM = Tso Morari (de Sigoyer et al., 2000; Pan et al., 2020), DM = Dora–Maira (Groppo et al., 2019), MR = Monte Rosa (Luisier et al., 2019; Vaughan-Hammon et al., 2021), BIU = Brossasco-Isasca Unit (Rubatto and Hermann, 2001), TS = Tien Shan (Tan et al., 2019). **c** Modified interpretation of seismic tomography (Zhao et al., 2015b; Schmid et al., 2017). Abbreviations: BIU = Brossasco-Isasca Unit, Br = Briançonnais domain, FPT = Frontal penninic thrust, PL = Piemonte–Liguria domain. **d** Comparison of petrologically determined exhumation velocities to estimates predicted by this study. Abbreviations: MR = Monte Rosa, ZS = Zermatt–Saas (de Meyer et al., 2014), TM = Tso Morari (de Sigoyer et al., 2000). Estimates of exhumation velocities from the Kokchetav, Western Gneiss Region and Dabie–Sulu are taken from Hermann et al. (2014). Peak metamorphic conditions and exhumation velocities predicted by our model agree with natural data from the European Western Alps, the Tso Morari and the Tien Shan.

5.1.2 From subduction initiation to (U)HP rock exhumation

Shear zones form in the upper crust shortly after the onset of convergence (110 Myr, Fig. 5.2d). The strongest part of the plate, the mantle lithosphere, remains relatively undeformed.

Fig.2: Thermal weakening induced subduction initiation

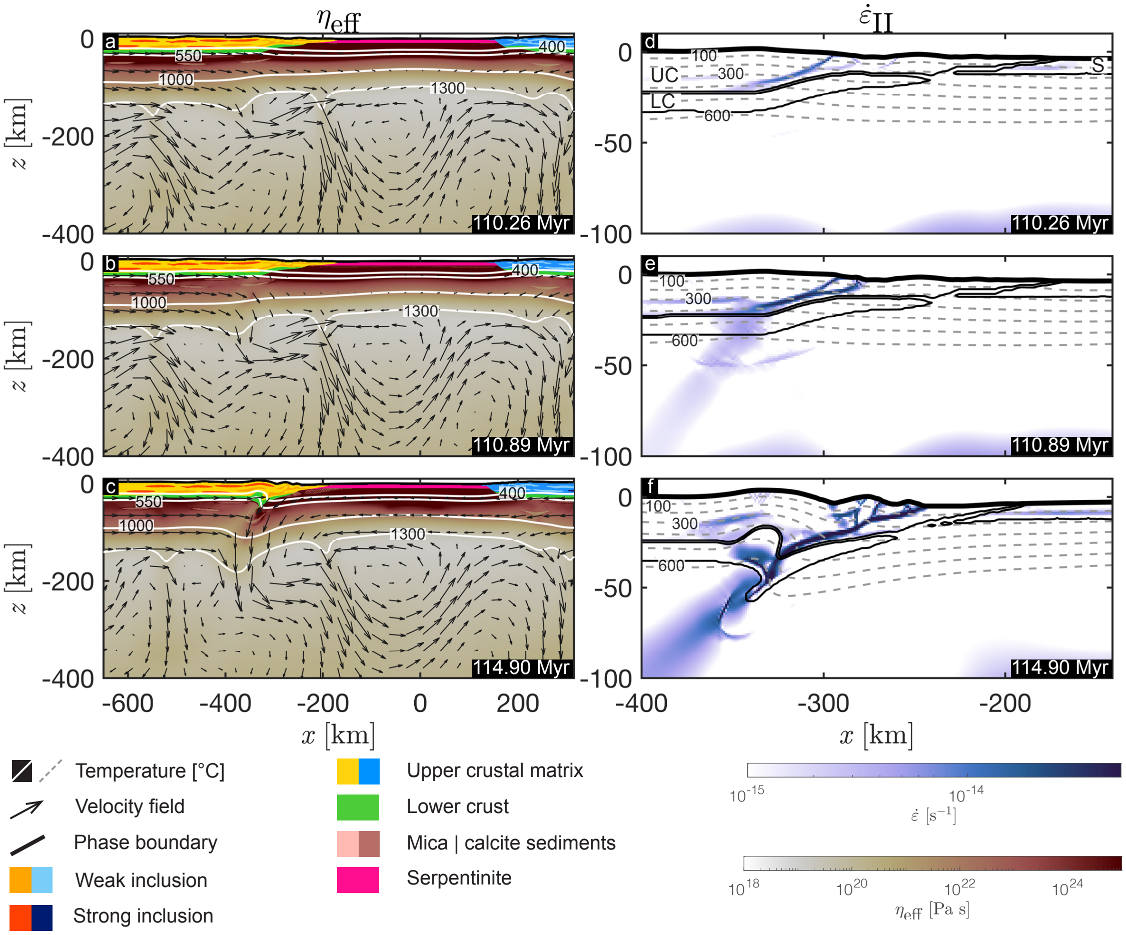

Figure 5.2: Stages of subduction initiation. Left column: effective viscosity calculated by the numerical algorithm and material phases colouring as indicated in the legend. White lines are several isotherms and glyphs indicate the velocity field calculated by the numerical algorithm. Right column: second invariant of deviatoric strain rate tensor components. Solid black lines are material phase boundaries and grey dashed lines are several isotherms. Abbreviations: UC = upper crust, LC = lower crust and S = serpentinites. Onset of compression leads to shear zone formation in the upper crust (**a** & **d**). The serpentinites, the lower crust and the lithospheric mantle remain undeformed. **d** & **e** Spontaneous formation of a broad shear zone across the mantle lithosphere and lower crust. This stage marks the subduction initiation (**e**). **c** & **f** Evolution of an embryonic subduction zone. The evolving slab penetrates into the upper mantle (see vertical glyphs below the left continental margin in **c**) and the two localised shear zones in the lithospheric mantle and the upper crust are now connected (**f**). Note that the serpentinites remain relatively undeformed indicating that they are not involved in the process of subduction initiation.

Stress built-up below one of the passive margins (Fig. A.3b,c) leads to spontaneous formation of a localised shear zone transecting the lithosphere (Fig. 5.2e). The spontaneous shear zone formation agrees with recent models of horizontally-forced (Crameri et al., 2020) and thermal softening–induced subduction initation at passive margins (Kiss et al., 2020; Auzemery et al., 2020). The serpentinite layer remains undeformed until an embryonic subduction zone has evolved (see Fig. 5.2e,f and Fig. A.3h-j). The serpentinite layer does, hence, not play a significant role for subduction initiation. Although the importance of serpentinites for mature subduction zones is well known (Hess, 1955; Raleigh and Paterson, 1965; Hacker et al., 2003), the actual mechanical strength of serpentinite is rather unknown (Idrissi et al., 2020; Hirauchi et al., 2020). In our model, the serpentinites control the effective strength of the emerging subduction interface. Sheared off the subducting plate, the serpentinites re-organise along the subduction interface and prove crucial for deep rock cycling (Fig. A.2c,d).

Figure 5.3 shows the model evolution from basin closure onward. While the serpentinized subduction interface is highly deformed, the subducting upper continental crust remains relatively undeformed (Fig. 5.3c). A shear zone forms spontaneously within the upper crust (light red narrow zone in Fig. 5.3c). The European lower crust escapes exhumation which is consistent with geophysical observations from the Western Alps (Fig. 5.1c, Schmid et al., 2017; Zhao et al., 2015a). Only minor volumes of deeply buried upper crustal units exhume individually along the subduction interface without significant internal deformation (see Fig. 5.3d,e,f).

5.1.3 Local upper-plate extension during regional plate convergence

During continental subduction, significant differential stresses build up within a thin upper crustal layer (Fig. 5.4f) which is mechanically stronger than the surrounding material. Compression of this rift-inherited mechanical heterogeneity induces a buckling instability (Fig. 5.4g) which is identified by the marker regions defined in Fig. 5.4g,h: while the top marker chain of the blue rectangle is extended, the bottom marker chain is shortened. This unit penetrates into the upper plate; compared to the average upper plate's horizontal velocity, a ca. 50 km wide upper crustal block moves ca. 1 $\mathrm{cm\,yr^{-1}}$ faster (Fig. 5.4c). This local extension induces necking of the upper crust (Fig. 5.4d) separating the 50 km wide block

Fig.3: Model Evolution

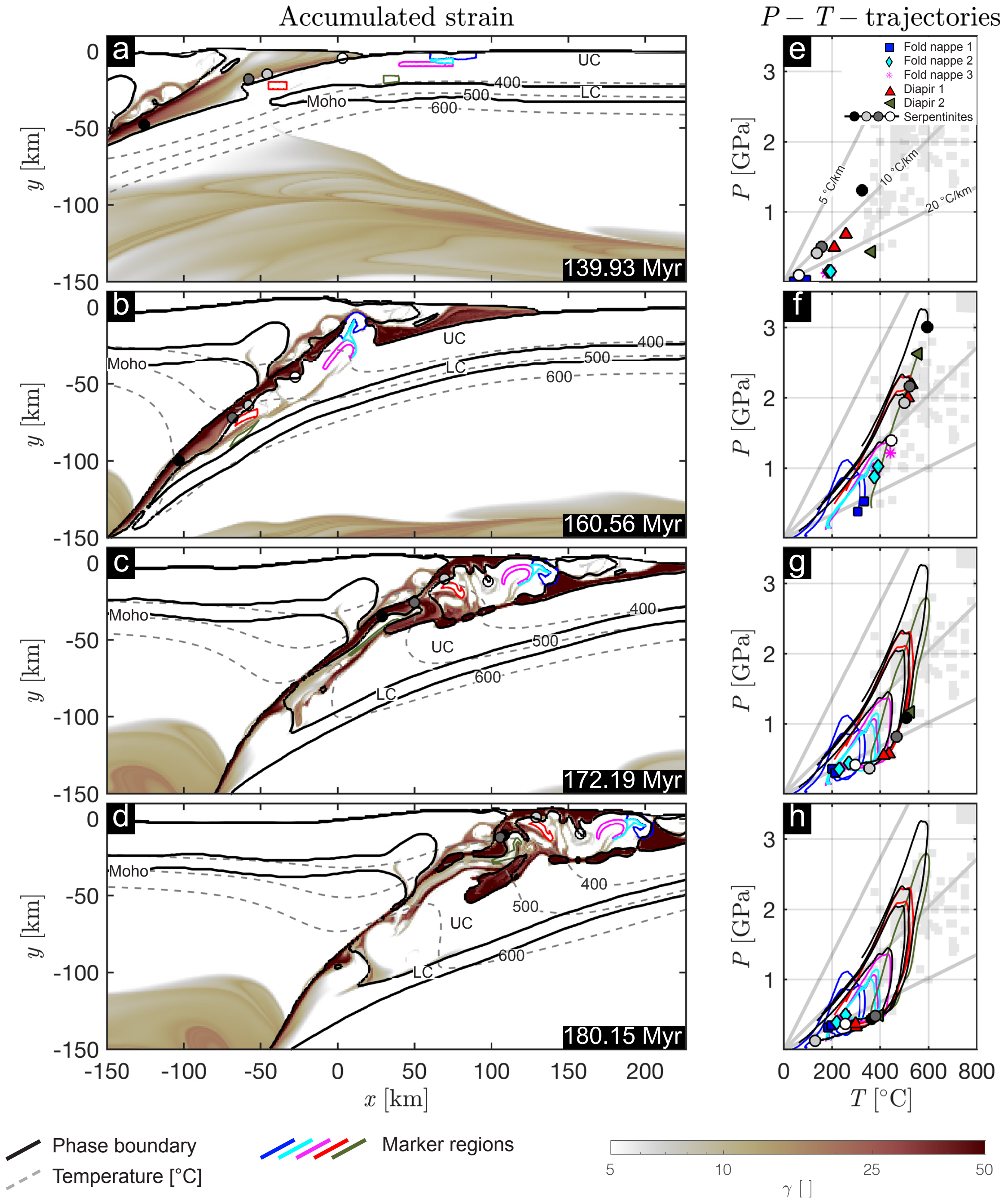

from the upper plate. Both mechanical instabilities are highly nonlinear, driven by differential, or deviatoric, stresses and rely on strength contrasts between the deforming unit and its surrounding matrix (Schmalholz and Mancktelow, 2016). The model captures these in-

Figure 5.3: White to red colour in **a-f** is the accumulated strain field calculated by the numerical algorithm, black lines are the upper crustal phase boundary and the Moho, coloured polygons are regions of selected markers, grey dashed lines are several isotherms. Symbols as explained in panel **g** are valid for all panels. Light grey boxes indicate peak metamorphic conditions estimated for the Alps (Penniston-Dorland et al., 2015) and light grey lines are characteristic subduction zone thermal gradients. **a** The polygons represent upper crustal regions of the lower plate and circles represent selected serpentinite markers. **b-f** Buckling induces synconvergent extension in the upper plate and enables buoyant uplift of deeply subducted ($>$ 100 km) serpentinites and more distal upper crustal units. Note that the deeply subducted crustal units exhume without significant internal deformation whereas serpentinites are highly deformed. **g-l** Recorded pressure–temperature trajectories indicate a large variety of peak metamorphic conditions depending on the paleogeographic location of the marker.

stabilities mainly for two reasons: (i) the initial configuration from the onset of convergence considers rift-inherited mechanical heterogeneities and (ii) strong units are preserved because no additional weakening is applied. Furthermore, stress built-up due to mechanical heterogeneities reaches differential stress magnitudes of up to ca. 500-600 MPa (Fig. 5.4e). This means that deviations from lithostatic pressure can be as high as 250-300 MPa. Our model therefore confirms magnitudes of so-called overpressure which have been proposed to explain variations in estimates of peak metamorphic conditions within coherent (U)HP terranes, such as for example the Monte Rosa unit in the Western Alps (Luisier et al., 2019).

5.1.4 Episodic and diapiric exhumation along the subduction interface

Deeply subducted units exhume episodically along the subduction interface (Fig. 5.5a) and vertical velocity magnitudes do not exceed 1.5 $\mathrm{cm\,yr^{-1}}$ and are discontinuous in space and time (Fig. 5.5b,c,d and Fig. A.4b). These discontinuous and episodic pulses indicate that buoyancy contrasts rather than pressure gradients drive exhumation along the subduction interface. The (U)HP units exhume as individual diapirs (Raimbourg et al., 2007) and do not flow like water running through a pipe (Poisseuille flow). The individual deeply buried continental crustal units exhume coherently (see Fig. 5.3 and evolution of red marker region in Fig. 5.5) without forming tectonic mélanges (Beaumont et al., 2009). This is important because it explains structural observations of coherent (U)HP basement nappes in the European Alps (Beaumont et al., 1996).

Fig.4: Synconvergent upper plate extension triggering (U)HP rock exhumation

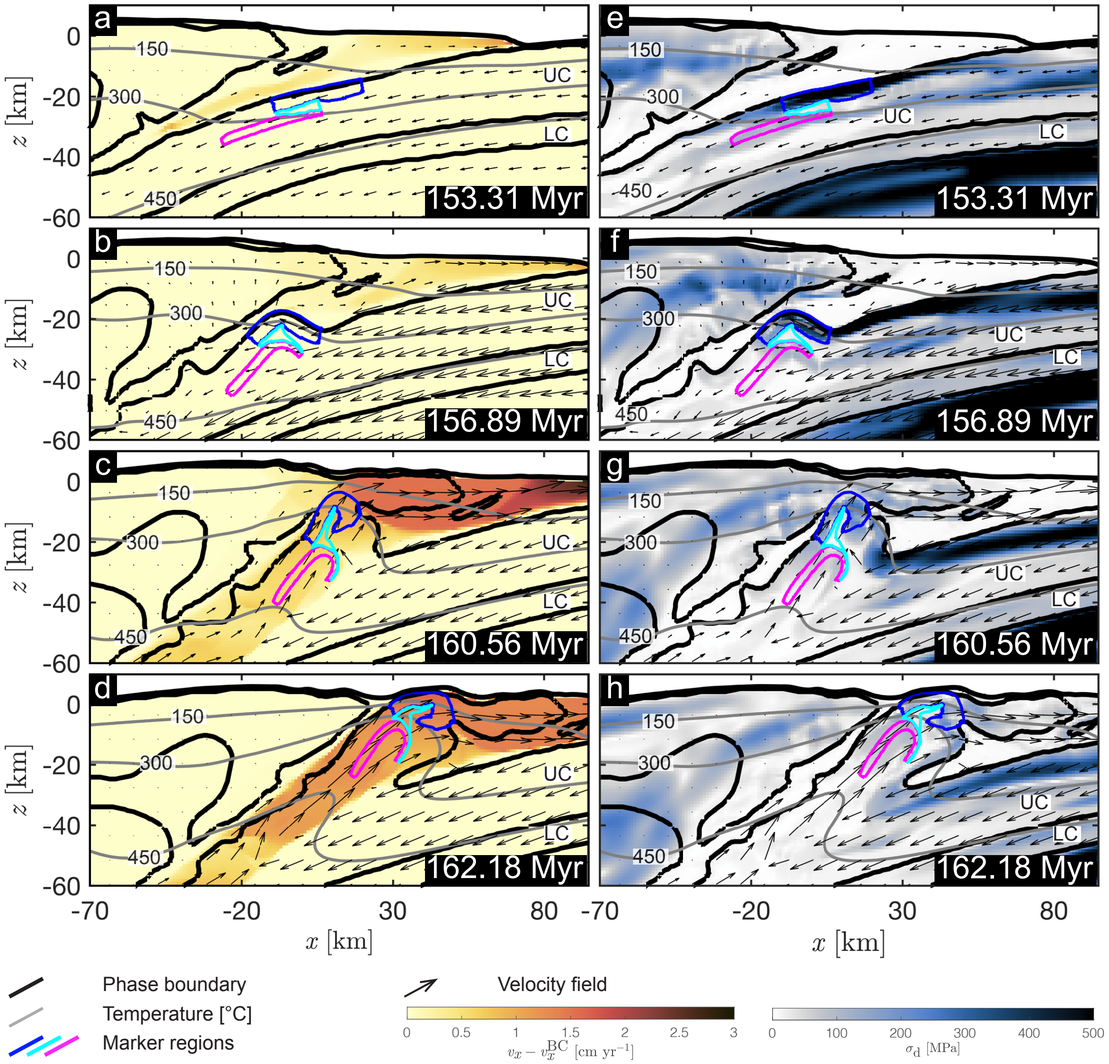

Figure 5.4: Left column: Deviation of horizontal velocity field from the applied horizontal boundary velocity. Right column: Differential stress calculated by the numerical algorithm. Black solid lines are crustal phase boundaries; grey solid lines are isotherms and polygons are regions of selected markers. Glyphs show the absolute velocity field calculated by the algorithm relative to the boundary velocity. (**e** & **f**) Stress build-up in the subducting upper crust induces a buckling instability. (**c&d**) Exhumation of this unit triggers necking in the upper plate. A ca. 50 km wide upper crustal block of the overriding plate is separated and overrides the subducting plate (**d**). Exhumation along the channel is not active from the beginning, but is caused by local upper plate extension (compare **b** to **d**).

Fig.5: Episodic exhumation along the subduction interface

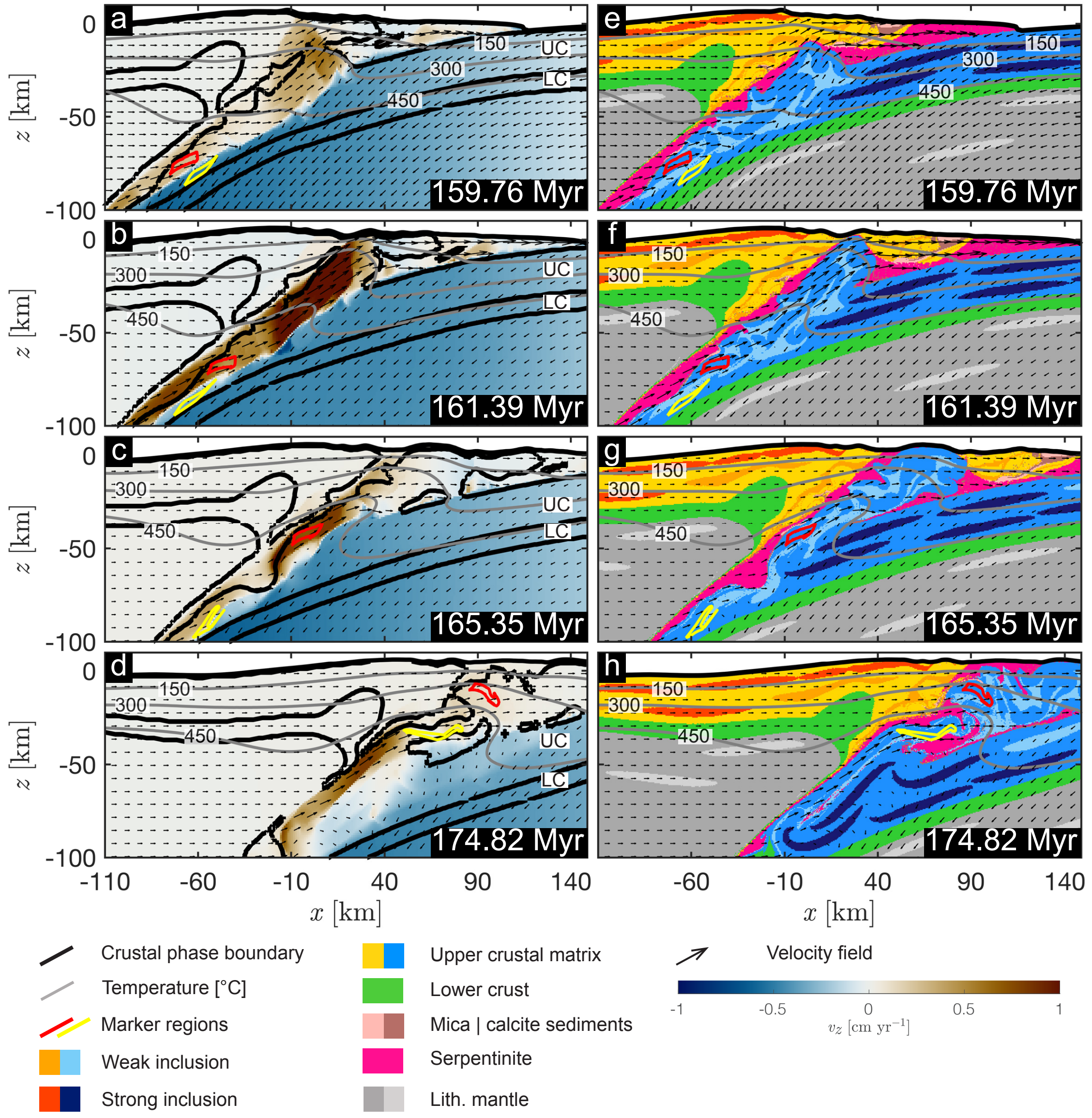

Figure 5.5: Left Column: Vertical velocity field calculated by the numerical algorithm. Right Column: material phases during model evolution. Colouring as indicated in the legend. Black solid lines are phase boundaries, grey solid lines are isotherms, yellow and red polygons mark individual units and glyphs indicate the velocity field calculated by the numerical algorithm. **a-d** Material transport along the channel is not continuous from large depths to the surface. Material is exhumed in form of individual units characterised by locally increased upward directed vertical velocities (see panel **c**). Deeply subducted units are not exhumed vertically as trans-mantle diapirs penetrating the upper plate (**e-h**). Instead, exhumation occurs along the subduction interface.

5.1.5 Application to the Western Alps and other orogens

Presumably, the far-field convergence of the Adriatic and European plates (McCarthy et al., 2020; Le Breton et al., 2020) induced subduction initiation at the magma-poor rifted Adriatic margin (Manzotti et al., 2014), closure of the Piemonte–Liguria oceanic domain, deep subduction of continental units from the European plate and exhumation of (U)HP rocks. Extensive research during the past decades unravelled various mechanisms explaining these processes during overall plate convergence as assumed for the Alpine orogeny (Yamato et al., 2008; Butler et al., 2014). Unlike most of these studies, our model predicts the correct location and polarity of subduction as suggested for the Alpine orogeny. Also, the serpentinized plate interface is not prescribed in the initial model configuration, but evolves model-internally consistent during the simulation. Therefore, our model confirms existing hypothesis for subduction zone evolution during the Alpine orogeny and potential geophysical evidence (Zhao et al., 2020) for a serpentinized interface between the European and Adriatic plate.

In our model, peak metamorphic conditions recorded by the exhumed units vary greatly depending on the paleogeographic location. Units located towards the continent show peak conditions of ca. 0.9-1.4 GPa and 370-420 °C and exhume during a first event (Fig. 5.3l). Located at the paleogeographic ocean–continent transition, the deeper buried units exhume during the second event reaching HP to (U)HP metamorphic conditions of ca. 2.3-2.8 GPa and 550-600 °C. Peak metamorphic conditions recorded within natural (U)HP terranes may also vary greatly (Fig. 5.1b). A popular example of local variations in peak metamorphic conditions within a single (U)HP terrane is the Dora–Maira (DM) massif located in the Western Alps. While peak metamorphic conditions of major (U)HP rock volumes indicate pressure and temperature magnitudes of ca. 2.2 GPa and ca. 500 °C, it includes a thin unit, the Brossasco–Isasca unit (BIU), recording pressure and temperature magnitudes of up to 3.5 GPa and ca. 750 °C. It is assumed that the BIU was exhumed rapidly (Rubatto and Hermann, 2001) close to the surface (Fig. 5.1d). Our model neither predicts these peak metamorphic conditions for any continental crustal unit, nor the suggested rapid exhumation rates. A possible explanation is that the model resolution is not high enough to capture deep burial and rapid exhumation of such small units. However, the predicted peak metamorphic conditions and the exhumation rates agree well with petrological estimates for major representative volumes of natural (U)HP terranes including the DM (Fig. 5.1b,d). Furthermore, predicted peak metamorphic conditions for the oceanic units in our model agree well with both major volumes of the HP Zermatt-Sass unit and the UHP Lago di Cignana unit (Fig. 5.1b). Another example of extremely varying estimates for peak metamorphic conditions is the Tso Morari in the Himalayas (Pan et al., 2020). Our predicted peak metamorphic conditions agree well with maximum pressure estimates for the Tso Morari between 2.2 and 2.7 GPa which is the lower range of end-member estimates (Fig. 5.1b). Further, the exhumation velocities also agree well (Fig. 5.1d) with estimates from de Sigoyer et al. (2000) for this unit. We also fit estimated peak metamorphic conditions of (U)HP terranes in the Tien Shan. Our predicted peak metamorphic conditions of exhumed (U)HP units agree well with estimates from several oceanic and continental (U)HP terranes worldwide. This observation provides confidence that our model is transferable and generally applicable to the formation and exhumation of natural (U)HP terranes.

Previous models of synconvergent (U)HP exhumation relied on additional mechanisms, such as for example excessive erosion (Butler et al., 2014). Application of these models to the Western Alps was criticised, because they predict high sediment volumes deposited in the basins which is inconsistent with the sedimentary record in the Alps (Malusà et al., 2015). Our model builds upon previous synconvergent exhumation models. For example, Warren et al. (2008) also observed local upper plate extension. However, in their model local upper plate extension was the triggered by buoyant uplift of (U)HP units and, therefore, a consequence of (U)HP rock exhumation rather than the cause of it. In our model, local upper plate extension is triggered by a tectonic-driven buckling instability and causes buoyant uplift of (U)HP units. Thus, our model presents a new mechanism triggering (U)HP rock exhumation, namely synconvergent tectonic-driven local upper plate extension. This mechanism does not rely on excessive erosion (Butler et al., 2014) or far-field divergent plate motion (Liao et al., 2018) to enable (U)HP rock exhumation.

5.2 Concluding remarks

Our model is based on the fundamental laws of physics and predicts two crucial stages of the geodynamic history of (U)HP terranes, namely (i) subduction initiation and (ii) synconvergent and coherent (U)HP rock exhumation in a single numerical simulation. While serpentinites do not impact on subduction initiation, they prove crucial for weakening the subduction interface and enable deep rock cycling. We identified a new tectonic-driven mechanism for synconvergent (U)HP rock exhumation without requiring excessive erosion or divergent plate motion. The exhuming units remain without significant internal deformation, consistent with structural observations from several (U)HP terranes worldwide. Further, peak metamorphic conditions predicted by the model agree well with petrological data from the Western Alps and the Tso Morari in the Himalayas. Reproducing several first-order observations and natural data and predicting two crucial stages in the burial-exhumation cycle of the crust provides confidence that the model is robust, transferable and applicable to (U)HP terrane formation within natural mountain ranges.

5.3 Methods

We present state-of-the-art two-dimensional high-resolution petrological–thermo-mechanical upper mantle-scale models of subduction initiation and (U)HP rock exhumation embedded in long-term (≈180 Myr) geodynamic extension–cooling–convergence cycles. Given the extensive physical time modelled and the high resolution required to resolve structural and thermal inheritances from all deformation periods, the applied software must efficiently leverage modern computational hardware. The applied numerical algorithm meets these challenges. The continuity, momentum and energy equations describing the motion of slow flowing fluids under gravity and boundary tractions are solved on a staggered finite difference Eulerian grid. A Marker-in-Cell method (Gerya and Yuen, 2003) is employed to transport physical properties through the grid. In total, the algorithm solves for 4.35 Million degrees of freedom and up to 56 Million Lagrangian markers are used for transport of physical properties at each time step. Computational efficiency is ensured by shared-memory parallelization. The mechanical solver is coupled to the Gibbs free energy minimization tool Perple_X (Connolly, 2009) via density. Based on equilibrium phase diagram calculations (see Table 5.2), density (Fig. A.7) is read in during the simulation according to pressure and temperature conditions locally at each finite difference grid cell. We employ the extended Boussinesq approximation, i.e. we include density changes only in the momentum equation. Otherwise, we consider incompressibility of materials and include adiabatic heating in the heat transfer equation. The latter is important to stabilise the thermal field and keep a constant adiabatic gradient in the mantle (Candioti et al., 2020). We consider visco-elasto-plastic deformation of material and employ experimentally determined non-linear rheological flow laws. The initial temperature, viscosity and density structure of the model is calibrated to natural data.

5.3.1 Model design

Model dimensions are 1600×680 km and we employ a global resolution of 1×1 km. Modelled units include a 25 km thick mechanically heterogeneous upper crust and an 8 km thick homogeneous lower crust (Fig. A.1b). The lithospheric mantle extends down to 120 km depth and we include the upper mantle down to a depth of 660 km. We apply tectonic forces by prescribing the material inflow/outflow velocities at the lateral boundaries (Fig. A.1a,d). The initial model configuration and the applied boundary velocities are motivated by geodynamic reconstructions from the Alpine orogeny. Presumably, the closure of the mainly embryonic Piemonte–Liguria ocean and collision of the magma-poor Adriatic and European margins lead to the formation of the Alpine mountain range (McCarthy et al., 2020; Le Breton et al., 2020). We therefore neglect partial melting in our models. The modelled cycle consists of 3 stages: First, we model the formation of magma-poor hyperextended margins and opening of a marine basin (ca. 400 km wide) floored by exhumed mantle during a rifting period (50 Myr, 1 $\mathrm{cm\,yr^{-1}}$ absolute extension velocity see Fig. A.2a). Second, a 60 Myr long period without active tectonic forcing (0 $\mathrm{cm\,yr^{-1}}$ absolute deformation velocity) is modelled. During these stages, crustal density is calculated via a linearized equation of state (Eq. 2.3). Mantle densities are always precomputed and based on phase equilibria calculations. Only for the last stage, the effective density for all materials is calculated based on phase equilibria models. This assumption is justified, because large density changes within the crust due to prograde metamorphic reactions are not expected to occur during rifting and cooling. At this stage, upper mantle convection establishes and stabilises the thermal structure of the evolved system self-consistently. At the end of this period, we parametrize a serpentinization front by replacing the rheological parameters of mantle material exhumed in the basin with parameters of antigorite material (see Fig. A.2b). The evolved and equilibrated system is shortened for 70 Myr until the end of the simulation. Including the upper mantle and modelling deformation stages prior to convergence is important, because mantle convection and rift-inherited structures likely impact on subduction initiation (Baes et al., 2018; Candioti et al., 2020) and on the dynamics of (U)HP rock exhumation during mountain building.

In total, we conducted 18 numerical simulations varying the depth of serpentinisation (3, 5, 6 km), the upper crustal flow law parameters (quartz- and feldspar-dominated rheology, see Table 5.1) and the absolute convergence velocities (1.5, 1 and 0.5 $\mathrm{cm\,yr^{-1}}$). The depth of serpentinisation, the rheological flow law employed for the upper crust and the convergence velocities applied are proxies for the degree of serpentinisation, the strength of the upper continental crust and advection or diffusion dominated subduction and exhumation dynamics, respectively. For the main model presented here we employed: a westerly granite upper crustal rheology (see Table 5.1), a 6 km thick serpentinite layer and 1 $\mathrm{cm\,yr^{-1}}$ convergence rate after basin closure. A detailed description of the numerical algorithm is given in *chapter* 2.

5.4 Appendix

5.4.1 Extended data figures and tables

Fig.A1: Initial configuration

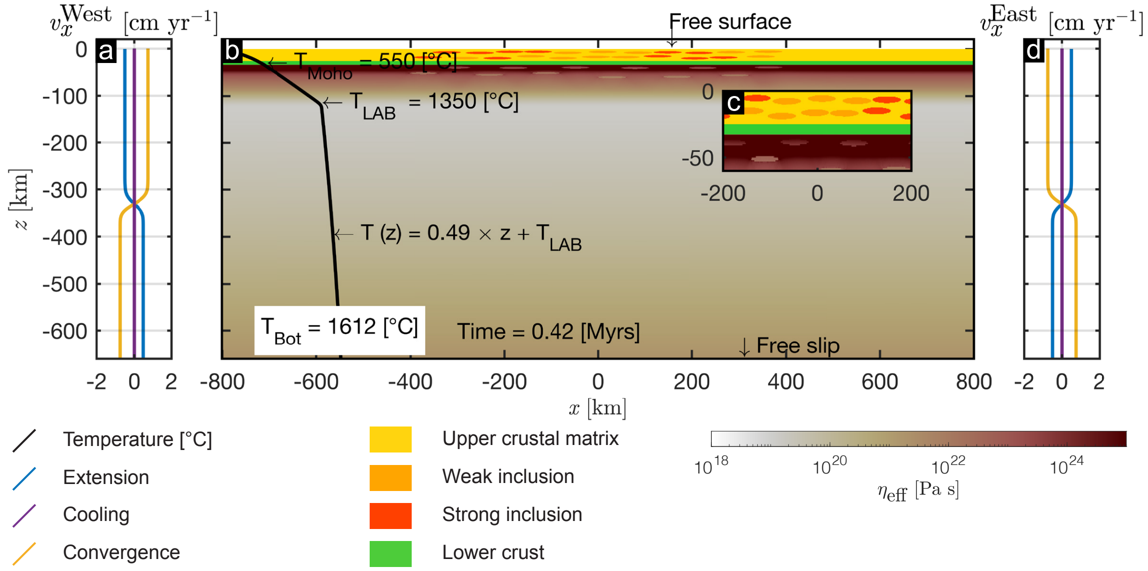

Figure A.1: **a** & **d** Material inflow/outflow velocities defined at the western and eastern boundary for extension (blue), cooling (purple) and convergence (yellow). Extension velocity is applied for 50 Myr, no deformation is applied for 60 Myr and convergence is applied until the end of the simulation. **b** Entire model domain, initial thermal profile and mechanical boundary conditions at the top and bottom boundary. White to red colour is the viscosity field in the mantle calculated by the numerical algorithm and yellow to orange and green colours are the upper and lower crust, respectively. **c** Enlargement showing the weak inclusions emplaced to localise deformation in the domain centre.

Fig.A2: Evolution of the extension–cooling–convergence cycle

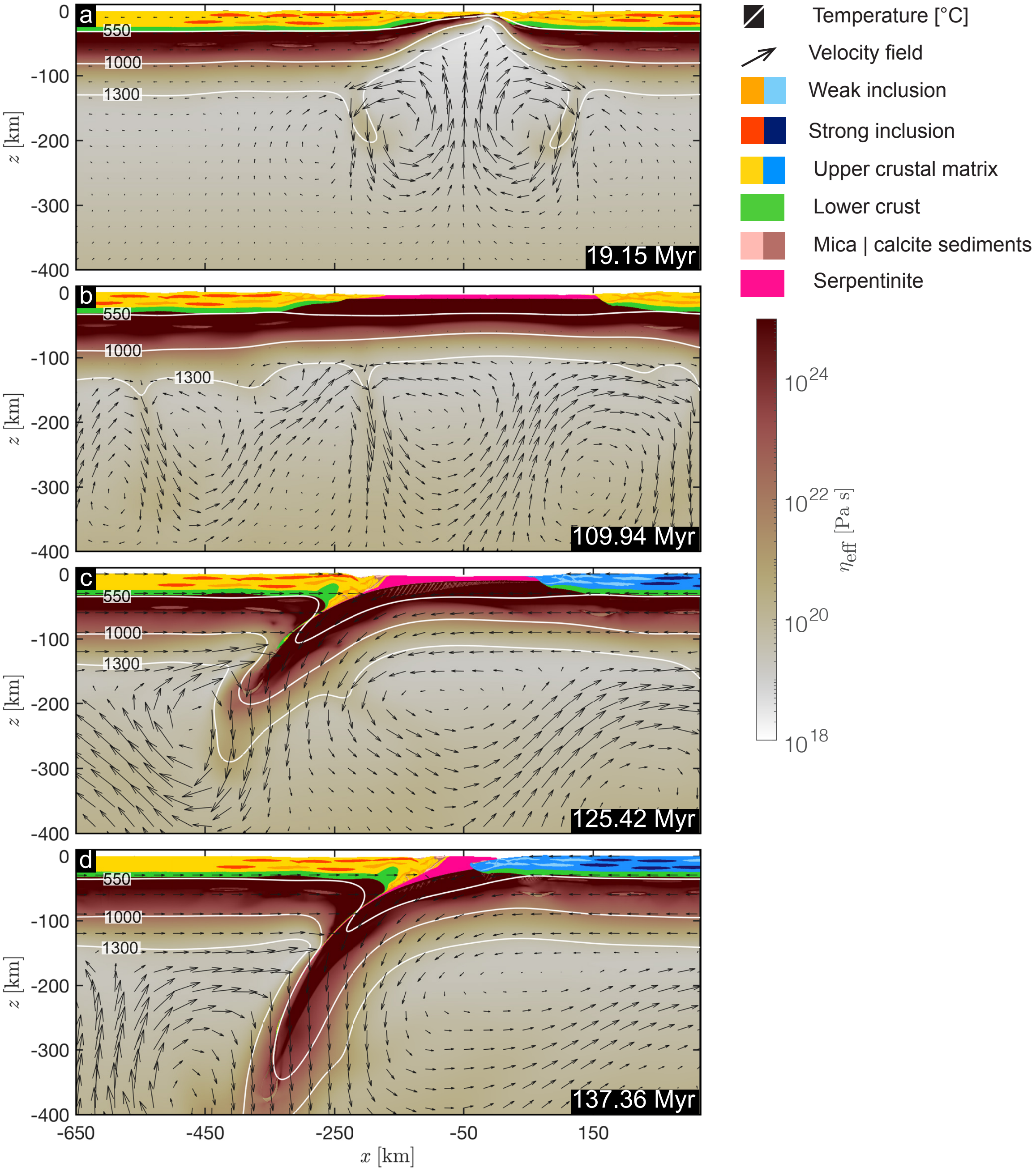

Figure A.2: White to red is the effective viscosity field and glyphs indicate the velocity field calculated by the numerical algorithm, yellow to orange and light to dark blue is the upper crust, magenta is the serpentinized mantle material and green is the lower crust. Not that the colouring of the upper crust changes from the convergence stage onward to distinguish between the upper and the subducting plate. The employed material parameters remain unchanged. White solid lines are several isotherms. For the convergence stage of this simulation we employed: a westerly granite upper crustal rheology (see Table 5.1), a 6 km thick serpentinite layer and 1 $\mathrm{cm\,yr^{-1}}$ convergence rate after basin closure. **a** Continental rifting leads crustal break-up and the formation of two asymmetric passive margins. Compared to the eastern margin, the western margin is characterized by a wider region of hyperthinned continental crust. In the upper mantle, convection cells begin to form in the horizontal centre of the domain transporting hot mantle material towards the rift centre. The 1300 °C isotherm remains at a depth of ca. 25 km typical of magma-poor rifted margin formation. **b** At the end of the extension and cooling period, convection in the upper mantle has stabilised the mechanical thickness of the lithosphere to ca. 120-130 km (region without glyphs). At this stage the rheological material parameters of the dry olivine flow law in the top 6 km of exhumed mantle are replaced by material parameters of an antigorite flow law (see Table 5.1) parameterizing a serpentinisation front. This layer is initially horizontal and not inclined. **c** Onset of convergence. Subduction is initiated and the serpentinite material is sheared off the subducting slab and reorganises along the subduction interface (**d**). The formation of the serpentinized plate interface is not prescribed a priori but is predicted model-internally consistent.

Fig.A3: Subduction initiation at a passive continental margin

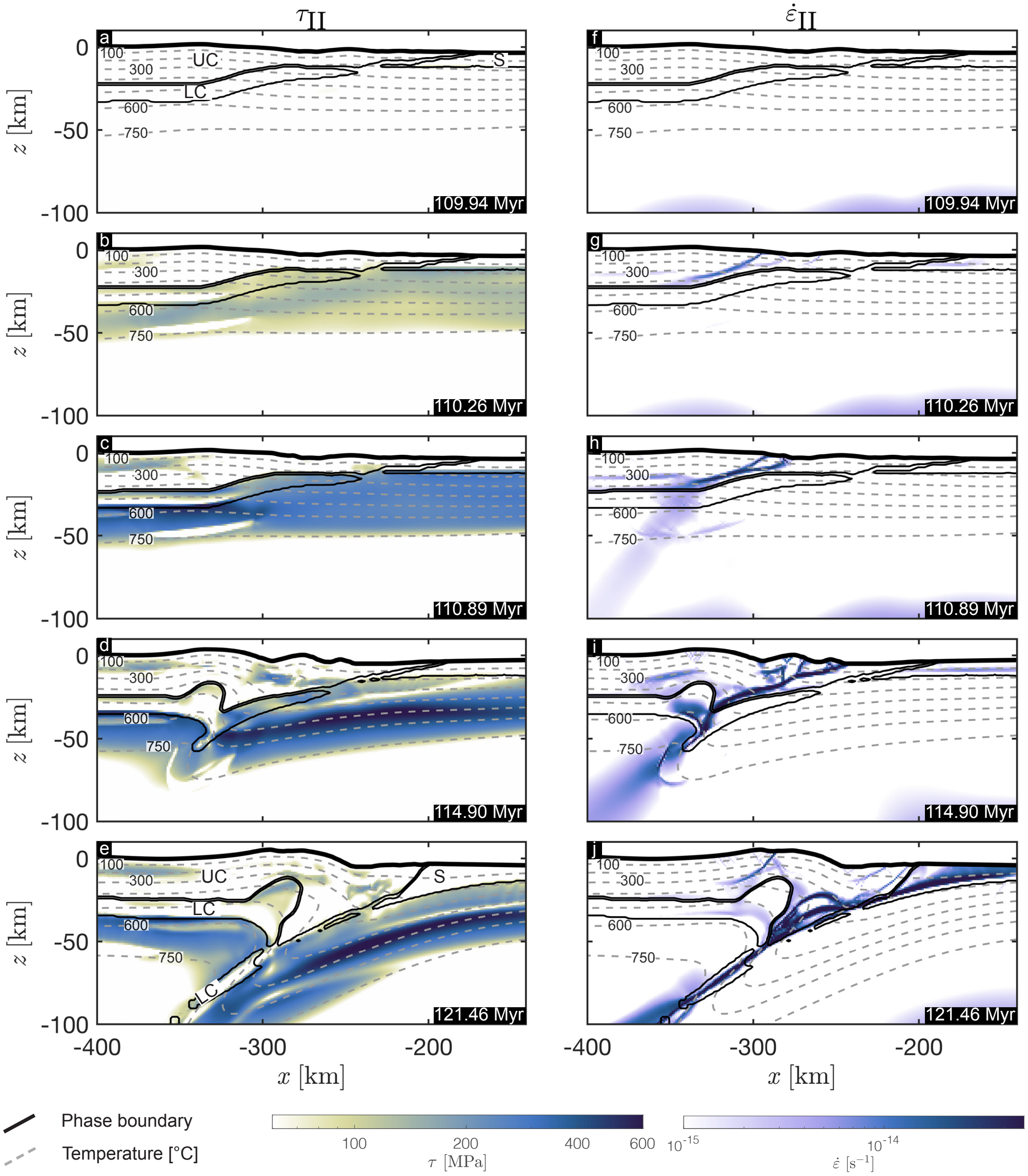

Figure A.3: Left column: second invariant of deviatoric stress tensor components. Right column: second invariant of deviatoric strain rate tensor components. Colouring as indicated in the legend. Solid black lines are material phase boundaries and dashed grey lines are several isotherms. Abbreviations: UC = upper crust, LC = lower crust and S = serpentinite. **a** & **f** Before the onset of convergence deviatoric stresses are close to zero everywhere in the domain indicating the long-term stability of the passive continental margins in this model. Elevated magnitudes of strain rate in the upper mantle indicates convection. **b** & **g** The onset of convergence leads to stress built-up in the mantle lithosphere. Within the continental upper crust, a shear zone forms which does not penetrate into the relatively stronger lower crust and lithospheric mantle. **c** & **h** In the lithospheric mantle and at the transition from the proximal margin to the necking domain, stresses localise (dark blue region a x≈-320 km) leading to the formation of a large scale shear zone transecting the mantle lithosphere. **d** & **i** The upper crustal and lithospheric mantle shear zones are connected and break through the lower crust and the entire lithosphere marking successful subduction initiation. Stresses in the serpentinite are close to zero and the serpentinite is relatively undeformed indicating that it is not involved in subduction initiation. Stresses along the trans-lithospheric shear zone begin to relax. **e** & **j** The upper crustal shear zone migrates towards the serpentinite–mantle phase boundary. Serpentinites are sheared off the subducting plate forming an accretionary serpentinite prism. Stresses along the subduction interface are relaxed and a lower crustal block is subducted.

Table 5.1: Physical parameters used in the numerical simulations.

Model unit	Rheology (Reference)		k [W m^{-1} K^{-1}]	H_R [W m^{-3}]	C [Pa]	φ [°]
Crustal matrix 1^{*,a}	Wet Anorthite (Rybacki and Dresen, 2004)		2.25	1.0200×10^{-6}	1×10^{7}	30
Crustal matrix 2^{*,a}	Westerly Granite (Hansen et al., 1983)		2.25	1.0200×10^{-6}	1×10^{7}	30
Weak inclusion^{*,a}	Wet Quartzite (Ranalli, 1995)		2.25	1.0200×10^{-6}	1×10^{6}	5
Strong inclusion^{*,a}	Maryland Diabase (Mackwell et al., 1998)		2.25	1.0200×10^{-6}	1×10^{7}	30
Calcite^{*,a}	Calcite (Schmid et al., 1977)		2.37	0.5600×10^{-6}	1×10^{7}	30
Mica^{*,a}	Mica (Kronenberg et al., 1990)		2.55	2.9000×10^{-6}	1×10^{7}	15
Lower crust^{*,b}	Wet Anorthite (Rybacki and Dresen, 2004)		2.25	0.2600×10^{-6}	1×10^{7}	30
Strong mantle^{*,c}	Dry Olivine (Hirth and Kohlstedf, 2003)		2.75	2.1139×10^{-8}	1×10^{7}	30
Weak mantle^{*,c}	Wet Olivine (Hirth and Kohlstedf, 2003)		2.75	2.1139×10^{-8}	1×10^{7}	30
Serpentinite^{*,d}	Antigorite (Hilairet et al., 2007)		2.75	2.1139×10^{-8}	1×10^{7}	25
Dislocation creep	A [Pa^{-n-r} s^{-1}]	ζ [ ]	n [ ]	Q [J mol^{-1}]	V [m^{3} mol^{-1}]	r [ ]
Crustal matrix 1	3.9811×10^{-16}	1.0	3.0	356×10^{3}	0.00×10^{-6}	0.0
Crustal matrix 2	3.1623×10^{-26}	1.0	3.3	186.5×10^{3}	0.00×10^{-6}	0.0
Weak inclusion	5.0717×10^{-18}	1.0	2.3	154×10^{3}	0.00×10^{-6}	0.0
Strong inclusion	5.0477×10^{-28}	1.0	4.7	485×10^{3}	0.00×10^{-6}	0.0
Calcite	1.5849×10^{-25}	1.0	4.7	297×10^{3}	0.00×10^{-6}	0.0
Mica	1.0000×10^{-138}	1.0	18.0	51.0×10^{3}	0.00×10^{-6}	0.0
Lower crust	3.9811×10^{-16}	1.0	3.0	356×10^{3}	0.00×10^{-6}	0.0
Strong mantle	1.1000×10^{-16}	1.0	3.5	530×10^{3}	14.0×10^{-6}	0.0
Weak mantle†	5.6786×10^{-27}	1.0	3.5	480×10^{3}	11.0×10^{-6}	1.2
Serpentinite	4.4738×10^{-38}	1.0	3.8	8.90×10^{3}	3.20×10^{-6}	0.0
Diffusion creep‡	A [Pa^{-n-r} m^{m} s^{-1}]	m [ ]	n [ ]	Q [J mol^{-1}]	V [m^{3} mol^{-1}]	r [ ]
Strong mantle	1.5000×10^{-15}	3.0	1.0	370×10^{3}	7.5×10^{-6}	0.0
Weak mantle†	2.5000×10^{-23}	3.0	1.0	375×10^{3}	9.0×10^{-6}	1.0
Peierls creep	A_P [s^{-1}]	Q [J mol^{-1}]	V [m^{3} mol^{-1}]	σ_P [Pa]	γ [ ]	
Mantle$^{\$}$	5.7000×10^{11}	540×10^{3}	0.0×10^{-6}	8.5×10^{9}	0.1	

Constant parameters: *A heat capacity $c_P = 1050$ [J kg^{-1} K^{-1}] is employed for all phases.
^{a,b,c}A constant shear modulus $G = 2\times10^{10}$ [Pa] is used. ^{d}A constant shear modulus $G = 1.81\times10^{10}$ [Pa] is used.
$^{a}\rho_0 = 2800$ [kg m^{-3}], $^{b}\rho_0 = 2900$ [kg m^{-3}] and $^{d}\rho_0 = 2585$ [kg m^{-3}], $^{a,b}\alpha = 3.5 \times 10^{-5}$ [K^{-1}] and $^{d}\alpha = 4.7 \times 10^{-5}$ [K^{-1}] and $^{a,b,d}\beta = 1 \times 10^{-11}$ [Pa^{-1}] are used for density calculations using a simplified equation of state during extension and cooling.
†A water fugacity $f_{\mathrm{H_2O}} = 1.0\times10^{9}$ [Pa] is used. For all other phases $f_{\mathrm{H_2O}}= 0.0$ [Pa].
‡A constant grain size $d = 1\times10^{-3}$ [m] is used.
$^{\$}$Reference: Goetze and Evans (1979) regularized by Kameyama et al. (1999). These parameters are used for both strong and weak mantle rheology.

Fig.A4: Time series of selected markers

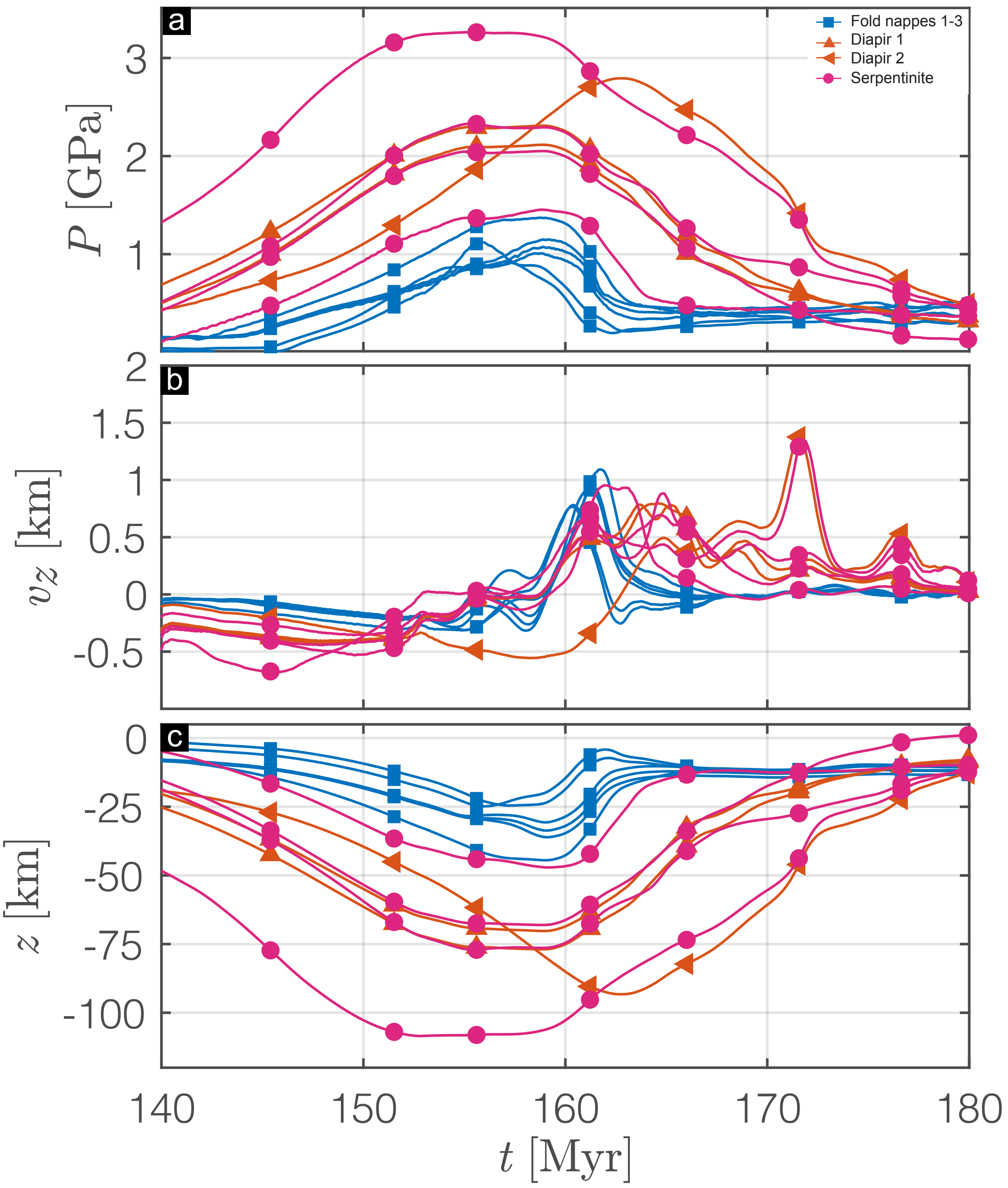

Figure A.4: Top row: pressure, middle row: vertical velocity and bottom row: depth of selected markers. Solid blue lines and squares are markers from the upper crust exhumed during the first exhumation event (buckling), and solid orange lines and triangles are markers from the deeper subducted upper crust exhumed during the second exhumation event (episodic diapiric uplift). Solid magenta lines and circles are markers from the serpentinite layer. Velocity signals show several pikes indicating that exhumation is not continuous but episodic.

Fig.A5: Quartz dominated rheology

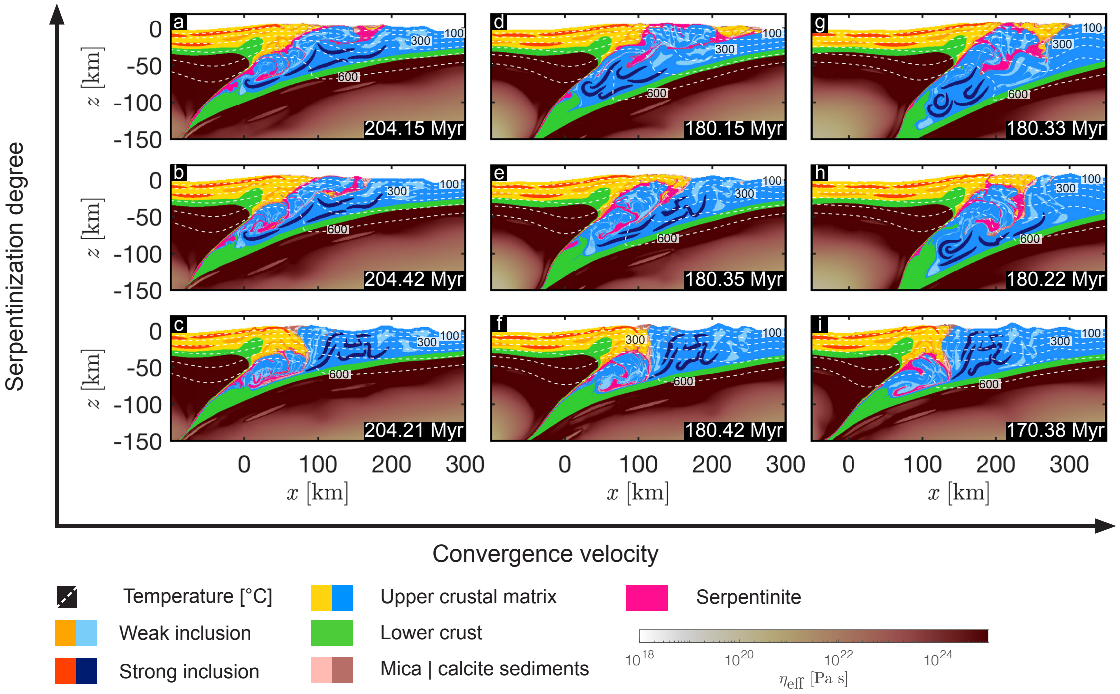

Figure A.5: For all panels: yellow to orange and light to dark blue indicate the upper crust, green is the lower crust, magenta is the serpentinite and white to red is the viscosity field in the mantle calculated by the numerical algorithm. Columns show models with increasing convergence velocity: left column = 0.5 $\mathrm{cm\,yr^{-1}}$, middle column = 1.0 $\mathrm{cm\,yr^{-1}}$ and right column = 1.5 $\mathrm{cm\,yr^{-1}}$. Rows show models with increasing serpentinite layer thickness: bottom row = 3 km, middle row = 5 km and top row = 6 km. With increasing convergence velocity advection dominates the dynamics. Although the general deformation style is very similar, magnitudes of temperature are slightly lower at faster convergence rates (compare depth of 600 °C isotherm in **c**,**f** & **i**). With increasing serpentinite layer thickness the deformation style changes significantly. **c**,**f** & **i** Upper crustal imbricated thrusting inhibits deep subduction of continental crust when the serpentinite layer is relatively thin. For serpentinite layer thicknesses $\geq$5 km, continental crust is subducted deep into the mantle and exhumed back to the surface as shown in the reference model (main section).

Fig.A6: Feldspar dominated rheology

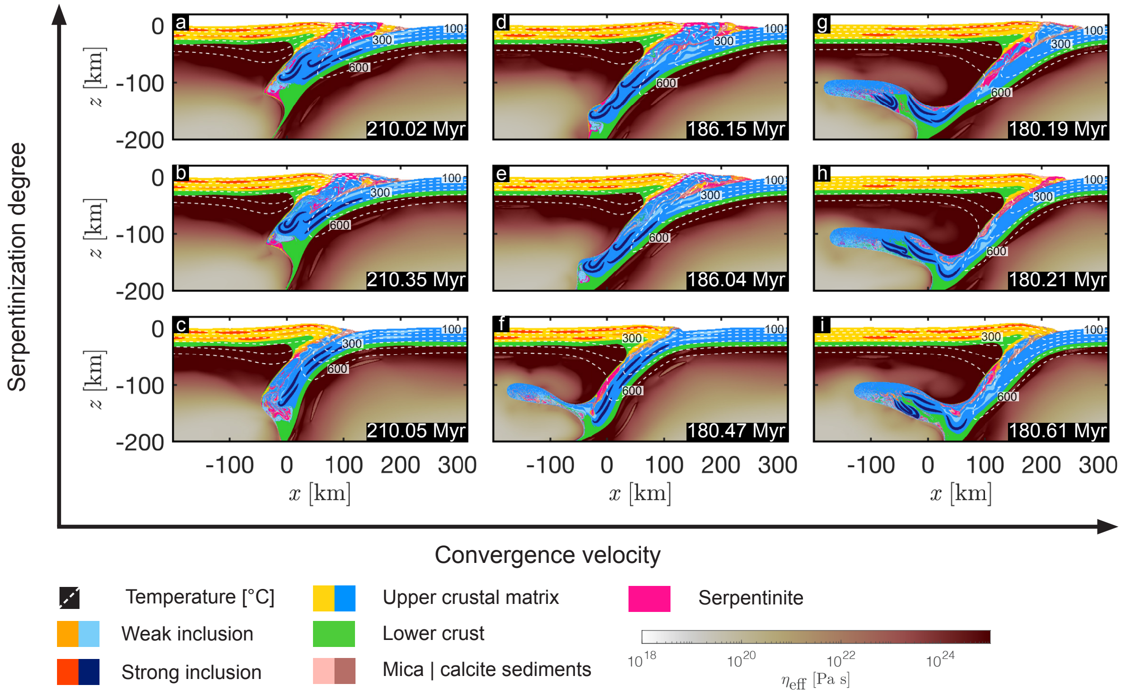

Figure A.6: For all panels: yellow to orange and light to dark blue indicate the upper crust, green is the lower crust, magenta is the serpentinite and white to red is the viscosity field in the mantle calculated by the numerical algorithm. Columns show models with increasing convergence velocity: left column = 0.5 $\mathrm{cm\,yr^{-1}}$, middle column = 1.0 $\mathrm{cm\,yr^{-1}}$ and right column = 1.5 $\mathrm{cm\,yr^{-1}}$. Rows show models with increasing serpentinite layer thickness: bottom row = 3 km, middle row = 5 km and top row = 6 km. With increasing convergence velocity, the deeply subducted crustal units cannot be exhumed back to the surface (**f**-**i**). For reduced convergence rates and increased serpentinite layer thickness (**d** & **e**) exhumation of deeply subducted crustal units along the subduction interface is still feasible.

Fig.A7: Phase equilibrium density tables

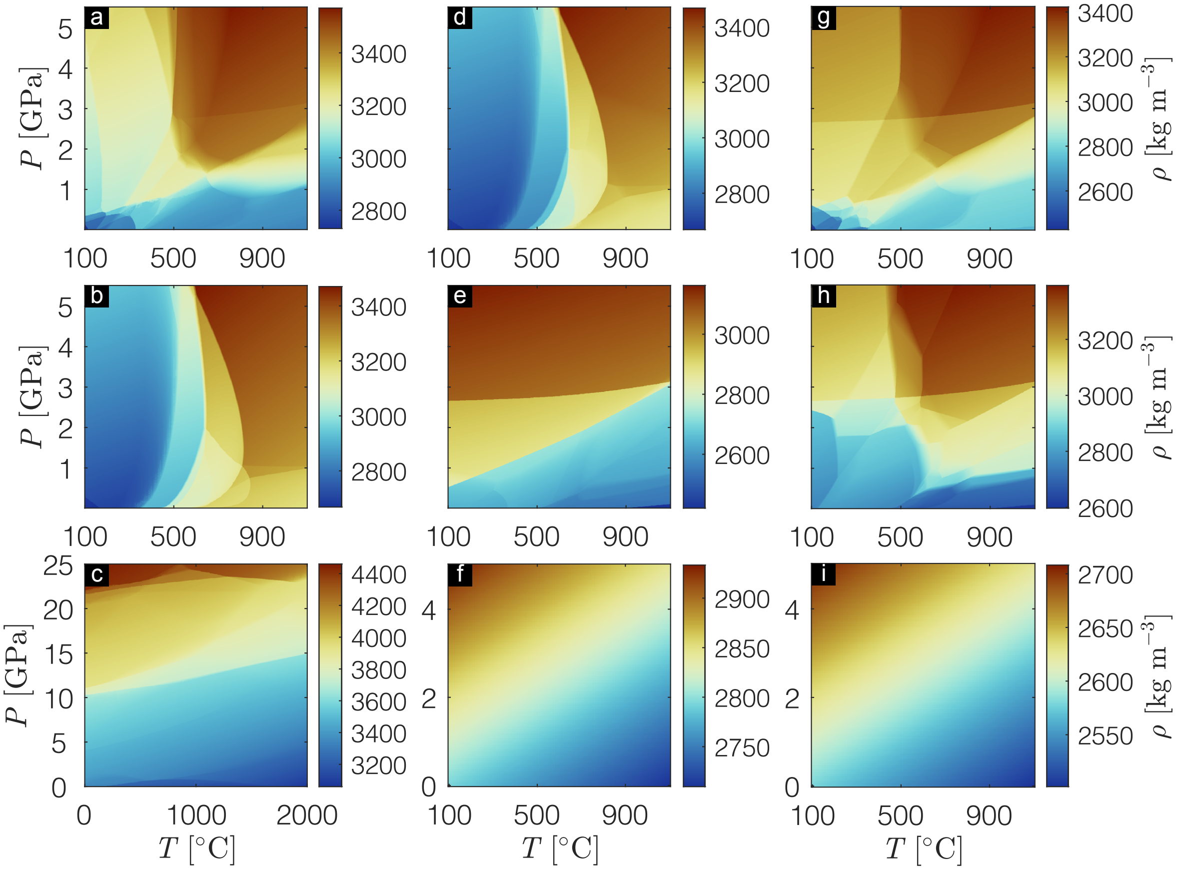

Figure A.7: **a** Mid-ocean ridge basalt (MORB), **b** serpentinite, **c** depleted MORB mantle (DMM), **d** hydrated peridotite, **e** rhyolite, **f** LEOS crust (2800 kg m^{-3}), **g** andesite, **h** pelite and **i** LEOS serpentinite (2585 kg m^{-3}). All input parameters for the phase equilibrium calculations are given in Table 5.2.

Table 5.2: Bulk rock composition for phase equilibrium calculations.

Oxides [wt%]	Pelite (avg.)^{1,4}	Rhyolite^{1,4}	Andesite^{1,4}	MORB^{1,4}	Hydr. Peridotite^{1,4}	Serpentinite^{2,4}	Bulk DMM^{3,5}
SiO_2	61.500	72.800	57.900	49.200	44.710	44.210	44.710
Al_2O_3	18.600	13.300	17.000	16.100	4.160	3.130	3.980
FeO	10.000	2.440	6.980	10.220	8.070	8.898	8.180
MgO	3.810	0.390	3.330	6.440	39.200	39.240	38.730
CaO	-	-	6.790	10.500	2.420	3.060	3.170
Na_2O	1.460	3.550	3.480	3.010	0.220	-	0.130
K_2O	3.020	4.300	1.620	1.100	-	-	-
H_2O	sat	sat	sat	sat	sat	sat	-
Solution models							
Opx(HP)	+	+	+	+	+	+	-
Gt(GCT)	+	+	+	+	+	+	-
feldspar	+	+	+	+	+	+	-
Chl(HP)	+	+	+	+	+	+	-
Sp(HP)	+	+	+	+	+	+	-
O(HP)	+	+	+	+	+	+	-
Stlp(M)	+	+	+	+	-	-	-
Carp	+	+	+	+	-	-	-
Sud	+	+	+	+	-	-	-
Bio(TCC)	+	+	+	+	-	-	-
St(HP)	+	+	+	+	-	-	-
Ctd(HP)	+	+	+	+	-	-	-
Pheng(HP)	+	+	+	+	-	-	-
hCrd	+	+	+	+	+	+	-
Omph	-	-	+	+	+	+	-
GlTrTsPg	-	-	+	+	+	+	-
Pu(M)	-	-	+	+	+	-	-
Act(M)	-	-	+	+	+	+	-
T	-	-	+	-	+	+	-
A-phase	-	-	-	-	+	+	-
Chum	-	-	-	-	+	+	-
B	-	-	-	-	+	+	-
Wus	-	-	-	-	+	+	-
Fperh	-	-	-	-	+	+	-
Atg(PN)	-	-	-	-	+	+	-
C2/c	-	-	-	-	-	-	+
Wus	-	-	-	-	-	-	+
Pv	-	-	-	-	-	-	+
Pl	-	-	-	-	-	-	+
Sp	-	-	-	-	-	-	+
O	-	-	-	-	-	-	+
Wad	-	-	-	-	-	-	+
Ring	-	-	-	-	-	-	+
Opx	-	-	-	-	-	-	+
Cpx	-	-	-	-	-	-	+
Aki	-	-	-	-	-	-	+
Gt_maj	-	-	-	-	-	-	+
Ppv	-	-	-	-	-	-	+
CF	-	-	-	-	-	-	+

Modified bulk rock after [1]Winter (2013), [2]Pelletier et al. (2008) [3]Workman and Hart (2005). We assume water saturation in all calculations.

Crosses denote solution models used for given lithologies.

Thermodynamic databases used: [4]Holland and Powell (1998) updated in 2002 and [5]Stixrude and Lithgow-Bertelloni (2011) for depleted MORB mantle (DMM).

Details on the solution models can be found in the solution_model.dat data file in Perple_X.

Bibliography

Andersen, T. B., Jamtveit, B., Dewey, J. F., Swensson, E., 1991. Subduction and eduction of continental crust: Major mechanisms during continent-continent collision and orogenic extensional collapse, a model based on the south norwegian caledonides. Terra Nova 3 (3), 303–310.

Angiboust, S., Agard, P., Jolivet, L., Beyssac, O., 2009. The zermatt-saas ophiolite: the largest (60-km wide) and deepest (c. 70–80 km) continuous slice of oceanic lithosphere detached from a subduction zone? Terra Nova 21 (3), 171–180.

Auzemery, A., Willingshofer, E., Yamato, P., Duretz, T., Sokoutis, D., 2020. Strain localization mechanisms for subduction initiation at passive margins. Global and Planetary Change 195, 103323.

Baes, M., Sobolev, S. V., Quinteros, J., 2018. Subduction initiation in mid-ocean induced by mantle suction flow. Geophysical Journal International 215 (3), 1515–1522.

Beaumont, C., Ellis, S., Hamilton, J., Fullsack, P., 1996. Mechanical model for subduction-collision tectonics of alpine-type compressional orogens. Geology 24 (8), 675–678.

Beaumont, C., Jamieson, R. A., Butler, J., Warren, C., 2009. Crustal structure: A key constraint on the mechanism of ultra-high-pressure rock exhumation. Earth and Planetary Science Letters 287 (1-2), 116–129.

Burov, E., Francois, T., Yamato, P., Wolf, S., 2014. Mechanisms of continental subduction and exhumation of hp and uhp rocks. Gondwana Research 25 (2), 464–493.

Butler, J. P., Beaumont, C., Jamieson, R. A., 2014. The alps 2: Controls on crustal subduction and (ultra) high-pressure rock exhumation in alpine-type orogens. Journal of Geophysical Research: Solid Earth 119 (7), 5987–6022.

Candioti, L. G., Schmalholz, S. M., Duretz, T., 2020. Impact of upper mantle convection on lithosphere hyperextension and subsequent horizontally forced subduction initiation. Solid Earth 11 (6), 2327–2357.

Chopin, C., 1984. Coesite and pure pyrope in high-grade blueschists of the western alps: a first record and some consequences. Contributions to Mineralogy and Petrology 86 (2), 107–118.

Connolly, J., 2009. The geodynamic equation of state: what and how. Geochemistry, Geophysics, Geosystems 10 (10).

Crameri, F., Magni, V., Domeier, M., Shephard, G. E., Chotalia, K., Cooper, G., Eakin, C. M., Grima, A. G., Gürer, D., Király, Á., et al., 2020. A transdisciplinary and community-driven database to unravel subduction zone initiation. Nature Communications 11 (1), 1–14.

de Meyer, C. M., Baumgartner, L. P., Beard, B. L., Johnson, C. M., 2014. Rb–sr ages from phengite inclusions in garnets from high pressure rocks of the swiss western alps. Earth and Planetary Science Letters 395, 205–216.

de Sigoyer, J., Chavagnac, V., Blichert-Toft, J., Villa, I. M., Luais, B., Guillot, S., Cosca, M., Mascle, G., 2000. Dating the indian continental subduction and collisional thickening in the northwest himalaya: Multichronology of the tso morari eclogites. Geology 28 (6), 487–490.

Duretz, T., Gerya, T., Kaus, B., Andersen, T., 2012. Thermomechanical modeling of slab eduction. Journal of Geophysical Research: Solid Earth 117 (B8).

England, P., Holland, T., 1979. Archimedes and the tauern eclogites: the role of buoyancy in the preservation of exotic eclogite blocks. Earth and Planetary Science Letters 44 (2), 287–294.

Escher, A., Beaumont, C., 1997. Formation, burial and exhumation of basement nappes at crustal scale: a geometric model based on the western swiss-italian alps. Journal of structural Geology 19 (7), 955–974.

Gerya, T., Stöckhert, B., 2006. Two-dimensional numerical modeling of tectonic and metamorphic histories at active continental margins. International Journal of Earth Sciences 95 (2), 250–274.

Gerya, T. V., Stöckhert, B., Perchuk, A. L., 2002. Exhumation of high-pressure metamorphic rocks in a subduction channel: A numerical simulation. Tectonics 21 (6), 6–1.

Gerya, T. V., Yuen, D. A., 2003. Characteristics-based marker-in-cell method with conservative finite-differences schemes for modeling geological flows with strongly variable transport properties. Physics of the Earth and Planetary Interiors 140 (4), 293–318.

Goetze, C., Evans, B., 1979. Stress and temperature in the bending lithosphere as constrained by experimental rock mechanics. Geophysical Journal International 59 (3), 463–478.

Groppo, C., Beltrando, M., Compagnoni, R., 2009. The p–t path of the ultra-high pressure lago di cignana and adjoining high-pressure meta-ophiolitic units: insights into the evolution of the subducting tethyan slab. Journal of Metamorphic Geology 27 (3), 207–231.

Groppo, C., Ferrando, S., Gilio, M., Botta, S., Nosenzo, F., Balestro, G., Festa, A., Rolfo, F., 2019. What's in the sandwich? new p–t constraints for the (u) hp nappe stack of southern dora-maira massif (western alps). European Journal of Mineralogy 31 (4), 665–683.

Guillot, S., Hattori, K., Agard, P., Schwartz, S., Vidal, O., 2009. Exhumation processes in oceanic and continental subduction contexts: a review. In: Subduction zone geodynamics. Springer, pp. 175–205.

Hacker, B. R., Peacock, S. M., Abers, G. A., Holloway, S. D., 2003. Subduction factory 2. are intermediate-depth earthquakes in subducting slabs linked to metamorphic dehydration reactions? Journal of Geophysical Research: Solid Earth 108 (B1).

Hansen, F., Carter, N., et al., 1983. Semibrittle creep of dry and wet westerly granite at 1000 mpa. In: The 24th US Symposium on Rock Mechanics (USRMS). American Rock Mechanics Association.

Hermann, J., Rubatto, D., et al., 2014. Subduction of continental crust to mantle depth: geochemistry of ultrahigh-pressure rocks. In: Treatise on Geochemistry, 2nd Edition. Elsevier.

Hess, H. H., 1955. Serpentines, orogeny, and epeirogeny. Geol. Soc. Am. Spec. Paper 62, 391–407.

Hilairet, N., Reynard, B., Wang, Y., Daniel, I., Merkel, S., Nishiyama, N., Petitgirard, S., 2007. High-pressure creep of serpentine, interseismic deformation, and initiation of subduction. Science 318 (5858), 1910–1913.

Hirauchi, K.-i., Katayama, I., Kouketsu, Y., 2020. Semi-brittle deformation of antigorite serpentinite under forearc mantle wedge conditions. Journal of Structural Geology, 104151.

Hirth, G., Kohlstedf, D., 2003. Rheology of the upper mantle and the mantle wedge: A view from the experimentalists. Geophysical Monograph-American Geophysical Union 138, 83–106.

Holland, T., Powell, R., 1998. An internally consistent thermodynamic data set for phases of petrological interest. Journal of metamorphic Geology 16 (3), 309–343.

Idrissi, H., Samaee, V., Lumbeeck, G., van der Werf, T., Pardoen, T., Schryvers, D., Cordier, P., 2020. In situ quantitative tensile testing of antigorite in a transmission electron microscope. Journal of Geophysical Research: Solid Earth 125 (3), e2019JB018383.

Kameyama, M., Yuen, D. A., Karato, S.-I., 1999. Thermal-mechanical effects of low-temperature plasticity (the peierls mechanism) on the deformation of a viscoelastic shear zone. Earth and Planetary Science Letters 168 (1-2), 159–172.

Kiss, D., Candioti, L. G., Duretz, T., Schmalholz, S. M., 2020. Thermal softening induced subduction initiation at a passive margin. Geophysical Journal International 220 (3), 2068–2073.

Kronenberg, A. K., Kirby, S. H., Pinkston, J., 1990. Basal slip and mechanical anisotropy of biotite. Journal of Geophysical Research: Solid Earth 95 (B12), 19257–19278.

Le Breton, E., Brune, s., Ustaszewski, K., Zahirovic, S., Seton, M., Müller, R. D., 2020. Kinematics and extent of the piemont-liguria basin – implications for subduction processes in the alps. Solid Earth Discuss. in review (https://doi.org/10.5194/se-2020-161).

Li, Z., Gerya, T. V., 2009. Polyphase formation and exhumation of high-to ultrahigh-pressure rocks in continental subduction zone: Numerical modeling and application to the sulu ultrahigh-pressure terrane in eastern china. Journal of Geophysical Research: Solid Earth 114 (B9).

Liao, J., Malusà, M. G., Zhao, L., Baldwin, S. L., Fitzgerald, P. G., Gerya, T., 2018. Divergent plate motion drives rapid exhumation of (ultra) high pressure rocks. Earth and Planetary Science Letters 491, 67–80.

Luisier, C., Baumgartner, L., Schmalholz, S. M., Siron, G., Vennemann, T., 2019. Metamorphic pressure variation in a coherent alpine nappe challenges lithostatic pressure paradigm. Nature communications 10 (1), 1–11.

Mackwell, S., Zimmerman, M., Kohlstedt, D., 1998. High-temperature deformation of dry diabase with application to tectonics on venus. Journal of Geophysical Research: Solid Earth 103 (B1), 975–984.

Malusà, M. G., Faccenna, C., Baldwin, S. L., Fitzgerald, P. G., Rossetti, F., Balestrieri, M. L., Danišík, M., Ellero, A., Ottria, G., Piromallo, C., 2015. Contrasting styles of (u) hp rock exhumation along the cenozoic adria-europe plate boundary (western alps, calabria, corsica). Geochemistry, Geophysics, Geosystems 16 (6), 1786–1824.

Mancktelow, N. S., 1995. Nonlithostatic pressure during sediment subduction and the development and exhumation of high pressure metamorphic rocks. Journal of Geophysical Research: Solid Earth 100 (B1), 571–583.

Manzotti, P., Ballevre, M., Zucali, M., Robyr, M., Engi, M., 2014. The tectonometamorphic evolution of the sesia–dent blanche nappes (internal western alps): review and synthesis. Swiss Journal of Geosciences 107 (2-3), 309–336.

Manzotti, P., Bosse, V., Pitra, P., Robyr, M., Schiavi, F., Ballevre, M., 2018. Exhumation rates in the gran paradiso massif (western alps) constrained by in situ u–th–pb dating of accessory phases (monazite, allanite and xenotime). Contributions to Mineralogy and Petrology 173 (3), 24.

McCarthy, A., Tugend, J., Mohn, G., Candioti, L., Chelle-Michou, C., Arculus, R., Schmalholz, S. M., Müntener, O., 2020. A case of ampferer-type subduction and consequences for the alps and the pyrenees. American Journal of Science 320 (4), 313–372.

Pan, R., Macris, C. A., Menold, C. A., 2020. Thermodynamic modeling of high-grade metabasites: a case study using the tso morari uhp eclogite. Contributions to Mineralogy and Petrology 175 (8), 1–28.

Pelletier, L., Müntener, O., Kalt, A., Vennemann, T. W., Belgya, T., 2008. Emplacement of ultramafic rocks into the continental crust monitored by light and other trace elements: An example from the geisspfad body (swiss-italian alps). Chemical Geology 255 (1-2), 143–159.

Penniston-Dorland, S. C., Kohn, M. J., Manning, C. E., 2015. The global range of subduction zone thermal structures from exhumed blueschists and eclogites: Rocks are hotter than models. Earth and Planetary Science Letters 428, 243–254.

Raimbourg, H., Jolivet, L., Leroy, Y., 2007. Consequences of progressive eclogitization on crustal exhumation, a mechanical study. Geophysical Journal International 168 (1), 379–401.

Raleigh, C. B., Paterson, M., 1965. Experimental deformation of serpentinite and its tectonic implications. Journal of Geophysical Research 70 (16), 3965–3985.

Ranalli, G., 1995. Rheology of the Earth. Springer Science & Business Media.

Reuber, G., Kaus, B. J., Schmalholz, S. M., White, R. W., 2016. Nonlithostatic pressure during subduction and collision and the formation of (ultra) high-pressure rocks. Geology 44 (5), 343–346.

Rubatto, D., Hermann, J., 2001. Exhumation as fast as subduction? Geology 29 (1), 3–6.

Rybacki, E., Dresen, G., 2004. Deformation mechanism maps for feldspar rocks. Tectonophysics 382 (3-4), 173–187.

Schmalholz, S. M., Mancktelow, N. S., 2016. Folding and necking across the scales: a review of theoretical and experimental results and their applications. Solid Earth 7 (5).

Schmid, S., Boland, J., Paterson, M., 1977. Superplastic flow in finegrained limestone. Tectonophysics 43 (3-4), 257–291.

Schmid, S. M., Kissling, E., Diehl, T., van Hinsbergen, D. J., Molli, G., 2017. Ivrea mantle wedge, arc of the western alps, and kinematic evolution of the alps–apennines orogenic system. Swiss Journal of Geosciences 110 (2), 581–612.

Stixrude, L., Lithgow-Bertelloni, C., 2011. Thermodynamics of mantle minerals-ii. phase equilibria. Geophysical Journal International 184 (3), 1180–1213.

Tan, Z., Agard, P., Monie, P., Gao, J., John, T., Bayet, L., Jiang, T., Wang, X.-S., Hong, T., Wan, B., et al., 2019. Architecture and pt-deformation-time evolution of the chinese sw-tianshan hp/uhp complex: Implications for subduction dynamics. Earth-Science Reviews 197, 102894.

Vaughan-Hammon, J. D., Luisier, C., Baumgartner, L., Schmalholz, S. M., 2021. Peak alpine metamorphic conditions from staurolite bearing metapelites in the monte rosa nappe (central european alps) and geodynamic implications. Journal of Metamorphic Geology article in press, https://doi.org/10.1111/jmg.12595.

Warren, C., 2013. Exhumation of (ultra)-high-pressure terranes: concepts and mechanisms. Solid Earth 4, 75–92.

Warren, C. J., Beaumont, C., Jamieson, R. A., 2008. Formation and exhumation of ultra-high-pressure rocks during continental collision: Role of detachment in the subduction channel. Geochemistry, Geophysics, Geosystems 9 (4).

Winter, J. D., 2013. Principles of igneous and metamorphic petrology. Pearson education.

Workman, R. K., Hart, S. R., 2005. Major and trace element composition of the depleted morb mantle (dmm). Earth and Planetary Science Letters 231 (1-2), 53–72.

Yamato, P., Burov, E., Agard, P., Le Pourhiet, L., Jolivet, L., 2008. Hp-uhp exhumation during slow continental subduction: Self-consistent thermodynamically and thermomechanically coupled model with application to the western alps. Earth and Planetary Science Letters 271 (1-4), 63–74.

Zhao, L., Malusà, M. G., Yuan, H., Paul, A., Guillot, S., Lu, Y., Stehly, L., Solarino, S., Eva, E., Lu, G., et al., 2020. Evidence for a serpentinized plate interface favouring continental subduction. Nature Communications 11 (1), 1–8.

Zhao, L., Paul, A., Guillot, S., Solarino, S., Malusà, M. G., Zheng, T., Aubert, C., Salimbeni, S., Dumont, T., Schwartz, S., et al., 2015a. First seismic evidence for continental subduction beneath the western alps. Geology 43 (9), 815–818.

Zhao, Z., Bons, P., Wang, G., Soesoo, A., Liu, Y., 2015b. Tectonic evolution and high-pressure rock exhumation in the qiangtang terrane, central tibet. Solid Earth 6 (2), 457.

CHAPTER 6

General Conclusion

This thesis aimed at shedding new light on the processes leading to the formation of orogenic belts embedded in the long-term geodynamic cycle of the lithosphere. To this end, state-of-the-art two-dimensional petrological-thermomechanical upper mantle-scale numerical models have been presented. Formation of hyper-extended magma-poor passive margins bounding a marine basin, upper mantle convection, subduction initiation and orogenic wedge formation have been modelled in a single and continuous numerical simulation. The following pressing scientific challenges have been met: (i) coupling of upper mantle convection to lithosphere deformation in long-term geodynamic cycles, (ii) quantifying the balance of buoyancy and shear forces and their impact on orogen dynamics and (iii) unveiling a new mechanism for synconvergent and coherent (ultra)high-pressure (UHP) rock exhumation consistent with several observations from natural (U)HP terranes. In Sec. 6.1 the main findings are summarized and discussed, model limitations are reviewed in Sec. 6.2 and an outlook to potential future steps is presented in Sec. 6.4.

6.1 Summary

6.1.1 Impact of coupled lithosphere–mantle deformation on subduction initiation

Including previous deformation phases such as hyperextension into subduction and collision models coupled to upper mantle convection has given new insights into the dynamics at convergent plate boundaries. Simulating the initial passive margin configuration for the subduction experiment under the same assumptions ensures consistency and provides further confidence that the model captures the first-order physics correctly.

In many models of coupled lithosphere–mantle deformation, vigorous convection is either suppressed by artificial viscosity limiters or only its thermal impact on lithosphere dynamics is included via effective conductivity parametrizations (Currie et al., 2008; Jammes and Huismans, 2012, , see also chapter 2). Both approaches modulate the velocity field in the upper mantle and directly impact on the subduction dynamics: the vigour of upper mantle convection is likely a controlling parameter driving either single-slab or divergent double-slab subduction following its initiation. Often, subduction initiation is prescribed by an already subducting embryonic slab (Kaus et al., 2009; Garel et al., 2014; Holt et al., 2017; Dal Zilio et al., 2018) meaning that the simulation starts after subduction initiation. Alternatively, a major weak zone across the lithosphere is commonly imposed to enable subduction initiation (Ruh et al., 2015; Zhou et al., 2020). Drawback of this prescription is a loss of predictability w.r.t. subduction initiation, because the location and polarity of the evolving subduction are known a priori. In the models presented here, upper mantle convection is modelled with sufficiently high resolution in space and time. The vigour of upper mantle convection is not artificially suppressed. Subduction initiation is not prescribed a priori, but the location and polarity of subduction evolves freely and is predicted by the models. The main localisation mechanism is thermal softening together with temperature-dependent rheological flow laws. Forces required for subduction initiation are much lower compared to previous predictions and are in the order of plate tectonic forces. This result is relevant, because the main argument against thermal softening as an important localization mechanism is that the required stresses are unrealistically high. In nature, more softening mechanisms act in concert with thermal softening, such as grain damage (e.g. Bercovici and Ricard, 2012; Thielmann and Schmalholz, 2020), fabric and anisotropy evolution (e.g. Montési, 2013) or reaction-induced softening (e.g. White and Knipe, 1978). Including additional softening mechanism likely further reduces the magnitude of forces required for subduction initiation in this kind of models.

6.1.2 Dominant forces forming orogenic belts

The ”classical” crustal wedge models (Platt, 1986; Dahlen, 1990; Malavieille, 2010; Dal Zilio et al., 2020b) focus mainly on upper-crustal levels. The evolution of the Alpine orogeny, however, involves the entire lithosphere in wedging (Nicolas et al., 1990). Dynamics within these lithospheric orogenic wedges can be controlled by either shear or buoyancy forces dominating in the force balance. Shear forces are mainly modulated by the strength of the deforming material. Assessing the rock strength deforming under natural conditions is impossible as tectonic deformation rates are extremely low. Estimates of rock strength are, therefore, determined in laboratory experiments conducted under accelerated deformation rates and are subject to significant uncertainty on the actual rock strength (Mancktelow and Pennacchioni, 2010; Idrissi et al., 2020). Numerical models are useful to test different end-member rock rheologies and to investigate the impact of rock strength on subduction and formation of collisional orogens. The numerical experiments conducted here show that especially the strength of serpentinite crucially impacts on the dynamics within growing Alpine-type orogens. High strength of serpentinite leads to formation of shear force-dominated orogenic thrust wedges. Large volumes of continental crust are sheared off the subducting plate and escape subduction early. In contrast, low serpentinite strength yields buoyancy force-dominated orogenic wedges and exhumation of deeply subducted crustal material. In nature, the serpentinite strength may vary along the subducting plate parallel or orthogonal to the subduction direction. This spatial variation may explain many differences in deformation style observed in natural collisional orogens.

The density contrast between the subducted crust and the surrounding upper mantle modulates the buoyancy forces. Many geodynamic models employ a linearized equation of state describing density as a function of pressure and temperature. A more complex model describes density as a function of pressure, temperature and petrochemical composition, i.e. it accounts for metamorphic reactions. An approach to employ this complex model, is to precompute the material densities using a thermodynamic tool that minimizes, for example, the Gibbs free energy (Connolly, 2009). This complex model has proven useful to explain observations including (i) varying sediment thickness accumulated during basin subsidence (Kaus et al., 2005), (ii) evolution of subducting slab dynamics (van Hunen et al., 2001; Toussaint et al., 2004) and (iii) the exhumation of (U)HP rocks (Yamato et al., 2007; Warren et al., 2008). In addition, the results presented here demonstrate that complex density models avoid unrealistically high topographic elevation during orogen formation. In fact, many orogenic wedge models for the Western Alps have been criticised for overestimating the mean topographic elevation (Kissling, 1993; Dal Zilio et al., 2020a). Therefore, coupling metamorphic reactions to thermo-mechanics is an important step towards more realistic orogenic wedge models.

6.1.3 From subduction initiation to (ultra)high-pressure rock exhumation

The models presented here are based on the fundamental laws of physics and predict two crucial stages of the geodynamic history of (U)HP terranes, namely (i) subduction initiation and (ii) (U)HP rock exhumation in a single numerical simulation. While serpentinites do not impact on subduction initiation, they prove crucial for weakening the subduction interface and enable (U)HP rock exhumation (*chapter* 4,5). These models build upon previous studies of synconvergent (U)HP rock exhumation (Warren et al., 2008; Butler et al., 2014). A new tectonic-driven mechanism for synconvergent (U)HP rock exhumation was presented which does not require excessive erosion (Butler et al., 2014) or divergent plate motion (Liao et al., 2018). Instead, buckling-induced local upper plate extension causes the exhumation of deeply buried units. In previous studies, local upper plate extension has also been observed, but was the consequence of buoyant uplift of (U)HP units (Warren et al., 2008). In the model presented here, the exhuming units remain without significant internal deformation, consistent with structural observations from several (U)HP terranes worldwide (Escher and Beaumont, 1997; Young et al., 2007). Further, peak metamorphic conditions predicted by the model agree well with petrological data from major volumes of (U)HP terranes from the Western Alps, the Tien Shan and from the Tso Morari, Himalayas. In addition, predicted exhumation velocities of the (U)HP units agree well with estimates from major volumes of the Western Alps and the Tso Morari. Reproducing several first-order observations and natural data and predicting two crucial stages in the burial-exhumation cycle of the crust provides confidence that the model presented here is robust, transferable and applicable to (U)HP terrane formation within in natural orogens.

6.2 Model limitations

”All models are wrong, but some of them are useful” is a quote often attributed to the statistician *George Box*. As a matter of fact, models are simplifying tools that help us to understand fundamental natural processes up to a certain level of complexity. For example, when *Isaac Newton* applied his laws of motion and gravity to predict the Earth’s orbit around the Sun, he assumed that the mass of both planetary bodies is concentrated in a point, a nondimensional object without any additional structure (Newton, 1833). Clearly, this is wrong and a simplifying assumption, but this model explains the Earth's yearly journey around the Sun and, therefore, extends our knowledge on the fundamental natural process of planetary motions. Generally, any modeller has to interpret his model results in context of (i) the model assumptions, (ii) the initial configuration of the experiment and (iii) the applied boundary conditions. In the previous section, benefits of the presented models have been discussed and this section discusses their limitations.

6.2.1 Model assumptions and boundary conditions

The models presented here are restricted to two dimensions and driven by far-field kinematic boundary conditions. Therefore, we can only capture first-order fundamental features of natural orogens. During model evolution, more and more crustal material is forced into subduction. In fact, the plate driving forces eventually reach again the magnitude necessary for subduction initiation after basin closure (see chapter 4). In nature, a new subduction zone would form at a different location and the active subduction zone would cease or slow down significantly. Although this cannot be observed, the models presented hear can at last predict an approximated timing of such an event after subduction initiation.

Here deformation is driven by constant material inflow/outflow velocities at the lateral boundaries causing the increase of plate driving forces after subduction initiation. Applying other types of mechanical boundary conditions, for example a constant force boundary condition, potentially avoids this effect. However, the choice of mechanical boundary conditions was made to drive plate motions consistent with estimates from plate motion reconstruction for Adria and Europe in the simplest possible way.

6.2.2 Initial conditions

The orogenic wedges modelled in *chapter* 4 are wider and deeper than the natural Alpine orogen. The size of the mechanical heterogeneities employed for the initial configuration is chosen based on the numerical resolution (1×1 km) and probably strongly impacts on the size of the modelled wedge. At higher numerical resolution, the size of the mechanical heterogeneities could be reduced and the modelled rifted margins might be thinner, leading to a more realistic pre-orogenic crustal thickness generated during the rifting period. In consequence, less material would be involved in subduction and the absolute magnitude of forces would change. However, the general model evolution, i.e. the relative increase of buoyancy forces with continuous subduction, would be most likely unchanged.

6.3 Concluding remarks

The models presented here are thoroughly calibrated to large-scale coupled lithosphere–upper mantle deformation and extend our knowledge on the long-term tectonic cycle of the lithosphere. In conclusion:

- Upper mantle convection indeed impacts on the initiation and evolution of subduction. Parameterizations of coupled lithosphere–upper mantle deformation lead to a different evolution of subduction compared to explicit coupling of lithosphere–upper mantle deformation.

- The rheology of serpentinite and the density structure crucially impact on the force balance within growing Alpine-type orogens modulating shear and buoyancy forces, respectively. Serpentinites may indeed reorganise along the subduction interface and significantly reduce its strength enabling deep burial of continental upper crust. However, serpentinites are not crucial for subduction initiation. Including petrologically determined density models reduces the topographic elevation significantly compared to standard linearized density models.

- Buckling-induced local upper plate extension triggering buoyancy-driven exhumation of deeply subducted (U)HP rocks is a feasible synconvergent exhumation mechanism. Not relying on unrealistically high erosion rates or divergent plate motion, this mechanism reproduces first-order structural, petrological and geophysical observation from natural (U)HP terranes.

6.4 Outlook

The two-dimensional high-resolution petrological-thermomechanical models presented here provide new insights into processes forming orogenic belts, such as the European Alps. Despite resolving many issues of previous models, this thesis raised no fewer questions.

(1) *Where is the Briançonnais domain?* Here, rifting leads to formation of two passive margins bounding a marine basin floored by exhumed mantle. Although boundary conditions are motivated by plate motion reconstructions from the European and Adriatic plate, the modelled margin geometries do not entirely reproduce paleogeographic reconstructions from the Alpine Tethys margins. Despite all efforts, the presented rifting models failed to predict the formation of the Briançonnais domain (e.g. Handy et al., 2010), which is important for the history of the Alpine orogeny. Mechanical inheritances prove crucial for the evolution of rifted margins (Duretz et al., 2016; Petri et al., 2019). Likely, the initial configuration from the onset of hyperextension in the presented experiments prevented from the formation of several continental micro-plates, such as the Briançonnais. Another explanation might be a fundamental softening mechanism missing in the model assumptions. To determine, which physical processes lead to formation of micro-continents during hyperextension, further investigations are required.

(2) *How much force is required for subduction initiation via shear heating only?* Thermal softening is an efficient, self-regulating mechanism explaining the first-order physics of horizontally-forced subduction initiation (Thielmann and Kaus, 2012; Kiss et al., 2020). Compared to previous studies relying on thermal softening, the models presented here predict subduction initiation for plate driving force magnitudes reduced by at least 40%. However, determining a minimum estimate of plate driving forces required for horizontally-forced subduction initiation via thermal softening was beyond the scope of this thesis and will be subject of future studies.

(3) *Are more complex physics needed?* This thesis has shown that serpentinisation plays a crucial role for the dynamics of the evolving orogen (see chapter 4). Here serpentinisation is parameterized and the underlying thermodynamic processes causing serpentinisation are not included in the governing equations. In nature, serpentinisation of the oceanic lithosphere is caused by hydrothermal alteration. The presence of water at the seafloor induces a chemical hydration reaction of olivine to serpentinite, magnetite, brucite and hydrogen (e.g. Malvoisin et al., 2012). To capture the process of serpentinisation and not only its impact on the subduction and collision phase of the orogeny, the governing equations of the mathematical model need to be adapted. Fluid flow and the thermodynamic principles describing mineral reactions need to be coupled to the thermomechanical system. Recent studies made a first step towards coupling mechanics to fluid flow and metamorphic reactions on the grain scale (Schmalholz et al., 2020). These advances give a promising prospect of future studies modelling coupled thermo-hydro-mechanical-chemical lithosphere deformation predicting, for example, serpentinisation of the oceanic lithosphere during rifting and basin subsidence.

(4) *The necessity of ultra-high resolution 3D models* The two-dimensional models presented here cannot capture three-dimensional characteristics of natural orogens. Especially during the collisional stage of the Alpine orogeny (<30 Ma), major strike slip deformation lead to a large rearrangement of plate boundaries. Furthermore, on a sphere the plates rotate around Euler poles and are in fact shells which exhibit a double-curvature. The effect of this curvature on the stress field during the formation of, especially, large mountain ranges and plateaus such as the Himalayas is still poorly understood.

The applied algorithm used for the numerical experiments presented here efficiently leverages modern CPU hardware architecture and allows running two-dimensional upper mantle-scale simulations at high resolution. Solving for more than 4.5 Million degrees of freedom, interpolating physical properties from the grid onto up to 56 Million markers and transporting them at each time step, some of the experiments conducted for this thesis ran for more than 12 weeks on 10 CPUs. Extending the presented models to three dimensions using the same software and hardware architecture while keeping the high resolution also in the third dimension is computationally likely unfeasible. However, recent advances in software and hardware architecture (Omlin et al., 2018; Räss et al., 2018) make three-dimensional ultra-high resolution models possible. In the future, such models may tackle complex three-dimensional problems and further extend our knowledge on physical processes that drive the dynamics on planet Earth.

Bibliography

Bercovici, D., Ricard, Y., 2012. Mechanisms for the generation of plate tectonics by two-phase grain-damage and pinning. Physics of the Earth and Planetary Interiors 202, 27–55.

Butler, J. P., Beaumont, C., Jamieson, R. A., 2014. The alps 2: Controls on crustal subduction and (ultra) high-pressure rock exhumation in alpine-type orogens. Journal of Geophysical Research: Solid Earth 119 (7), 5987–6022.

Connolly, J., 2009. The geodynamic equation of state: what and how. Geochemistry, Geophysics, Geosystems 10 (10).

Currie, C. A., Huismans, R. S., Beaumont, C., 2008. Thinning of continental backarc lithosphere by flow-induced gravitational instability. Earth and Planetary Science Letters 269 (3-4), 436–447.

Dahlen, F., 1990. Critical taper model of fold-and-thrust belts and accretionary wedges. Annual Review of Earth and Planetary Sciences 18 (1), 55–99.

Dal Zilio, L., Faccenda, M., Capitanio, F., 2018. The role of deep subduction in supercontinent breakup. Tectonophysics 746, 312–324.

Dal Zilio, L., Kissling, E., Gerya, T., van Dinther, Y., 2020a. Slab rollback orogeny model: A test of concept. Geophysical Research Letters 47 (18), e2020GL089917.

Dal Zilio, L., Ruh, J., Avouac, J.-P., 2020b. Structural evolution of orogenic wedges: interplay between erosion and weak décollements. Tectonics, e2020TC006210.

Duretz, T., Petri, B., Mohn, G., Schmalholz, S., Schenker, F., Müntener, O., 2016. The importance of structural softening for the evolution and architecture of passive margins. Scientific reports 6, 38704.

Escher, A., Beaumont, C., 1997. Formation, burial and exhumation of basement nappes at crustal scale: a geometric model based on the western swiss-italian alps. Journal of structural Geology 19 (7), 955–974.

Garel, F., Goes, S., Davies, D., Davies, J. H., Kramer, S. C., Wilson, C. R., 2014. Interaction of subducted slabs with the mantle transition-zone: A regime diagram from 2-d thermomechanical models with a mobile trench and an overriding plate. Geochemistry, Geophysics, Geosystems 15 (5), 1739–1765.

Handy, M. R., Schmid, S. M., Bousquet, R., Kissling, E., Bernoulli, D., 2010. Reconciling plate-tectonic reconstructions of alpine tethys with the geological–geophysical record of spreading and subduction in the alps. Earth-Science Reviews 102 (3-4), 121–158.

Holt, A., Royden, L., Becker, T., 2017. The dynamics of double slab subduction. Geophysical Journal International 209 (1), 250–265.

Idrissi, H., Samaee, V., Lumbeeck, G., van der Werf, T., Pardoen, T., Schryvers, D., Cordier, P., 2020. In situ quantitative tensile testing of antigorite in a transmission electron microscope. Journal of Geophysical Research: Solid Earth 125 (3), e2019JB018383.

Jammes, S., Huismans, R. S., 2012. Structural styles of mountain building: Controls of lithospheric rheologic stratification and extensional inheritance. Journal of Geophysical Research: Solid Earth 117 (B10).

Kaus, B. J., Connolly, J. A., Podladchikov, Y. Y., Schmalholz, S. M., 2005. Effect of mineral phase transitions on sedimentary basin subsidence and uplift. Earth and Planetary Science Letters 233 (1-2), 213–228.

Kaus, B. J., Liu, Y., Becker, T., Yuen, D. A., Shi, Y., 2009. Lithospheric stress-states predicted from long-term tectonic models: Influence of rheology and possible application to taiwan. Journal of Asian Earth Sciences 36 (1), 119–134.

Kiss, D., Candioti, L. G., Duretz, T., Schmalholz, S. M., 2020. Thermal softening induced subduction initiation at a passive margin. Geophysical Journal International 220 (3), 2068–2073.

Kissling, E., 1993. Deep structure of the alps—what do we really know? Physics of the Earth and Planetary Interiors 79 (1-2), 87–112.

Liao, J., Malusà, M. G., Zhao, L., Baldwin, S. L., Fitzgerald, P. G., Gerya, T., 2018. Divergent plate motion drives rapid exhumation of (ultra) high pressure rocks. Earth and Planetary Science Letters 491, 67–80.

Malavieille, J., 2010. Impact of erosion, sedimentation, and structural heritage on the structure and kinematics of orogenic wedges: Analog models and case studies. Gsa Today 20 (1), 4–10.

Malvoisin, B., Brunet, F., Carlut, J., Rouméjon, S., Cannat, M., 2012. Serpentinization of oceanic peridotites: 2. kinetics and processes of san carlos olivine hydrothermal alteration. Journal of Geophysical Research: Solid Earth 117 (B4).

Mancktelow, N. S., Pennacchioni, G., 2010. Why calcite can be stronger than quartz. Journal of Geophysical Research: Solid Earth 115 (B1).

Montési, L. G., 2013. Fabric development as the key for forming ductile shear zones and enabling plate tectonics. Journal of Structural Geology 50, 254–266.

Newton, I., 1833. Philosophiae naturalis principia mathematica. Vol. 2. typis A. et JM Duncan.

Nicolas, A., Hirn, A., Nicolich, R., Polino, R., 1990. Lithospheric wedging in the western alps inferred from the ecors-crop traverse. Geology 18 (7), 587–590.

Omlin, S., Räss, L., Podladchikov, Y. Y., 2018. Simulation of three-dimensional viscoelastic deformation coupled to porous fluid flow. Tectonophysics 746, 695–701.

Petri, B., Duretz, T., Mohn, G., Schmalholz, S. M., Karner, G. D., Müntener, O., 2019. Thinning mechanisms of heterogeneous continental lithosphere. Earth and Planetary Science Letters 512, 147–162.

Platt, J., 1986. Dynamics of orogenic wedges and the uplift of high-pressure metamorphic rocks. Geological society of America bulletin 97 (9), 1037–1053.

Räss, L., Simon, N. S., Podladchikov, Y. Y., 2018. Spontaneous formation of fluid escape pipes from subsurface reservoirs. Scientific reports 8 (1), 1–11.

Ruh, J. B., Le Pourhiet, L., Agard, P., Burov, E., Gerya, T., 2015. Tectonic slicing of subducting oceanic crust along plate interfaces: Numerical modeling. Geochemistry, Geophysics, Geosystems 16 (10), 3505–3531.

Schmalholz, S. M., Moulas, E., Plümper, O., Myasnikov, A. V., Podladchikov, Y. Y., 2020. 2d hydro-mechanical-chemical modeling of (de) hydration reactions in deforming heterogeneous rock: The periclase-brucite model reaction. Geochemistry, Geophysics, Geosystems 21 (11), e2020GC009351.

Thielmann, M., Kaus, B. J., 2012. Shear heating induced lithospheric-scale localization: Does it result in subduction? Earth and Planetary Science Letters 359, 1–13.

Thielmann, M., Schmalholz, S. M., 2020. Contributions of grain damage, thermal weakening, and necking to slab detachment. Frontiers in Earth Science 8, 254.

Toussaint, G., Burov, E., Jolivet, L., 2004. Continental plate collision: Unstable vs. stable slab dynamics. Geology 32 (1), 33–36.

van Hunen, J., van den Berg, A. P., Vlaar, N. J., 2001. Latent heat effects of the major mantle phase transitions on low-angle subduction. Earth and Planetary Science Letters 190 (3-4), 125–135.

Warren, C. J., Beaumont, C., Jamieson, R. A., 2008. Formation and exhumation of ultra-high-pressure rocks during continental collision: Role of detachment in the subduction channel. Geochemistry, Geophysics, Geosystems 9 (4).

White, S. t., Knipe, R., 1978. Transformation-and reaction-enhanced ductility in rocks. Journal of the Geological Society 135 (5), 513–516.

Yamato, P., Agard, P., Burov, E., Le Pourhiet, L., Jolivet, L., Tiberi, C., 2007. Burial and exhumation in a subduction wedge: Mutual constraints from thermomechanical modeling and natural p-t-t data (schistes lustrés, western alps). Journal of Geophysical Research: Solid Earth 112 (B7).

Young, D. J., Hacker, B. R., Andersen, T. B., Corfu, F., 2007. Prograde amphibolite facies to ultrahigh-pressure transition along nordfjord, western norway: Implications for exhumation tectonics. Tectonics 26 (1).

Zhou, X., Li, Z.-H., Gerya, T. V., Stern, R. J., 2020. Lateral propagation–induced subduction initiation at passive continental margins controlled by preexisting lithospheric weakness. Science Advances 6 (10), eaaz1048.

Acknowledgements

I thank all my friends and family, especially my mother *Karin Candioti*, my father *Francesco Candioti* and my brother *Matteo Candioti* for their constant support during my studies.

This work was supported by the *Swiss National Science foundation* (SNF grant No. 200020 163169).